A Critical Investigation into the Spray-Drying of Hydroxyapatite Powder for Thermal Spray Applications

By

Qasim Murtaza, BSc. Engg, M.Tech.

Supervisors

Dr. Joseph Stokes and Prof. M.S.J. Hashmi

School of Mechanical and Manufacturing Engineering
Dublin City University

Ph.D **May 2006**

Declaration

I herby certify that this material, which I now submitted for assessment on the programme of study leading to the award of Doctor of Philosophy is entirely my own work and has not been taken form the work of others and to the extent that such work has been cited and acknowledged within the text of my work.

Qasim Murtaza

ID No: 52163334

Dedication

This thesis is dedicated to my father Prof. Ghulam Murtaza and My mother Razia Sultana whose inspiration and constant support allowed me to come up to this success and to me who are the symbol of love , trust and greatest personality.

Acknowledgements

The author wishes to express his heartiest gratitude and profound indebtness to his thesis supervisors Dr Joseph Stokes (main supervisor), lecturer in the School of Mechanical and Manufacturing Engineering, Dublin City University, for their constant guidance, friendly enthusiasm, constructive criticism, valuable suggestions, encouragement, benevolent help and practical hand on assistance in carrying out the research work as well as in writing this thesis and Prof. M.S.J.Hashmi (co-supervisor), Head of the School, DCU, for their fatherhood encouragement and support.

Author wishes his thanks to Dr Malika Ardhaoui, of the School of Mechanical and Manufacturing Engineering for her support and guidance with design of experiments.

Author also, express to thanks Dr. Aran Rafferty, Ceramic Research officer, and Dr Tim Prescott, Senior Research Officer, for their help and training on the characterisation equipment.

Author would like to express special thanks to Spraynet of Thematic Network of European Union without whose funding this project would not have been made possible.

Sincere thanks are due to school technicians for their generous assistance; especially appreciation goes to Mr Liam Senior Technician, Mr Keith Hickey IT Administrator and Mr Michael May, Technician, thanks are also due to the officers and staff of the school for their help in various stages of the study. The author would like to thank all friends and colleagues.

The author wishes to express his heartfelt gratitude and love to his fiancée Zainab Naqvi for provide her continuous love, support, inspiration and long weekend calls.

Author wishes thanks to his Alma-matar Aligarh Muslim University. Special thanks to all his past teachers and my ex-colleagues of the Department of Mechanical Engineering for their encouragement namely Prof. M. Hamidduin who was also my Master degree project guide, Prof. Zaheer Haider, Prof. Aliul H. Rizvi, Prof. A.A. Nizami, Dr. Mohd Muzammil, Mr. Khusro Qasim, and special thanks for my best friend Dr. Abid Ali Khan who have provided him with much inspiration to further his education.

At last but never the least, the author wishes to express her gratitude to his family, especially his brother Moshin Murtaza and sister Tasneem Fatima for their continued encouragement and inspiration throughout his life as well as this research work.

A Critical Investigation into the Spray-Drying of Hydroxyapatite Powder for Thermal Spray Applications

By
Qasim Murtaza B.Sc Engg, M.Tech

ABSTRACT

This work examines the investigation of the spray drying process of Hydroxyapatite powder (HA) used as a thermal spray deposit in the application of orthopaedic femoral implants. In this research, the Niro-Minor™ mixed spray dryer was used for both modelling and experimental studies. The process parameters investigated included HA slurry viscosity, temperature, and air flowrate. Computational Fluid Dynamic (CFD) modelling and validation of the spray drying of HA powder was performed. An analysis of the spray drying of the HA slurry, was performed using the UMETRI AB, MODDE 7 software.

For the CFD analysis, the Spray dryer was divided into the three parts; two-fluid nozzle, the drying chamber, and atomisation. The Standard K-ϵ, Reliable K-ϵ and Reynolds Stress Model models were used to predict velocity profiles of the air, feed pipe of the two external nozzle and temperature profile for the drying chamber. Different model results were compared, studied and compared with experimental results. The standard K-ϵ method is found to have good agreement with the experiment data in predicting the air and feed nozzle velocities, and the Reliable K-ϵ simulated the temperature profile of the drying chamber. These results were also used to predict atomisation modelling. The models hence have proved to be an innovative method of understanding the dynamics of the spray drying technique.

In the statistical analysis of the spray drying process, factors such as temperature and flowrate of the inlet hot air in the spray dryer, viscosity of feed/ HA and responses (chamber powder size, cyclone powder size, deposition of powder on the wall of spray dryer and overall thermal efficiency) were determined using a Multiple Linear Regression (MLR) method and the statistical analysis of main and interaction effects were quantified using the ANOVA test. For the chamber particle size, the statistical analysis showed that the viscosity of the HA slurry is most significant and for the cyclone particle size, the main affects are temperature, viscosity and flow rate, and also the interaction effect of temperature and viscosity were significant. Wall deposition is influenced by temperature and the interaction of both temperature and viscosity. The spray dried HA powders were also studied in terms of morphology. The two main shapes observed are a doughnut and solid sphere shape as a result of the different input parameters. A solid sphere of HA spray dried powder with pores was observed when a viscosity of 75 mPa.s was applied to all three levels of drying temperature. Doughnut shaped particles were observed when a slurry viscosity of 50 mPa.s was utilised. This doughnut phenomenon was more pronounced with an increase in the spray drying air temperature (461K) in the chamber powders. While a viscosity of 50 mPa.s and temperature of 461K yielded the ideal particle size and range, in terms of HA morphology, where a mix of solid and doughnut shape powder was produced. This is beneficial for HA thermal spray coatings as they require porous coatings to help the growth of the cells inside the coating to provide a strong bioactive bond between the implant and bone. This research provides a deeper understanding into the spray drying of hydroxyapatite powders providing data to improve its application in the use of HA deposits to anatomically join femoral implants to human tissue.

Table of CONTENTS

Page

Declaration ---------- I

Acknowledgements ---------- II

Abstract ---------- III

Table of Contents ---------- IV

List of Figures ---------- X

List of Tablets ---------- XVII

Chapter 1 Introduction

2.1 Introduction ---------- 1

Chapter 2 Literature Review

2.1 Introduction ---------- 6

2.2 Powder Production ---------- 7
- 2.2.1 Crushing ---------- 7
- 2.2.2 Agglomeration ---------- 7
- 2.2.3 Chemical ---------- 8
- 2.2.4 Atomisation ---------- 8

2.3 Spray Drying Process ---------- 10
- 2.3.1 Spray Drying Atomization ---------- 10
- 2.3.2 Spray – Air Contact (Mixing and Flow) ---------- 16
- 2.3.3 Spray – Evaporation ---------- 18
- 2.3.4 Production Separation ---------- 20

2.4 Operating Variables of a spray Dryer ---------- 22
2.4.1 Energy Available for Atomization ---------- 22
2.4.2 Feed Properties ---------- 22
2.4.3 Feed Rate ---------- 23
2.4.4 Air Flow ---------- 23
2.4.5 Drying Temperatures ---------- 23

2.5 Powder Characterisation of Spray Dried Products ---------- 25
2.5.1 Bulk Density ---------- 25
2.5.2 Powder Flowability ---------- 26
2.5.3 Particle Friability ---------- 28
2.5.4 Particle Morphology ---------- 28

2.6 Computational Fluid Dynamic (CFD) Spray Dryer ---------- 31
2.6.1 Introduction ---------- 31
2.6.2 Modelling of Slurry and Droplets ---------- 32
2.6.3 Evaporation Models ---------- 33
2.6.4 Commercial Softwares for Spray Dryer ---------- 34

2.7 Thermal Spray Powders ---------- 39
2.7.1 Plasma Arc Spraying ---------- 40

2.8 Spray Dried Thermal Spray Powders ---------- 42
2.8.1 Hydroxyapatite Thermal Spray Powder ---------- 42
2.8.2 Manufacturing of HA Powder ---------- 43

2.9 Summary/Overview ---------- 46

Chapter 3 Experimental Equipment & Procedures

3.1 Introduction ---- 48

3.2 Description of the Spray Dryer ---- 50
3.2.1 Drying Chamber ---- 51
3.2.2 The External Two–Fluid Nozzle Atomiser ---- 51
3.2.3 Operating Panel ---- 52

3.3 Operation Procedure ---- 54

3.4 Viscosity of HA Slurry ---- 57
3.4.1 The Falling Sphere Method ---- 58
3.4.2 Rotational Type Viscometer ---- 59

3.5 Airflow Measurement ---- 61
3.5.1 Nozzle Velocities ---- 61
3.5.2 Air Flow inside the Spray Dryer ---- 62

3.6 Feed Flow Measurement ---- 65

3.7 Temperature Devices ---- 66

3.8 Spray Droplet Size Devices ---- 69

3.9 Powder characterisation ---- 72

Chapter 4 Simulation and Modelling

4.1 Introduction ---- 73

4.2 Turbulence Models ---- 78
4.2.1 Standard $k-\varepsilon$ Model ---- 79
4.2.2 Realizable $k-\varepsilon$ Model ---- 79
4.2.3 Reynolds Stress Model (RSM) ---- 79

4.3 Modelling of the Spray Dryer ---- 81

4.4 Geometry Creation ---- 81

4.5 Meshing of Spray Dryer ---- 83
4.5.1 Meshing of Two-Fluid Nozzle and Spray Dryer ---- 83
4.5.2 Mesh Checking ---- 86
4.5.3 Analysis of Skewness ---- 87

4.6 Fluent Solvers ---- 90
4.6.1 Nozzle Modelling ---- 91
4.6.2 Drying Chamber Modelling ---- 92
4.6.3 Atomisation Modelling ---- 93
4.6.4 Solver Numerical Schemes ---- 94
4.6.5 Linearization ---- 95
4.6.6 Discrete Phase Model ---- 95
4.6.7 Spray Model ---- 98

4.7 Post Processing ---- 99

Chapter 5 Results and Discussion

5.1 Introduction ---------- 100

5.2 Calibration and Model Checks ---------- 100
5.2.1 Viscosity Results ---------- 100
5.2.2 Air Drying Temperature versus Air Flow ---------- 101

5.3 Experimental Analysis ---------- 102
5.3.1 Data Analysis and Optimisation ---------- 103
5.3.2 Statistical Design Analysis ---------- 104
5.3.3 Particle Size Distribution ---------- 113
5.4.4 Morphology of HA Spray Dried Powder ---------- 117
5.5.5 Comparison of Statistical Model ---------- 125
105

5.4 The External Two-Fluid Nozzle Simulation---------- 127
5.4.1 Air Pipe Simulation ---------- 127
5.4.2 Feed Pipe Simulation ---------- 132

5.5 Temperature Profile Simulation in the Spray Dryer ---------- 135

5.6 Atomisation Simulation ---------- 141

5.7 External Two-Fluid Nozzle Comparison ---------- 147

5.8 Temperature Profile Comparison ---------- 157

5.8 Atomisation Comparison ---------- 158

Chapter 6 Conclusions and Recommendations

6.1 Conclusions ---------- 160

6.2 Recommendations---------- 164

Publications Arsing From This Research 165

References 166

Appendix-A ---------- 183

Appendix-B ---------- 186

Appendix-C ---------- 198

Appendix-D ---------- 222

List of Figures

Figure 2.1: Schematic sketch of the Atomisation Processes. ---------- 9

Figure 2.2: Various Stages of the Spray Drying Process. ---------- 11

Figure 2.3: Different types of atomizers. ---------- 13

Figure 2.4: A systematic sketch of external-two-fluid nozzle. ---------- 14

Figure 2.5: An industrial (Niro-Type) External-Two-Fluid Nozzle. ---------- 15

Figure 2.6: Air -flow patterns in spray dryers. ---------- 17

Figure 2.7: Mixed air-flow pattern in a spray dryer used in the present research. ------- 18

Figure 2.8: Drying rate curve. ---------- 19

Figure 2.9: Different shapes of spray dried thermal spray powder. ---------- 20

Figure 2.10: Schematic cross-section of spray dryer. ---------- 21

Figure 2.11: Different shaped powders which cause different types of flow behaviour of spray dried powder ---------- 27

Figure 2.12: Different types of particle morphology of spray dried powders. ---------- 28

Figure 2.13: Equipments involved in the plasma thermal spray process. ---------- 40

Figure2.14: A systematic of plasma arc coating process. ---------- 41

Figure 3.1: Equipment and parameters used in the experimental phase of the research. ---------- 49

Figure 3.2: Systematic sketch of the spray dryer (Niro-Minor Production). ---------- 50

Figure 3.3: Schematic cross-section of the external two-fluid nozzle. ---------- 52

Figure 3.4: Operating panel of the spray dryer. ---------- 53

Figure 3.5: Assembly of the external two fluid nozzle with adjusting screw to set the spray angle. ---------- 54

Figure 3.6: Viscosity measurement techniques: (A) Cylinder and falling sphere method, (B) Rheology international series 2 viscometer. ---------- 58

Figure 3.7: Cone and Plate Viscometer ----- ---------- 60

Figure 3.8: Velocity measured at the top of the spray dryer by electronic potentiometer ---------- 62

Figure 3.9: Air nozzle of two fluid nozzle velocity measured by electronic potentiometer. ---------- 62

Figure 3.10: Pressure tapping of inlet and outlet of the manometer to measure the flowrate inside the spray dryer. ---------- 64

Figure 3.11: Mesh points used to measure the temperature experimentally. ---------- 67

Figure 3.12: Mesh to hold the thermocouple inside the spray dryer to measure the temperature profile. ---------- 68

Figure 3.12: Systematic sketch the principle of MasterSizer 2000. ---------- 71

Figure 4.1: Fluid region of pipe flow is discretized into a finite set of control volumes (mesh). ---------- 75

Figure 4.2: Systematic sketch used to solve complex physical fluid problems. --------- 77

Figure 4.3: Gambits graphical user interface (GUI). ---------- 81

Figure 4.4: Geometry model (Faces) of the feed and air pipe nozzles. ---------- 82

Figure 4.5: Axis-symmetric section of the chamber of the spray dryer. ---------- 82

Figure 4.6: Mesh of air pipe of external two-fluid nozzle. ---------- 84

Figure 4.7: Mesh of feed pipe of external two-fluid nozzle of spray dryer. ---------- 85

Figure 4.8: Mixed mesh of axis-symmetric spray dry chamber. ---------- 86

Figure 4.9: Equi-angle skew for the air-pipe of the external two-fluid nozzle. ---------- 88

Figure 4.10: Equi-angle skew for the feed-pipe of the external two-fluid nozzle. -------- 88

Figure 4.11: Equi-angle skew for the spray dryer. ---------- 89

Figure 4.12: Systematic plan for the spray dryer modelling. ---------- 90

Figure 4.13: The flow path for nozzle simulation. ---------- 91

Figure 4.14: The flow path for drying chamber of the spray dryer simulation for temperature and velocity profile. ---------- 92

Figure 4.15: Systematic step to solve the spray dryer modelling with discrete phase.--- 93

Figure 4.16: Overview of the segregated solution method. ---------- 94

Figure 4.17: Heat, mass, and momentum transfer between the discrete and continuous phases. ---------- 97

Figure 4.18: Systematic sketch of heat and mass transfer of particle in the spray.---------- 97

Figure 5.1: Summary of fit for the experimental matrix for Multi- Linear Regression. - 104

Figure 5.2: 3D surface and contour response of particle size collected in the main drying chamber of the spray dryer for various flow rates. ---------- 108

Figure 5.3: 3D surface and contour of response of particle size collected in cyclone of the spray dryer. ---------- 109

Figure 5.4: 3D surface and contour of response of wall deposition inside the spray dryer. ---------- 110

Figure 5.5: 3D surface and contour of response of over-all thermal efficiency of the spray dryer. ---------- 111

Figure 5.6: Side wall deposition and the circulation of the velocity vector inside the spray dryer. ---------- 112

Figure 5.7: Particle size distribution at feed viscosity of HA slurry 25 mPa.s. ---------- 115

Figure 5.8: Particle size distribution at feed viscosity of HA slurry 50 mPa.s. ---------- 116

Figure 5.9: Particle size distribution at feed viscosity of HA slurry 75 mPa.s. ---------- 116

Figure 5.10: SEM micrographs of spray drying (for an inlet temperature of 398K) HA powder. ---------- 120

Figure 5.11: SEM micrographs of spray drying (for an inlet temperature of 421K) HA powder. ---------- 121

Figure 5.12: SEM micrographs of spray drying (for an inlet temperature of

461K) HA powder. ---------- 122

Figure 5.13: Different solid sphere shapes of HA powder. ---------- 123

Figure 5.14: Different doughnut shapes of HA powder. ---------- 124

Figure 5.15: Comparison of responses of experiment and statistical model for optimization of the spray dryer factors (Temperature, Viscosity and Flowrate). ---------- 126

Figure 5.16: (a) Velocity profile (b) turbulence intensity and (c) temperature distribution at 5.48 m/s inlet. ---------- 129

Figure 5.17: Velocity vector at 5.48 m/s inlet velocity of the air pipe. ---------- 129

Figure 5.18: Outlet velocity at air pipe of the two-fluid nozzle at 5.48 m/s inlet velocity. ---------- 130

Figure 5.19: Peristaltic pump flow rate as a function of peristaltic pump rpm. ---------- 132

Figure 5.20: The feed pipe velocity profile and vector at 7.6e-7 m^3/s flowrate of peristaltic pump. ---------- 133

Figure 5.21: Velocity profile at outlet of Feed pipe of two-fluid nozzle. ---------- 134

Figure 5.22: Temperature profile by SK-ϵ, RK-ϵ and RSM methods (inlet condition Temp-398 K, velocity-12.7m/s). ---------- 137

Figure 5.23: Temperature gradient along the axis of the spray dryer (inlet condition; temperature 398K and Velocity 12.7m/s). ---------- 138

Figure 5.24: Velocity vector using the SK-ϵ methods (inlet condition Temp-398 K, velocity-12.7m/s). ---------- 138

Figure 5.25: Velocity vector using the RK-ϵ method (inlet condition Temp-398 K, velocity-12.7m/s). ---------- 139

Figure 5.26: Velocity vector by RSM method (inlet condition Temp-398 K, velocity-12.7m/s). ---------- 139

Figure 5.27: Particles diameter, evaporation and temperature of HA slurry (Viscosity 25 mPa.s) atomisation at the hot inlet temperature 461K and flowrate 16.6 m/s. ---------- 144

Figure 5.28: Particles diameter, evaporation and temperature of HA slurry (Viscosity 50 mPa.s) atomisation at the hot inlet temperature 461K and flowrate 16.6 m/s. ---------- 145

Figure 5.29: Particles diameter, evaporation and temperature of HA slurry (Viscosity 75 mPa.s) atomisation at the hot inlet temperature 461K and flowrate 16.6 m/s. ---------- 146

Figure 5.30: Velocity vector (at 2 mins unsteady simulation) at (a) 2.19 (b) 2.95 (c) 3.65 and (d) 4.38 m/s inlet velocity (by S K-ϵ method) in the spray dryer to compare the nozzle exit velocity. ---------- 149

Figure 5.31: Velocity vector and profile at 5.48 m/s inlet velocity the nozzle (for 2 minutes (a) S K-ϵ (b) RSM, and (c) R K-ϵ method) in the spray dryer to compare the nozzle exit velocity. ---------- 150

Figure 5.32: Velocity vector and profile at 5.48 m/s inlet velocity the air pipe nozzle (for 20 minutes (a) R K-ϵ and (b) RSM method) in the spray dryer to compare the nozzle exit velocity. ---------- 151

Figure 5.33: Velocity Profile at the top of spray dryer. ---------- 152

Figure 5.34: Velocity profile along the axis of air nozzle pipe. ---------- 154

Figure 5.35: Temperature profile measured experimentally (inlet condition tem-398 K, velocity-12.7m/s). ---------- 155

Figure 5.36: Temperature profile by SK-ϵ, RK-ϵ and measured (inlet condition tem-398 K, velocity-12.7m/s). ---------- 157

Figure 5.37: Comparison of temperature gradient along the axis inside the spray dryer (inlet condition; temperature 398K and Velocity 12.7m/s). ---------- 157

Figure 5.38: Comparison of mean particle size of simulated and experimental data of spray dried HA powder. ---------- 158

Figure 5.39: The roof of the spray dryer with deposition of HA slurry after spray drying of HA slurry (inlet temp 461K, flow rate 16.6 m/s). ---------- 159

Figure B.1: Air nozzle pipe (Niro Production Minor). ---------- 186

Figure B.2: Feed nozzle pipe (Niro Production Minor). ---------- 187

Figure B.3 Spray dryer (Niro Production Minor). ---------- 188

Figure B.4: Atomisation condition of the spray dryer. ---------- 189

Figure B.5: K factor as a function of product and gas ratio. ---------- 190

Figure B.6: Initial air velocity of air pipe nozzle at calibrated scale ---------- 193

Figure B.7: Calibration graph between HA feed slurry viscosity and density. ---------- 194

Figure B.8: Calibration graph between HA feed slurry flowrate and rpm of peristaltic pump. ---------- 194

Figure B.9: Preparation of HA slurry in-house for the spray drying. ---------- 196

Figure B.10: HA XRD spectra and final sintered HA XRD spectra. ---------- 197

Figure D.1: Velocity profile at 2.19 m/s inlet velocity of air pipe nozzle, turbulence intensity and temperature distribution. ---------- 224

Figure D.2: Velocity profile at 2.95 m/s inlet velocity of air pipe nozzle, turbulence intensity and temperature distribution. ---------- 224

Figure D.3: Velocity profile at 3.65 m/s inlet velocity of air pipe nozzle, turbulence intensity and temperature distribution. ---------- 225

Figure C.4: Velocity profile at 4.38 m/s inlet velocity of air pipe nozzle, turbulence intensity and temperature distribution. ---------- 225

Figure D.5: Velocity profile at 7.31 m/s inlet velocity of air pipe nozzle, turbulence intensity and temperature distribution. ---------- 226

Figure D.6: The feed pipe velocity profile and vector at 50 rpm of peristaltic pump. ---------- 227

Figure D.7: The feed pipe velocity profile and vector at 75 rpm of peristaltic pump. ---------- 227

Figure D.8: The feed pipe velocity profile and vector at 100 rpm of peristaltic pump. ---------- 228

Figure D.9: Temperature profile and velocity vector using the SK-ϵ, RK-ϵ, RSM methods, and measured (inlet condition tem-398 K, velocity-14.6m/s). ---------- 229

Figure D.10: Temperature profile and velocity vector using the SK-ϵ, RK-ϵ, RSM method, and measured (inlet condition tem-398 K, velocity-16.6m/s). ---------- 230

Figure D.11: Temperature profile (a) and velocity vector (b) using the SK-ϵ, RK-ϵ, RSM methods, and measured (inlet condition tem-421 K, velocity-12.7m/s). ---------- 231

Figure D.12: Temperature profile (a) and velocity vector (b) using the S*K*-ϵ, R*K*-ϵ, RSM method, and measured (inlet condition tem-421 K, velocity-14.6m/s). ---------- 232

Figure D.13: Temperature profile (a) and velocity vector (b) using the S*K*-ϵ, R*K*-ϵ, RSM method, and measured (inlet condition tem-421 K, velocity-16.6m/s). ---------- 233

Figure D.14: Temperature profile (a) and velocity vector (b) using the S*K*-ϵ, R*K*-ϵ, RSM method, and measured (inlet condition temperature-461 K, velocity-12.6m/s). ---------- 234

Figure D.15: Temperature profile and velocity vector using the S*K*-ϵ, R*K*-ϵ, RSM method, and measured (inlet condition temperature-461 K, velocity-14.6m/s). ---------- 235

Figure D.16: Temperature profile and velocity vector using S*K*-ϵ, R*K*-ϵ, RSM method, and measured (inlet condition temperature-461 K, velocity-16.6m/s). ---------- 236

List of Tables

Table 5.1: Air drying temperature and air flow rate at the different positions. -------- 101

Table 5.2: Experimental value for different response for various conditions. ---------- 103

Table 5.3: R-Squared of the polynomial models and p-values of both linear and interaction effects of responses. ---------- --- 105

Table 5.4: Optimisation factor and target for validation of statistical model. -------- 125

Table 5.5: Inlet and exit velocity of air nozzle pipe or various atomising scales. ------ 127

Table 5.6: Iterations to converge the solution with standard criteria at 5.48m/s inlet velocity. ---------- 131

Table 5.7: Iterations to converge the solution with standard criteria for feed nozzle.-- 134

Table 5.8: Mean zone temperatures found for varying hot air velocities. ---------- 140

Table 5.9: Boundary conditions used for atomisation simulation (HA Slurry of 25 mPa.s). ---------- 141

Table 5.10:- Iterations to Converge the Solution with Standard Criteria for the air nozzle. ---------- 148

Table A.1: Limit of allowable trace elements in HA product. ---------- 183

Table A.2: Properties of HA and Plasma spray parameter for coating. ---------- 185

Table B.1: Inlet air flow rate of the spray dryer. ---------- 192

Table B.2: Properties of HA slurry; viscosity, density and flowrate. ---------- 195

Table B.3: Physical properties of HA Powder. ---------- 197

Table D.1: ANOVA ---------- 222

Table D.2: HA slurry properties used in atomisation simulation. ---------- 237

Table D3: Injection of nozzle properties. ---------- 237

Nomenclature

A	Area (m/s)
A_p	Surface area of the particle (m²)
C_D	Drag coefficient
C_d	The coefficient of discharge
c_p	Heat capacity of the particle (J/kg-K)
$C_{i,s}$	Vapour concentration at the droplet surface (kgmol/m³)
$C_{i,\infty}$	Vapour concentration in the bulk gas (kgmol/m³)
$c_{p,i}$	Heat capacity of volatiles evolved (J/kg)
D	Diameter (m)
$D_{i,m}$	Diffusion coefficient of vapour in the bulk (m²/s)
d_p	Particle droplet diameter (m)
F_{other}	Other interaction forces (N)
G_b	Generation of turbulence kinetic energy due to buoyancy
h	Convective heat transfer coefficient (W/m²-K)
h_{fg}	Rate of evaporation (kg/s)
h_l	Latent heat of volatiles evolved (J/kg)
h_{pyrol}	Heat of pryrolysis as volatiles are evolved (J/kg)
I	Radiation intensity (cd)
$\vec{J}_j$	Diffusion flux of species j
k	Thermal conductivity (W/m-K)
k_p	Particle thermal conductivity (W/m-K)
K_S	Wave number
Kn	Kundsen number
k_c	Mass transfer coefficient (m/s)
k_∞	Thermal conductivity of the continuous phase (W/m-K)
k_{eff}	Effective conductivity (W/m-K
$M_{w,i}$	Molecular weight of species i (kg/kgmol)
$m^{\cdot}$	Mass flow rate (kg/s)

m_p	Mass of the droplet (kg)
$\dot{m}_p$	Mass flow rate of the particles
$\overline{m}_p$	Average mass of the particle in the control volume (kg)
$m_{p,0}$	Initial mass of the particle (kg)
$\dot{m}_{p,o}$	Initial mass flow rate of the particle injection tracked (kg/s)
Δm_p	Change in the mass of the particle in the control volume (kg)
N	Nusselt number
N_i	Molar flux of vapour (kgmol/m²-s)
Oh	Ohnesorge number
P	Pressure (Pascal)
Pr	Prandtl number
Q	Volumetric flowrate m³/sec
r	radius (m)
Re	Reynolds number
Re_d	Reynolds number based on the particle diameter
Sc	Schmidt number
S_h	Heat of chemical reaction
S_m	Mass added to the continuous phase from the dispersed phase (kg)
S_ϕ	Surface of ϕ per unit volume
T	Temperature (k)
T_p	Droplet temperature (k)
T_∞	Temperature of continuous phase (K)
T_p	Temperature of the particle upon exit of the control volume (K)
T_{ref}	Reference temperature of enthalpy (K)
ΔT_p	Temperature change of the particle in the control volume (K)
Δt	Time step (s)
u	Axial component of velocity at the injector exit (m/s).
u_p	Velocity of the particle (m/s)
v	velocity (m/sec)
We	Weber number
Y_j	Mass fraction of species j (%)
Y_M	Fluctuating dilatation in turbulence to the overall dissipation rate.
ε_p	Particle emmissivity (dimensionless)
σ	Stefan-Boltzmann constant ($5.67*10^8$ W/m²-K⁴)
θ_R	Radiation temperature (K)
ϕ	Fluid Property
∇	Gradient of ϕ
Γ	Diffusion coefficient ϕ
μ	Viscosity of the fluid (Pa.s)

ρ_p	Droplet density (kg/m³)
ε_p	Latent heat (J/kg)
σ	Particle emissivity (dimensionless)
σ_ε	Turbulent Prandtl number
θ	Angle (degree)
η	Initial wave amplitude (m)
Ω	Rotation (rpm)

1

Introduction

1.1 INTRODUCTION

The Spray drying technique is a continuous process of drying slurry. The process involves the atomisation of a feedstock into a spray, and then the interaction between the spray and the drying medium results in moisture evaporation. The resulting dried product converts either into a free flowing powder, granule or agglomerate type of material and its type depends upon the physical and chemical properties of the feedstock, dryer design and its operating parameters [**1,2**]. The dried powder can be easily controlled to its precise quality standards such as particle size, particle size distribution, bulk and particle density, friability, dispersibility and flowability with careful choice of its initial parameters [**3**].

Powders can be used to produce thermally sprayed coatings to improve the serviceability of engineering components and biomedical implants [**1,4**]. This process involves powders been carried into a thermal spray combustion chamber which heats/melts and then propels it onto a substrate as a coating. This coating provides the substrate with a protective layer from wear, corrosion and thermal effects. In the case of bio-coatings, these coatings are the attachment of cells onto femoral implants. Thermal spray powders can be coated by High Velocity Oxy-Fuel (HVOF) or Plasma spray techniques [**5**]. These thermal spray coatings have lenticular or lamellar grain structure due to quick solidification of small globules, and are flattened due to them striking a cold surface at high velocities [**6**]. In most cases, the in-flight particles are molten or partially molten before impact and solidify a few microseconds after impact and this depends upon the particle size and shape during the production of the thermal spray powder [**6**]. The powder properties and characteristics have a direct impact on coating quality, ease of application and performance in its end use

thus depend upon the methods of manufacture, purity, morphology and particle size distribution which yields free flow powders [7]. Therefore thermal spray powders should be free flowing with narrow distribution size and have spherical shape [8].

In general, there are four basic methods of producing powders for thermal spraying; crushing, agglomeration, chemical and atomisation [9]. Each method can be further sub-divided and powders can also be produce by various combinations from each group. Among all, spray-drying is becoming an important tool in the production of thermal spray powders [6,7,10,11]. There are several hundred commercial powders specifically developed for the various spray drying process; metals, metals alloys, ceramics, carbides and polymers [10,11].

Thermal spray powders are produce using a mixed type spray dryer, as it gives higher temperature exposure and more residence time of spray to evaporate in the drying chamber. Wherein the external-two fluid nozzle of the mixed spray dryer system is preferable in producing thermal spray powders so as to avoid clogging and to control powder size by varying atomising pressures and this nozzle atomisation are generally form coarse particle powders with good flowability and the variation of the pressure allows control over the feed rate and the spray characteristics [1,2,12]. The emerging droplets from the nozzle are then dried by hot air entering from the top of the drying chamber. The dried droplets convert into particles and are collected either at the bottom of the chamber (large dense particles) or from a cyclone (small low density particles). Further treatment may be necessary such as blending /crushing before the powder can be used in thermal spray deposition.

In the present research, the mixed spray dryer is investigated for Hydroxyapatite (HA) thermal spray powder, as HA powder has a similar chemical and phase composition to that of living bone and is often applied as a coating onto metal orthopaedic implants because the bioactive behaviour of HA coatings have proved to speed up the integration of prosthesis with living cells in the human body.

An implant is typically made of a titanium alloy and the HA coating covers the part that will enter into direct contact with the bone. The plasma spraying technique is used to produce the coating in medical industrial practice [**1,4**], however, the problem related to this type of processing is the possible decomposition of HA phase resulting from an incongruent melting of hydroxyapatite and a formation of an amorphous phase resulting from rapid solidification [**13**]. This decomposition causes different phases to form such as; $Ca_4P_2O_9$ (TP) or $Ca_3(PO_4)_2$ (TCP) as well as amorphous HA, which are less bioactive than crystalline HA, therefore, the content of which in a sprayed coating should be kept low. This may be achieved by the production of a narrow distribution size of powder, thus the spray dryer becomes an important tool in the HA manufacturing route. However, the spray drying of Hydroxyapitite (HA) for clinical applications has posed numerous problems in industry such as varying morphology, inconsistent drying and variation in size of the powder produced [**14**].

To improve the performance of spray dryer, over the past decades research in this field of spray dryer modelling has primarily dealt with the practical effectiveness of spray dryers in various industries [**15**]. These designs are mainly empirically and artistically in nature. However, experiments on full-scale spray dryer posses major difficulties, not only because of their large sizes and massive costs involved, but also because of their complex and hostile environment in which to measure the velocity of hot air, temperature profiles and particle thermal histories within the drying chamber. On the other hand, these are essential to understand the spray drying process completely. This understanding will lead to good productivity, low energy consumption and high final product quality. These short comings are encouraged and lead to take the proposed study of a full-scale spray dryer using computational fluid dynamics (CFD) techniques, and to investigate a statistical analysis of the spray drying process for HA powder production.

Chapter two is a review of literature relevant to this study. A wide ranging literature survey has been identified on all aspects of spray drying, powder characterisation of spray dried powders, computational fluid dynamic modelling of spray dryers, spray dried thermal spray powders and the HA thermal spray powder. The Chapter focuses initially on various types of spray drying and atomization techniques and especially mixed type spray dryer

with the external two-fluid nozzle, which is often used for ceramic and thermal spray powder. CFD modelling of the spray drying technique is also reviewed in detail and also, the commercial softwares available to analyse such models. Various spray dried thermal spray powders are examined and in particular the HA powder manufacturing route.

The experimental equipment involved in the spray dryer and validations of the spray dryer model, is presented in Chapter 3. The facility includes the auxiliary equipment used to calibrate the temperature and flow rate inside the drying chamber, and the feed and viscosity measurement of the HA slurry. This Chapter also includes a description of equipment used for particle size measurement, powder morphology and the procedures used to produced the results.

The computational fluid dynamic modelling of the spray dryer process, specifically velocity vector, temperature profile and atomisation model is presented in Chapter four. This chapter describes the meshing of the models and the procedures used to apply the boundaries conditions, turbulent models and solution schemes.

In Chapter five the modelling and experimental results with their associated discussions are presented. At first, the calibration of the process parameters used in the spray drying process and HA slurry properties (such as viscosity, flow rate and density) are determined. These HA slurry and spray dryer parameters are then used in the modelling methods. The modelling results show the velocity vector of the air and feed pipe of the external two-fluid nozzle, the temperature profile of the drying chamber used to predict the thermal histories of the particles with validation of the data, and the atomisation of the HA slurry. Different turbulent models are analysed and discussed during the modelling results. The analysis of the spray drying process for HA slurry drying together with a statistical experimental matrix, presents the factors (temperature, flowrate of inlet hot air and viscosity of HA slurry) and responses (the drying chamber, cyclone particle size, wall deposition and overall thermal spray dryer efficiency) in terms significant effects using ANOVA analysis. The resulting HA powder morphologies produced for various viscosities and temperatures are also presented and discussed.

Finally, Chapter six summarises the conclusions found from the results and presents recommendations for future research. The future research includes expanding the current studies to predict complete modelling using the different atomisation models so that different spray drying combinations could be modelled and other thermal spray powders investigated.

2

Literature Review

2.1 INTRODUCTION

Spray drying is not a new technology. Spray drying is the continuous process of drying and has been used in the food and pharmaceutical industries for over a century. Spray drying has many applications from foodstuff (milk powder, instant coffee, frozen vegetables) to household commodities (household detergents, plastic utensils) and manufacturing components (metal powders used in sintering and thermal spray applications) [**1**].The resultant powder produced can easily be controlled to yield precise quality standards such as; particle size, particle size distribution, bulk and particle density, friability, dispersibility and flowability.

Real engineering environments are normally complex, combining loading with chemical and physical degradation near the surface of the component. One of the most common failure mechanism in engineering service is surface wear damage. Metallic/Ceramic powders can be sprayed using thermal spraying to improve the serviceability of, engineering components or in the present research biomedical implants [**4,5**] There are various methods used to produce thermal spray powders but Spray Drying is becoming a more useful tool in the production of powders for this process. The following sections will focus powder production for thermal spraying applications on the spray-drying process, product morphologies, and the role of computational fluid dynamics in the prediction of the velocity and temperature effects on the spray dried product.

2.2 POWDER PRODUCTION

There are four basic methods of producing powders for the thermal spraying; crushing, chemical, agglomeration and atomisation [**10,16**]. Each method can be further sub-divided and powders can also be made by various combinations from each group. As a result there are a wide range of production routes available, each producing powders with their own particular characteristics and it will be demonstrated how Spray-drying is becoming an important tool used in the production of thermal spray powders [**11,17**].

2.2.1 CRUSHING

Crushing, milling or grinding have the same meaning and are generally used in the production of ceramic powders. However, it is also used to manufacture some metals and metal alloys. The most common use of this technique is in the manufacture of alumina, carbide powders and zirconia powders [**18**]. The powders produced are very dense but also have coarse, irregular, and of blocky morphologies [**18,19**]. These methods are used but not generally are suitable for the production of thermal powders as the chance of contamination from the production process and the irregular shape causes problems (choking of powder in the nozzles) during in the thermal spray deposition process [**19**].

2.2.2 AGGLOMERATION

The most common method of agglomeration is where the constituents are physically mixed together with an organic binder. The solvent is then driven off by a heat source and the resultant material sized. This binder can often be burnt off during spraying [**18,19**]. The use of spray drying has become another common method for the agglomeration technique of producing powders. Here, slurry would be formed with the constituents and this can then be fed into a rotary spray head or nozzle. This method can be used for ceramics thermal spray powders such as zirconia and cermets such as WC-Cobalt [**18**]. The powder is largely spherical but in the as-spray dried state it can be porous and friable [**19**]. The material is often densified and stabilised by sintering and/or spray densification. Sometimes sintering can be carried out to improve the crystallinity of the spray dried powders [**18**].

2.2.3 CHEMICAL

There are numerous chemical methods used in the production of powders. Chemical methods results in very fine powder particle sizes [**20**]. Such methods include; Sol Gel, Chemical Precipitation, Reaction, Reduction (hydrogen in an autoclave to reduce metal salts in the metal), Decomposition (for example metal carbonyls [**20**] and Electrolytes [**18**]). The Sol-Gel method was originally developed to produce ceramic materials for the nuclear industry in order to avoid dust (particle sizes less than 20 nm) generated in the grinding and sieving processes, and such powders have excellent flow characteristics [**21**]. Nowadays, this method has been frequently used to produce a number of ceramic powders for the thermal spraying of Hydroxyapatite, Chromia, Alumina and the stabilized Zirconia, which often contain different steps like the precursor, sol and gelation, to produce a powder [**22-24**].The gel can be shaped to the required morphology and often appears as spheres of fibres. Thermal spray powders of spherical morphology are then produced using the spray drying process post these chemical processes. [**25**].

2.2.4 ATOMISATION

Atomisation methods include; Rotating Electrode, Vibrating Electrode (arc), Centrifugal (from a melt) and Rapid Solidification (for example aluminium ribbon). However, by far the most commonly used methods are either water or gas atomisation [**17-19**]. In this process, the cheapest method is that of water atomisation whereas the most expensive is argon atomisation [**2**]. The advantage of the latter process is the better control of oxygen levels in oxygen sensitive materials such as MCrAlY's [**2**].

Some schematic processes of metal atomisation are shown in Figure 2.1. It can be observed that in an atomisation model for gas and water atomised metal powders also include the formation of highly irregular or membrane-shaped particles [**11**], as well as the occurrence of collisions between particles. Thus in conventional gas and water atomisation processes, five distinct stages can be observed [**18**];

- Stage 1: Wave formation through the initiation of small disturbances at the surface of the liquid.
- Stage 2: Wave fragment and ligament formation through shearing forces of the disturbances from stage 1.

- Stage 3: Breakdown of ligaments into droplets (primarily atomisation); regular particle shape powder when high surface tension and cooling rate exist; irregular particle shape powder by low surface tension and high cooling rate.
- Stage 4: Further deformation and thinning of droplets and wave fragments into smaller particles (secondary atomisation).
- Stage 5: Collision and coalescence of particles.

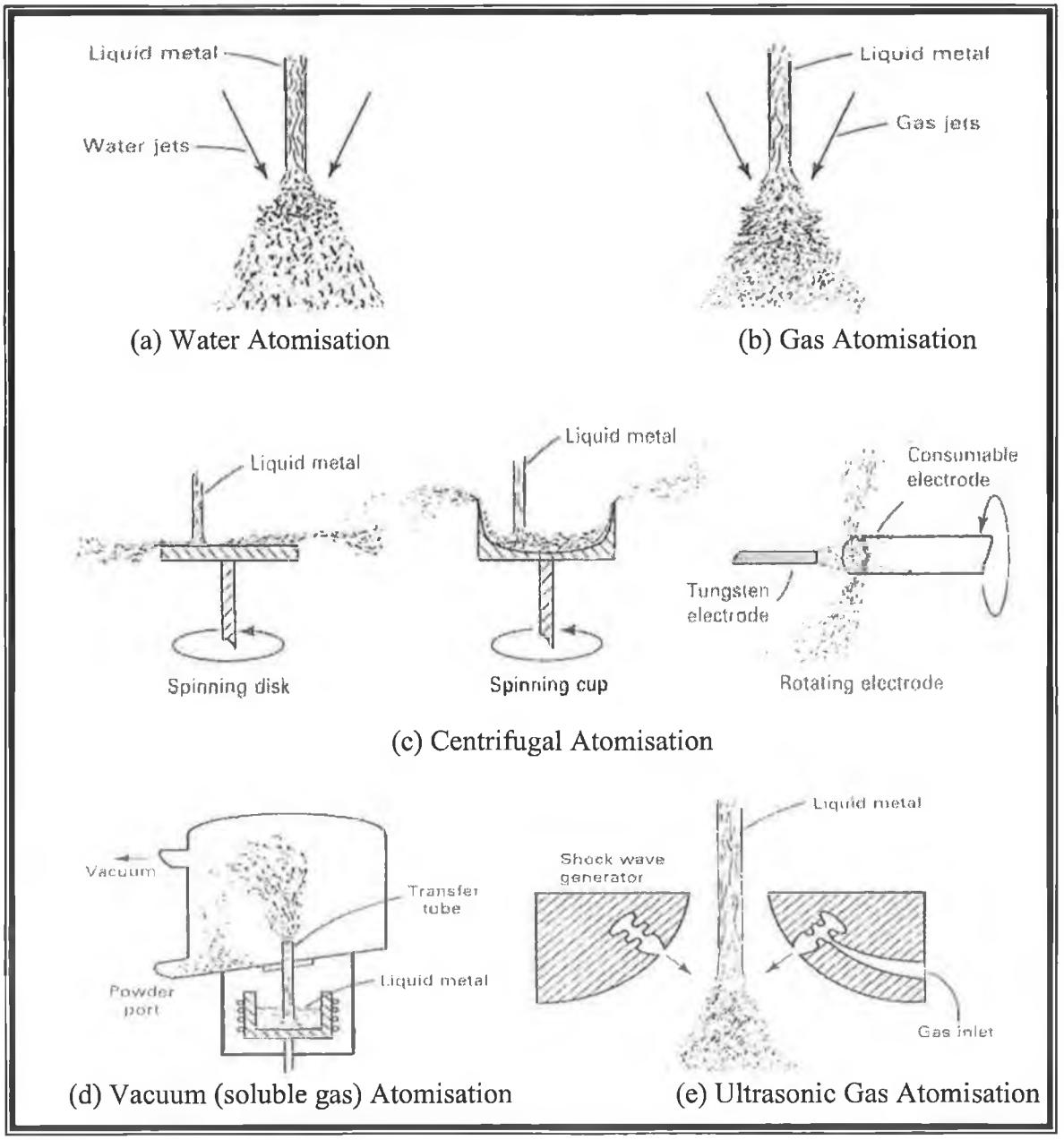

Figure 2.1: Schematic sketch of the Atomisation Processes [2, 18].

2.3 SPRAY DRYING PROCESS

The spray drying process involves the atomization of a feedstock into a spray, and then the interaction between the spray and the drying medium results in moisture evaporation. Hence in a typical spray dryer, the feedstock is transformed from a fluid state into a dried particulate form by spraying the feedstock into a hot drying medium [**1,2,18**]. The feedstock can either be a solution, suspension or paste. The drying continues until the dried product is obtained and the product has been recovered from the air. The resulting dried product converts either into a powder, granule or agglomerate type of material and its type depends upon the physical and chemical properties of the feedstock, the dryer design and the dryers operating parameters [**1**]. A typical spray drying process can be divided into four stages (Figure 2.2) [**26**].

- Atomisation
- Spray-air contact
- Spray evaporation
- Product separation

2.3.1 SPRAY DRYING ATOMISATION

The atomisation process is a reduction of fluid into fine droplets of spray (with a high surface/mass ratio). The basic mechanism and early theories on atomisation have been explained by a number of researchers [**27-30**]. Lord Raleigh [**27**] explained that a jet becomes unstable and is ready to be disturbed if its length is greater than its circumference. Weber [**28**] extended this prediction to include viscosity, surface tension, and liquid density effects. Haelin [**29**] investigated that an orderly wave formation at a jets surface, caused by a high-velocity airflow, becomes completely irregular as the velocity increases. Ohnesorge [**30**] described with the Reynolds number relationship, that the tendency of the jet to disintegrate can be expressed in terms of liquid viscosity, density, surface tension and jet size. The mechanism of liquid break-up can be expressed by the magnitude of a dimensionless number Z, (the ratio of Weber number to Reynolds number) [**30**]. In fact, all of these mechanisms act simultaneously thus influencing the spray characteristics by varying degrees [**1, 2,18, 26**].

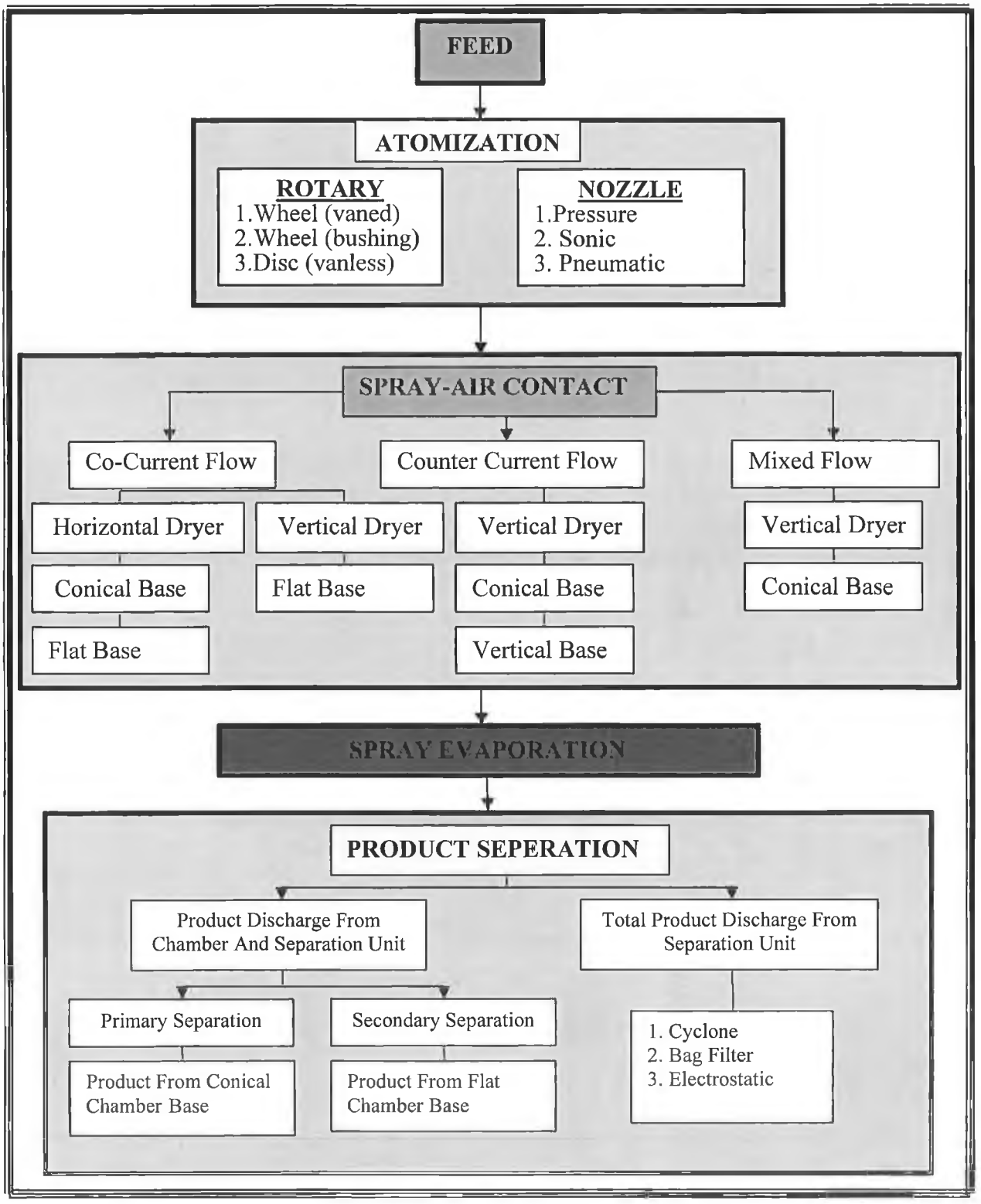

Figure 2.2: Various Stages of the Spray Drying Process, adopted from [1, 2,16].

The atomiser can be classified on the basis of the different energies (such as; centrifugal, pressure and kinetic) applied to break up the liquid bulk (Figure 2.3). Many atomizers are available such as rotary, pressure, pneumatic and sonic nozzles but this research utilises the two-fluid pneumatic nozzle, hence this type will only be described. Nozzles are generally used to form coarse particle powders that have good flowability and the variation of pressure allows control over the feed rate and the spray characteristics of the process [**1, 31**]. The droplet size produce by the nozzle spray depends upon the feed viscosity and surface tension, spray angle and pressure [**1, 26**].

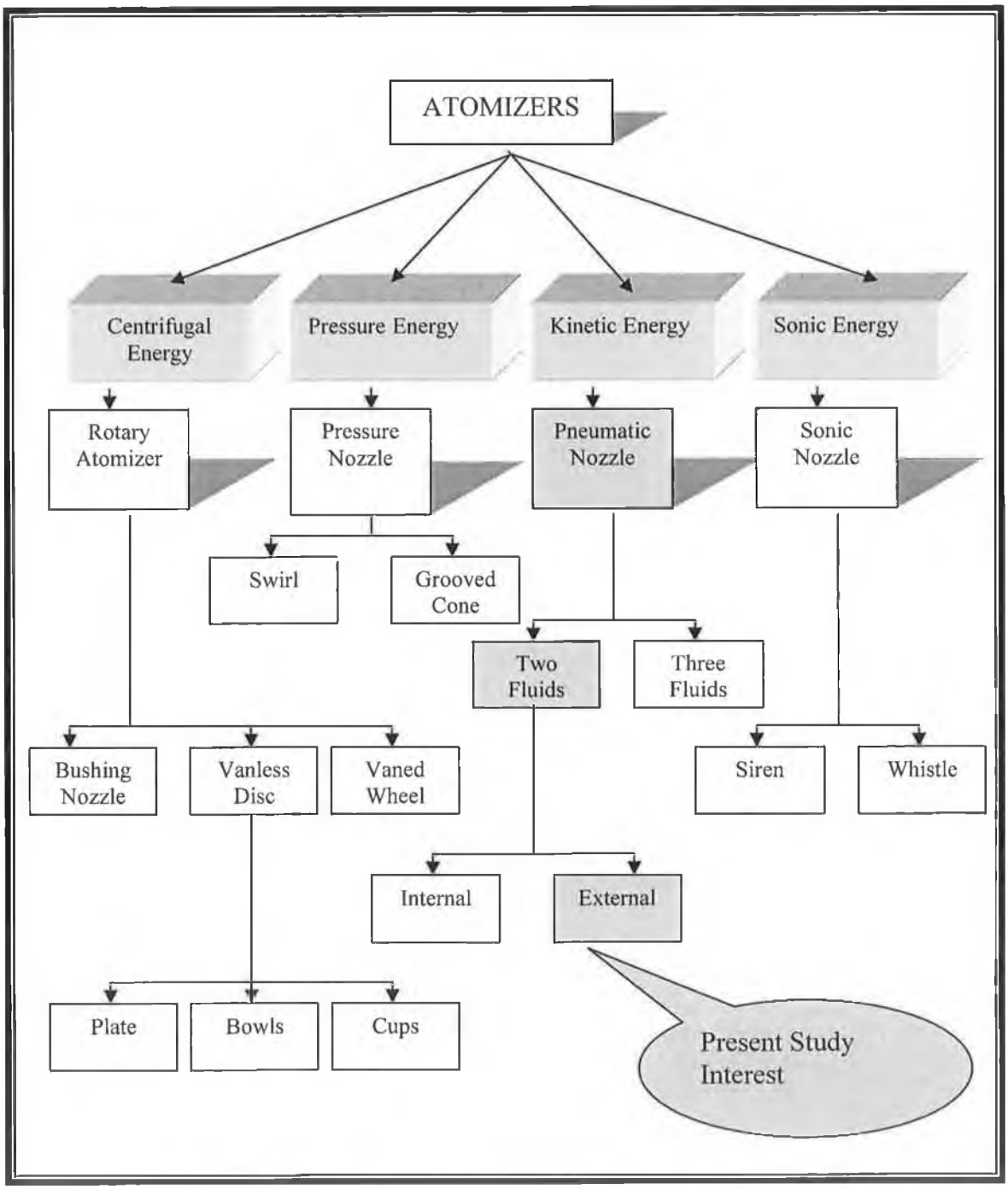

Figure 2.3: Different types of atomisers adopted from [1, 32].

(A) Pneumatic (Two-Fluid) Nozzle Atomisation

The external two-fluid nozzle is commonly used for thermal spray powder production [**1, 2,6,10,11,32**], and hence was used in the investigation in this research. Pneumatic nozzles atomised by impacting a liquid bulk (feed stock) with a high velocity gas (normally air) as shown in the Figure 2.4 and 2.5.

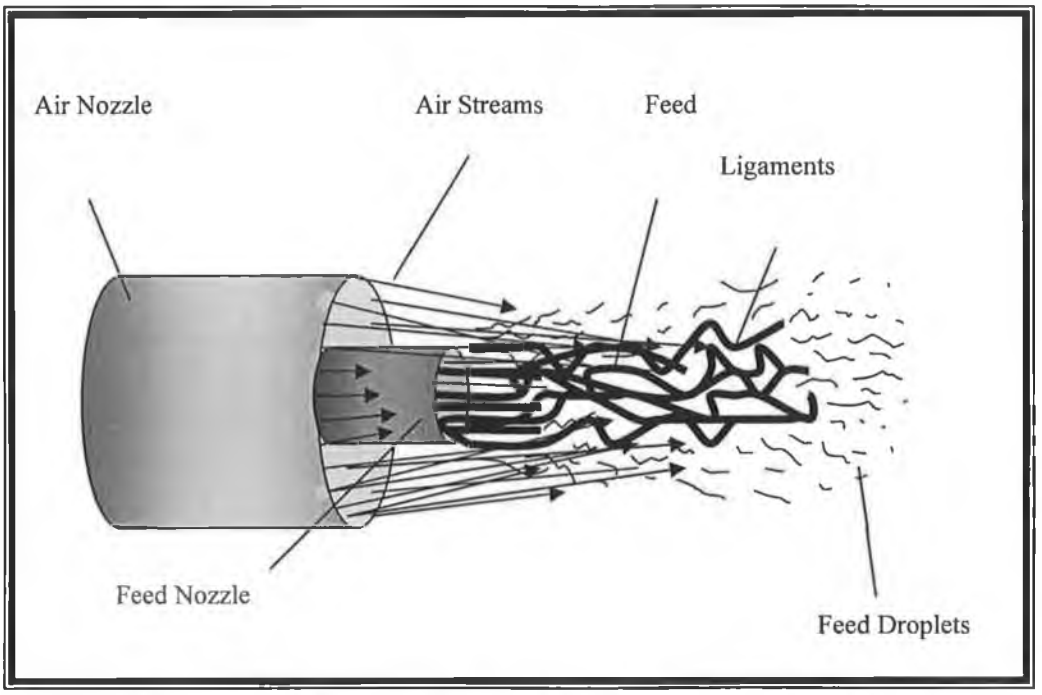

Figure 2.4: A systematic sketch of external-two-fluid nozzle.

The high velocity gas creates high frictional forces over the liquid surface causing the liquid to disintegrate into spray droplets. The liquid disintegration occurs in two phases. The first phase involves the tearing of the liquid into ligaments and large droplets and the second phase completes the atomisation by breaking these liquid forms (ligaments and large droplets) into smaller and smaller droplets. The entire process is influenced by the magnitude of the surface tension, density and viscosity of the liquid and the gaseous flow properties; velocity and density [**1, 27-30**]. The gaseous media used in the pneumatic nozzle atomisation include generally either; air, steam or inert gases (for example nitrogen and argon are chosen for metal powder production in closed cycle spray systems) [**2,10**]. The pneumatic nozzle generally uses one of four methods to provide effective air–liquid contact and breakdown of the liquid into either ligament or individual droplets forms. They are as follows [**1,16,26**]:

(i) Contact with air and liquid within the nozzle head (internal mixing).

(ii) Contact with air and liquid outside the nozzle head (external mixing – present research).

(iii) Combined internal and external mixing by using two airflows within the nozzle head (three-fluid nozzle)

(iv) Contact with air and liquid at the rim of a rotating nozzle head (pneumatic cup atomizer).

The external mixing (ii) permits greater control of atomisation by independent control of both liquid and air streams. It also produces less clogging as compared with internal and combined forms of internal and external mixing nozzles [**1**].

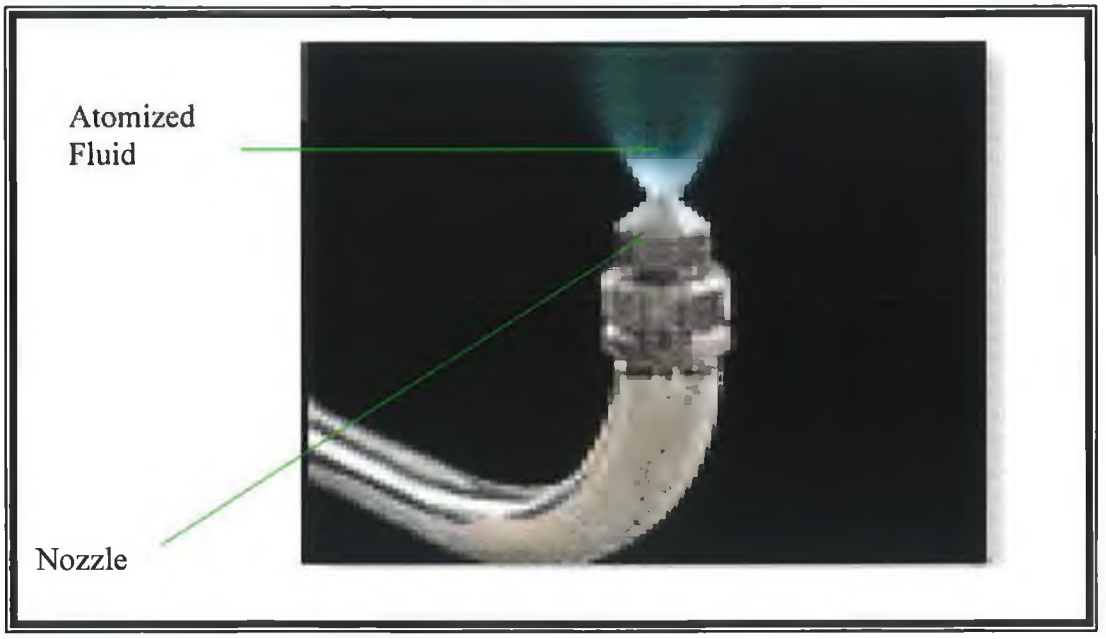

Figure 2.5: An industrial (Niro-Type) external-two-fluid nozzle [33].

The pneumatic nozzle has greater flexibility in producing small droplet sizes over a wide range of feed rates. The droplet size characteristics can be varied by adjusting the feed-air flow ratio of the nozzle head. The effect of the relative velocity between the air and liquid is dominant in determining droplet size formation. Increasing the relative velocity, decreases the mean droplet size, (as the point of contact increases the air dynamic force for atomisation increasing) [**1,2,17-19,31**]. Further, the relative velocity between droplets and the air also influence moisture evaporation rates from the spray, however others factors also include; are feed rate, operating feed pressure, cone angle, and spray pattern [**1,17-19, 26**].

The major advantage of using the external-two-fluid nozzle arrangement is to produce homogenous and small mean droplet size particles [**1,2,26**]. These characteristics can be

achieved over a wide range of operating conditions, while handling either high or low-viscosity feeds [**1,2,26**]. The pneumatic nozzle has normally a large liquid orifice compared to those used in the centrifugal pressure nozzles, thus reduce the likelihood of nozzle clogging under normal conditions. The disadvantages of the pneumatic nozzle arrangement are the high cost of compressed air usage, the reduction in spray thermal capacity due to cold atomising air entering the chamber, and very low nozzle efficiency. In the present study the two-fluid nozzle was used for atomisation and simulation for thermal spray powders in the spray drying process, as this was the process available and the type used in the production of Hydroxyapatite (HA) powders for thermal spray applications.

2.3.2 SPRAY-AIR CONTACT (MIXING AND FLOW)

The spray to air contact is determined by the position of the atomizer in relation to the drying air inlet and three types exist; co-current, counter current and mixed current types of air-flow (Figure 2.6) [**1,26**]. The co- current air mixing type is used for heat-sensitive products, and hence not suitable for thermal spray powders as they are generally non-sensitive to heat [**32**]. The counter-current arrangement is suitable for producing coarse, high bulk-density products that can withstand very hot environments [**32**]. The product particles generally have low porosity due to the reduced tendency of the droplet to expand rapidly, fracture during evaporation, and have low residence time in the main chamber which is not beneficial for thermal spray powders, as requires time to evaporate.

The air mixing system investigated in this research was of a mixed flow type. It incorporates both co-current and counter-current air mixing systems. In the air mixing flow system, the feed been atomized and hot air comes in contact in the opposite directions. Figure 2.7 shows the exact layout of the mixed flow system used in the present research. This system is effectively Figure 2.6(c) turned up-side down. Therefore the hot air enters from the top of the drying chamber and the feed spray from the bottom, both meet near the top of the chamber (evaporation occurs) and then the feed and air fall back down towards the bottom of the camber. The dried powder is collected at the bottom of the drying chamber

The feed is sprayed into the coolest gas first, and gradually flows towards the hottest zone near the top of the chamber decreasing the instantaneous rate of drying and directionally producing a higher density product. Therefore the system can be used for heat sensitive products where coarse powder requirements necessitate the use of nozzle atomizers. The particle trajectory is increased (double as compare with co-current or counter-current flow mixing systems), allowing for extra drying time, thus decreasing the overall spray dryer height required [**1,18**].

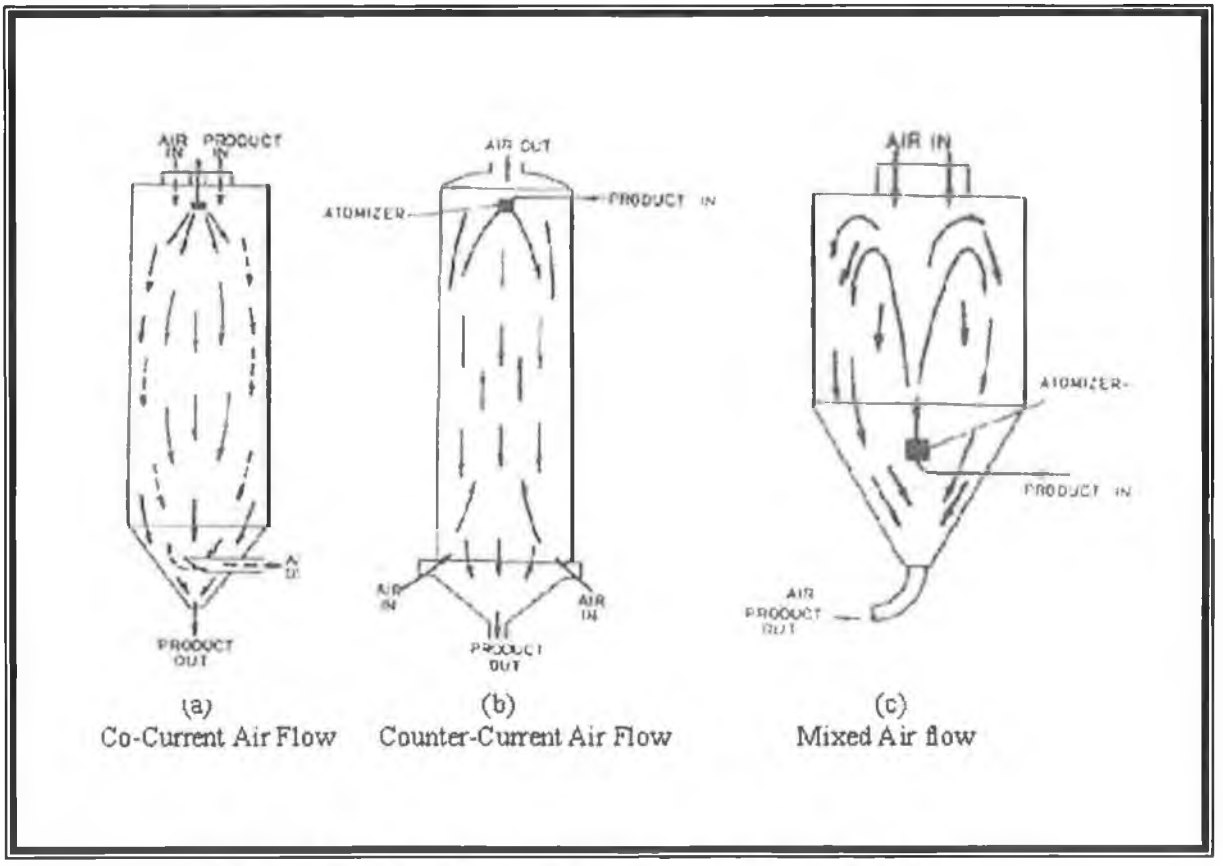

Figure 2.6: Air -flow patterns in spray dryers [1,5,19].

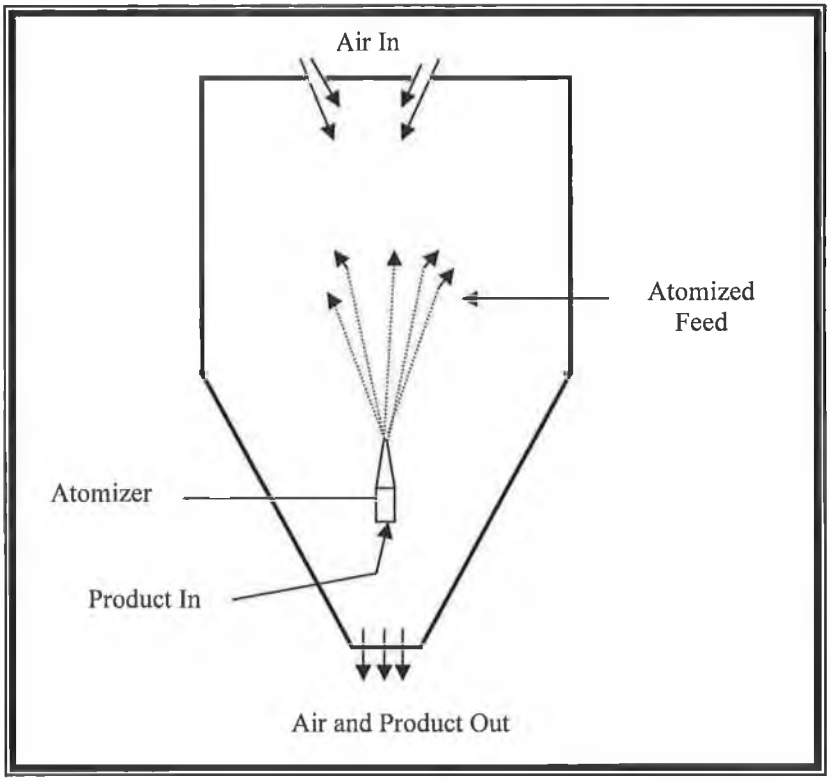

Figure 2.7: Mixed air-flow pattern in a spray dryer used in the present research.

2.3.3 SPRAY-EVAPORATION

The spray–airflow mixing can be defined as the spray behaviour such as trajectories, evaporation rate, and residence time in the drying chamber [**1,34-36**]. Drying of the droplets is carried out in two stages [**1,26,32**]. First, diffusion of moisture from within the droplet maintains a saturated condition, that means the temperature at the droplet surface approximates to the wet bulb temperature of the drying air, and as long as this lasts evaporation can be maintained at a constant rate. It is known as the constant rate period or the first period of drying [**1**]. When the moisture content becomes too low to maintain saturated conditions and it reaches a critical point where a dried shell forms on the droplet surface, evaporation now becomes dependent upon the rate of moisture diffusion through the dried surface shell. The thickness of the dried shell increases with time, causing a decrease in the rate of evaporation. This is called the falling rate of or the second period of drying [**1,26**]. This is described by the drying rate curve shown in Figure 2.8. The droplet residence time in the chamber depends upon the drying chamber design and the air flow rates (co-current, counter current and mixed current) [**35**]. Different products can exhibit different evaporation characteristics, some tend to expand, and others collapse, fracture,

leading to porous, irregularly shaped particles [**1,26,38**], as shown in Figure 2.9. Others maintain a constant spherical shape or even contract, thus the particles become more dense. The extent of any change in particle shape, and hence the dried-powder characteristics, are closely connected to the drying rate [**37**]. The thermal spray process requires its powders to be spherically shaped and have a uniform size distribution so as to achieve maximum flowablity characteristics [**12,32**].

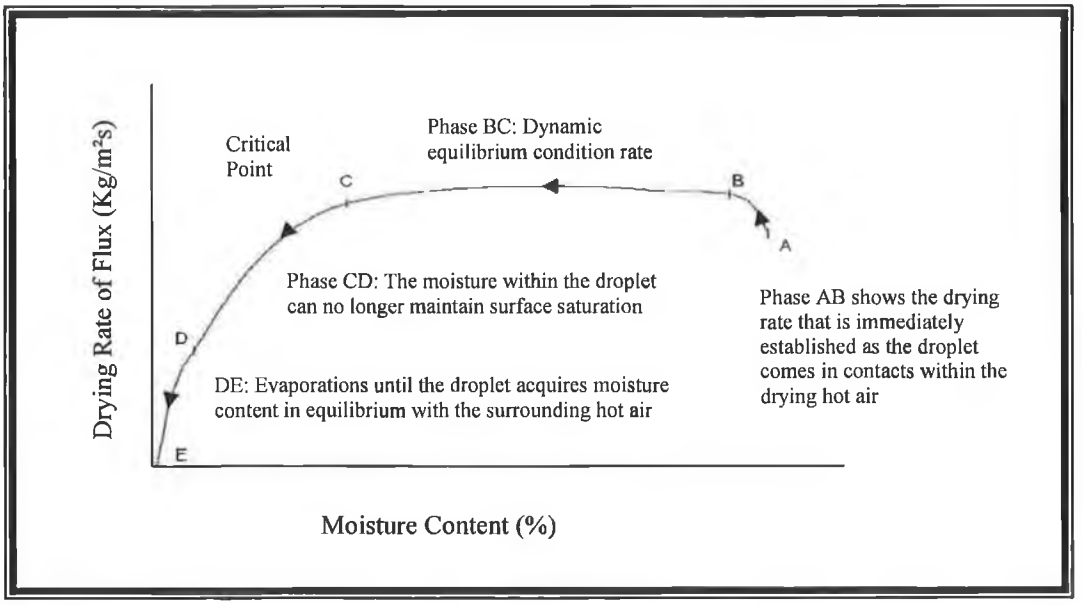

Figure 2.8: Drying rate curve [1,37].

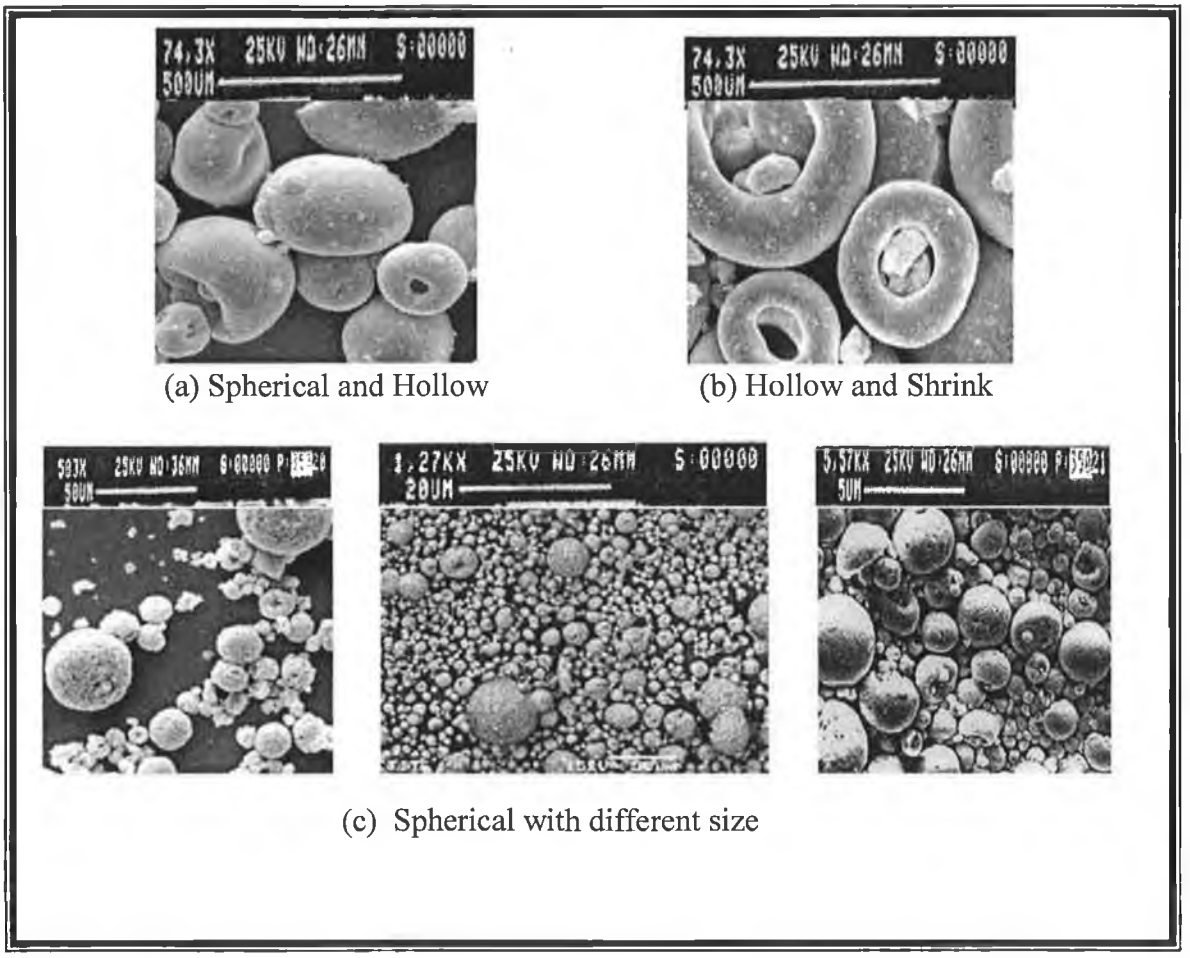

(a) Spherical and Hollow (b) Hollow and Shrink

(c) Spherical with different size

Figure 2.9: Different shapes of spray dried thermal spray powder [9,39].

2.3.4 PRODUCT SEPARATION

There are two systems used to separate the dried product from the hot air [**1**]:

System I: Primary separation of dried product takes place at the base of the drying chamber. During operation, the majority of product falls to the end of the chamber (heavier particles) due to gravity, while a small fraction (lighter particles) pass out entrained in the air and are recovered by separation equipment. Such separation equipment includes cyclones and dry collectors (Figure 2.10).

System II: This system is used for total recovery of the dried product, and takes place in the separation equipment. This system places great importance in the separation efficiency of the spray dryer and separation equipment, but this system is often not utilised.

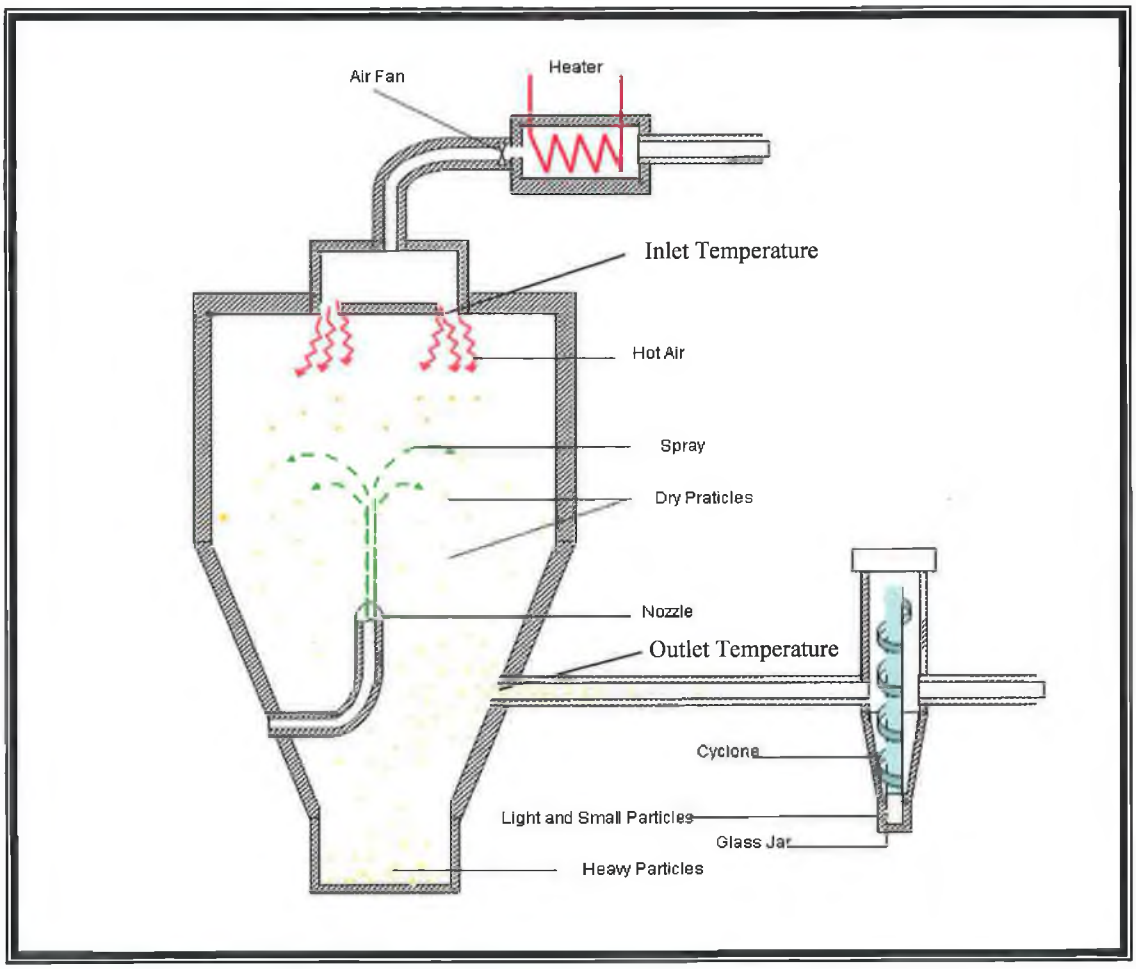

Figure 2.10: Schematic cross-section of a spray dryer.

2.4 OPERATING VARIABLES OF A SPRAY DRYER

They are many operational variables associated with the atomization and drying operation of a typical spray dryer, which offer the means of altering the characteristics of the dried product. The most important variables are; atomisation energy, feed rate, the hot inlet air flow, drying temperature and the type of equipment used [**1,2,26**].

2.4.1 ENERGY AVAILABLE FOR ATOMISATION

An increase in energy available for atomization will cause the spray dryer to produce smaller droplet sizes at constant feed conditions [**1,16,26**]. An increase in nozzle pressure for atomisation, or air-fluid flow ratio in the two-fluid nozzle arrangement decreases the mean size of the spray droplet [**2**], however the spread of droplets sizes in the spray distribution may not be appreciably changed. Producing greater amounts of the fine particles can often form a product with higher bulk density. The greater numbers of smaller particles produced, fill the voids between the larger and smaller particles [**1,2,26,40,41**].

2.4.2 FEED PROPERTIES

Increasing the feed viscosity, by increasing the amount of feed solids or reducing the feed temperature will produce coarser sprays during atomisation [**1,16**]. It has been reported that surface-tension effects during atomisation appeared minor, however an increase in feed solids has an effect on the evaporation characteristics where generally there is an increase in particle and bulk density [**1,2,40**]. The importance of the slurry formulation on the characteristics of the produced granules for thermal spray applications is not a negligible factor. Takahashi et al. [**42**] found that decreasing the pH value of aqueous silicon nitride slurries dispersed with nitrilotriethanol deflocculant caused the slurry to flocculate and produces granules with reduced density. Walker et al. [**43**] made correlations between aqueous alumina slurry formulation (binder type, solid loading and deflocculant level), slurry yield stress and the end product characteristics produced. It was also reported that a high deflocculant level which corresponds to a low slurry yield stress, results in hollow granules [**43**]. Cao et al. [**9**] researched on ZrO_2–Al_2O_3 ceramics and confirmed that the suspension preparation was a controlling factor of the properties of spray-dried powders. Tsubaki et al. [**44**] showed that granules prepared from a dispersed slurry were irregularly shaped and dimpled whereas flocculated slurry results were essentially spherical and

homogeneous granules. Sizgek et al. [**45**] reported that the well-dispersed TiO_2/ZrO_2 selections invariably lead to hollow particles, whereas solid microspheres were produced from partially aggregated under specific conditions.

Brentrand et al. [**3**] studied the correlation between the slurry formulation (by varying the pH, the amount of dispersant and the binder) and the characteristics of the spray dried granules for two oxide ceramics; alumina and zirconia. It was shown that there was a qualitative relation between the sedimentation behaviour (measured by the sediment ratio (SR)) and the granule shape (solid or hollow). Low SR values (below 0.6 and 0.7 on the scale of 1 which shows maximum settled volume of flocculated slurries for zirconia and alumina respectively) attributed to dispersed slurries producing hollow dried spheres whereas high SR values (achieved with flocculated slurries) led to solid dried granules.

2.4.3 FEED RATE

An increase in feed of slurry rate at a constant atomising energy produces coarser sprays and un-dried products or mean droplet size increase with decrease the relative velocity of air and feed in the external two-fluid nozzle [**1,2,26**]. Decrease of the relative velocity between air and feed at the point of contact decreases energy available for atomisation, however, for small feed rates, high velocity air can readily penetrate, causing the necessary turbulence to form the narrow mean particle sizes spray. Whereas at the larger feed rates, even high-velocity air cannot cause complete atomisation hence, a wide droplet-size distribution throughout the resulting spray.

2.4.4 AIR FLOW

The rate of airflow controls to a certain extent the residence time of the droplets in the drying chamber [**1,18**]. Increased residence time of droplets in the drying chamber leads to a greater degree of moisture removal, therefore reducing the air velocity, assists in the fast product recovery from the drying chamber [**1,2,26**].

2.4.5 DRYING TEMPERATURES

There are two temperature points of importance: inlet and outlet temperatures as shown in Figure 2.10.

(A) Inlet: An increase in inlet temperature increases the dryer evaporative capacity at constant air rates. Higher inlet temperatures yield a more thermally efficient dryer operation. Increased temperature often causes a reduction in bulk density, as evaporation rates are faster and products dry to a more porous or fragmented structure [**2,26**].

(B) Outlet: For a fixed moisture content and dryer design, the outlet temperature must be kept within a narrow range to maintain the power packing and flow requirements [**41**]. An increase in outlet temperature decreases the moisture content, at constant airflow and heat-input conditions [**41**]. Operation at low outlet temperature produces powder with high moisture content, often used when agglomerated forms of powder are required [**26**].

2.5 POWDER CHARACTERISATION OF SPRAY DRIED PRODUCTS

Powder characterisation post spray drying is generally carried out to measure the bulk density, particle size, powder flowability and particle friability of spray dried powders [**46**]. For thermal spray powders, the characteristics such as particle size, particle size distribution and particle shape (morphology) are of most important and these all effect both bulk density and powder flowability, as they have a bearing on transport costs [**46,47**]. HA powder used for coated titanium implants have been identified as class 3^{Rd} medical devices in accordance with the Food and Drug Authority (FDA) regulations [**48-54**]. The chemical and physical parameter of optimum HA powder properties with respect to elemental analysis, Ca/P ratio, density and solubility of HA powders (Appendix-A).

2.5.1 BULK DENSITY

Bulk density is defined as the weight per unit volume of powder. Bulk density provides a gross measure of particle size and dispersion which can affect material flow consistency. Bulk density of HA powder according FDA is 3.05 g/cm^3 for thermal spray [**51**]. Walton and Mumford [**46**] measured bulk densities of spray dried powders ranging from 0.147 g/cm^3 for coffee to 3.674 g/cm^3 for tungsten carbide. The research showed that the bulk density was influenced by the initial density of the materials, where an increase in solid density produced an increase in bulk density. A proportional increase would have been be apparent if the particle shape, and particle size distribution of all the powder samples produced and measured were identical. Duffie and Marshall [**34**] found that whilst the bulk density of some materials decreased with an increase in drying temperature and feed temperature, with others, increased, even if when spray-dried under identical conditions. Factors, such as feed rate, powder temperature and residual moisture content also influenced bulk density [**34**]. Chu et al. [**54**] also studied the effects of operating parameters on the bulk density and moisture content of synthetic detergents. Bulk density was found to decrease with an increase in atomization pressure, whereas, moisture content showed a slight increase. Additionally, an increase in a feed concentration produced an increase in the bulk density and a decrease in moisture content, however, the bulk density decreased with an increase in the feed temperature.

2.5.2 POWDER FLOWABILITY

Powder flowability is the ability of a powder to flow. In most engineering design situations, bulk powder can often be regarded as a plastic continuum, that is the powder exhibits a rheological behaviour relating to both Hookean (where the ratio of stress to strain remains constant, within the elastic limit of the body) and plastic deformation [**18**]. A powder is subjected to a continuous stress first deforms elastically (almost in a Hookean manner), but as the stress increases the powder starts to yields and eventually fails completely, after which, deformation becomes completely plastic, the powder dilates and flow sets in [**18**]. This approach although relatively successful, fails to give any consideration of; particle surface morphology and rheology like- surface asperities of adjacent particles interlocking, particle size, particle shape and particle packing, inter-particle force (Van der Waals electrostatic surface forces). Walton [**55**] used an inclinometer to test the flowability of spray dried powders. It was designed to measure the angle of repose of small quantity of powder (approximately 1.1 cm^3). The authors showed that all the samples demonstrate one of three distinct types of flow behaviour; free-flowing, semi-free-flowing or cohesive flow. Powder samples demonstrating free-flowing behaviour flow readily in an even, unbroken manner (due to having individual shapes, Figure 2.11(a)) and have flow patterns characterised by a high percentage (usually 100%) of the powder being displaced from the inclinometer at relatively low angles of repose. The displacement generally occurs over a narrow angle repose (approximately 7°) [**55**]. Semi-free-flowing powder tend to flow in an uneven and broken manner (due to having irregular elongated shaped particle mixed with spherical particles, Figure 2.11(b)) with the bulk powder showing signs of brittle fracture as it is separated at a 20° angle of repose [**55**]. Walton [**55**] also demonstrated that particle size and its distribution had a considerable influence on powder flowability. Therefore the larger the particle size and the narrower the particle size distribution, the more free flowing the powder [**55**]. The author also, suggested a correlation between particle morphology and powder flowability. In a free flowing powder, particles should ideally be spherical with no surface asperities, have a relatively large particle size and be moisture and static free [**55**]. Variation in powder moisture content (experiments were performed by Walton [**55**] at ambient temperature with powders humidity was ranging from 15% to 100%) had little effect on powder flowability so particles must be moisture free to see any difference in flow. It was shown,

that Van der Waals and electrostatics forces promoted agglomeration within the powder. In cohesive flow, (for particles less than 5μm), these forces become very large compared to the weight of the particle (Figure 2.11(c)). Such small particles are naturally cohesive and form agglomerates.

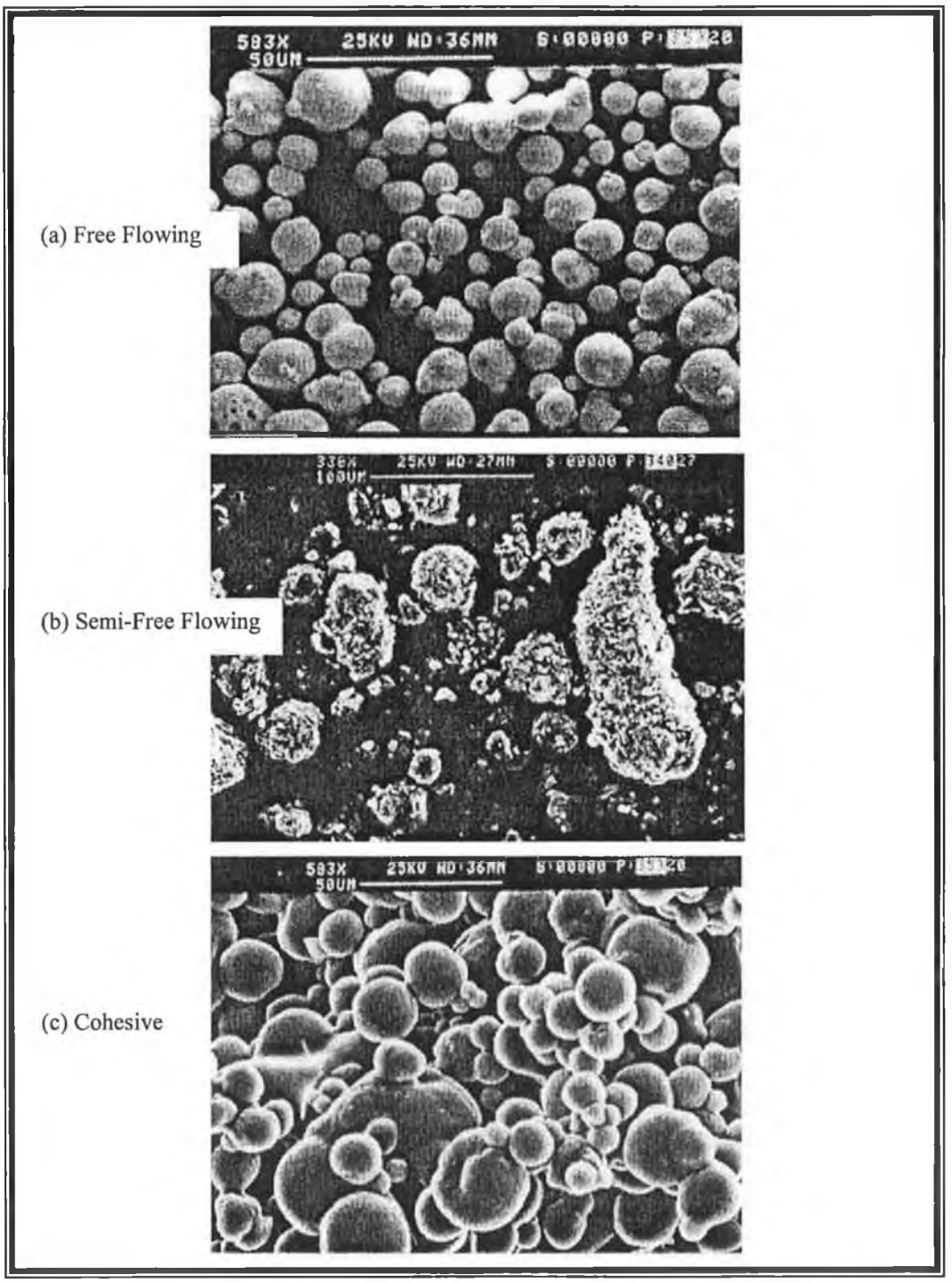

Figure 2.11: Different shaped powders which cause different types of flow behaviour of spray dried powder [50].

2.5.3 PARTICLE FRIABILITY

The physical strength or friability of a single spray dried particle is very difficult to determine due to its small size and the minute force would be of the μN range [**55**]. The methods used to determine the friability of powders like; tensile, compressive, attrition/abrasion and impact testing, are not applicable to single particles as the properties of the particles in bulk vary compared to that of individual particles [**55**]. Ghardiri [**56**] demonstrated a nanotester for measuring the strength of single crystals approximately 2nm to 5nm in diameter; unfortunately, most spray dried particles are many timers larger. However, Walton [**55**] determined the friability of individual spray dried particles by applying light pressure to individual particles and estimating their relative resistance to compression.

2.5.4 PARTICLE MORPHOLOGY

It is described that process variables like; the residence time of particles with the drying chamber, the type of spray to air contact, and feed parameters such as concentration, temperature and the degree of feed aeration, all effect particle morphology [**32**,**55**]. Three distinct morphological features have been identified namely; agglomerate, skin-forming and crystalline spray-dried products (Figure 2.12) [**57**]

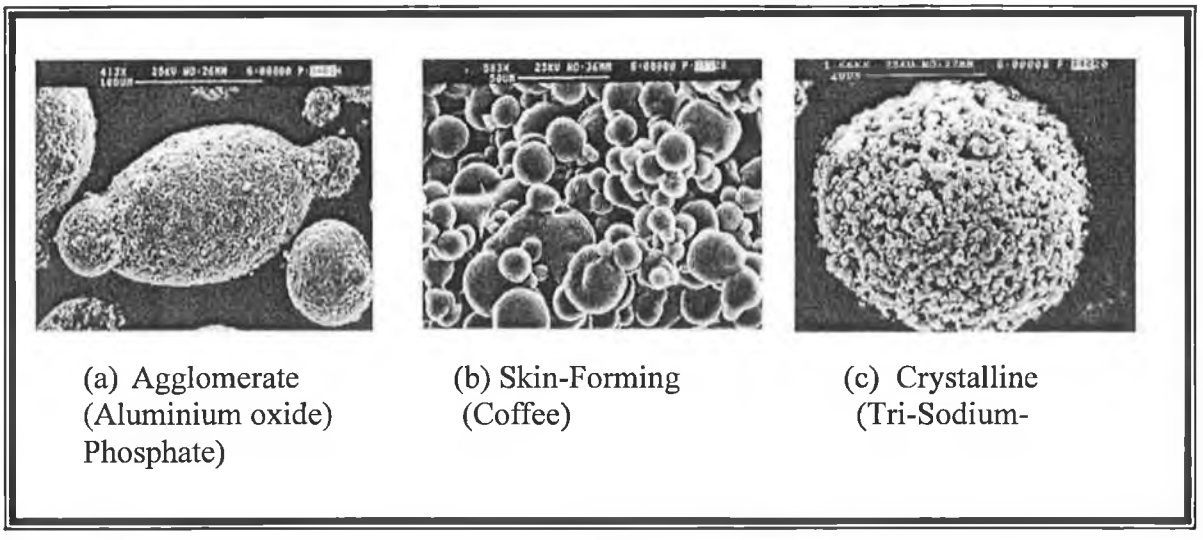

(a) Agglomerate (Aluminium oxide) Phosphate)

(b) Skin-Forming (Coffee)

(c) Crystalline (Tri-Sodium-

Figure 2.12: Different types of particle morphology of spray dried powders [57].

(A) Agglomerate- An agglomerate is a particle composed of individual grains of material bound together by sub-micron dust (material less than 1 μm in diameter and/ or a binder) [7]. It has been suggested that agglomeration occurs due to static electrical effects [**57**]. Many of the particles produced by spray drying form porous or hollow particles. Particle expansion has been found to increase with particle size or feed concentrations [**58**]

(B) Skin-forming- A particle composed of large individual crystal nuclei bound together by a continuous non-liquid phase which is polymeric or sub-microcrystalline in nature is known to have skin forming morphologies [**57**].

(C) Crystalline structure- A particle composed of large individual crystal nuclei bound together by a continuous microcrystalline structure is known as a crystalline structure [**57**].

Buckham and Moulton [**58**] spray dried aqueous ammonium sulphate solutions and found that the drying rate had a considerable effect on the morphology in the final powder. Under the same spray dryer conditions, the larger particles tended to dry to a less dense product compared to the smaller particles, indicating a grater tendency on the part of larger particles to from porous or hollow spheres. Dlouhy and Gauvin [**59**] studied the evaporation and drying rates of calcium lignosulphate solutions (palletizing agent) and drying at different inlet air temperatures produced considerable differences in particle size and shape. At inlet air temperatures of 52 to 64 °C, the particles appeared to be smaller and more regular-shaped than those dried at 192 to 215 °C. A greater proportion of hollow particles were also produced at the higher temperature.

Beltran et al. [**60**] reported that their final product (40% maltodextrin) showed a formation of thick, compact and irregular crust, which was more evident for low-temperature drying (110/70 °C) than when drying at higher temperatures (170/145 and 200/173 °C) in which smooth and regular surfaces of completely broken material were observed. Ghardiri [**56**] found that the inorganic materials fell typically into the crystalline and agglomerate category and could be further subdivide according to their aqueous solubility that materials which were readily soluble in water tended to have crystalline morphologies whereas, insoluble or partially –soluble materials tended to form agglomerate structures

The main characteristic of the spray-dried powder is a spherical external shape. However within such a shape, two kinds of granule morphologies are often formed by spray drying either "solid" or "hollow", and for the same hollow granules at least three types have been identified: thin-walled fractured, thin-walled dimple and thick-walled spherical [**3,46,47**]. The researchers [**46,47,55-42**] observation suggested that a different shape of spray dried powder is due to it in suite material properties and drying history. Particle blowholes and catering due to the high porous or open nature of the particle structure allowing the flow of water, water vapour and possibly dissolved gases form the interior of the particle to its surface, with the minimal amount of resistance, thus minimizing internal pressure build-up and particle distortion or inflation. Hollow particle with a blow hole may be due to rapid evaporation of volatile solvent exceeding the rate of liquid and /or vapour diffusion through the porous particle structure. An example tungsten carbide spray dried powder. The internal structure of spray dried particles may be either solid or hollow. If solid may be due to the wall structure are relatively thick in relation to overall particle diameter; if hollow, the particles can sometimes contains trapped air/gas bubble. If particles with excessive surface cracking and large number of broken shells, this may be due to the formation of relatively nonporous, rigid particle structure, where evaporation of the internal liquid has resulted in particle fracture and possibly explosion, example- trisodium orthophosphate. The mushroom cap shape of clay spray dried powder may be due to the result of the particle's resistance to airflow as it moves though the drying chamber.

2.6 COMPUTATIONAL FLUID DYNAMIC (CFD) - SPRAY DRYER

2.6.1 INTRODUCTION

Computational fluid dynamics (CFD) can play an effective role in the optimisation of parameters for the spray dryer process, such as the initial droplet diameter, the location and orientation of sprays, and the mass flow rate of the sprayed material [**1,64**]. Before the advent of CFD, there were many attempts to formulation mathematical models to predict spray drying processes [**65**]. At the earliest stage of the spray drying modelling era, there were many phenomena which were difficult to represent by mathematical models such as polydispersity of spray, entrainment effects, or problems of internal heat and mass transfer in a dispersed phase. A significant changed was marked in the 1970's when Parti and Palancz [**66**] formulated the principles of momentum, heat and mass balances between the continuous and disperse phase, and particularly when Gauvin and Katta [**35**] presented a model which took into account entrainment effects and non-uniformity of atomisation. A spray drying model solution which accounts for axial and tangential velocity distributions of air inside the drying chamber was also described [**35**]. However, a land mark change occurred when Crowe et al. [**35,67**] demonstrated a so-called Particle Source in Cell (PSI-Cell) model for gas-droplet flows. It was based on the Navier-Stokes and continuity equations where the droplets were treated as sources of mass, momentum and energy is the gaseous phase. Using this concept, any influences on the spray was initially neglected in calculating the axial, radial and tangential components of the gas velocities. A large number of droplets were then tracked through the gas inside the chamber; these droplets were chosen to represent the range of droplet sizes leaving the atomizer, so that the sum of the flowrates of each droplet size equalled the total liquid flowrate. In the model proposed originally by Crowe et al. [**38**] many simplified assumptions were made that referred mainly to the calculation of trajectories and temperatures of particles. Further extensive studies resulted in the development of more sophisticated version of the PSI- Cell model, including also commercial packages such as FlOW3D and PHOENICS and the latest commercial software; FLUENT and CFX were all based on this fundamental principle [**68**].

A dispersed liquid phase species in the form of a large number of discrete droplets convecting and vaporising in a continuous gas phase species and their mathematical

description, involves complex nonlinear couplings of momentum, energy and mass exchange [**69**]. Regardless of the macroscopic complexity of the flow field, the traditional modelling approach for such flows generally involves specifying the governing equations for a single, isolated droplet including drag, convective heat transfer, mass transfer and effects due to finite droplet Reynolds numbers. The derived equations were then used either for every individual droplet (as in direct numerical simulations) or for a subset of statistically representative droplets or "test particles" (as in various forms of two-phase turbulence and spray modelling) [**69**].

2.6.2 MODELLING OF SLURRY AND DROPLETS

A slurry plays an important role as it can break up into droplets, hence it is controlled by viscosity and kinetic energy. Kadja and Bergeles [**70**] modelled a slurry droplet undergoing drying. The model was based on heat, mass and momentum transfer between the slurry droplet and gas flow and this was investigated numerically. The model was solved using finite volume methods which had been developed by Varonos and Bergeles [**71**]. The model showed that the total evaporation time for droplets with a high solid content was small and indicated that higher rates of evaporation would be obtained when the injected slurry was atomised into very small droplets and low effects of evaporation was observed when the relative motion between the droplet and the surrounding gas was increased at the point of injection.

Modern direct numerical simulations currently treat as many as 106 individual solid particles undergoing dispersion in simplified turbulent flow configurations; however, such large computations are relatively new for evaporating droplets due to the numerical complexity added by the droplet heat and mass transfer [**72**]. Mashayek et al. [**73**] simulate droplet dispersion in isotropic turbulence in which the evaporation was governed by the classical "D^2 law" (Godsave, [**74**] and Spalding [**75**]) and the mass loading was considered small enough to neglect turbulence modulation in the dispersed phase (one-way coupling). More recently, Mashayek [**76**] removed this restriction and considered droplet dispersion in compressible homogeneous turbulence with two-way coupling and droplet evaporation governed by a heat–mass transfer analogy model as first used by Crowe et al. [**77**]. Their simulations employed 963 spectral points for the gas phase discretisation and include as

many as 5.5×10^5 sets of Lagrangian equations for the three dimensional positions; velocity, temperature and mass of each droplet. Stoichastic approaches in which only representative droplets are followed, have received more attention than direct simulation approaches; as they work out to be less expensive computationally [**77**].

2.6.3 EVAPORATION MODELS

Stevenson et al. [**78**] showed that over the last few decades, five different approaches have been developed and used to describe the drying of droplets [**78**]. The first approach assumed the droplet was assumed to be at a uniform temperature and the moisture was to diffuse through the solid and evaporate at the surface of the droplet. The second approach was based on the formation of a crust, with a receding crust–bulk interface [**79**]. The crusts internal heat was ignored, which would have an effect on the calculated droplet temperature during the periods of drying. A third approach was based upon a proper receding interface model with a droplet core temperature different to that of its surface [**78**]. However, the core temperature was not linked to the air wet-bulb temperature. This model was simplified by ignoring the heating of the crust, but was complicated by the requirements to solve the diffusion equation for the crust and increasing the number of physical parameters that were evaluated experimentally. However the major drawback of this analysis was the assumption of the linear temperature distribution in the crust, which may be correct for flat geometries but not for spherical ones.

The fourth method was based on the reaction engineering approach to describe the drying of a single droplet of milk [**32,80**]. In this approach, neither temperature nor water concentration distributions in the droplet were considered. As the water in the droplet depleted, the effective water vapour pressure (or water activity) at the surface was reduced causing continuous reduction in drying rate. This model was modified later by incorporating the mass transfer resistance of the crust [**80**]. The modified model was semi-empirical in nature and only useful for fast computations.

The fifth and final model was developed to predict the change in droplet mass and temperature when it was exposed to hot air [**80**]. The droplet was assumed first to undergo sensible rapid heating with no mass change. Then the droplet experienced some shrinkage,

with no temperature change but rapid mass loss, followed by a period of crust formation with a significant change in droplet mass and temperature, and finally a short period of sensible heating of the dried particle. This model, unlike previous models, accounted for shrinkage and for the temperature distribution in the droplet. It provided good predictions for the change in droplet temperature and mass, compared with experimental measurements and was used in numerical solutions [**32**].

2.6.4 COMMERCIAL SOFTWARES FOR SPRAY DRYER

Zbicinski [**65**] showed how the commercial software CFX was very useful for development and experimental verification of momentum, heat and mass transfer model on a spray drying processes. Uneven distribution of particles and entrainments effects were taken into account in the model. The model compared to experimental results (investigated using water evaporation) at different initial air temperatures, feed rates, flow rates of the drying agent and different parameters of atomisation, spray cone angle and initial particle size distribution. However, it was found that the model was not validated with the experimental data.

Oakley and Bahu [**64**] used FLOW3D [**76**] to describe a discrete droplet model (adapted from Crowe et al. [**75**]) to predict the behaviour of water and milk droplets and particles. This model had serious limitations like low accuracy for swirling flows. The model was earlier version of spray drying process where primary K-ϵ model used and the specification of gas velocity component u, v and w, and value of K and ϵ defined by user. The model was used body fitted girds and validated with water and milk spray.

Harvine et al. [**82**] analysed a tall form of spray dryer (co-current rotary type) used for diary products, where a two phase simulation was used to evaluate the applicability of the commercial software CFD model and CFX 4.3, and to examined the characteristics of the flows that existed within these complex devices. The model used K-ϵ turbulence model with standard coefficient and employed to simulate heat and mass transfer between the feed particles and the surrounding gas that was based on the concept of a general characteristic of drying curve.

Langrish and Kokel [**83**] also used this model to simulate the velocity flow fields, temperature profiles, mass fraction fields, and milk particle behaviour. Results [**82,83**] showed that the final particle moisture contents were of a similar magnitude to those measured experimentally. The major draw back of these models was that they could not predict any atomisation.

Verdurmen et al. [**84**] used the software DrySim. The software was mainly used for diary products and specific types of dryers. The software was developed under Nizo food research. It was based on a tailor made simulation program for spray dryers, making used of computational fluid dynamics (CFD) techniques. The DrySim used a two dimensional simulation model of a spray dryer to calculate the flow pattern, temperature and moisture content of air; the trajectories of the atomized particles and the drying behaviour of the individual particles. The gas flow was described by the time-averaged Navier-Stokes equations in combination with a standard K-ϵ turbulence model (to be described in Chapter 4). In DrySim, a particle tracker based on the equation of motion was used to simulate the particle trajectories. Since the particles affect the gas-flow (and vice versa), an iteration procedure was used to solve the equations. The drying of droplets was influenced in DrySim by both external transport phenomena (from particle surface to surrounding air) and internal transport phenomena (diffusion of water within particles). The differential equation that describes the diffusion process of spherical particles was solved numerically, simultaneously with the equations for external heat and mass transfer. In order to obtain reliable results using DrySim, it took several hours using a personal computer (800 MHz, 128 Mb RAM) to carry out one simulation. Sub-models for the formation of insoluble material or for describing the stickiness of particles had option in DrySim. Three industrial cases was described to show that DrySim was an effective tool for giving indications of how to adapt industrial dryers, for example to obtain a better product quality, a higher capacity or to reduce fouling. DrySim validated for rotary and nozzle atomizer with co-current air flow drying system for dairy products. In DrySim modelling initial particle leaving at nozzle or rotary was assigned by measurement or manually and was not support by any atomization model. However, the mixed spray dryer is preferable for thermal spray powders drying. In present study, FLUENT software has given more insight as it governs all the aspects of CFD than DrySim.

The CFD technique also plays an important role in assessing design alternatives in the spray dryer process [**86,87**]. Southwell et al. [**85**] used CFD software as a tool to investigate several design alternatives to overcome poor flow distributions in a plenum chamber for a pilot-scale co-current spray dryer. It was simulated using the CFD codes CFX4 and CFX5 to correct the uneven inlet air distributions, which influenced the spray dryer performance, airflow patterns, inlet conditions and significantly affected particle trajectories in such spray dryers. It was stated that considerable difficulty was encountered in obtaining adequate grid resolution for the holes in the distributor plate while keeping the required computational resources with realistic limits. The model was meshed with 532,000 cells to give a satisfactory accuracy of simulations but it took a long time to converge. All simulation results were based upon the assumptions of isothermal and incompressible flow and used K-ϵ turbulence model. It was evident from the models results that the pressure and velocity profile distributions around the distributor plate were not as smooth as they would have been expected physically. Hence redesign corrected this problem. The CFX4 used multi block geometries, and had problems solving, however CFX5 (just as FLUENT does, the software used in this research) had the added benefit of using an unstructured mesh, so that the flow could be solved simultaneously throughout the flow domain, rather than on a block by block basis.

Fontana et al. [**88**] conducted a study on the flow distribution inside a spray dryer for ceramic powders. The objective of the study was to analyse the motion of the air and the process of evaporation inside the drying chamber. The research initially simulated the motion of the air in isothermal conditions because of the complexity of the mathematical model and the geometry had a 145000 grid cell. The spray dryer was divided into three main parts; the hot air distributor located at the tip of the dryer, the cylinder (where evaporation take place) and the lower cone (where the spray dried product was collected). The research concluded that the CFD technique gave an insite into the complex physical phenomena involved in mixed spray dryer techniques used in the production of ceramic powders.

Numerous authors [**89-94**] have investigated liquid spray atomisation based on the Taylor Analogy Breaking-up (TAB) and Wave model [**92,93**]. In the traditional approach for

spray atomisation computation, the Eulerian equations for gaseous phase are solved along with a Lagrangian model for particle transport with two-way coupling of mass, momentum, and energy exchange between the two phases [**89**]. The spray atomization process is modelled by standard deterministic breakup models based on Taylor analogy breakup (TAB) [**90**] or wave [**91**] models. In the TAB model [**90**], oscillations of the parent droplet are modelled in the framework of a spring mass system and breakup occurs when the oscillations exceed a critical value. Where as, in the wave model, new droplets are formed based on the growth rate of the fastest wave instability on the surface of the parent blob [91]. Both models are deterministic with 'single-scale' production of new droplets. In many spray atomisation applications, injection of liquid jet takes place at high relative velocity between the two phases (high initial Weber number). Under these conditions, intriguing processes such as turbulence-induced breakup [91], multiple droplet collision in the dense spray region [**91**], fluctuations due to cavitating flow inside the injector [**92**], contribute to the process of atomization. At each spray location, this may result in droplet formation over a large spectrum of droplet-sizes and is not captured by the above models. In order to improve the TAB model, [**93**] used an enhanced TAB model (ETAB), where the product droplet size was obtained via a breakup cascade modelled by an exponential law. Therefore, the parameters of this distribution function were derived from experimental data to achieve better performance of the model.A novel numerical algorithm capable of simulating spray droplets with similar properties commonly known as parcels can be modelled and compared with standard parcel-approaches as usually employed in the computation of multiphase flows [**94**].

Langrish and Zbicinski [**95**] used a CFD programme to reduce the wall deposition rate in a spray dryer, using the K-ϵ model for turbulence. To validate the model, a solution of sodium chloride containing 20% by mass of the salt was sprayed at the rate of 0.0012kg/sec from a two fluid nozzle into a 0.935m diameter, 1.69m high cylinder-on-cone chamber. The CFD program was used to explore methods for decreasing the wall deposition rate, including simple modification to the air inlet geometry (to eliminate swirl) and a reduction in the spray cone angle from 60 to 45 degrees. Using the constraints imposed by the experimental equipment, the programme suggested that the maximum spray angle (60 degree) and the maximum amount of swirl in the inlet air would minimise

the wall deposition rate. Even though the quantitative agreement for the changes in geometry was poor when compared to experimental results, however the trends were reproduced well, demonstrating the usefulness of the technique. To the present no research has described the use of FLUENT codes to solve spray drying problems but a few researchers [**96**] used the code in spray dryer cyclone simulations which gave good correlation to that found experimentally. The reason for this may lie in the fact that FLUENT is commonly used in space research rather than in drying research [**76**].

2.7 THERMAL SPRAY POWDERS

Surface engineering is an important branch of engineering and has a significant effect on the serviceability and life of a component [**4**]. Engineering environments are normally complex, combining loading with chemical and physical degradation to the surface of the component [**97**]. One of the most common failures in the service engineering is surface wear damage [**98**]. Studies show that 80% of the total costs for the protection of metals are related to coating applications [**97**]. Surface protection can be produce in two ways. Firstly, material physical, chemical, and mechanical properties may be altered. Such methods are carburising, carbonitriding, and aluminising and so on, however these processes are time consuming [**97**]. Secondly, a coating of a hard material can be applied over a base material to act as a shield against the environment. Several coatings methods exist, however thermal spraying (Figure 2.13) is one of the most common [**35**].

All thermal spraying processes are based on the same principle, heating a feed stock material (powder or wire), accelerating it to a velocity, allowing the particles to strike the substrate surface, and the particles then deformed and solidified onto the substrate [**36**]. The thermal spray basic definition can be divided into three divisions; materials, heat and speed [**99,100**]:

(A) Materials-The spray materials include a wide range of ceramics, carbides, plastics and metals, available in powder or wire from [**12**]. The large variety of materials with varying physical and chemical properties explains why the thermal spraying is the most versatile and diversified technology among surface treatment processes [**32,101**].

(B) Heat-Introducing the feed stock material into a hot gas stream is produced by either a chemical reaction and/or by a physical reaction. The temperatures vary from 3000°C for the combustion of oxygen gas mixing, to 20000°C for a plasma arc [**102-104**].

(C) Speed-The particles are accelerated towards the substrate by the gas stream and deform on impact to form a coating. The speed is an essential element, which directly influences the coating properties [**12,101**].

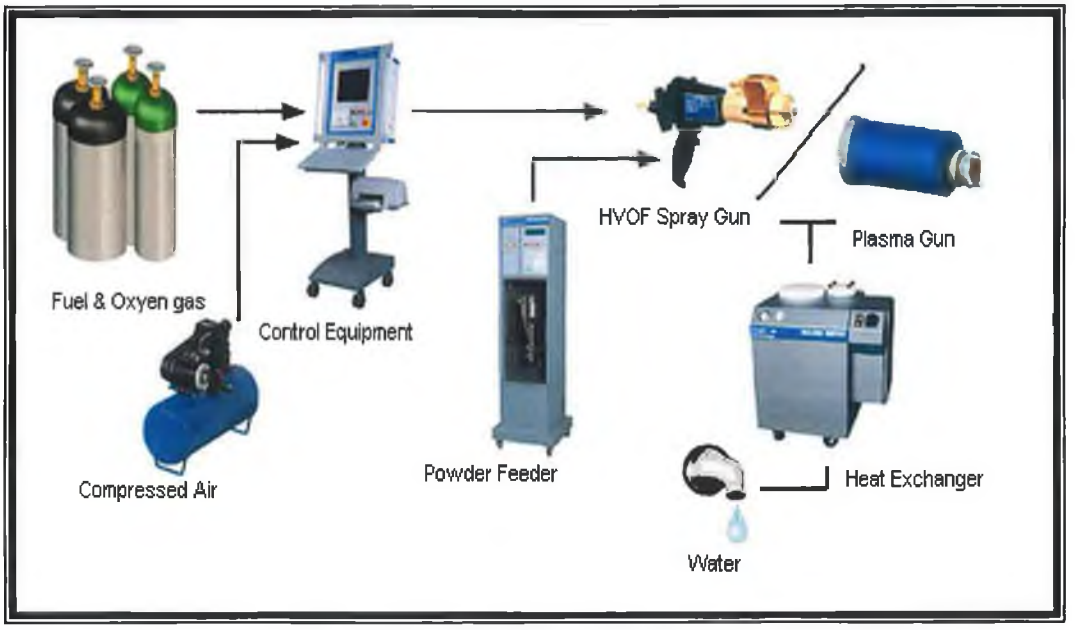

Figure 2.13: Equipments involved in the plasma thermal spray process [104].

The most common thermal spraying process are Plasma Arc and High Velocity Oxy-Fuel (HVOF) **[99]**, however plasma spray will be referred to in this research as the method used to apply Hydroxyapatite (HA) material, so this will be discussed here.

2.7.1 PLASMA ARC SPRAYING

The plasma arc spray process (Figure 2.14) uses an arc between two consumable electrodes materials as a heat source and a compressed gas to atomise and propel the coating material onto the substrate. The plasma spray gun electrodes usually are made of a copper anode and tungsten cathode, both of which are water cooled. The Plasma gases (argon/nitrogen and hydrogen/helium) flow around the cathode and through the anode in a constricting nozzle. The plasma is triggered by a high voltage discharge which causes localised ionisation and a conductive path for a DC arc (14000 °C) to form between cathode and anode **[105]**. As the heat causes the gas to reach extreme temperature it resistance dissociates and ionise into a plasma. The plasma exist the anode nozzle as a free or neutral plasma flame for spraying. Powder is fed into the plasma flame by an external powder port mounted near the anode nozzle exit. The powder is so rapidly heated and accelerated that spray distances between the coating on the substrate can be in the order of 25 to 150 mm **[106]**.

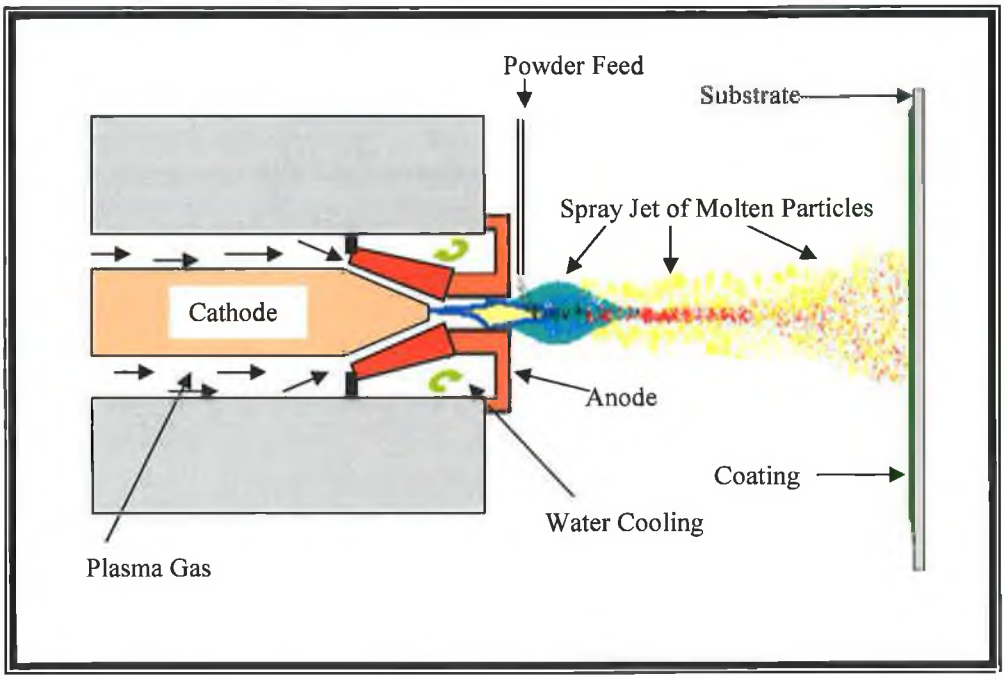

Figure 2.14: A systematic of plasma arc coating process.

Thermal spray coatings have lenticular or lamellar grain structures resulting from a rapid solidification of small globules, flattened due to the striking of molten particles on a cold surface at high velocities [**99,100**]. In most cases, the flight particles are molten or partially molten before impact and solidify a few microseconds after impact and this depends upon the particle size and shape, and upon on the production of thermal spray powder [**12,32, 95-103**]. Powder properties and characteristics have a direct impact on the coating quality, ease of application and performance in the end use, and this depends upon on methods of manufacture and powder purity, morphology and particle size distribution [**99-111**]. Thermal spray processes are most efficient if their powders are spherical in shape and have a low size distribution of a mean size of 40 μm [**111,112**].

2.8 SPRAY DRIED THERMAL SPRAY POWDERS

There are several hundred commercial powders specially developed for the various thermal spray processes, and the most common are listed below [**12,32, 99,113-121**]:

(1) Metals:- Molybdenum, Nickel, Chromium, Silicon, Ferrous, Aluminium, Zinc

(2) Metals Alloys:- Carbon Steel, Stainless Steel, Nickel- Chromium, Nickel chromium- Aluminium, Magnesium-Chromium-Aluminium-X, Bronze, Cobalt-Molybdenum- chromium- Silicon, Cobalt-Chromium-Nickel-Tungsten.

(3) Carbides (Cermets):- Tungsten-Carbon-Cobalt, Tungsten-Carbon-Chromium, Tungsten-Carbon-Nickel, Chromium-Carbon-Nickel-Chromium.

(4) Oxides (Ceramics):- Chromium oxide, Aluminium oxide, Aluminium oxide-Titanium oxide, Zirconium oxide-Yttrium oxide.

(5) Abradables:- Aluminium- Silicon- Polyester, Aluminium- silicon –Graphite.

(6) Composites:- Aluminium oxide-Titanium oxide- Polytetrafluoroethylene (PTFE).

(7) Polymers:- Polytetrafluoroethylene, Polyetheretherketone (PEEK)

Several powders could have been identified in the present research however, the spray drying of Hydroxyapitite (HA) for clinical applications has posed numerous problems in industry such as varying morphology, inconsistent drying and variation in size of powder produced. These factors had a huge effect on the plasma spraying of this HA powder and resulting coating performance. Hence this is focus for the reminder of the report.

2.8.1 HYDROXYAPATITE THERMAL SPRAY POWDER

Hydroxyapatite and other related calcium phosphate minerals have been utilized extensively as biomedical implant materials for many years due to their identical chemical composition and high biocompatibility with natural bone, whose primary function is to withstand load bearing situations [**122-127**]. Generally, HA has poor bulk properties therefore it is normally used as a coating applied by plasma spray on to load bearing metallic prosthetic implants [**125,126**]. HA is used as surface coating on bio-inert metallic substrates such as; titanium alloy, Ti-6Al-4V and stainless steel 316 [**128-133**] (Physical properties of HA and plasma spray parameter used in coating is given in Table A2 in Appendix-A). Variation in process parameters such as powder morphology can induce

microstructural and mechanical inconsistencies which effect service performance of the coating [**112**]. Kweh et al. [**122**] confirmed that the quality of a coating is closely dependent on the overall attributes and characteristics of the manufacturing route of these powders. These attributes include particle size, particle-size distribution and particle morphology, and all of these contribute to the flow characteristics of the HA particles in the powder-feed system of thermal spray systems and their subsequent melting behaviour in the plasma jet [**122**]. Cheang and Khor [**125**] also studied the preparation of HA powders and coating by plasma spray process and suggested that the state of the starting powder adversely affected the coating characteristics. The raw HA powders were synthesized by spray drying and calcinations. The final thermal spray coating contained large particles (above 55 μm in size) which remained unmelted with little or no change in shape and structure. Spray particles from 55 to 30 μm had mixtures of crystalline and amorphous phases but the shape of the particles were generally spherical or oval. Sprayed particles less than 30 μm were predominantly spherical and contained large amount of amorphous phases. Calcium oxide phase was detected in the size range 10-20 μm which is undesirable in biomedical coatings. Hence this particle–plasma interaction suggested that particle size and stability during deposition was an important factor in the final characteristic of coating in terms of phase, crystallinity and microstructure and it could be controlled to some extent during the spray drying of HA slurry. Khor et al. [**133**] and Guipont et al. [**129**] studied sprayed dried hydroxyapatite and concluded that good flowability was a great advantage in producing higher reliable coatings with reproducible spraying parameters. Furthermore, a spherical shape was the best in promoting homogeneous heating of the particles in the plasma gun. Consequently, the use of powder particles with spherical geometry and narrow size distributions so as to induce excellent heat transfer and consistent melting capabilities, increase the deposition efficiency and decreases coating porosity [**119,133**].

2.8.2 MANUFACTURING OF HA POWDER

Many manufacturing methods for HA have been published, such as, precipitation, solid-state synthesis, hydrolysis, and hydrothermal and sol-gel methods [**122,123**]. As this research focuses on spray drying techniques, therefore the precipitation method will be described briefly as this method is been used by another researcher in the Materials

Processing Research Centre and it is the method used by industry to produce HA for clinical applications.

Precipitation method: This is the reaction of orthophosphoric acid with calcium hydroxide in equation 2.1:

$$10Ca(OH)_2+6H_3PO_4 \longrightarrow Ca(PO_4)_6(OH)_2+18H_2O \text{----------Equation 2.1}$$

This method is a more convenient process and suitable for the industrial production of HA since the only by-product is water and the probability of contamination during processing is very low [**121-138,135,136**]. Ideally, the ratio (stoichiometric equation for pure and single phase) of calcium to phosphorus for orthopaedic applications in the form of thermal spray coating is 1.677 [**121**]. In the case of precipitation, nanometric-size crystals can be prepared. The crystallinity and Ca/P ratio depend strongly upon the preparation conditions like ph level, assys time and spray dryer parameter conditions **[135, 137]**. The resultant precipitate (feedstock/slurry) is then dried in a spray dryer to control particle size and morphology.

Luo and Nieh [**123,138**] produced HA powder with varying morphologies. The granules obtained were particles with an average crystalline size ranging from 1 to 8μm when the slurry was spray dried at a slurry feed of 0.25, 0 and 0.167 Volume % and a nozzle atomisation pressure of 1, 3, and 5 kg/cm^2 with an inlet air temperature of 200°C and outlet air temperature of 100°C. The authors concluded that the morphologies of the granules were controlled by adjusting the spray-drying conditions; the volume fraction of feed slurry and atomisation pressure. It was also noted that the spray-dried granules produced were doughnut, solid and hollow sphere shaped.

Kweh et al. [**122**] produced and characterised HA powder. The HA slurry was spray dried in a co-current flow dryer and then calcined at 900°C. The spray dried precipitated powder were examined for purity, phase composition and morphology. The author observed that the spray dried powder had good purity, spherical shape, flowablity and amorphous phases. After calcination, the spray dried powder showed a great improvement in crystallinity but

had a reduction in flowabilty which had an effect when used as a feedstock powder in thermal spraying.

The literature survey on HA powder suggests that spray drying is still has an important role in the manufacturing of raw HA powder for thermal spray deposition to produce a bioactive material onto clinical implants. The spray dryer parameters like feed rate, atomization air and inlet temperature can easily control the particle size of HA powder which influences the decomposition of powder particles during thermal spray deposition into undesirable phases. However, experimentation and optimisation of various feed stock with varying parameters to produce 'ideal' powders post spray drying is time-consuming. Therefore knowledge of the drying mechanism within the spray dryer will reduce the number of experimental trials. To date no research paper/work has reported on the simulation of the spray drying of HA, nor on the simulation of spray dryer used for HA synthesis. Hence this research will focus on simulation using finite element analysis the internal mechanism within the spray dryer, validated the results found with experimental and instrumentational data to predict how to produce powders with 'ideal' morphologies and size as required for thermal spraying.

2.9 SUMMARY / OVERVIEW

Literature review shows spray drying still has a great important in the food, detergent and pharmaceutical industries. Its major application is the drying of milk and other food products, where the researchers are working to improve the quality of food products by analysing moisture content, aroma loss, flowability and powder size. Other researchers are working to improve the optimum condition of the spray dryer to overcome the difficulties that exist in spray dryers like deposition onto the wall of the spray dryer. The dominant spray dryer technique used in the food industries is the rotary type atomizer with co-current air flow. This food industry spray dryers contain a large drying chamber, drying of feed slurry at low inlet temperature as compare with the thermal spray powders because food products are very sensitive to temperature.

On the other hand, other researchers are working to control the physical performance of the spray dryer using modelling techniques. Overall quality of spray drying depends upon a large number of factors including process variables and characteristics of the drying product; feed, viscosity, density, inlet and outlet temperature, type of atomizer, energy to atomization, dimension of drying chamber, sensitivity of product towards to temperature, hygroscopic nature. The major issue in dryer operation is flow stability and the need to avoid highly unsteady flows. Such flows can lead to significant wall deposition of partially dried product which sticks to the wall and builds up a crust. In the past decade, despite their importance, the modelling of the physical processes governing the performance of dryers is relatively poorly developed. But recently there has been much development in the field of computational fluid dynamics (CFD) to determine the optimum parameters of physical drying process which helps researcher to design spray dryers and processes.

Nowadays, thermal spray powders take an important position in surface engineering to improve wear resistance and temperature resistance. Researchers are often use finding to powders produced by spray drying as it is fast, continuous producing and has better control over particle size and morphology. In literature very little has been reported about spray dryer performance used to produce thermal spray powders. Some papers have reported that mixed type air flows using the two-fluid nozzle atomisation provide the best results if used to produce the thermal spray powder **[6, 8, 16, 23, 108].** It is compact in design and gives

more residence time to particles and this is ideal as thermal spray powders are less sensitive to heat. There is a need to transfer the knowledge and experience of spray dryers used in the food industries into the application of producing thermal spray powders.

3

Experimental Equipment and Procedures

3.1 INTRODUCTION

In the present research, the two fluid nozzle mixed spray dryer used to produce hydroxyapatite thermal spray powders was simulated using finite element modelling and validated experimentally using a Niro spray dryer. For the experimental analysis a factorial design was chosen using orthogonal blocking together with the Box-Behnken scheme, as experiments would prove tedious and costly. The Box-Behnken scheme is an independent quadratic design to investigate treatment combinations at the edges of a process space and its centre. These designs are rotatable (or near rotatable) and require three levels of each factor. The designs have limited capability for orthogonal blocking compared to the central composite designs. The Box-Behnken scheme requires fewer treatment combinations than a central composite design in cases involving 3 or 4 factors. For this research, Box-Behnken scheme reduced the experiments form 27 to 13 which contained all of information except the corner data (Table 5.3).

This chapter describes the equipment used in the experimental and validation procedures, along with the parameters, the process and the characterisation equipment (Figure 3.1).

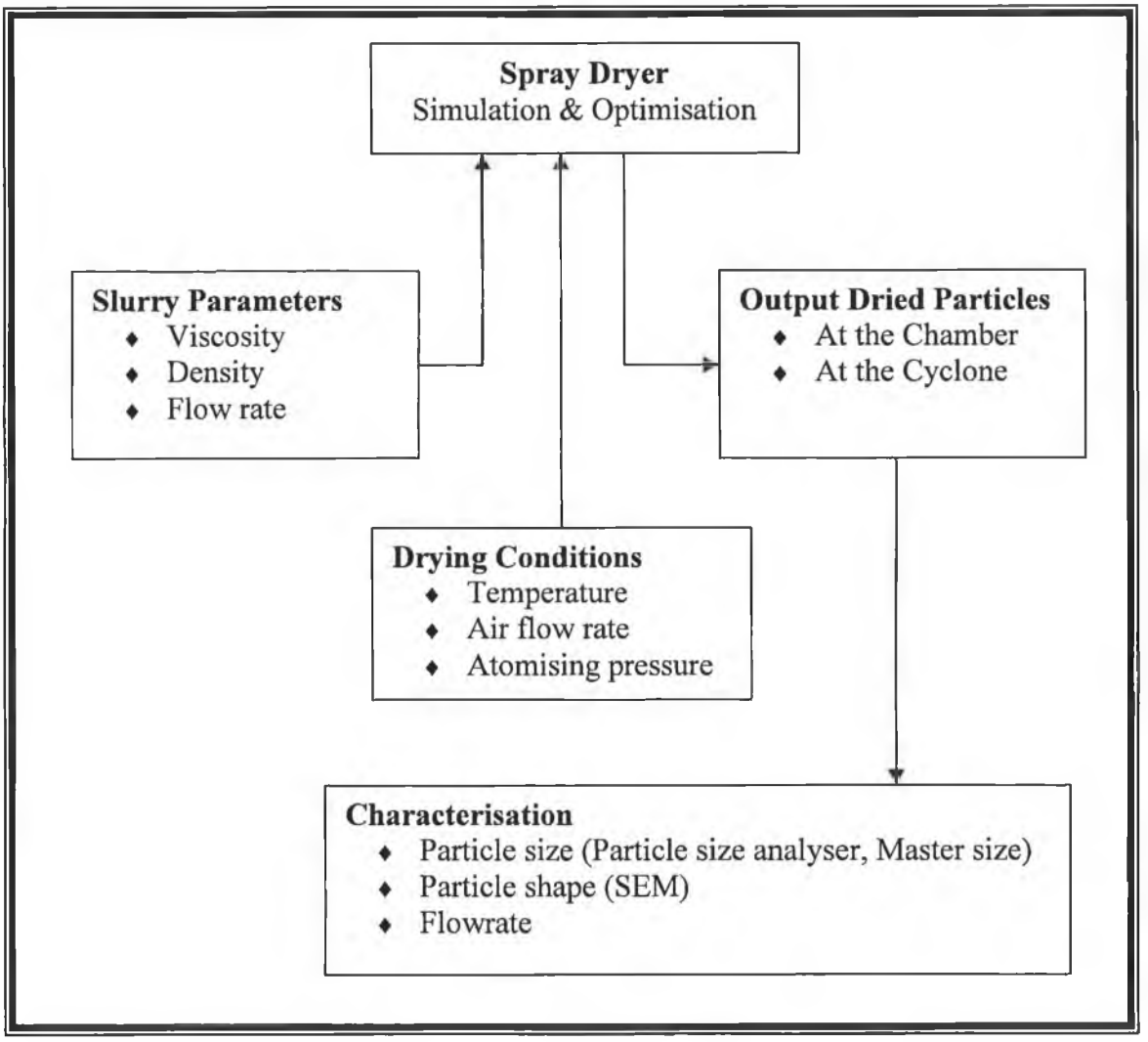

Figure 3.1: Equipment and parameters used in the experimental phase of the research.

3.2 DESCRIPTION OF THE SPRAY DRYER

A systematic of the Niro-Minor spray dryer used in the present research, is shown in Figure 3.2. The two fluid mixed spray can be divided into a number of major parts. This unit consists of an insulated drying chamber mounted rigidly within a framework. The framework supports the auxiliary equipment, namely the instrument control panel, product recovery cyclone, air heater, and fan. The Feed liquid (in this case HA slurry) is fed to the atomizer by a small capacity peristaltic pump, and atomised into a fine spray of droplets. The spray is driven into contact with the hot air entering the chamber through a ceiling air disperser (Figure 2.10). The ceiling air disperser is located at the centre of the chamber lid. Removal of moisture from the droplets is accomplished virtually instantaneously, and although residence time of the product in the drying chamber is short, dry powder is drawn with the air towards the base of the chamber. The powder and air mixture (generally fine particles) are then sucked out to a small highly efficient cyclone where the powder is separated away from the air and collected in a glass jar. However dense particles collect at the base of the chamber and collected from this point. The specific details of the above components of a spray dryer will be discussed in the following sections.

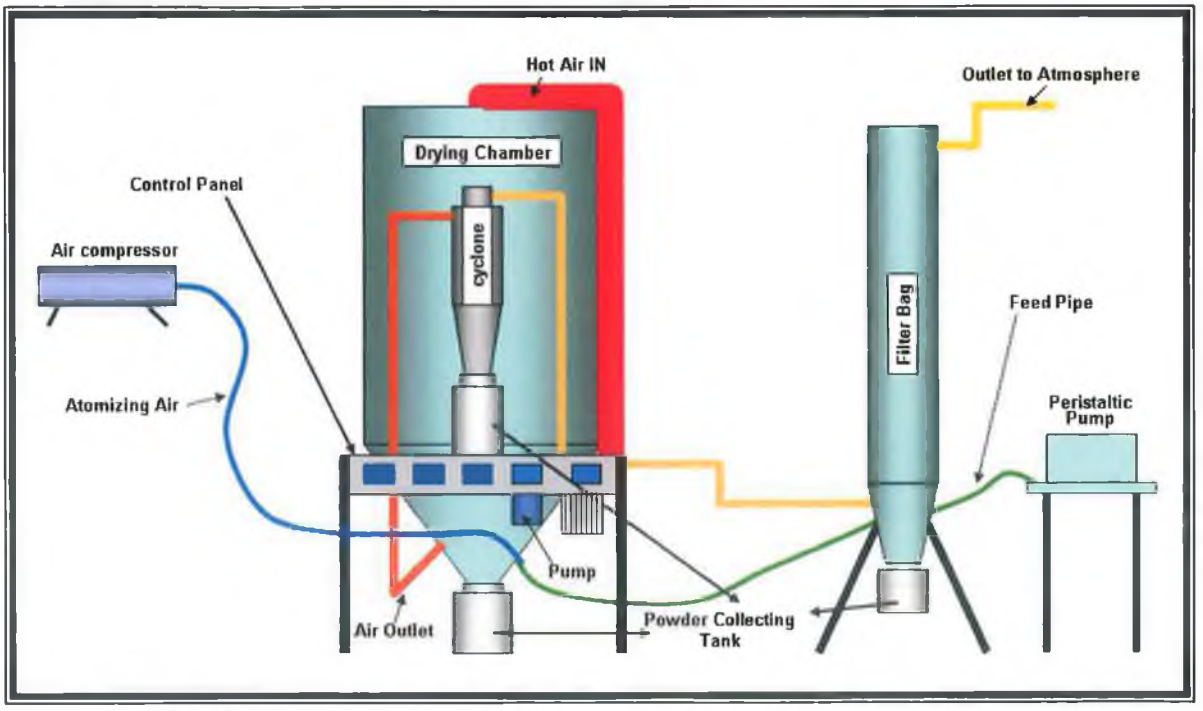

Figure 3.2: Systematic sketch of the spray dryer (Niro-Minor Production).

3.2.1 DRYING CHAMBER

The drying chamber is 800mm in diameter, with a 600 mm cylindrical height and a conical based. The cone angle is 60 degrees. All of the internal surfaces are made of smooth stainless steel AISI 316. Air enters from the top and leaves the base of the chamber through a duct, which connects the chamber base to the cyclone (Figure 2.10). The chamber is insulated so that heat loss is minimised.

(A) Inlet Drying Air

The hot air injected from the top of drying chamber, is heated by electric heaters that are placed inline with the air supply between the inlet air supply port in the drying chamber and the air filters. A fan is mounted under the instrumental panel on the exit side of the cyclone, and draws air though; the heater, air disperser, chamber and cyclone. The maximum capacity of air drawn through the drying chamber is 80kg/hr at 80°C. (Specification details in Appendix-B).

(B) Outlet of Product and Air

The dried powder is collected at the bottom of main drying chamber and cyclone in buckets that are placed and locked in at the each of the collection points (Figure 3.2). Heavy particles drop due to gravity into the main drying chamber bucket; where as lighter particles due to their light by weight are carried by the air to the cyclone and collected in the cyclone bucket, leaving the clean air to exit.

3.2.2 THE EXTERNAL TWO-FLUID NOZZLE ATOMISER

The two-fluid nozzle atomizer (Figure 3.3) was used to breakdown the feed (it's positioned is shown in Figure 2.10). The positioned is axially down the centre of the drying chamber so that feed comes in contact with the centrally opposite direction of the hot air coming from the top of the drying chamber roof. The feed and air are injected using separate nozzles (Figure 3.3(b)). The feed is pumped by a peristaltic pump and the compressed air is fed to the air nozzles using a calibrated scale.

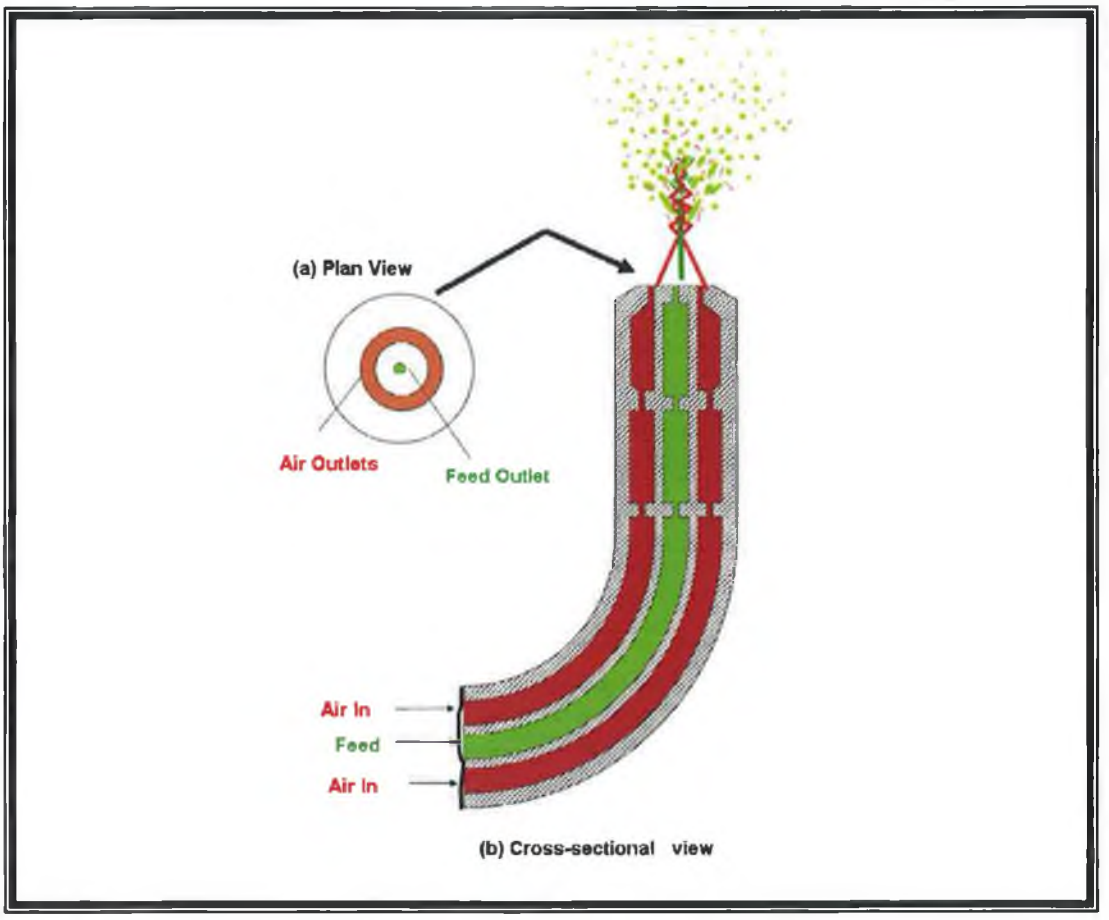

Figure 3.3: Schematic cross-section of the external two-fluid nozzle.

3.2.3 OPERATING PANEL

Two digital temperature controllers are mounting on the panel of the spray dryer (Figure 3.4). The inlet (HBO 433.206) and outlet (HBO 331.103) temperature controllers (Figure 3.4) are encased by a black metal housing with the front sealed off water tight. The inlet and outlet temperature indicators have a range of 0 to 500°C and 0 to 200°C respectively with an error of ±1°C **[139]**. The operation switch on the operating panel controls various operations such as:

Position O; Turns on the chamber light and panel live indicator light.

Position M; Fan motor on.

A complete description of the operation of the Niro spray dryer may be found in its manual **[139]**. The position selected depends on the inlet drying air temperature required for the drying operation that enables heaters on and the exact inlet and outlet temperatures are controlled by inlet and outlet temperatures indicators on the panel. For example to set

220°C inlet drying temperature, turn on position III, sets 220°C using a little knob, on the inlet temperature indicator.

Position I Produce drying temperature up to 125°C in the chamber

Position II Chamber drying temperature between 125 and 200°C

Position III For temperature greater than 200°C

The inlet drying temperature thermocouple is located near the heaters, far away at the inlet of drying chamber, so exact inlet temperatures are measured at the inlet of drying chamber and calibrated with an accuracy ±1°C.

Inlet drying air flow rate is controlled by a knob at the end on the operating panel. It has 6 levels between closed to open condition.

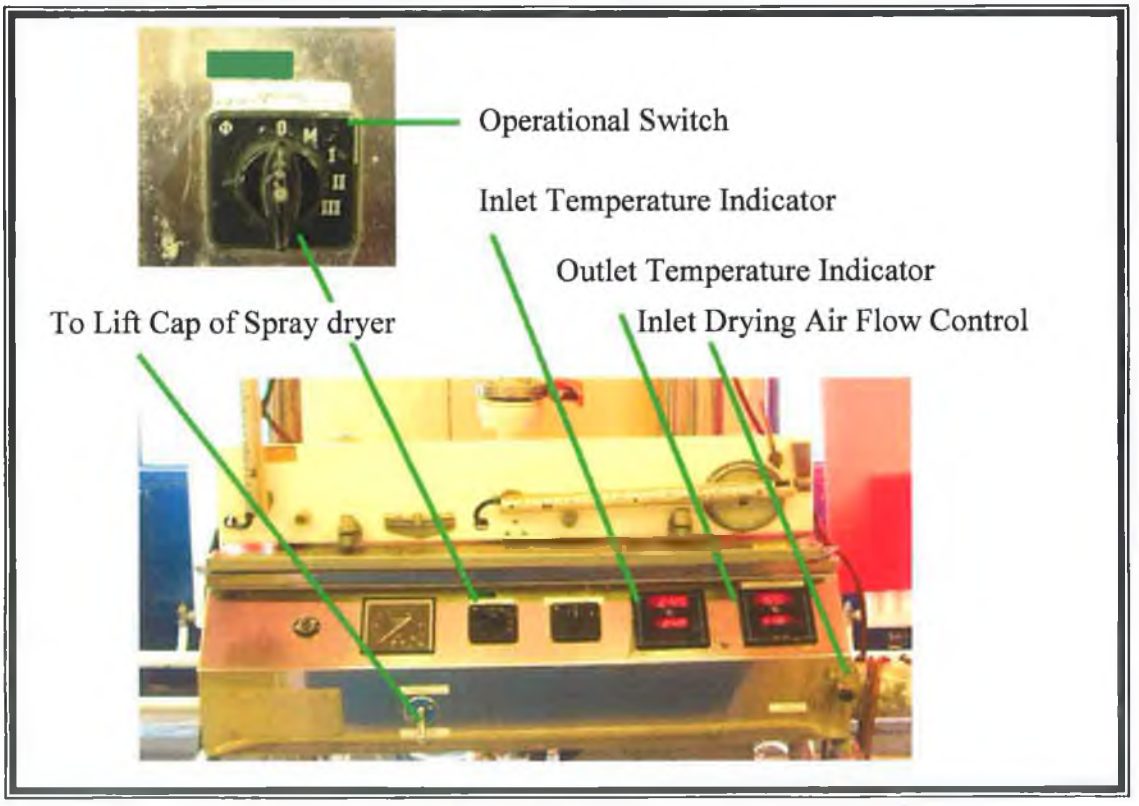

Figure 3.4: Operating panel of the spray dryer.

3.3 OPERATION PROCEDURE

Before start up, the spray dryer must be checked that all duct connections are tightened and mounted correctly such as; the connection between chamber and cyclone, the chamber roof is in the correct position (and air tight), and that the air and liquid connections are properly installed. Centralising the nozzle position is an important to achieve the maximum interaction of the nozzle spray with the hot air. Centralising of nozzle means placed the nozzle along the axis of incoming hot air from the top of the spray dryer. This was done by the adjusting four screws to fix its position to get the maximum atomisation at a given viscosity (Figure 3.5). The spray cone angle was adjusted to 45 degrees outside the main drying chamber before been placed in side the drying chamber. It was fixed by screw on the nozzle pipe. All experiments were run with this setting of the spray angle, and once the nozzle was placed in the correct central position in the drying chamber, maximum direct interaction of the nozzle spray was achieved with the hot air [**139**].

Figure 3.5: Assembly of the external two fluid nozzle with adjusting screw to set the spray angle.

The spray drying operation for the external two-fluid nozzle is as follows [**139**];

- The air disperser cover is centred over the drying chamber and once the chamber roof is in the correct position, it is then sealed.
- The connection between the chamber and cyclone is tightened and the rubber gaskets are checked that they are in their proper position.
- Powder collecting jars are placed under the chamber and cyclone respectively.
- The dampers of outlet chamber and cyclone at the jar positions are open to collect the dried powder.
- The nozzle is assembled, and the air and liquid connections are connected with the feed tube.
- The nozzle is centrally aligned in the chamber
- The feed pipes are thoroughly tightened.
- The compressor is turned on and allowed to generate sufficient pressure to above 5 Bar before atomisation commences.
- A check is made that the fan and pump both rotate in the clockwise direction.
- The fan and the air heater are turned on.
- The damper on the exhaust duct is adjusted to control the inlet hot air flow rate (for an example 5 Nm^3/hr)
- Set inlet and outlet temperatures on the inlet and outlet temperature indicator on the control panel to 461K and 110K respectively.
- Wait until the set temperatures reach are reached (usually it takes 1 hour).
- When the outlet temperature has reached approximately 110°C, air is passed to the nozzle at a flow rate corresponding to 75% of the maximum Flow meter readings
- The air and water-flow rates are gradually built up while maintaining the pressure; the outlet temperature must not be lower then 110°C, as long as water is fed into the nozzle.
- As soon as, the temperature remains constant for 10 minutes, HA slurry can be supplied to the nozzle and drying begins.
- Now set the feed rate to start the spray drying process. Observe whether there is pronounced splashing of partially dried product on the glass window of drying

chamber. If excessive splashing, switch back to water and re-check nozzle position and spray characteristics.

- During operation, the chamber jar must be changed before it totally fills up and the jar under the cyclone is also changed (the outlet of cyclone damper must be closed).
- For the shut-down procedure, the jars are to be changed. The feed of the pump is changed from HA slurry to water, to clean the pump and feed system, the feed pump is then stopped. Shut-off heater. After the plant has cooled down, shut-off the compressed air supply and then stop the fan.

3.4 VISCOSITY OF HA SLURRY

Viscosity plays an important role in the breaking up of liquid jet into spray [**140-142**]. Viscosity is the property of a fluid that characteristics it's perceived "thickness" or resistance to shear and defined as the measure of the internal friction of a fluid [**143**]. The greater the friction, the greater the amount of force required to cause fluid flow, which is called "shear". Shearing occurs wherever the fluid is physically moved or distributed, as in pouring, spraying, mixing, and so on [**144**]. All fluids can be classified into two types; newtonian and non-newtonian fluids. Many real fluids cannot be described by a simple rheolgical equation. The apparent viscosity of more complex fluids depends not only on the rate of shear, but also on the time the shear has been applied [**144**]. These fluids may be subdivided into two classes according as the shear stress decreases or increases with time when the fluid is sheared at a constant rate; Thixotropic or Rheopectic fluids [**144**]. A thixotropic fluids has the apparent viscosity decreases with time because the rate of breakdown of a structure during shearing at a given rate will depend on the number of linkages available for breaking and must therefore decrease with time [**145**]. In the rheopectic fluid, the flow is caused by gradual formation of a structure by shear. This results in the fluids viscosity increasing with time as it is sheared at a constant shear rate. The HA slurry falls into the latter case (rheopectic fluid) as with time the particle settles down, causing thickening of the slurry. During the spray drying process, the HA slurry is continuously stirred to maintain a uniform mixture and thus keep the viscosity constant with time. As viscosity has an influence on the rate of flow, it was necessary to measure the viscosity of the HA fluid and match it to an ideal slurry feed rate. The ideal rate sends the slurry into the heating zone (hot air) for efficient drying. Flow rates that are too high (or using low viscous fluids) cause the slurry to be driven up into the heating vent, therefore blocking the hot air chamber inlet. Low flow rates (or high viscous fluids) would find it difficult to raise the slurry towards the heating zone, thus the slurry would collect at the base of the chamber.

There were two main types of viscometry measurement technique (Figure 3.6) that were used for the determination of the viscosity of the HA fluids [**145**]:

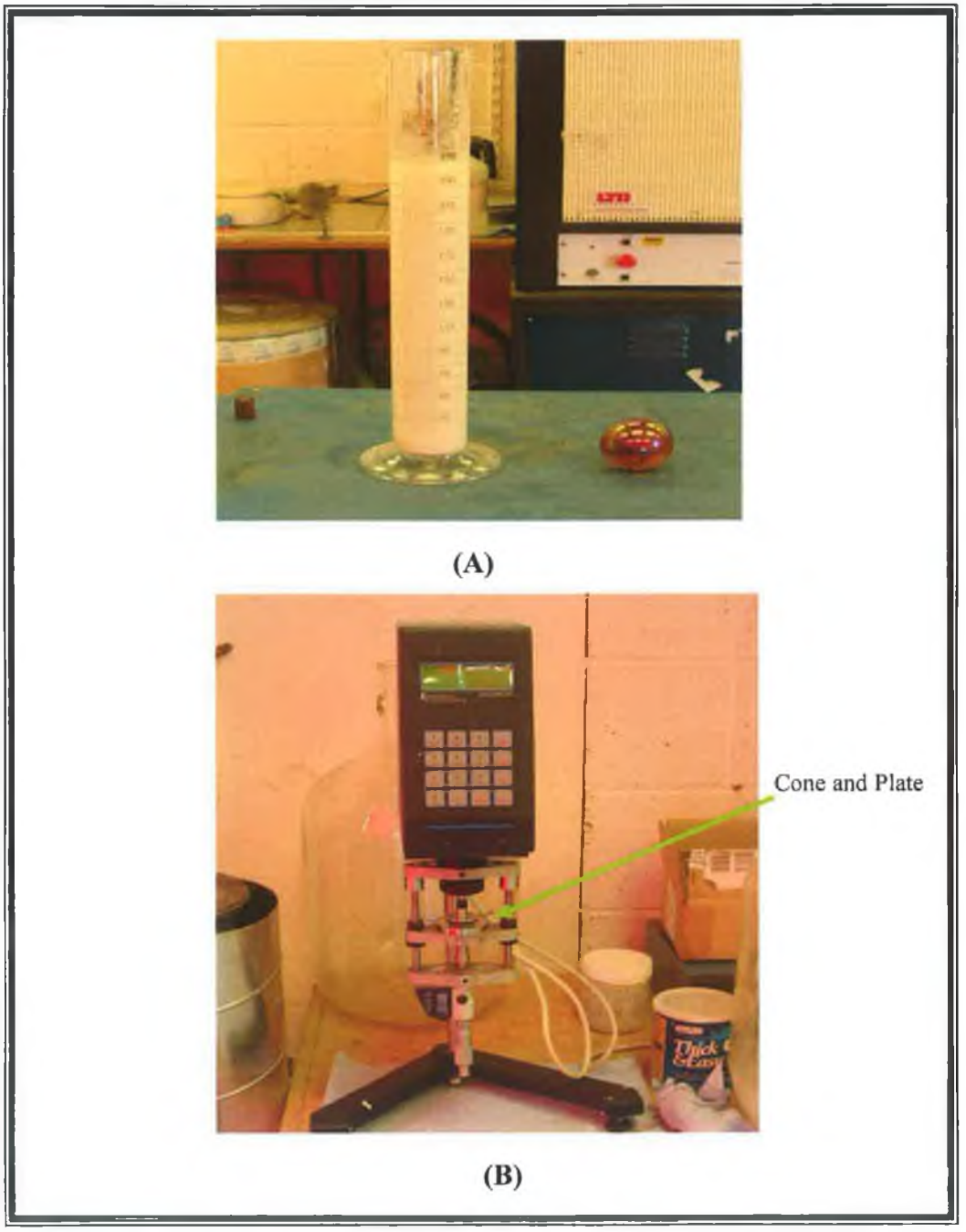

Figure 3.6: Viscosity measurement techniques: (A) Cylinder and falling sphere method, (B) Rheology international series 2 viscometer.

3.4.1 THE FALLING SPHERE METHOD

The falling sphere method was used to determines an approximate viscosity of a HA fluid by measuring the time taken for a sphere of known mass and volume to fall freely in the fluid of interest. Knowing this time, the viscosity of the fluid can then be determined mathematically using the following equation:

$$\text{Viscosity} = \eta = \frac{2(\Delta\rho)gR^2}{9V} \quad \text{----------Equation 3.1}$$

Where, $\Delta\rho = \rho_s - \rho_f$, ρ_s is the density of sphere, ρ_f is the density of the liquid, R is the radius of sphere, V is the velocity of the sphere in the fluid, g is the gravity. This viscosity was then compared to a chart in the rotational type viscometer [**145**] to select the ideal share rate to be used to accurately measure the viscosity of the fluid.

3.4.2 ROTATIONAL TYPE VISCOMETER

In the present study, the cone and plate rotational type viscometer was used to measure the accurate viscosity of the liquid feeds (HA slurry). It involves direct determination of the relation between shear stress and shear rate by subjecting the entire sample to a uniform rate of shear in a suitably designed instrument [**145**].The cone and plate viscometer was appropriate for such a fluid as it contains small particles, and because the cone angle is so small (3°) and the average gap width is correspondingly small (less than 0.5mm) errors due to surface tension were negligible, therefore, the apparent viscosity of the fluid was be calculated using [**145**]:

$$\mu_a = \frac{3M\Omega}{2\pi R^3\theta} \quad \text{----------Equation 3.2}$$

Where, M is the torque, Ω is the rotational speed (rpm), R is the radius of cone plate, θ is the angle of cone plate. The Rheological International Series 2 viscometer provide the viscosity value for you once the correct shear rate is selected (this was ensued using the falling sphere method).

The procedure involved taking a small sample of fluid (HA slurry) and placing in onto the plate. The plate was then raised using a micrometer until a gap of 0.1mm was achieved. The shear rate (determined form the falling sphere method) was applied and the viscometer gave out viscosity readings for their fluid. Results were taken every 2 seconds for 4 minutes to determine an accurate average viscosity value.

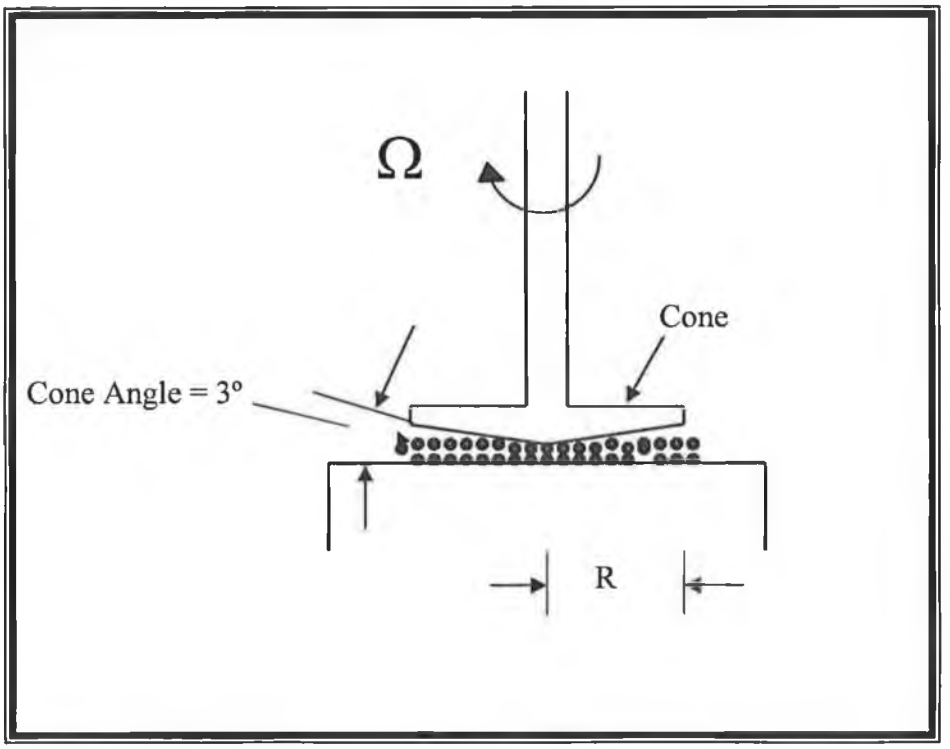

Figure 3.7: Cone and Plate Viscometer [145].

3.5 AIRFLOW MEASUREMENTS

Most spray dryers are constructed in such a way that the air enters tangentially inside the main chamber of the spray dryer. This is defined as swirl [**142**]. The degree of swirl is expressed by the swirl angle which is defined as the angle between the axial and tangential velocity components of the drying air at the inlet. This swirl angle has a great influence on the airflow pattern [**142**], as at small swirl angles the airflow pattern consists of a fast flowing core with slow circulation around it. When the swirl angle is increased, at a certain value (critical swirl angle) a vortex breakdown will occur, hence the direction of the velocity in the centre of the original vortex will be reversed [**142**]. The air flow velocity and direction was important as these measured values were inputted into the model to simulate the spray drying process.

3.5.1 NOZZLE VELOCITIES

(A) Air pipe

The atomised air was stored in the compressor at 6 Bar used to supply the air pipe of the two-fluid external nozzle. The atomisation air was controlled using a calibrated volumetric flow scale set at 5 Bar (given in the range 0 to 100%). Initially air was fed into the air pipe nozzle through four pipe chambers. The exit velocities of air nozzle at the different calibrated volumetric flow percentage were measured using an electronic potentiometer (Figure 3.8, 3.9) which had a range of 0.0 to 30 m/s and an accuracy of ± 0.01m/s (and using equations 3.3 and 3.4 as air flow volume was divided into four parts (Appendix-B)) . The air nozzle velocities were measured by two methods at the different calibrated percentage scale; firstly the air nozzle was placed inside the drying chamber and then the velocities were measured at the top of spray dryer without its roof (Figure 3.8), and secondly the air nozzle was placed in an open space horizontally to measure velocities along the axis at the different distances (Figure 3.9).

$$Q = 4\,Av \qquad \text{Equation 3.3}$$

$$v = Q/4A \qquad \text{Equation 3.4}$$

The procedure involved, velocities taken at intervals of 10%, from 30 to 100% of calibrated volumetric flow scale at 5.0 Nm^3/hr. In both procedures values were taken every

10 mm across the top of the chamber or axially out form the horizontally placed nozzles to give a two dimensional representation of the nozzle air flow.

Figure 3.8: Air nozzle velocity measured at the top of the spray dryer by electronic potentiometer.

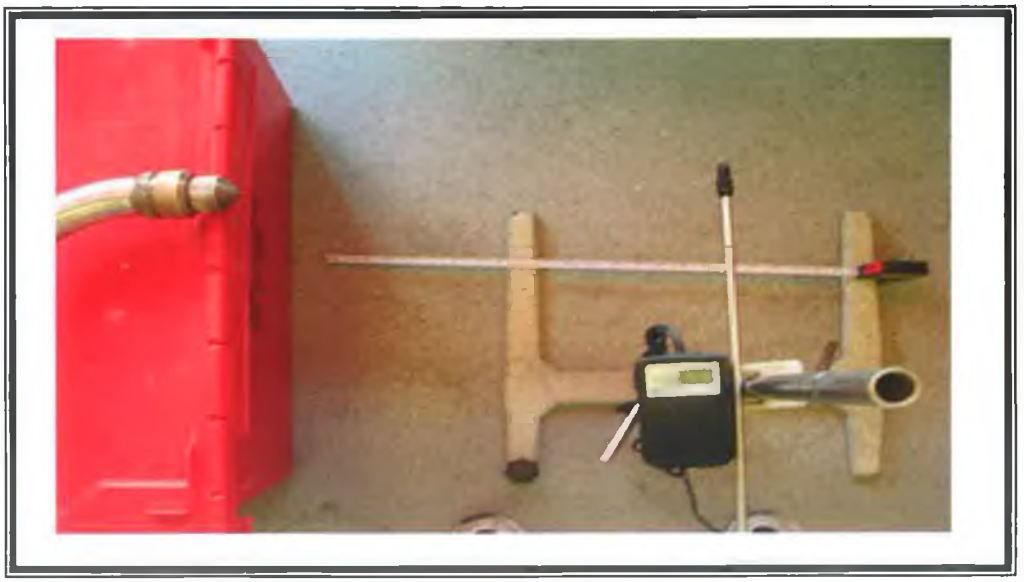

Figure 3.9: Air nozzle of two fluid nozzle velocity measured by electronic potentiometer.

3.5.2 AIR FLOW INSIDE THE SPRAY DRYER

The hot air flow rate was measured by the pressure drop across the cyclone of the spray dryer because the inlet hot air was coming directly from heater in the sealed cover so there was no point to measure at, and the hot air after the main chamber was flowing in a closed

circuit by only one pipe line passing through cyclone, scrubber and then exhaust to atmosphere. With the consultation Niro Company, the hot air flow measured across the cyclone and the company provided K chart which used in the later calculations (Appendix-B).

The hot air flowrate inside the spray dryer was measured by manometer (Figure 3.10) with a range of 500mm and accuracy of ±1mm of H_2O. The inlet and outlet of the manometer were fitted before and after the cyclone respectively by drilling and tapping into the pipe line. The flow rate was read directly by the pressure drop on a calibrated scale and given by the following numerical equations [**146**]:

$$PGR = K * D^2 * \sqrt{\rho * \Delta p} \text{ (Kg/hr)}\text{----------Equation 3.5}$$

$$D = \sqrt{\frac{PGR}{K}} * \frac{1}{\sqrt{\rho * \Delta p}} \text{ (m)}\text{----------Equation 3.6}$$

$$\Delta p = \frac{PGR^2}{K^2 * D^4 * \rho} \text{ (mmWG)}\text{----------Equation 3.7}$$

Where, PGR is the process gas rate through cyclone, D is the cyclone diameter, POR is the product rate into cyclone, ρ is the Gas density at cyclone inlet, K is the capacity factor $\frac{POR}{PGR}$.

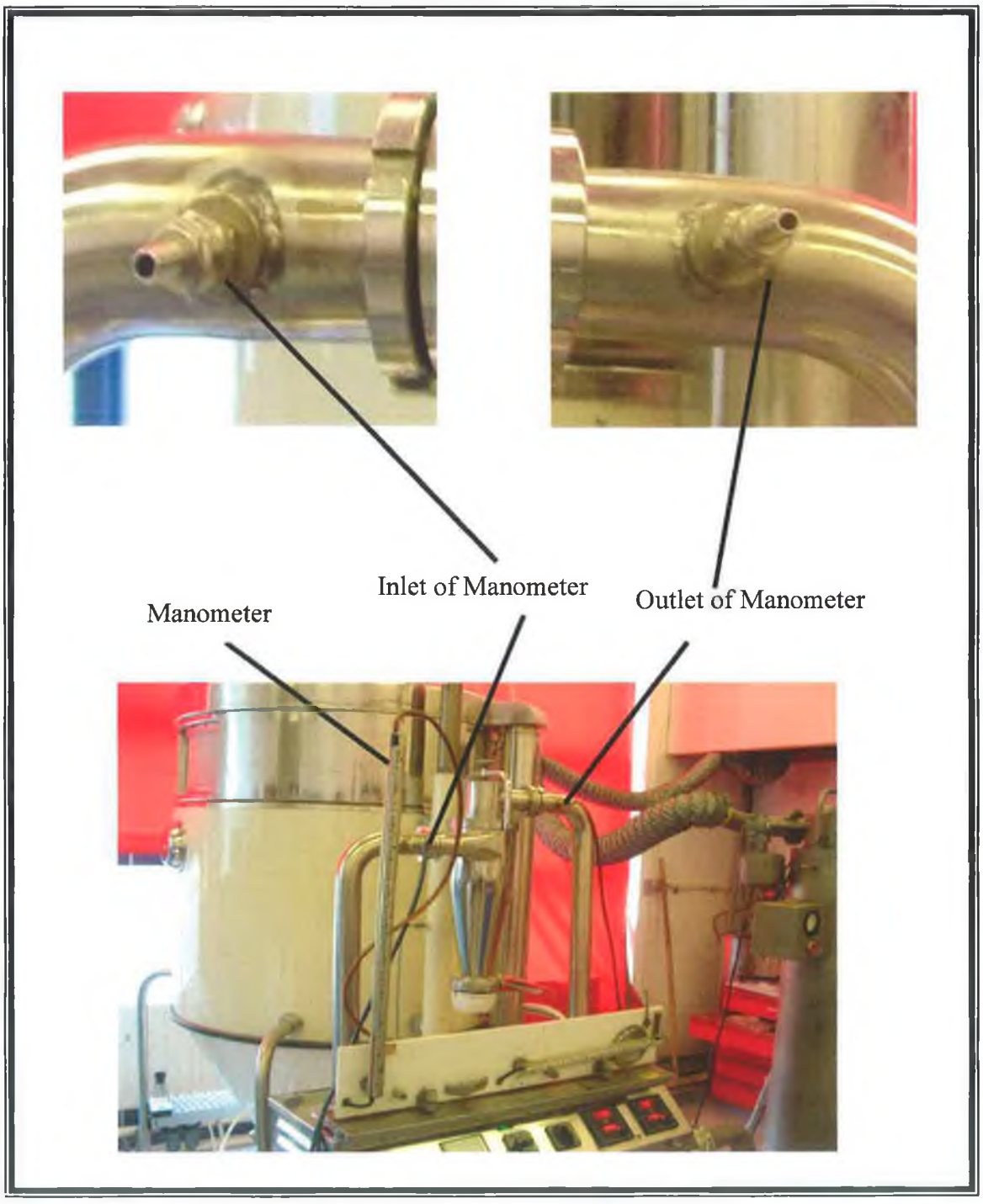

Figure 3.10: Pressure tapping of inlet and outlet of the manometer to measure the flowrate inside the spray dryer.

3.6 FEED FLOW MEASUREMENT.

The feed pipe of the external two-fluid nozzle is located at the centre of the nozzle. It is separated from the air pipe and feed pumped by a peristaltic pump directly in the main drying chamber.

In this research, the HA slurry solution was pumped through the nozzle at a volumetric flow rate, measured by collecting a known volume in a graduated cylinder over a set time for different speeds of the peristaltic pump, using the equation for an incompressible fluid (Appendix-B):

$$Q = A\,v \qquad \text{Equation 3.9}$$

Where Q is the volumetric flow rate (m^3/s), A the cross-sectional area (m^2) and v is velocity (m/s) of the fluid. The velocity of the slurry for different peristaltic pump settings (rpm) was measured using equation 3.9 and getting mass flow rate of feed by below equations 3.10 and 3.11.

$$\text{Measured Volume rate} = Q = Av = (\pi d^2/4) \times v \qquad \text{Equation 3.10}$$

$$\text{So Mass flow rate} = \dot{m} = \rho_f (\pi d^2/4)\, v \ (kg/sec) \qquad \text{Equation 3.11}$$

ρ_f is the feed density (kg/m^3) and d is diameter of feed pipe (m).

3.7 TEMPERATURE DEVICES

The temperature profile was very important in the main spray drying chamber as the evaporation of the fluid in this slurry of HA depends upon the occupation of the slurry in various temperature zones. The temperature measurement had the two approaches: one can measure with an unprotected probe and the second is protecting probe [**147**], subsequently, the probe must be cleaned before another measurement cycle can begin. The time span over which actual temperatures can be measured using an unprotected probe are limited by the temperature equilibration of the probe and the rate of particle deposition. This meant that in most sprays the response time of the probe should be very short while the density of the spray should be low. The other approach is to prevent the probe from begin hit by droplets [**147**]. Avoiding wetting of the probe, requires placing a shield over the probe, and these vary from simple shields to so-called aspirated probes. Papadakis [**148**] used a simple shield to protect the probe from being hit by droplets mainly from one direction only. It is clear that such arrangements do not work in flow systems with circulations or large eddies. Goldberg [**149**] developed a shield to protect the probe from particles coming from all directions. In such arrangements the problems arises that the probe is also measuring the temperature surrounded by the cooler walls of the shield. To avoid this, Nijhhawan et al. [**150**] described that the shield should be aspirated. Kieviet et al. [**151**] developed a temperature and humidity device which was based on protecting the temperature probe from being hit by particles by removing the particles from the gas stream. This was good in the sense that it gave results for the two air parameters, but gave no results for the effect on the particles themselves.

Rainbow refractometry has been used to measure the temperature of droplets which is based on the refractive index that is a function of temperature, because the density changes in condensed materials with changes in temperature [**151**]. Gemic et al. [**152**] measured the temperature using such a method. This method gave good results because the device doesn't come in contact with droplets.

Unfortunately the budget of this research did not extend to purchasing any of the above equipment so a simpler procedure was adopted. In this research, the temperature profiles were measured by using K type thermocouples (range -50 to 1000 °C and accuracy ± 2 °C)

at different points inside the main drying chamber (Figure 3.11 and 3.12). For that a mesh was designed and placed inside the chamber to hold the thermocouples at fixed positions. The thermocouples extension wires were taken out from the gasket of the drying chamber roof to measure the temperature at the different points. Then, lid was place to seal the drying chamber. The spray dryer was then run without the feed. The temperature was recorded at 15 point at one time when the inlet and outlet temperatures reached at the set value (for example inlet temperature 461K and outlet temperature 383K) and stabilised for 10 minutes.

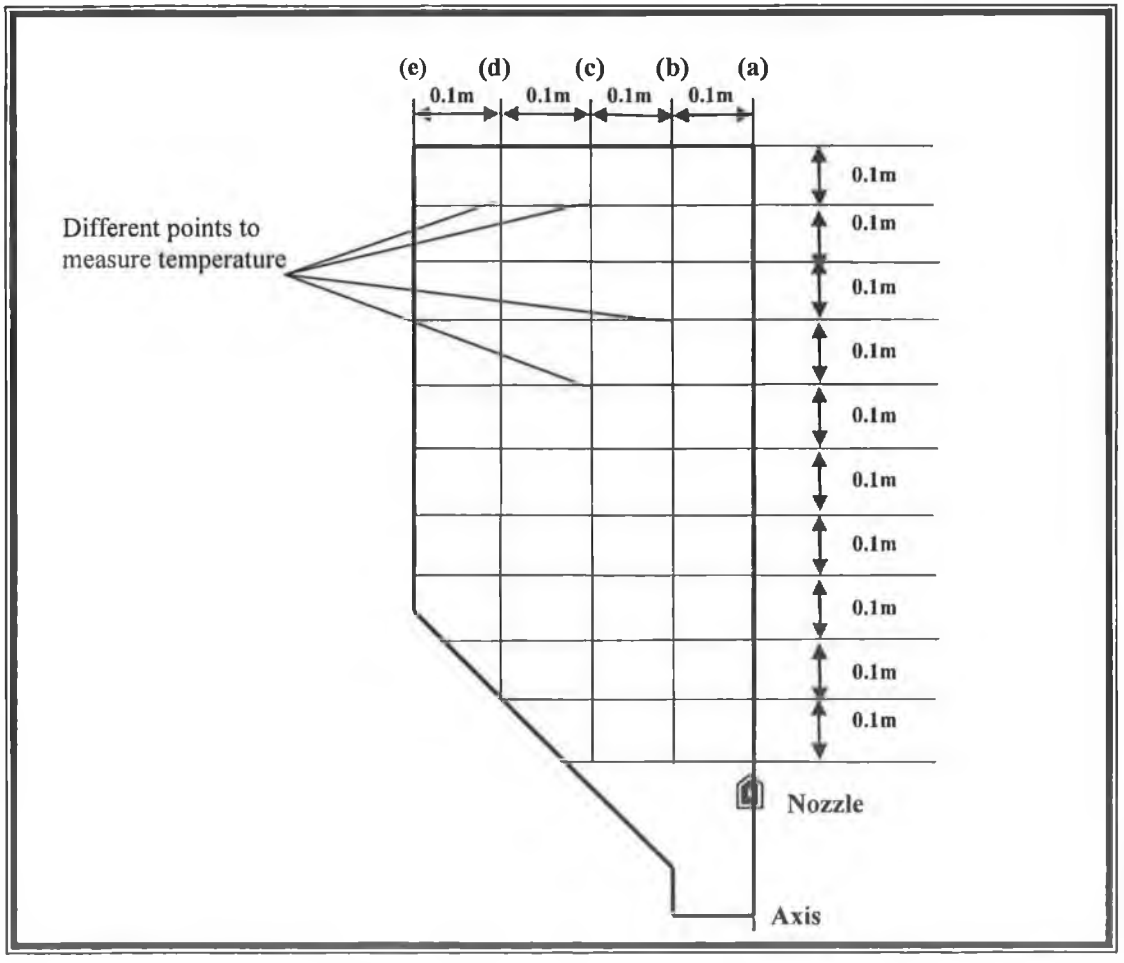

Figure 3.11: Mesh points used to measure the temperature experimentally.

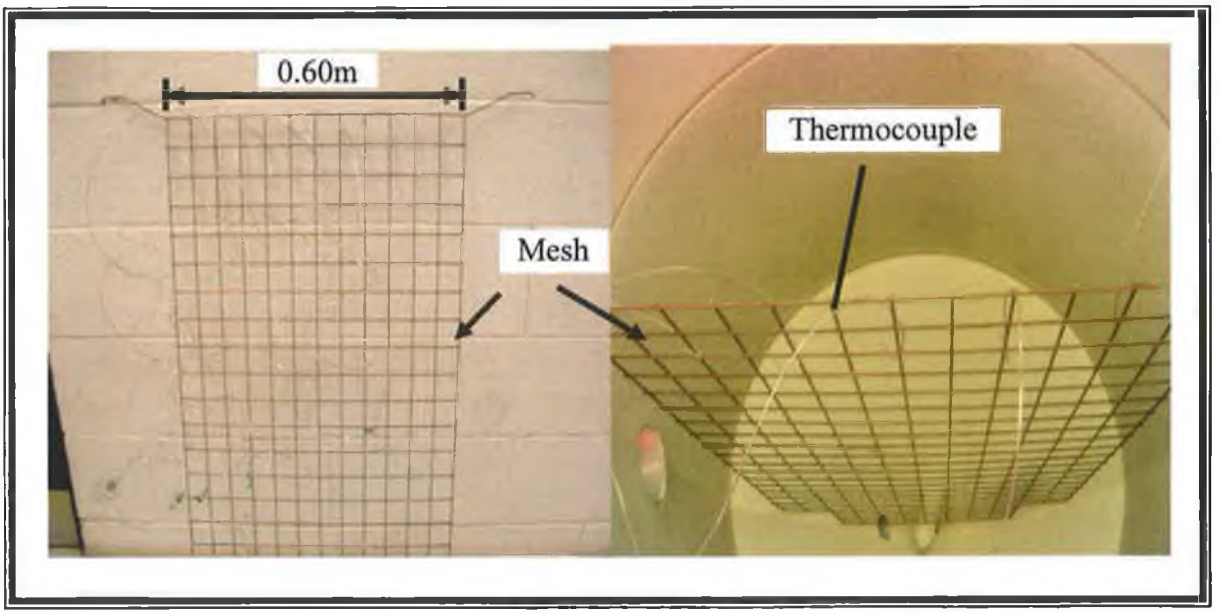

Figure 3.12: Mesh to hold the thermocouple inside the spray dryer to measure the temperature profile.

3.8 SPRAY DROPLET SIZE DEVICES

To understand the droplet behaviour inside the spray dryer, not only the averaged size and velocity distributions of droplets are of importance, but also the instantaneous properties of individual droplets are required to understand the unsteady state of droplets, the flow structure and to evaluate heat and mass transport processes **[153-160]**. Glover et al. **[153]** used interferometric laser imaging (ILIDS) for droplet sizing which was based on an instantaneous spatial distribution of droplet size by analysing the out-of –focus image of droplets. Maeda et al. **[154, 150]** and Kawaguchi et al. **[155]** converted circular images with fringes into linear images by optical squeezing (defocusing horizontally and focusing vertically). The squeezing technique reduced the noise, thus and the signal to noise, ratio of the interferogram becomes more enhanced compared to that of conventional techniques. To improve the understanding of swirling flow, a number of studies have been carried out. Sommerfeld and Qiu **[157]** studied the particle dispersion characteristics in a confined swirling flow. In this research a phase doppler technique and numerical technique were used. The Phase Doppler Anemometry (PDA) which is an extension of a laser Doppler velocimetry, gives the size and velocity of individual spherical particles simultaneously. However the PDA is a point measurement technique; while the imaging method Interferometric Laser Imaging Technique (ILIDS) provides instantaneous spatial distribution of the droplets. The results demonstrated the behaviour of different sized particles in a complex flow and the spatial change of the particle size distribution throughout the flow field.

Takeuchi et al. **[158]** studied the spatial distributions of droplet size and velocity in air heated spray, measured by (ILIDS). Kobayashi et al. **[159]** improved this method by creating an automated system for high speed processing using high resolution computer control digital camera and computing system so that the validation and accurate explanation of fringe spacing may be easily performed. These new optics have over come the previous techniques using photographs. This system measures denser spray during avoiding overlapping of images, however this system has reported an error of 4% on the mean diameter during measurements, but still provides effective measurement, of droplet sizes ranging from a few micrometers to several hundred micrometers.

The Standard Rainbow Thermometry (SRT) measures the diameter and temperature of one droplet at a time. The impossible detection of non-spherical droplets constitutes one of the most important problems for this technique. The effect of a non-spherical droplet on SRT pattern is to shift and distort it, making the analysis of the interference pattern impossible to identify. Beeck et al. [**160**] developed the Global Rainbow thermometry technique for measuring directly averaged temperature and average droplet size of spray. This was possible by constructive interference of laser-light scattering of the spherical droplets. The non-spherical droplets and liquid ligaments fall into the background and thus do not influence the interference pattern from which average size and temperature was derived. This was a large improvement with respect to standard rainbow thermometry, which is strongly influenced by particle shape. Moreover, the Global Rainbow technique was easily applicable for smaller droplets, as the global pattern was not affected by a ripple structure. Measurements carried out on water spray, showed the mean diameter obtained from the rainbow pattern was smaller than the arithmetic mean diameter measured by the phase-doppler anemometry.

Vetrano et al. [**161**] tried to improve the Global Rainbow thermometry technique, by looking at the influence of droplet non-sphericity on the size and temperature measurements of liquid droplets suspended in a liquid or a gaseous bulk. The research the simulation and experimental results gave satisfactory agreement, in measuring irregular droplet size. The GRT technique has already been applied to flat fan water sprays in air and flashing jets [**160**]. These new techniques GRT and ILIDS give a detail analysis and insight of atomisation in spray dryers. They identify the exact phenomena of breakdown of liquid sheet into droplets coming out from the nozzle in spray dryers together with thermal behaviour of droplets when using modelling techniques, and are quite useful to validate the simulation of droplets size, temperature and velocity inside the spray dryer.

In this study the spray was closed and sealed during the spray drying. It was not possible to use the above techniques to measure the particle and droplet sizes in the drying process due to lack of equipment and funding. So an attempt was made to look at the particle size distribution before and after the drying process was completed. The hydroxapatite powder

slurry was manufacturing in house (Appendix-B) with varying viscosities and before been pumped into the nozzle it was measured.

The dried powder was collected at the base of drying chamber and cyclone. The particle size was measured using the Malvern Mastersizer 2000. The basic principle of this device is shown in Figure 3.12. In the master size analyser, the particles are passed through the focus point of a laser beam. On interaction, these particles scatter laser beam light at an angle that is inversely proportional to their size. The angular intensity of the scattered light is then measured by a series of photosensitive detectors to give optimised resolution across a board range of sizes.

The following procedure was used to prepare the spray dried HA powder particle samples as dispersed solutions for particle size distribution in the Malvern Mastersizer. 1 gram of sodium pyrophosphate or dispersant was mixed intensively via a magnetic stirrer in 1000ml of deionised water to act as a dispersant. Then 0.5 gram of HA powder was dispersed in 30 ml of the above prepared dispersant in an 80-100ml heavy-duty beaker. The suspension was then stirred for a period of more than 2 minutes to ensure that the HA powder and dispersant had formed a suspension. The stirred suspension was then placed in an ultrasonic bath for a 5 minutes period. The scattered light data was then transferred to the software running on the computer. The D [4,3] or equivalent volume mean used to analysed the particle size distribution as laser diffraction gives the best result [**2,162**].

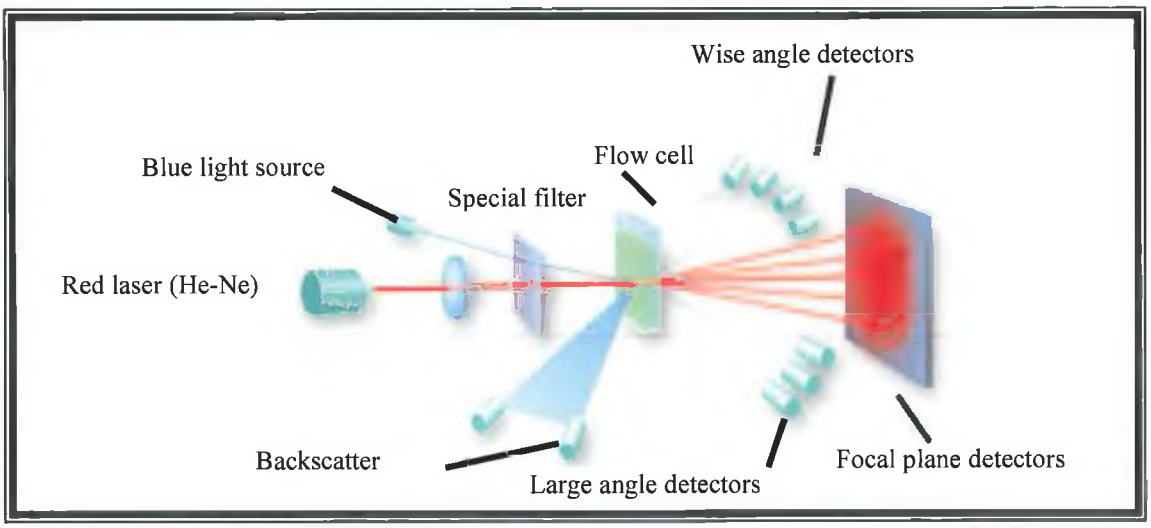

Figure 3.12: Systematic sketch the principle of Mastersizer 2000, adapted from [162].

3.9 POWDER CHARACTERISATION

In the powder manufacturing process, powder characterisation is very important to maintain quality and acceptance of the resulting powder for thermal spray applications (like powder size and powder shape) [**163**]. There are numerous techniques available including the Optical Microscope (OM), Scanning Electron Microscope (SEM) and X-ray diffraction. An optical light microscope was not sufficient to study powder shape as the image reveals only two dimensional surfaces. When viewing powder particles on the OM, only one particle can be focused at a time and the rest become out of focus producing a blurred image. The microscope, SEM has a superior resolution and depth of focus and can reveal the morphology characteristics of the powder. The SEM can produce a three dimensional image but it can only be attained by using two pictures taken at different angles [**164**]. The SEM operates by firing electrons onto the surface of a charged sample (HA samples has prepared by gold coating) and cathode detectors detect the reflection of this electron producing an image on a computer screen. Various HA powders in this research were produced in the spray dryer and their morphological shape was analysed using the SEM, the results of which are presented in Chapter 5.

4

Simulation and Modelling

4.1 INTRODUCTION

The experimental data was either used as inputs or to validate the simulation results reduced by the FLUENT 6.2 software. This chapter will describe the Computational Fluid Dynamic (FCD) background to the software and the procedures used in this research to model spray drying. CFD is solely concerned with obtaining a numerical solution to fluid flow problems using computer software [**165**]. The advent of high speed and large memory computers has enabled users to obtain solutions to many flow problems including those that are compressible or incompressible, potential or non-potential, laminar or turbulent, multiphase, chemically reacting or non-reaction [**166**]. The equations governing the fluid flow problem are the continuity (conservation of mass), the Navier-Stokes (conservation of momentum), species, and energy equations, and these equations makeup a system of coupled non-linear partial differential equations [**165,166**]. Due to nonlinear terms in these partial differential equations, these analytical methods yield very few solutions. In general, closed form analytical solutions are possible only if partial differential equations are made linear or higher orders are neglected of linearity. In most engineering flow situations, the non-linearity cannot be neglected and there the only option left; therefore numerical methods are needed to obtain solutions. CFD replaces the partial differential equation governing the fluid flow, with algebraic equations, which in turn can be solved with the aid of a digital computer to get an approximate solution [**167**]. Various discretization methods exits in CFD; finite difference methods (FDM), finite volume method (FVM), finite element method (FEM) and boundary element method (BEM) [**168,169**]. FDM was the most commonly used method in CFD applications but it has been replaced by FVM

because it has advantage of allowing direct discretization in the physical space, for arbitrary mesh configuration, without the necessity of an explicit computation of metric coefficients [**167,168**]. The most advanced CFD commercial softwares available are FLUENT Inc and CFX, both using FVM.

Discretization is carried out done by a control-volume-based technique to convert the governing equations into algebraic equations so they can be solved numerically [4]. CFD involves firstly discretizing the physical domain into a set of control volumes or cells that the flow occurs within, such as the interior of a spray nozzle or the drying chamber system of a spray dryer. This discretization is straightforward for very simple geometries such as rectangles or circles, but is a difficult problem in Computer Aided Design (CAD) Software for more complicated geometries. Currently automatic "mesh generators" are simply but not adequate in these cases, requiring extensive investment of time on the part of the scientist or engineer to generate mesh geometries [**169,170**]. This leads to problems in Human-Computer Interfaces (HCI). In a discretized mesh (Figure 3.1) the Navier-Stokes equations take the form of a large system of nonlinear equations; going from the continuum to a discrete set of equations is a problem that combines both physics and numerical analysis. For example, it is important to maintain the conservation of mass in the discrete equations. Between 3 and 20 variables are associated, at each node in the mesh; the pressure, the three velocity components, density, temperature, and so on. Furthermore, capturing physically important phenomena such as turbulence requires extremely fine meshing in parts of the physical domain. Currently meshes with 20000 to 2000000 nodes are common, leading to systems with up to 4.0×10^7 unknowns [**171**].

A system of nonlinear equations is typically solved by a Newton-like method, which in turn requires solving a large, sparse system of equations in each step [**172**]. Sparsity here means that the matrix of coefficients for the linear system consists mainly of zeros, with only a few nonzero entries. With 4.0×10^7 unknowns, clearly the system cannot store the matrix as a two dimensional array with 1.6×10^{15} entries; therefore storing the coefficients requires the development of efficient data structures which require little overhead storage but allow the necessary manipulations to be performed efficiently [**172**].

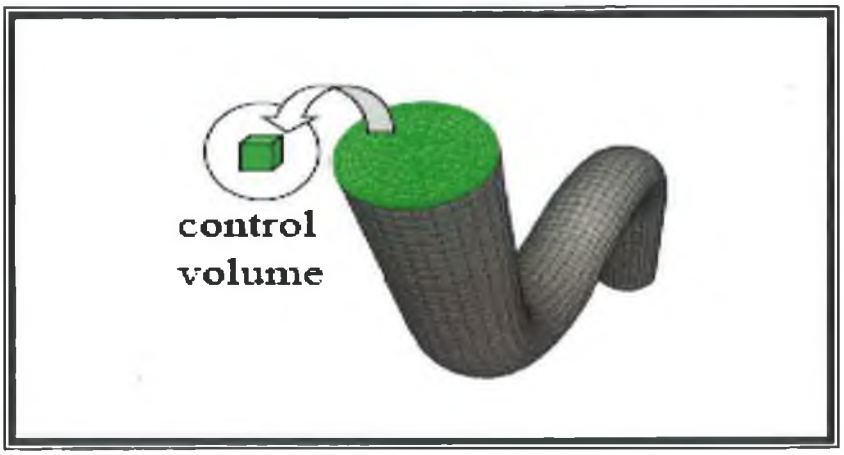

Figure 4.1: Fluid region of pipe flow is discretized into a finite set of control volumes (mesh) [166].

Methods for solving a large sparse systems of equations is currently been resolved [**170**]. As often this is the most time-consuming part of the program, and because the ability to solve these systems is the limiting factor in the size of problem and complexity of the physics that can be handled. Direct methods, which factor the matrices, require more computer storage than that permissible for all but the smallest problems. Iterative methods use less storage but suffer from a lack of robustness; they often fail to converge. The solution is to use preconditioning; that is, to pre-multiply the linear system by some matrix that makes it easier for the iterative method to converge [**173**].

CFD problems are restrained by the limits of computational power, so parallel programming methods are often used [**169-173**]. Therefore research problem often tries to identify ways of how to partition the data and to assign parts of it to different processors, hence usually domain decomposition methods are applied [**173**]. Domain decomposition is often expressed as a graph partitioning problem, namely finding a minimum edge cut partitioning of a discrete mesh, with roughly the same number of nodes in each partition set. This helps to used rapid heuristics approach to gain quick solutions [**169-173**]. An additional problem with parallel programming is that enhanced methods for solving the resultant linear systems often have inherently sequential characteristics, while parallel solution methods are not robust enough to tackle real world problems.

Once the solution has been found, analysing, validating, and presenting the result uses visualisation and graphical techniques. These techniques are not useful for viewing the computed flow field, but can help with understanding the nature of the problem, the interaction of algorithms with the computer architecture, performance analysis of the code, and most importantly, debugging.

In a research lab, a pilot plant (Bench sized version) spray dryer yields given perfect dried product results. However the industrial success of a new spray dryer depends upon it meeting its specified performance in all respects; therefore this is possible only by providing better scale-up kits [**174**]. It has been reported that there are two aspects to spray dryer scale-up; process and component [**175**]:

(A) Process scale-up: This requires the industrial plant to operate and produce a powder quality specified through process development and testing on a much smaller scale. Process scale-up also involves the aspects of health and safety, and environmental protection.

(B) Component scale-up: This involved mechanical design and the ability to reproduce similar performance on larger dryer sizes.

Without the component scale-up, process scale up could never be achieved. Commercial scale up involves the designing of atomizers that not only reproduce droplet size distributions and higher feed rates but are also are completely reliable [**176**]. The modelling could help to scale up in both ways, process and component to look in details design of spray dryer.

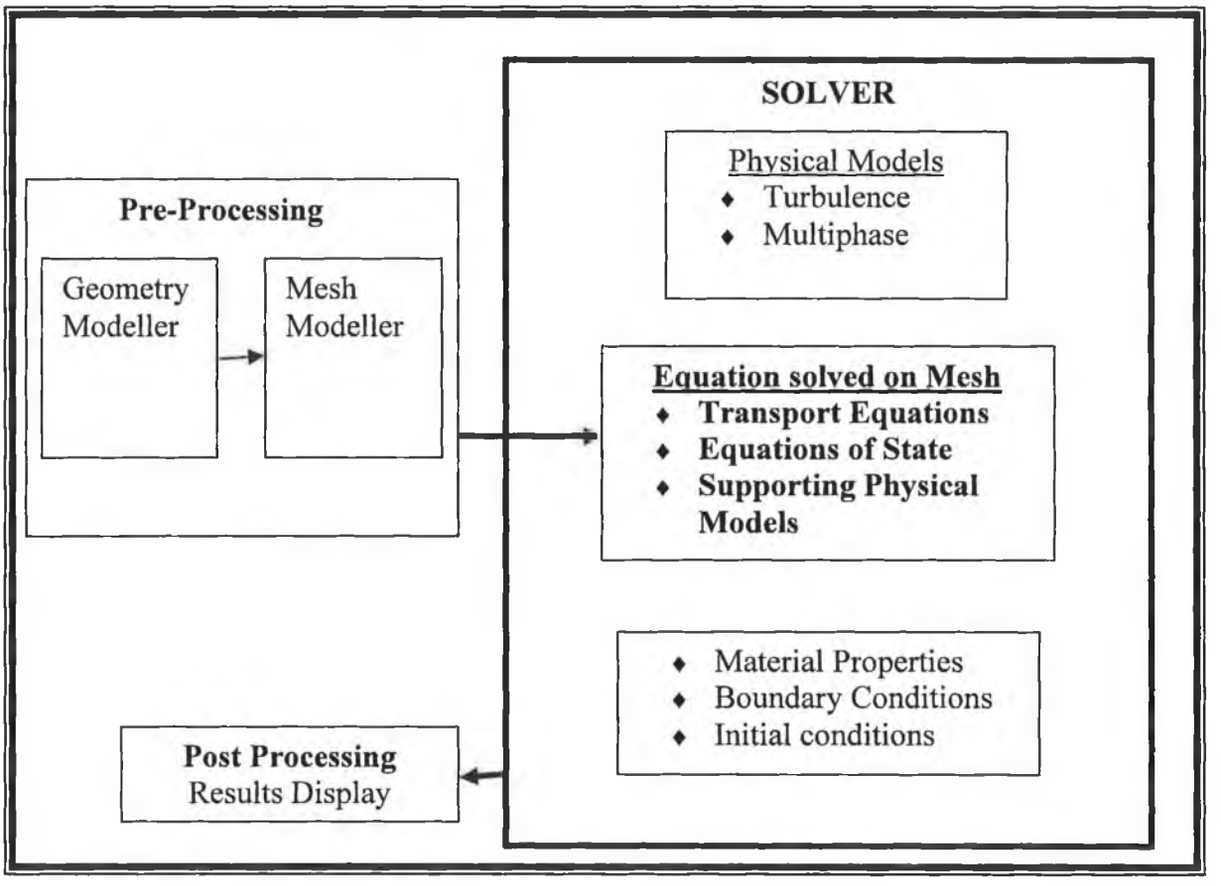

Figure 4.2: Systematic of CFD method used to solve complex physical fluid problems.

4.2 TURBULENCE MODELS

There are a number of turbulence models available to solve various fluid problems. The choice of turbulence model will depend on considerations such as; the physics encompassed in the flow, the established practice for a specific class of problem, the level of accuracy required, the available computational resources, and the amount of time available for the simulation. To make the most appropriate choice of model for a certain application, the user most to understand the capabilities and limitations of the various models [**168, 170**]. The Different types of turbulence models are [**169,170,177**]:

- Spalart-Allmaras model
- K-Є models
  - Standard K-Є model (used in present research
  - Renormalisation-group (RNG) K-Є model
  - Realisable $k-\varepsilon$ model (used in present research)
- $k-\omega$ models
  - Standard $k-\omega$ model
  - Shear-stress transport (SST) $k-\omega$ model
- ν^2-f model
- Reynolds stress model (RSM) (used in present research)
- Large eddy simulation (LES) model

In the present study, the Standard K-Є, the Realizable K-Є and RSM models were used for the modelling of the spray dryer. Within these three groups the standard K-Є, Realizable K-Є and RSM models were used for nozzles simulations and continuous phase of drying chamber, while the Realizable K-Є model was used for the atomizer models. Therefore the following sections will only describe these models.

4.2.1 THE STANDARD *K*-ϵ MODEL

The standard *K*-ϵ model is the simplest, fastest and most validated model for turbulence [**170,178**]. It brings the solution of two separate transport equations and allows the turbulent velocity and length scales to be independently measured [**178**]. The standard *K*-ϵ model in FLUENT has been defined as the "workhorse" of practical engineering flow calculations, since it was first proposed by Launder and Spalding [**180**] in 1974. Robustness, economy, and reasonable accuracy for a wide range of turbulent flows explains its popularity in industrial flow and heat transfer simulations [**171**]. It is a semi-empirical model, and the derivation of the model equations relies on phenomenological considerations and empiricism (mathematical expression in Appendix-C). Two improved versions of the standard model are also available in FLUENT, namely the RNG *K*-ϵ model [**180**] and the realizable *K*-ϵ model [**177,181**].

4.2.2 THE REALIZABLE *K*-ϵ MODEL

The realizable *K*-ϵ model contains a new formulation for turbulent viscosity was derived. A new transport equation for the dissipation rate, ϵ , This provides an exact equation for the transport of the mean-square vorticity fluctuation (mathematical expression in Appendix-C) and thus the model satisfies certain mathematical constraints in terms of Reynolds stresses, which is consistent with the physics of turbulent flows [**182**].

The one limitation of the realizable *K*-ϵ model is that it produces non-physical turbulent viscosities when the computational domain contains both rotating and stationary fluid zones (multiple reference frames, rotating sliding meshes). But the realizable model gives a good result when used for spray models [**182**].

4.2.3 THE REYNOLDS STRESS MODEL (RSM)

The RSM is the most classical model which is based on the initial work of launder (1975) [**178**]. The RSM solves the transport equations for the Reynolds stresses, together with an

equation for the dissipation rate, which means five additional transport equations are required in 2D flows and seven additional transport equations must be solved in 3D (general expression in Appendix-C).: The RSM model has a greater potential to represent turbulent flow phenomena more correctly than the other two equations described models but takes more computational time and is slow to converge [**183**].

The RSM is an excellent model to study the effects of streamline curvature, swirl, rotation, and rapid changes in strain rate in a more thorough manner than one-equation and two-equation models and has the more potential to give accurate predictions for complex flows. However, the dependability of RSM predictions is still restricted by the closure assumptions employed to model various terms in the exact transport equations for the Reynolds stresses; the modelling of the pressure-strain and dissipation-rate terms is particularly challenging, and often considered to be responsible for compromising the accuracy of the RSM predictions [**184,185**].

These turbulence models solution converged after a number of iterations would be independent of the initial values for SK-ϵ [**183**]. However, for a fast convergence, it is important to use a reasonable initial guess for K and ϵ. For spray dryer complex flows (flows with multiple inlets with different conditions), 5 to 10% turbulence intensity is enough to represent fully-developed turbulence.

4.3 MODELLING OF THE SPRAY DRYER

In the present research the Spray dryer was divided into the three parts; two-fluid nozzle, atomisation, drying chamber. For the CFD analysis the following steps were used;

- Geometry Creation
- Meshing
- Solver
- Post-processing

4.4 GEOMETRY CREATION

The spray dryer geometry was created in the Gambit pre-processor which is an integrated packaged for CFD analysis. The Gambit allows geometry to be constructed using bottom-up or top down techniques or imports geometry from alternative packages with either include: ACIS solid modelling capabilities or IGES import, cleanup and modification capabilities. The Gambit allows the user to construct and mesh the models by means of its graphical user interface (Figure 4.3).

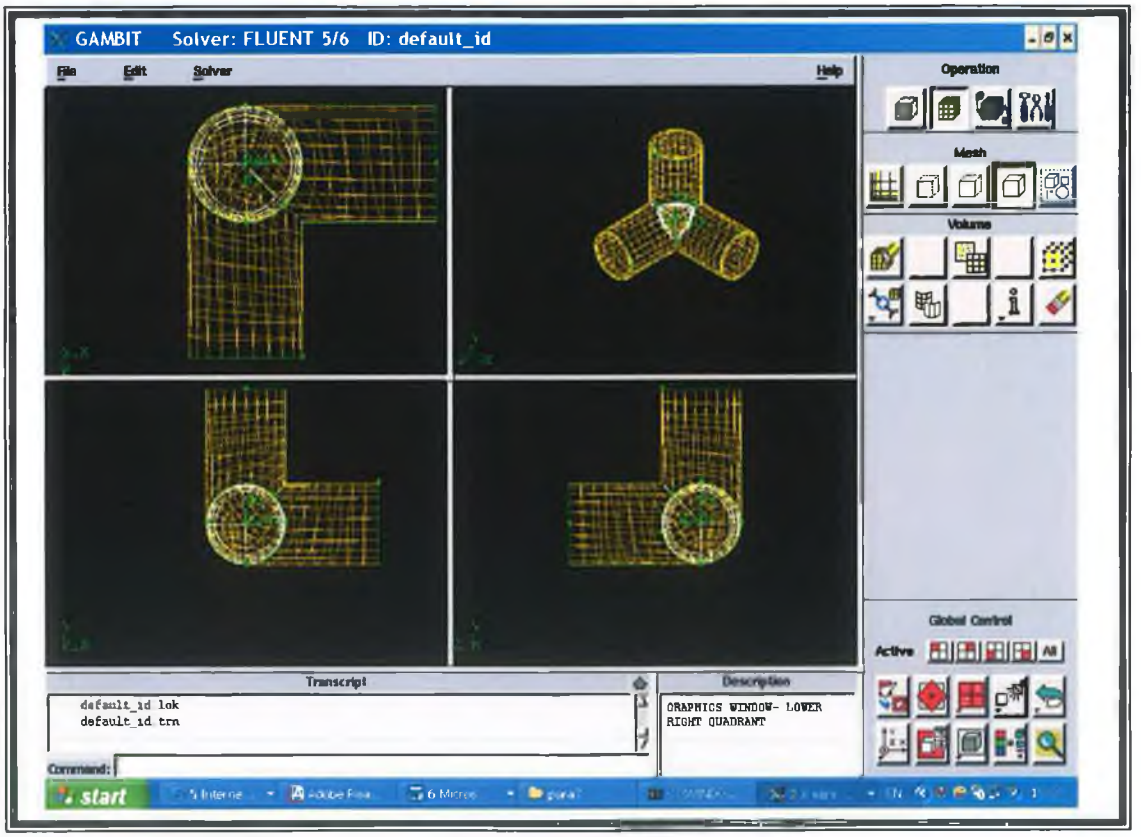

Figure 4.3: Gambits graphical user interface (GUI).

The spray dryer was divided into two parts; A two-fluid nozzle and a drying chamber. Both

geometries were accurately created using vertices, lines and then connected faces. The air nozzle, spray feed pipe nozzle and dryer chamber geometry models were created using by 7, 8 and 4 quadrilateral connected faces respectively due to complexity of their shapes so that forced quadrilateral map meshing scheme would be applied (Figure 4.4 & 4.5).

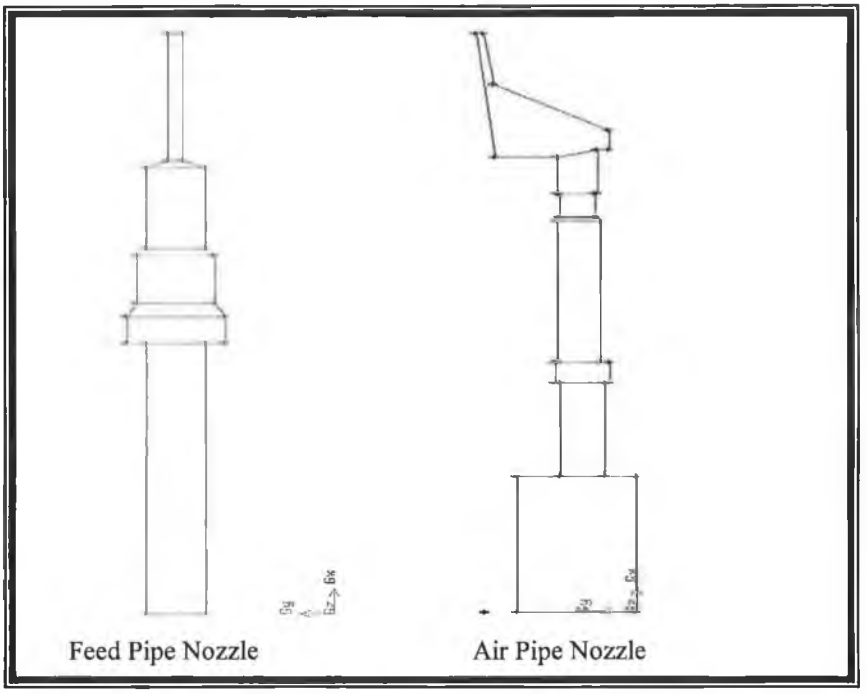

Figure 4.4: Geometry model (Faces) of the feed and air pipe nozzles.

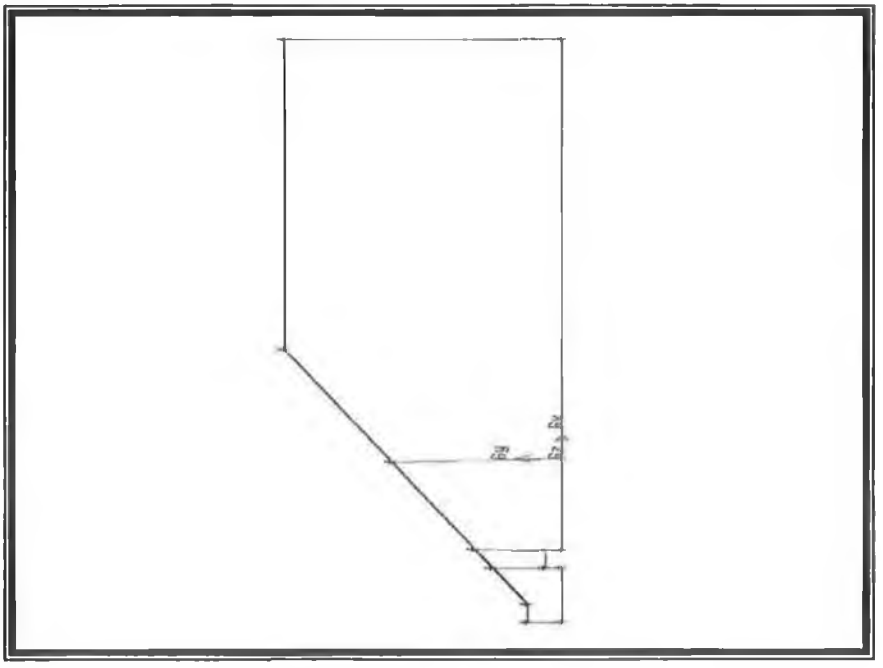

Figure 4.5: Axis-symmetric section of the chamber of the spray dryer.

4.5 MESHING OF SPRAY DRYER

The meshing of model geometry is an important and still challenging task because the quality of the mesh affects both the accuracy of solution, the CPU time and memory requirements [**184**]. The model geometry of the spray dryer was meshed in GAMBIT 2.1. The general meshing tools available in the GAMBIT 2.1 include; edge, face and volume direct meshing. The edge meshing may be done thorough spacing, grading using single or double sided elements, interval size and count element types [**186**]. Face meshing offers a range of element /scheme type combinations [**186**];

- Quadrilateral: map, submap, tri-primitive and pave
- Quadrilateral/Triangle: map, pave and wedge
- Triangle: pave

When the geometry model is complex, it must be decomposed into a simpler form [**187**], to reduce discretization errors. Upon the selection of a volume for meshing Gambit automatically chooses the type of mesh it will use based on the solver selected and the edges types available [**186**]. Options include quadrilateral, triangle and wedge elements used to define the geometry.

Alternatively, a map scheme provides a perfect quadrilateral element distribution through out the model geometry, but where the edges do not from a proper rectangle; the elements become distorted and require smoothing the sides of elements [**186**]. This scheme was used extensively to mesh both the two-fluid nozzle and the drying chamber of spray dryer in the present research.

4.5.1 MESHING OF TWO-FLUID NOZZLE AND SPRAY DRYER

The air and feed pipe were separately meshed using the quadrilateral map scheme. The air and feed pipe were represented by 660 and1070 quadrilateral elements respectively (Figure 4.6 & 4.7). In two-fluid nozzle each connected face of the geometry was meshed separately however the connecting edge of each face had the same number of nodes to maintain the continuum. Each side of the face was first graded and then forced with quadrilateral map element scheme. However, the first face of the air pipe had 7 faces, to represent a logical rectangle, a face must included four end type vertices and all other vertices associated with

the face must be designated as side type vertices to make mappable. Therefore side edges act as vertices so that the gird closely follows the streamlines of the flow, especially for the convective terms (Figure 4.6). The main spray chamber was meshed with 63000 quadrilateral elements (Figure 4.8). The major challenge here was the meshing of the very small spray dryer injector (air/fluid nozzle) 0.75 mm which required 10 elements compared to the large drying chamber (1.6 m in height). To over come this problem the both side grading method was used to give proper number of element to capture the full effect of inlet condition without the limitation of the computer facilities. The successive ratio of both side grading was 1.02.

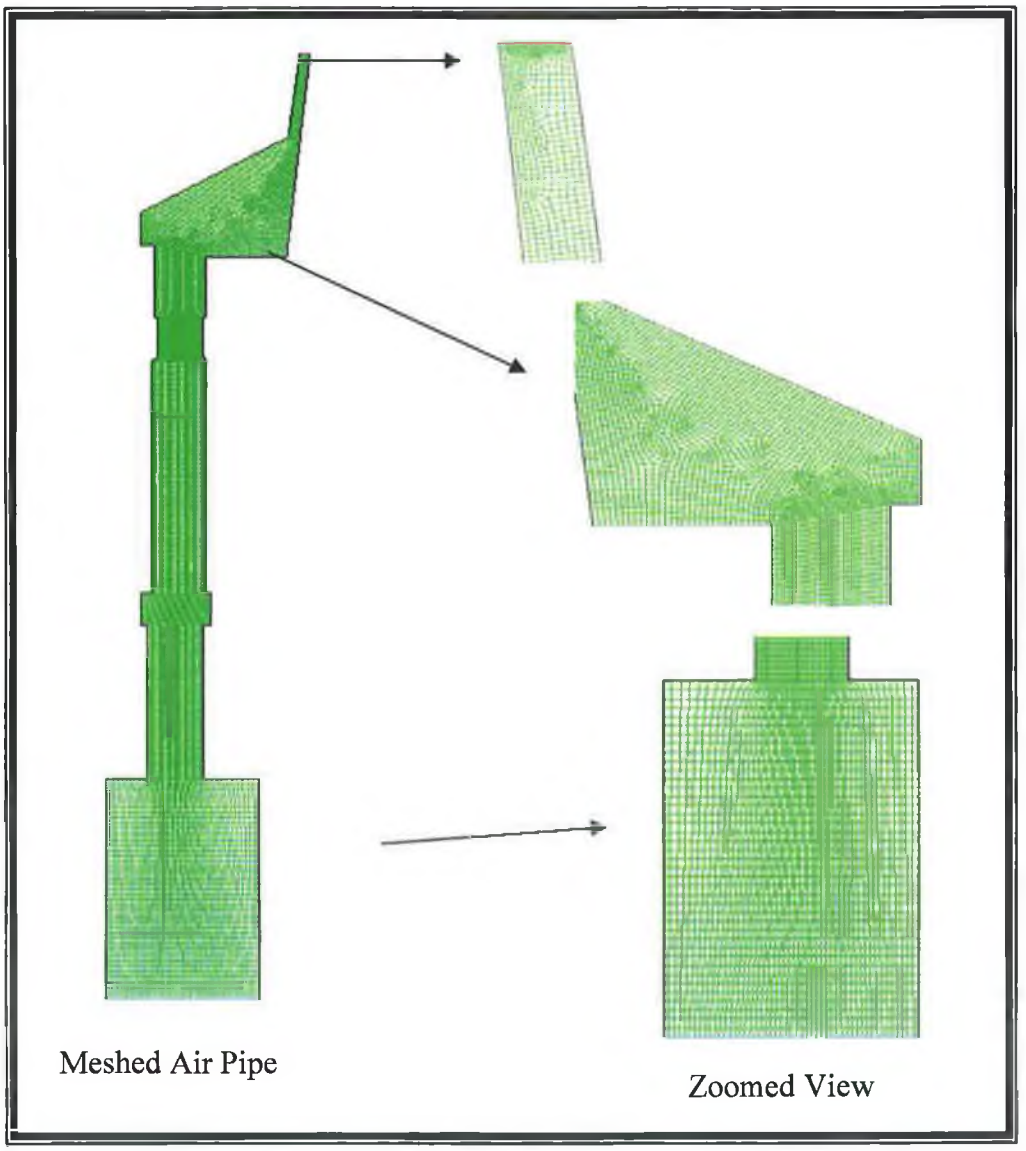

Figure 4.6: Mesh of air pipe of external two-fluid nozzle.

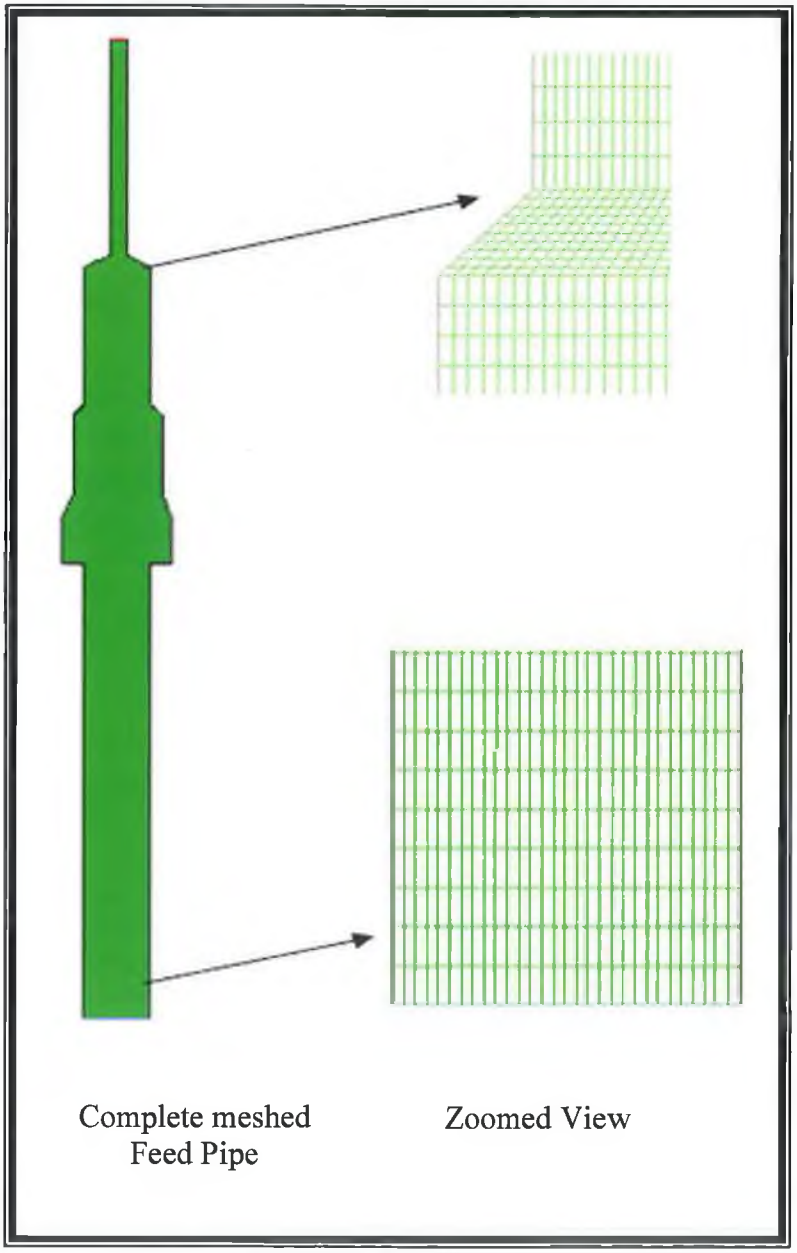

Figure 4.7: Mesh of feed pipe of external two-fluid nozzle of spray dryer.

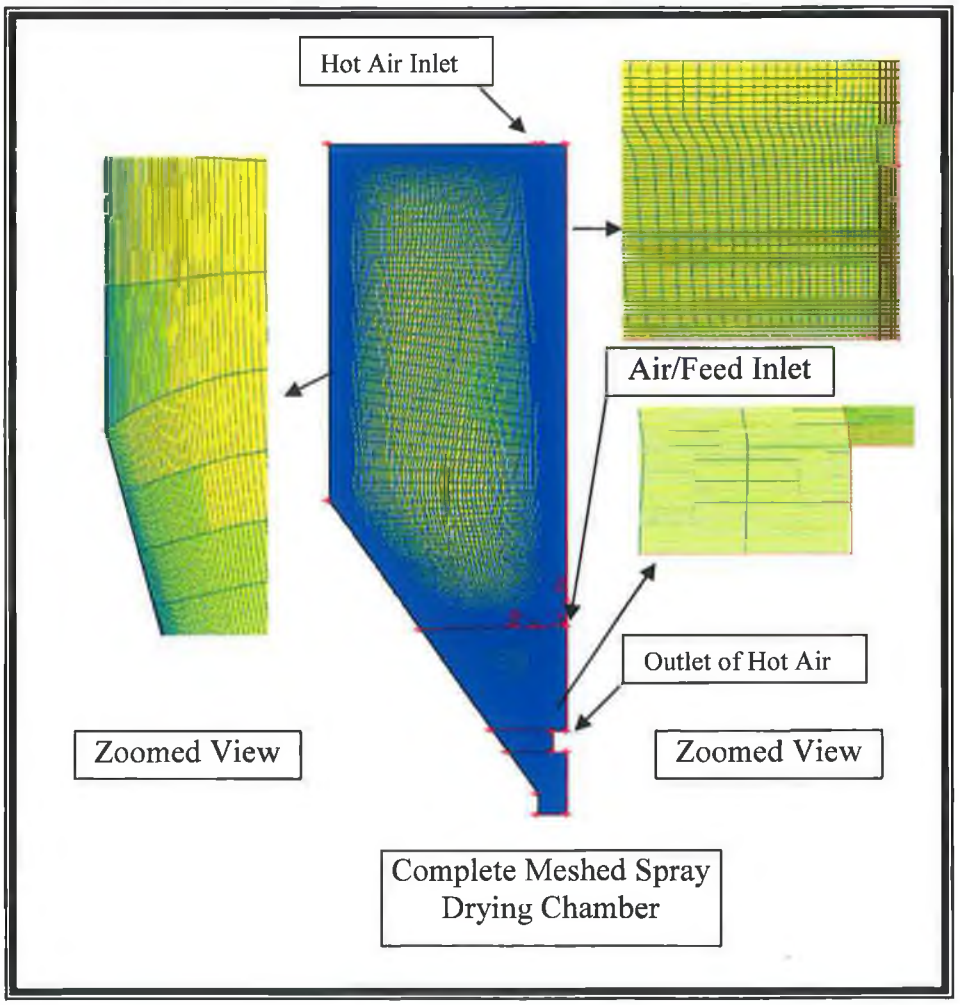

Figure 4.8: Mixed mesh of 2D axis-symmetric spray dry chamber.

4.5.2 MESH CHECKING

The quality of a mesh plays an important role in the accuracy and stability of the CFD results which is based on node point distribution, smoothness and skewness. As a flow is a continuous domain and is defined by discretion. The flow salient features (such as shear layer, separated region, shock waves, and mixing zones) are depended on the density and distribution of nodes in the mesh. In many cases poor resolution in critical region could dramatically alter the flow characteristics [**188**]. Therefore, a small boundary in the spray dryer model such as inlet of the hot air compared with other boundaries, was meshed using 10 nodes and all other inlet and outlet boundaries were more than 20 nodes.

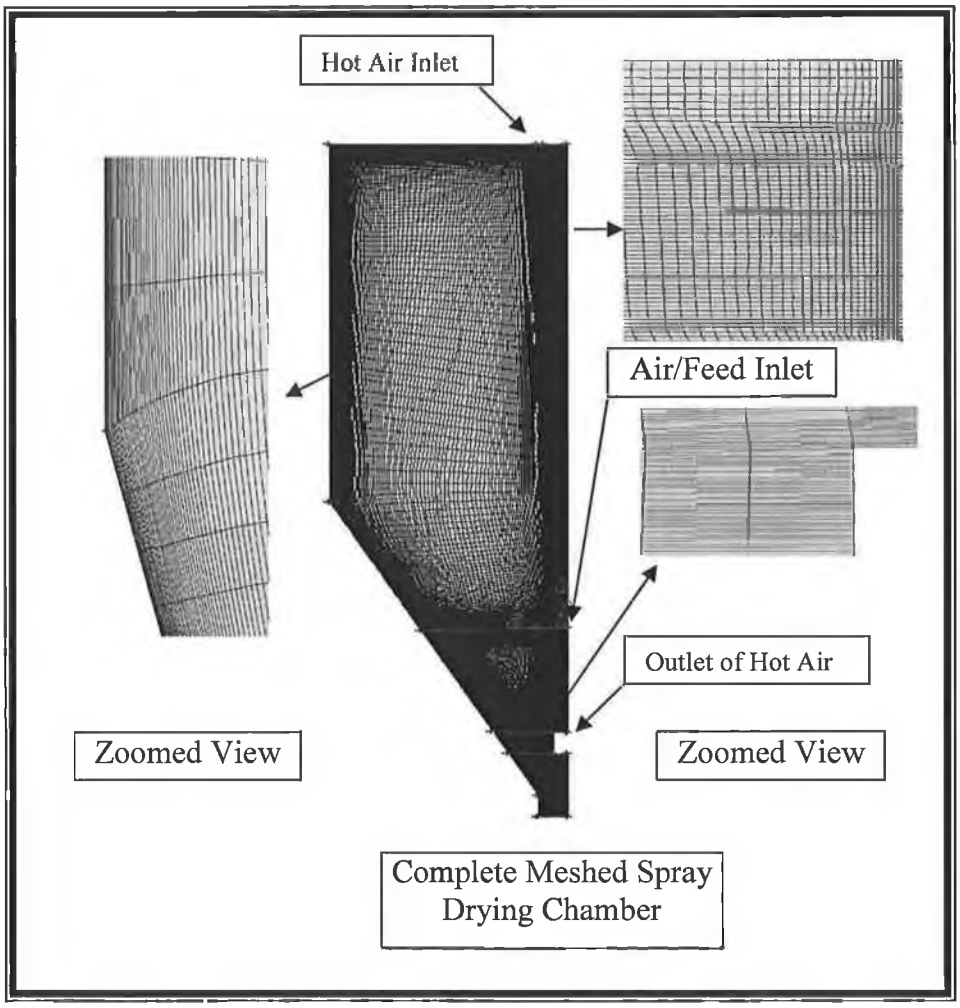

Figure 4.8: Mixed mesh of 2D axis-symmetric spray dry chamber.

4.5.2 MESH CHECKING

The quality of a mesh plays an important role in the accuracy and stability of the CFD results which is based on node point distribution, smoothness and skewness. As a flow is a continuous domain and is defined by discretion. The flow salient features (such as shear layer, separated region, shock waves, and mixing zones) are depended on the density and distribution of nodes in the mesh. In many cases poor resolution in critical region could dramatically alter the flow characteristics [**188**]. Therefore, a small boundary in the spray dryer model such as inlet of the hot air compared with other boundaries, was meshed using 10 nodes and all other inlet and outlet boundaries were more than 20 nodes.

The mesh was checked in the GABMBIT 2.1 program which was based on Equi-angle skew techniques and can be described by [**188**].

$$\max\left[\frac{\theta_{\max}-\theta_e}{180-\theta_e}, \frac{\theta_e-\theta_{\min}}{\theta_e}\right] \text{----------Equation 4.1}$$

where, $\theta_{\max}$ $\theta_{\min}$, θ_e are the largest, smallest and equiangular angle face (60 for triangles and 90 for square), the quality of mesh is measured by the skewness range. The poor quality of grid will cause in accurate solutions and / or slow convergence [**187**]. The important factors in the checking of mesh are to [**189**]:

- Minimise equi-angle skew; skewness should not exceed 0.75
- Minimise local variation in cell size; the adjacent sides should not have a size ratio greater than 1.6
- If these parameters are out of range, it is recommended that the mesh is deleted, and re-meshed.

The Gambit 2.1 program allows the user to carry out this check in its examine mesh display. Several techniques for the refinement and improvement of meshes in two dimensions have been considered in the last 20 years [**126**]. Initially meshing using various strategies failed on one or both of the above points, which meant that the mesh model was gird dependent. Later in models edge, grading on one or both sides and Winslow smoothing scheme were applied to get the desired quality of mesh [**187**]. It is very important to check the quality of the resulting mesh, because it properties such as skewness can greatly affect the accuracy and robustness of the CFD solution.

4.5.3 ANALYSIS OF SKEWNESS

The feed pipe of the two-external fluid nozzle was meshed by 660 quadrilateral elements. All were checked for skewness. The air nozzle pipe was mesh in the same manner but the geometry of nozzle pipe was more complex to ensure all elements were under the 0.5 skewness (Figure 4.9). More than 99% of elements were under 0.6 skewness and only 1% of the elements were in the range of 0.6 to 0.75 due to the sharp edge of the nozzle pipe (Figure 4.10). The spray dryer was meshed axis-symmetrically due to it symmetric shape and to reduce calculation times. The main spray chamber was meshed with 63000 quadrilateral elements. However, no cells were found with a skewnness more than 0.5 (Figure 4.11).

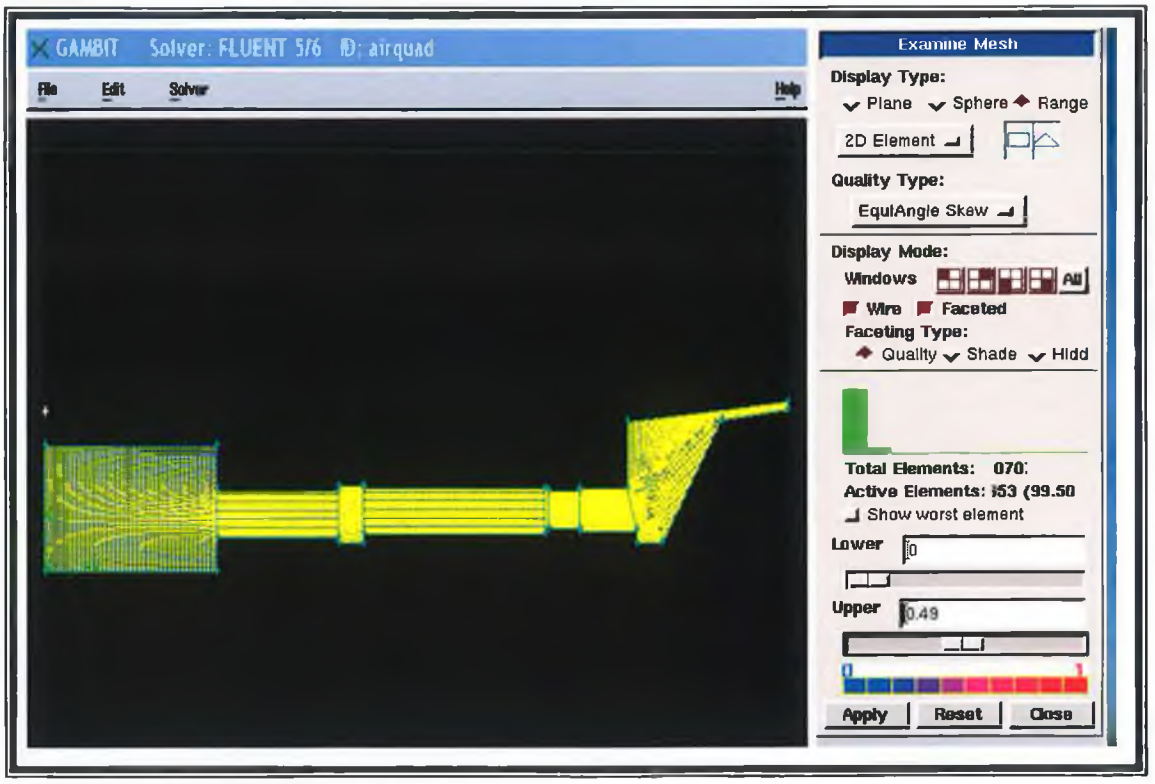

Figure 4.9: Equi-angle skew for the air-pipe of the external two-fluid nozzle.

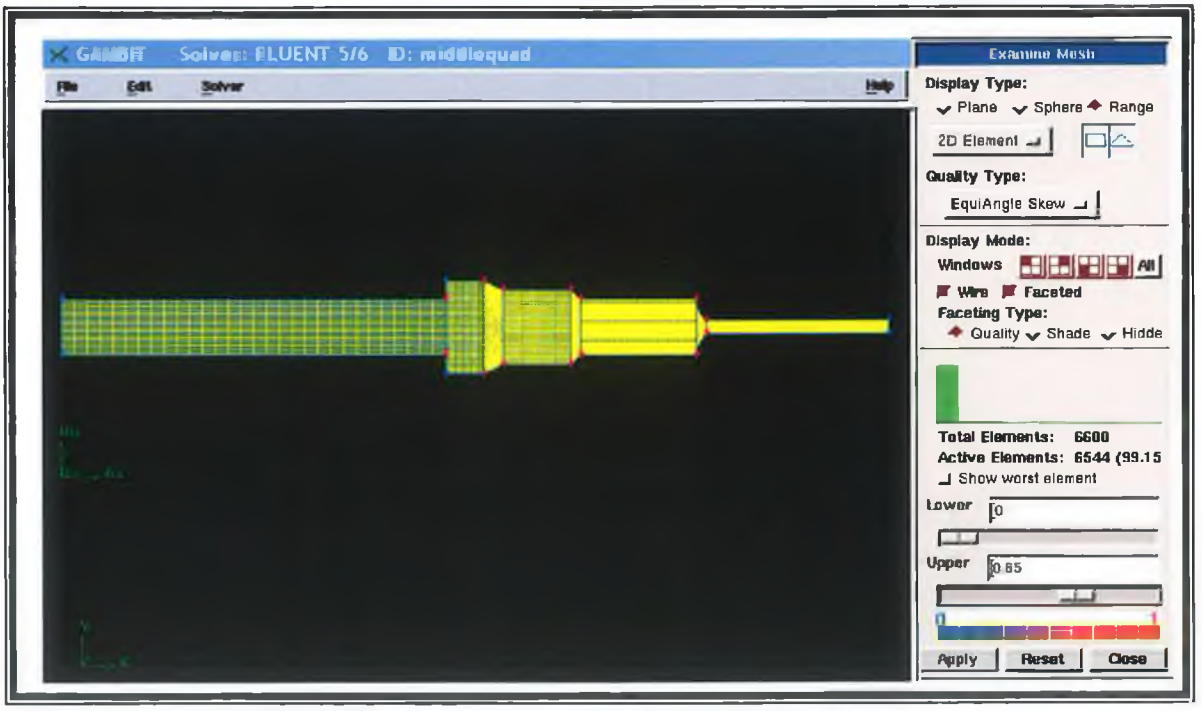

Figure 4.10: Equi-angle skew for the feed-pipe of the external two-fluid nozzle.

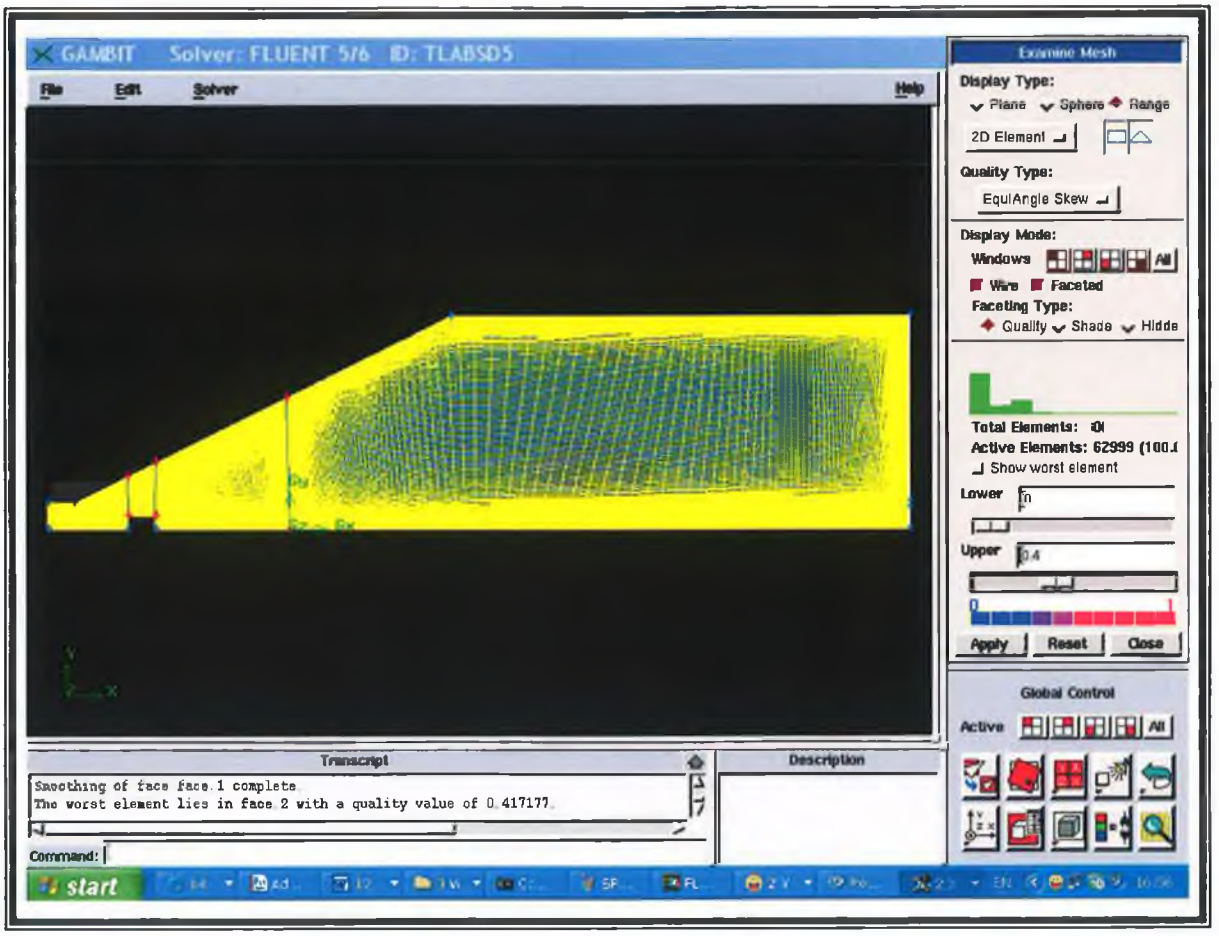

Figure 4.11: Equi-angle skew for the spray dryer.

4.6 FLUENT SOLVER

The FLUENT 6.1 solver provides comprehensive modelling capabilities for a wide range of incompressible and compressible, laminar and turbulent fluid flow problems. In FLUENT, a broad range of mathematical models for transport phenomena (like heat transfer and chemical reactions) is combined with the ability to model complex geometries. Examples of FLUENT applications include; laminar non-Newtonian flows in process equipment; conjugate heat transfer in turbomachinery and coal combustion in utility boilers; external aerodynamics; flow through compressors, pumps, and fans; and multiphase flows in bubble columns and spray dryer atomizer models and fluidized beds.

An important useful group of models in the FLUENT is the set of free surface and multiphase flow models. These can be used for the analysis of gas-liquid; gas-solid, liquid-solid, and gas-liquid-solid flows. For these types of problems, FLUENT uses the volume-of-fluid elements (VOF), mixture, and Eulerian models, as well as the discrete phase model (DPM). The DPM performs Lagrangian trajectory calculations for dispersed phases (particles, droplets, or bubbles), including coupling with the continuous phase. Examples of multiphase flows include channel flows, sprays, sedimentation, separation, and cavitations. In the present research, the spray dryer modelling was divided into three parts; two-fluid nozzle simulation, temperature simulation of the main chamber and atomisation of HA slurry (Figure 4.12). To setup the simulation problem in CFD, the following few steps are needed to initiate the modelling like the selection of numerical schemes to solve the governing equations, linearization of governing equations from the partial differentiation equations, activate the physical laws to study the required properties of fluid or droplets such as energy equation and read out the result through post processing like temperature, velocity and droplets of HA slurry.

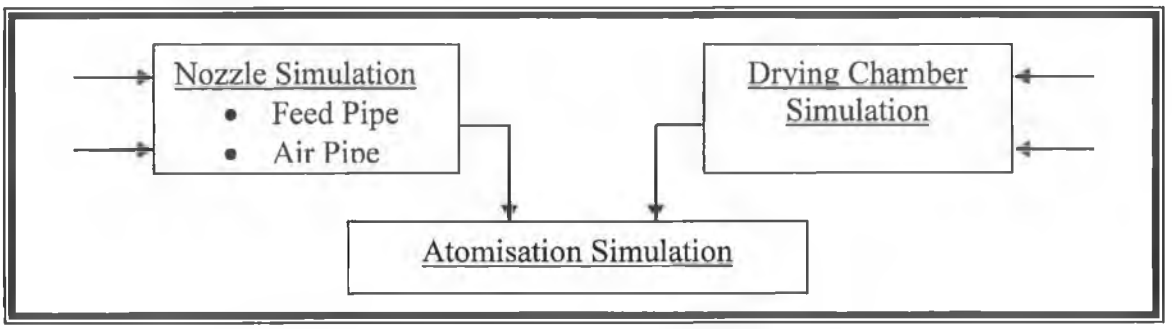

Figure 4.12: Systematic plan for the spray dryer modelling.

4.6.1 NOZZLE MODELLING

Figure 4.13 shows the sketch of nozzle (air/feed pipe) modelling steps in FLUENT software. In the post processing, the results, outlet velocities was used as an input in the atomisation model of drying chamber.

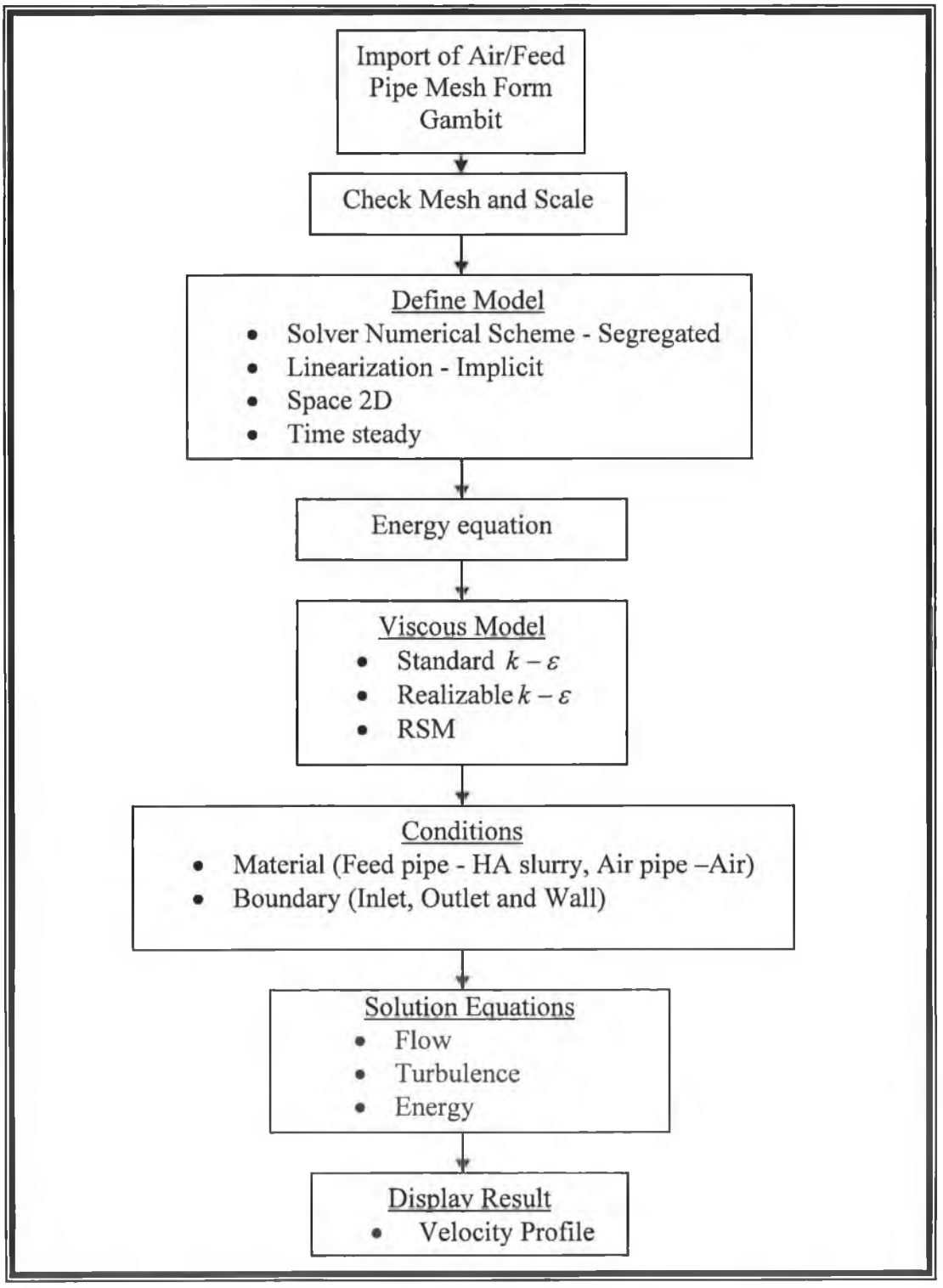

Figure 4.13: The flow path for nozzle simulation.

4.6.2 DRYING CHAMBER MODELLING

The drying chamber was modelled for the temperature and velocity profile to initiate the atomisation in the spray dryer. Figure shows 4.14 the brief steps of it.

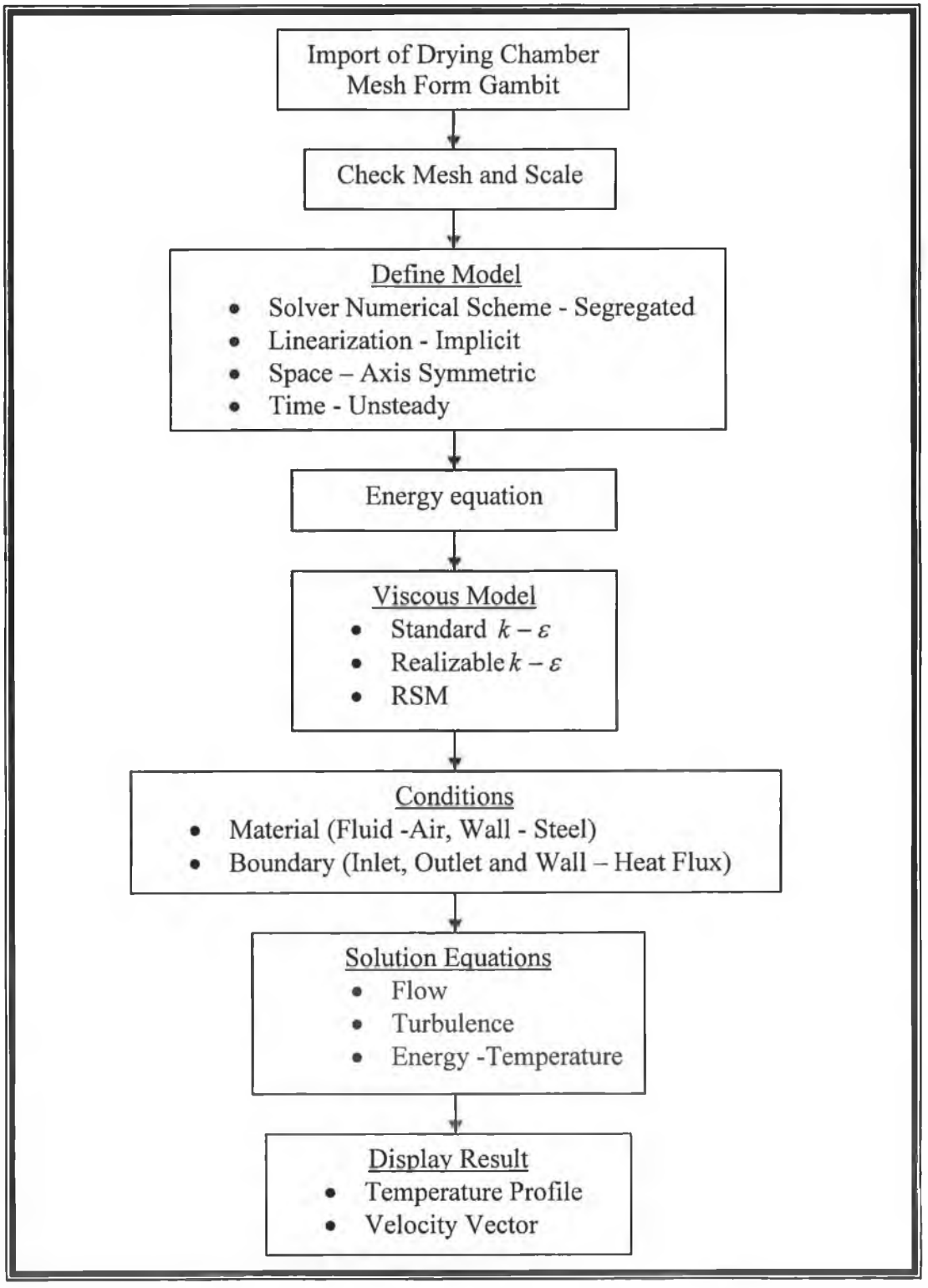

Figure 4.14: The flow path for drying chamber of the spray dryer simulation for temperature and velocity profile.

4.6.3 ATOMISATION MODELLING

In the atomisation modelling of the spray dryer, the nozzle exit velocity and drying chamber temperature and velocity profiles were taken as an input and steps is shown in the Figure 4.15. For atomisation modelling, temperature profile was solved in Eulerian approach then discrete phase of air blast model was activated in Lagrangian. Further steps of this model are discusses in subsequent sections 4.6.4 and 4.6.5, and mathematical equations in Appendix-C.

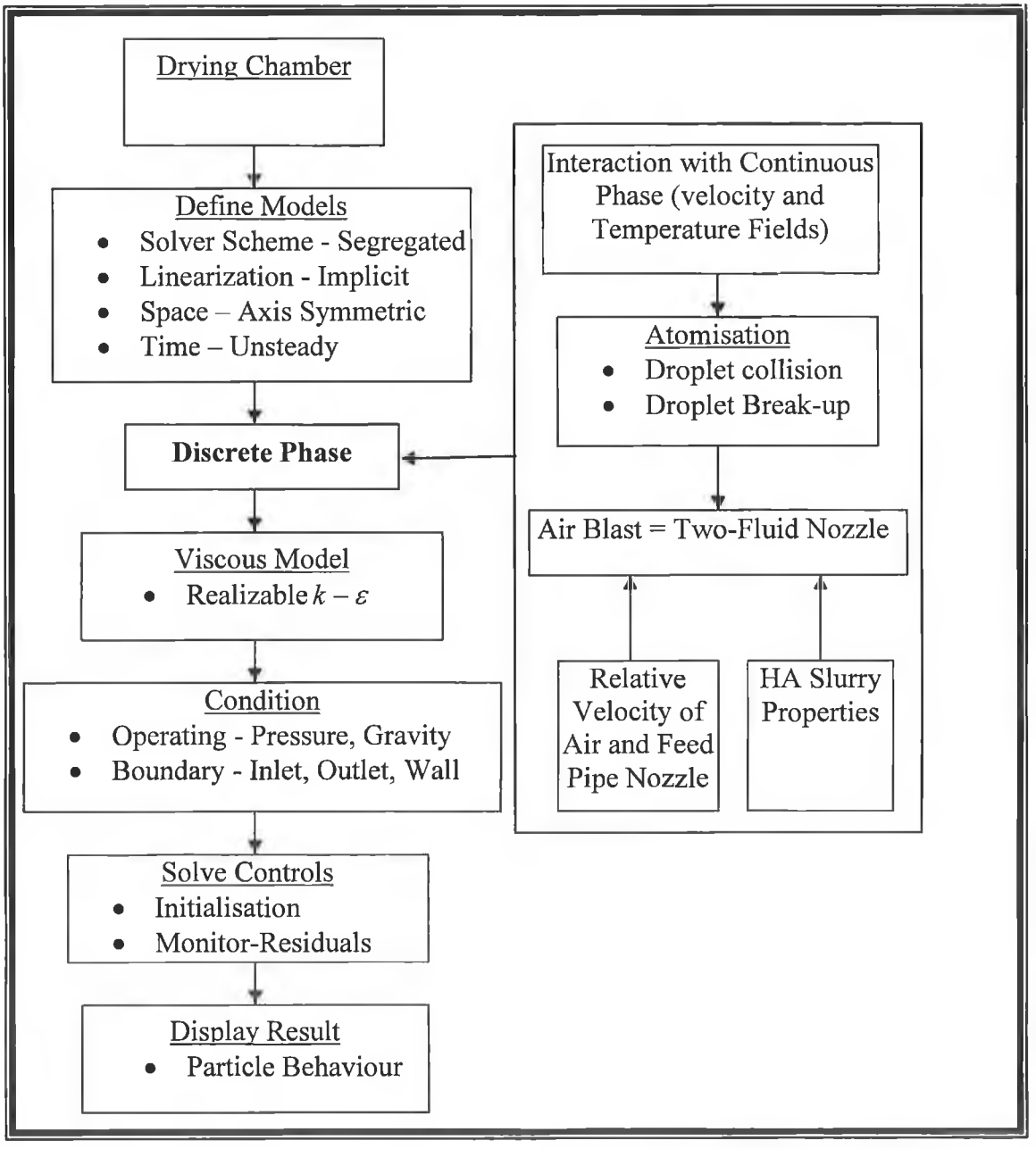

Figure 4.15: Systematic step to solve the spray dryer modelling with discrete phase.

4.6.4 SOLVER NUMERICAL SCHEMES

Generally, two numerical methods are used to solve the fluid flow problems [**190**]:

- coupled solver
- segregated solver

The coupled solver solves the governing equations of continuity, momentum, and energy and species transport simultaneously (coupled together). These governing equations for additional scalars are solved sequentially, because the governing equations are non-linear (and coupled), several iterations of the solution loop must be performed before a converged solution is obtained [**190**]. Where as, The segregated solver algorithm solves governing equations sequentially (segregated from one another) to obtain the solution and each iteration follows the path shown in Figure 4.13 and loops until the convergence criteria are met, such as, residual of continuity, momentum energy and other scalar quantities. In the present research segregated solver is used which is fast and takes less memory [**190**].

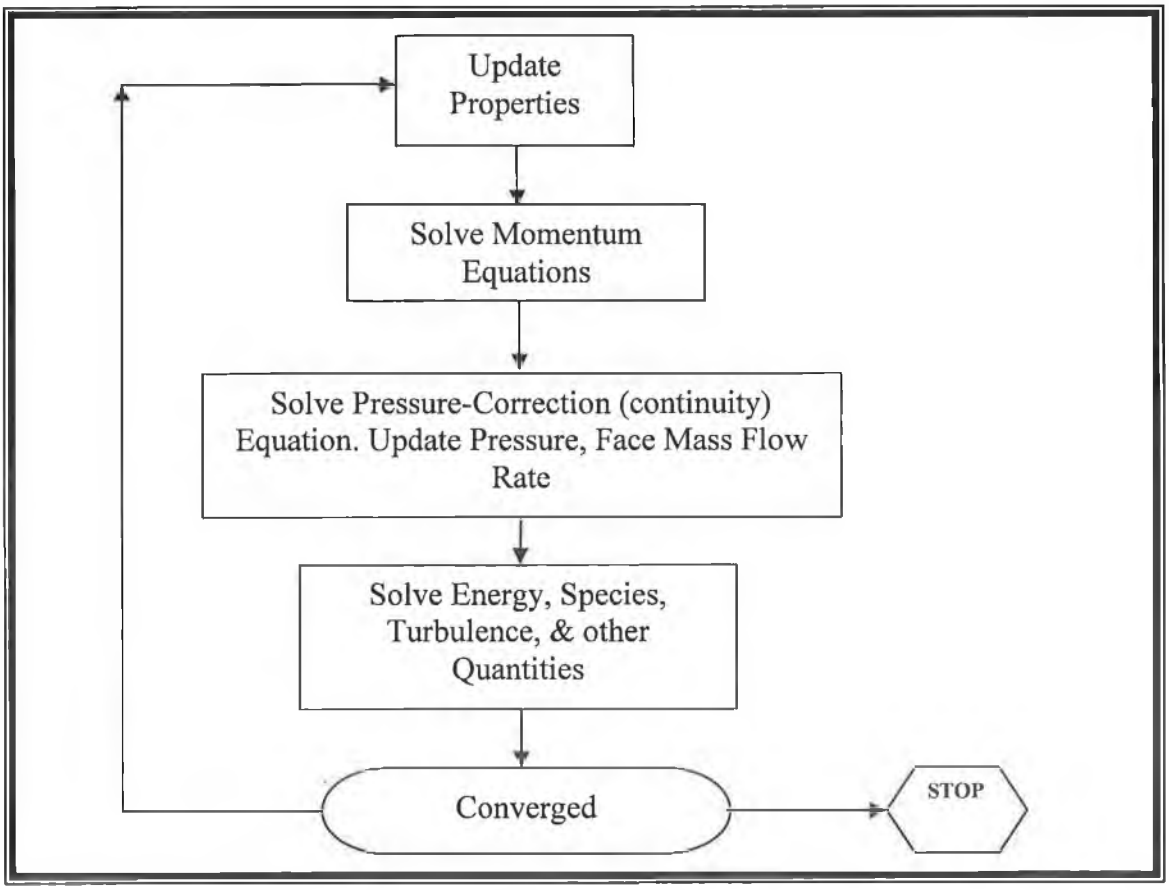

Figure 4.16: Overview of the segregated solution method [177].

4.6.5 LINEARIZAITON

In solver numerical schemes methods, the discrete non-linear governing equations are linearized to convert a system of equations for the dependent variables in every computational cell of mesh geometry. The resultant linear system can then be solved to yield an updated flow-field solution [**191**]. The approach in which the governing equations are linearized is either "implicit" or "explicit" with respect to the dependent variable (or set of variables) of interest.

- Implicit: For a given variable, the unknown value in each cell is computed using a relation that includes both existing and unknown values from its neighbouring cells. As a result each unknown will appear in more than one equation in the system, and these equations can be solved simultaneously to provide the unknown quantities.

- Explicit: For a given variable, the unknown value in each cell is computed using a relation that includes only existing values. Therefore each unknown will appear in only one equation in the system and the equations for the unknown value in each cell can be solved one at a time to provide the unknown quantities.

In the present research modelling, the implicit linearization option is used with the segregated solver. In the implicit scheme, a single variable field (for an example velocity) is considering all cells at the same time and then solve for the next variable field by again considering all cells at the same time and so on that gives initially fast convergence and reduce the chance of divergent of residual errors [**192**].

4.6.6 DISCRETE PHASE MODEL

Previously, spray drying modelling has been based on the discrete phase modelling, where Euler/Lagrange approaches are used, where the gas field is calculated first (Euler). This is done by calculating an approximate solution for the Navier-Stokes and continuity equations on a grid of contour volumes, subsequently the particles are tracked individually (Lagrange) and then computes the trajectories of these discrete phase entities, as well as heat and mass transfer to/from them [**193-203**]. The steps in the discrete model (Figure 4.15) in the present research are as follows;

- Prediction of the effects of turbulence on the dispersion of particles due to turbulent eddies present in the continuous phase.
- Heating/cooling of the discrete phase.
- Vaporization and boiling of liquid droplets.
- Optional coupling of the continuous phase flow field prediction to the discrete phase calculations.
- Droplet break-up and coalescence

After the solving the continuous phase fields (temperature and velocity), the discrete phase activate. As the trajectory of a particle is computed, the model in the FLUENT keeps track of the heat, mass, and momentum gained or lost by the particle stream that follows that trajectory and these quantities can be incorporated in the subsequent continuous phase calculations. The continuous phase impacts the discrete phase and discrete phase trajectories effect on the continuum. This two-way coupling in the model is accomplished by alternately solving the discrete and continuous phase equations until the solutions in both phases have stopped changing. This interphase exchange of heat, mass, and momentum from the particle to the continuous phase is showed qualitatively in Figure 4.17. When the droplets come in contact with hot air in the main drying chamber, the heat and mass transfer in the spray dryer, assumed the droplet has exposed the temperature to heating/evaporation and boiling (Figure 4.18). It depends upon the droplet size and surrounding hot air temperature conditions. The model assumed that the second phase is sufficiently dilute; by volume fraction the discreet phase less than 10-12% because to maintain particle-particle interactions and the negligible effects of the particle volume fraction on the gas phase [**204**]. This assumption is well suited in spray dryer conditions and therefore is often used modelling. The major disadvantage is that, it is dependent on predicting the chaotic motions of individual droplets to provide an overall picture of the spray [**205**]. The stochastic models employed in producing this chaotic motion requires a large number of drop parcels to produce a smooth representation of the spray and are therefore computationally expensive, however, generally accepted to be more efficient in this regards than the current alternatives [**205**]. Recently, other alternative approaches were suggested by Beck and Watkins [**206**], where the liquid and the gas were both used in Eulerian formulation (by considering the liquid and gas as separate phases, which reduced the number of equation to be solved) [**206**].

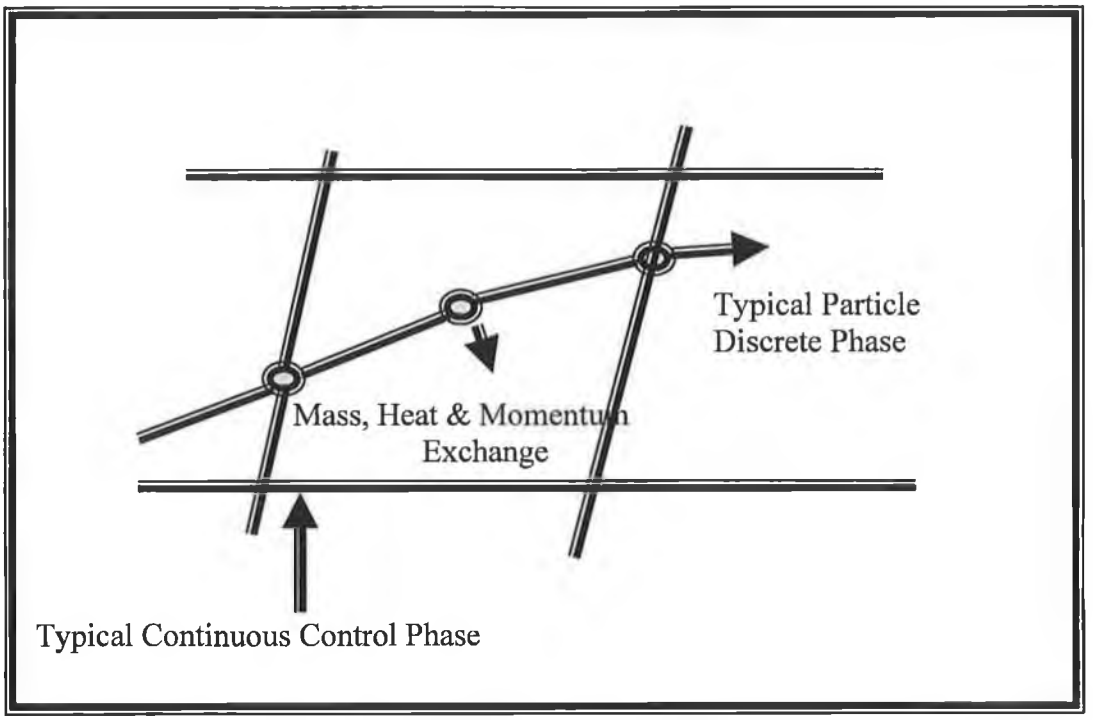

Figure 4.17: Heat, mass, and momentum transfer between the discrete and continuous phases.

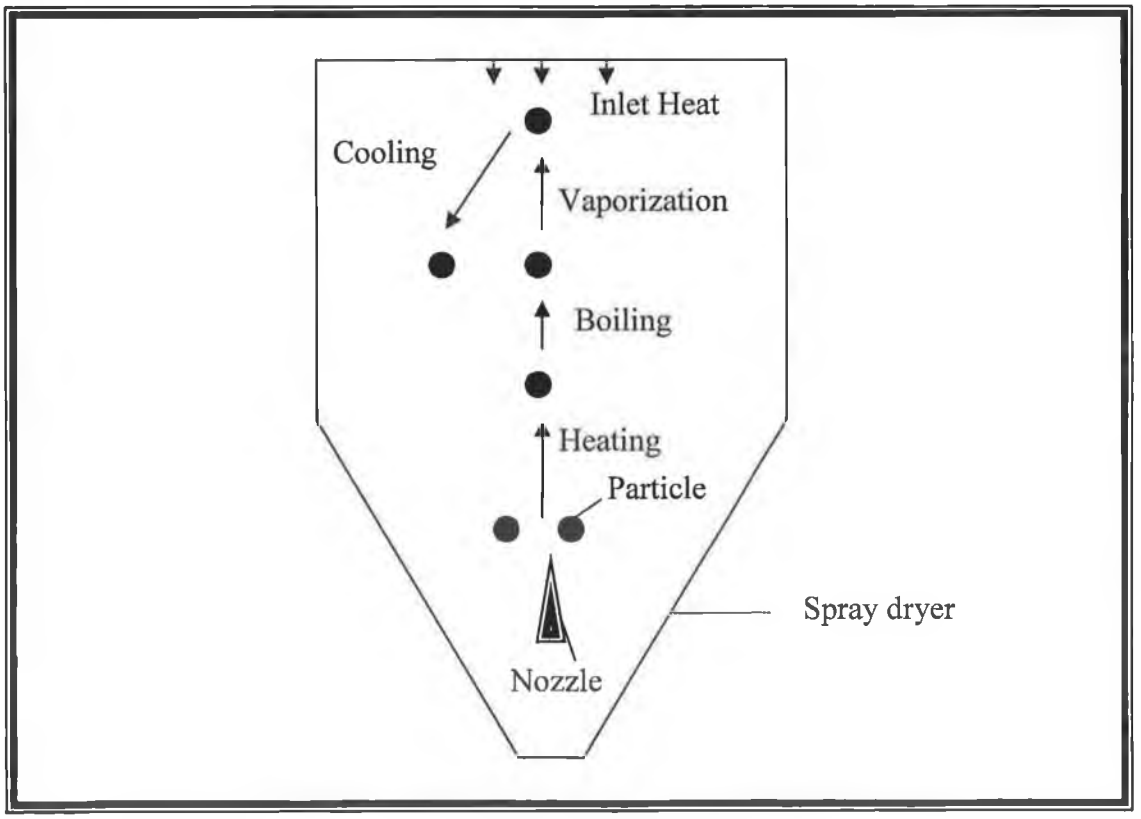

Figure 4.18: Systematic sketch of heat and mass transfer of particle in the spray dryer.

4.6.7 SPRAY MODEL

FLUENT has a number of spray models like plan-orifice, pressure-swirl, flat-fan, air-blast/air assisted and effervescent atomizers [**177**]. The air-blast model was selected for the presented study as it replicates of the external two-fluid nozzle atomizer (mathematical expression in Appendix-C). The FLUENT software represents the external two fluid nozzle atomizer where as an air stream used to accelerate the break-up of a liquid sheet from an atomizer. This air may also help to disperse the droplets, preventing collisions between them. The inputs into this model are sheet thickness, maximum relative velocity, mass flow rate, and spray angle [**207**]. The analogy of the external two-fluid nozzle was defined by a Linearized Instability Sheet Atomisation (LISA) model produced by Schmidt et al. [**207**]. The LISA model was divided into two stages [**208-211**]:

- Film formation
- Sheet break-up and atomisation

The atomizer model currently used in FLUENT uses a slightly improved form of that model proposed by Schmidt et al. [**207**], in which, the physical mechanism of sheet disintegration, for long waves, ligaments are assumed to form from the sheet break-up process once the unstable waves reached a critical amplitude [**211**]. Break-up from ligaments to droplets is assumed to behave according to Weber's [**212**] analysis for capillary instability. This break-up/spray atomisation process has option modelled by standard deterministic break-up models based on Taylor analogy break-up (TAB) or wave models [**213,214**]. This procedure determines the most probable droplet size [**212**].

The mesh files were imported from GAMBIT 2.1 to FULENT 6.1 solver. Before the model was solved, the following setting applied; the mesh was checked and physical model applied. The mesh was checked to ensure the quality of domain cells. In which any cell that may cause problem of convergence were adjusted. Once the checking of mesh was completed, the scale and units were applied following with physical models.

In this research, segregate, implicit second order schemes and discrete phase model were applied; these FLUENT solver setting were employed that were based on the best the

current practice in the spray dryer modelling. The turbulence models applied included S*K*-ϵ and realizable S*K*-ϵ and Reynolds Stress Models. These viscous models were selected, on the fact that they are robust and the most widely validated models currently available in the literature. The constants employed in these models were the default models used within the FLUENT 6.1 package.

4.7 POST PROCESSING

After CFD solution, results views in the post processing panel and also, save hardcopy files of graphics displays for further analysis. The software has option to generate graphics displays showing grids, contours, profiles, vectors, and pathlines. The discrete model, results display the particle trajectories and particle diameter. In addition to the many graphics tools FLUENT also provides tools that allow to generate XY plots and histograms of solution, file, and residual data., modify the colours, titles, legend, and axis and curve attributes to customize plots.

In the present research, the nozzle results were displayed as velocity vectors and profiles, the drying chamber simulations results were analysis as temperature profile and velocity vectors, and spray atomisation were examined as particles trajectory and particle diameter.

5

Results and Discussion

5.1 INTRODUCTION

The research results will be divided into three main parts; analysis of the spray dryer process for HA powder production, simulation and comparison of the spray dryer. The simulation results are presented using the coupled scheme where each spray dryer part was separately simulated and analysed and later combined together with the others simulations to predict the operational behaviour of the Niro spray dryer. The initial velocity of the air/feed was known however the simulation then produced a velocity at the exit of the nozzle, this value was used as the atomization velocity in the chamber to predict the results found in the chamber. The simulated chamber results (using air flow and feed simulation values) were then compared using experimental data. During the modelling, care was taken with all major influencing factors; effect of computing technology, model building and mesh generation, mathematical methods and numerical analysis, relevant physical models, comparison, post-processing and data extraction. Before simulation and comparison could commence, equipment calibration and model checks had to be performed, only then could the model results be compared to experimental data.

5.2 CALIBRATION AND MODEL CHECKS

5.2.1 VISCOSITY RESULTS

Three viscosity levels (25, 50 and 75 ± 5% mPa.s) of HA slurry viscosities were produced for spray drying and as inputs in the simulations of the feed nozzle and atomisation. This range was controlled by the addition/taking out of deionised water from the HA slurry

when the participation reaction was completed. This viscosity range was selected after measuring the HA slurry at an industrial manufacturing plant where produce HA powder is produce for thermal spray applications (used in the production of human hip implants) and it was found to be region of 48 ± 5 mPa.s. It has been reported by many researchers [**122,123,215, 216**] that the feed HA slurry has a great impact on the atomisation in spray drying process such as particle size distribution, atomization and morphology of dried droplet. Luo and Nieh [**123**] reported that at higher viscosities (45.9 mPa.s) of HA slurry, the spray dryer produces solid sphere types and higher mean diameter of droplets. During the spray drying, it is mandatory that the HA slurry is continuous stirred as its viscosity is effected by particles sedimentation and separating out from the water. At the higher viscosities of HA slurry such as 75 mPa.s, spray dryer nozzle sometimes blocked due to fast sedimentation and higher solid content. However, if other binders used, this higher solid content of HA slurry can be spray dried successfully at 70 to 80 % solid content levels according to Athena et al. [**215**].

5.2.2 AIR DRYING TEMPERATURE VERSUS AIR FLOW

Calibration of the air drying temperature versus airflow positions I, II , and III (see page Chapter 3), produced the following results described in Table 5.1 the temperature increased from 398K to 461K from position I to III respectively.

Table 5.1: Air drying temperature and air flow rate at the different positions.

	Drying Air Flow Rate (m/s) at Temperature (K)		
	398K	**421K**	**461K**
Position I	12.738	12.712	12.704
Position II	14.642	14.628	14.612
Position III	16.643	16.631	16.601

5.3 EXPERIMENTAL ANALYSIS

The present work deals with the optimisation of the HA spray drying process by using an experimental design methodology. Based on the literature data, three major spray drying factors; the temperature of the inlet hot air in the spray dryer, the flow rate of the inlet hot air in the spray dryer and the HA slurry viscosity were selected for the analysis. The average viscosity of HA slurry was found to be with the range of 25 to 75 mPa.s.

In these experiments, the feed flowrate used was 7.6×10^{-7} m^3/s because the spray dryer initial test run gave the best result at this setting in terms of minimum deposition onto the top inside of the spray dryer and in term of producing free flowing powder. The range of flowrate of slurry to rpm of peristaltic pump used is shown in the Appendix-B. The kinetic energy for atomisation of the feed (feed flow rate 9.655×10^{-4} Kg/s and atomisation pressure 75% on the calibrated scale) was kept constant.

To take into account the influence of the interactions between the different factors, the use of an experimental design methodology was more suitable than an OVAT (one variable at a time) method. This approach has already proved successfully in bioprocesses, allowing a rapid and robust optimisation of several processes [**218**].

A factorial experimental design with interaction effects was built using MODDE 7.0® software. Three factors with three levels were investigated (Table 5.2). As experiments are tedious and costly, a factorial design was chosen on orthogonal blocking using the Box-Behnken scheme. The design contains thirteen experiments (Table 5.2). The performance and optimisation of spray dryer for the production of thermal spray powder (HA powder) was evaluated by analysing following responses: (1) Chamber powder size (Dch) (μm), (2) Cyclone powder size (Cyl) (μm) (3), Deposition of powder onto the wall of the spray dryer (Wd) (graded in terms of numbers 1-10), the deposition onto the wall grade implies that 1 is (no deposition) and 10 is (complete deposition)) and (4) Overall thermal efficiency (Th) (%).

Table 5.2: Experimental value for different response for various conditions of variable.

Exp.	Variables			Responses			
	T* (K)	Fl* (m/s)	Vis* (mPa.s)	Dch (µm)	Cyl (µm)	Wd (No)	Th (%)
1	389	14.60	25	9.40	6.80	8	45.00
2	461	14.60	25	18.80	11.50	3	60.06
3	389	14.60	75	39.80	8.50	6	54.24
4	461	14.60	75	41.60	25.60	6	64.00
5	389	12.70	50	26.90	9.92	7	56.80
6	461	12.70	50	33.05	19.70	4	58.78
7	389	16.60	50	29.40	15.40	6	48.97
8	461	16.60	50	36.85	20.25	7	52.60
9	421	12.70	25	19.03	9.030	4	65.32
10	421	12.70	75	39.70	13.92	4	60.16
11	421	16.6	25	16.43	8.43	6	56.40
12	421	16.60	75	40.45	24.45	6	53.45
13	421	14.60	50	30.42	18.72	5	50.21

* T= Temperature, Fl= Flow rate of hot inlet air, Vis= Viscosity of HA slurry

A second order polynomial model was used to describe relationships between responses and experimental factors:

$$Y = \beta_0 + \sum_{i=1}^{3} \beta_i X_i + \sum_{i=1}^{2} \sum_{j=i+1}^{3} \beta_{ij} X_i X_j$$ ----------Equation 5.1

Where Y is the response, β_0 is the constant coefficient, X_i and X_j are the variables, β_i are the linear coefficients and β_{ij} are interaction coefficients. This polynomial model was fitted to the four responses.

5.3.1 DATA ANALYSIS AND OPTIMISATION

The MODDE 7.0® software was applied and the correlations between factors; Temperature of the inlet hot air in the spray dryer (T), Flow rate of the inlet hot air in the spray dryer (Fl.), Viscosity of feed/ HA slurry (Vis), and the responses were determined using a Multiple Linear Regression (MLR) method, and the statistical analysis of main and interaction effects were quantified using an ANOVA test.

5.3.2 STATISTICAL ANALYSIS

Table 5.3 and Figure 5.1 (gives the analysis of the regression coefficients of polynomial models describing the relationships between Chamber powder size (Dch), Cyclone powder size (Cyl), Deposition of powder on the wall of spray dryer (Wd) (in terms of numbers (1-10) and Overall thermal efficiency (Th) and the studied factors. It indicates that the two responses (V_{ir}, V_{id}) can be described well by polynomial models with good coefficients of determination (R^2). ANOVA analysis table D.1 is given in Appendix-D.

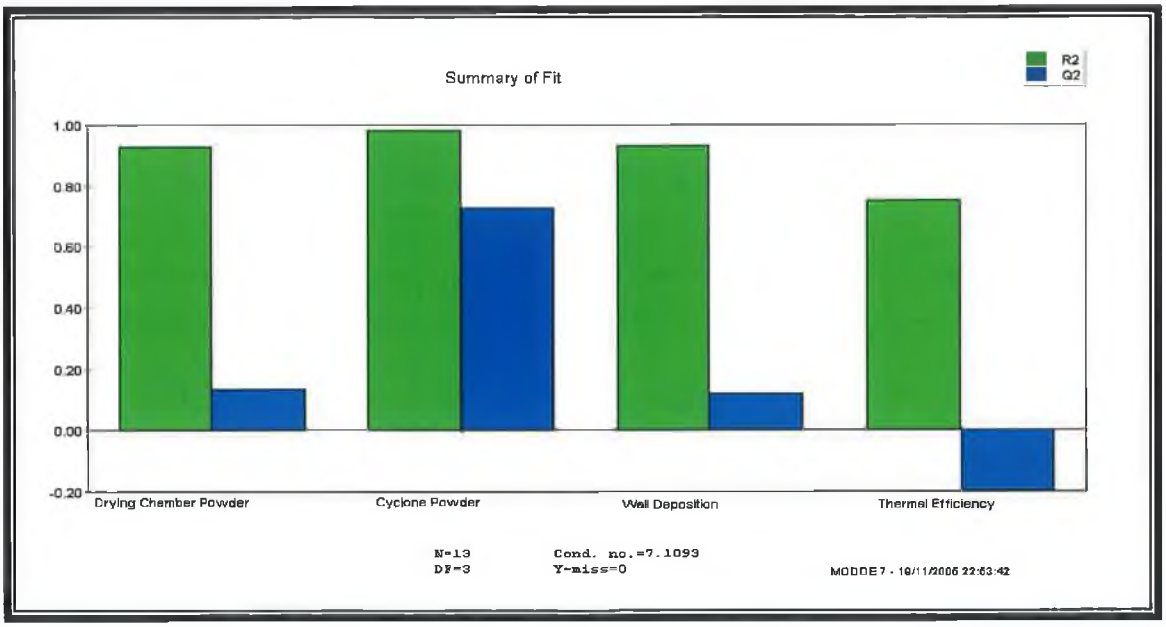

Figure 5.1: Summary of fit for the experimental matrix for Multi- Linear Regression.

Figure 5.1 represents the quality of the fit of the model, R^2 is the fraction of the variation of responses by the model and Q^2 is of the variation of the response that can be predicated by the model R^2 every time. The R^2 in this model is excellent for all the responses ($R^2 \geq 0.8$) however, Q^2 is quite acceptable for the drying chamber powder, cyclone powder and wall deposition, but un acceptable for the thermal efficiency (which is negative) which is poor due to noise present or unexpected behaviour of this response.

For the chamber particle size, the statistical analysis of the data showed that viscosity (Vis) had the most significant effect (P-value<0.05 or 95% confidence level). However, the main effects of temperature and flow rate and the six interaction effects were not significant. The main effects on the cyclone particle size, the main effect were temperature, viscosity and

flow rate are significant (P-value<0.05) but only the interaction T*Vis effect is significant. The obtained data also demonstrates also that for wall deposition (Wd), it is effected by temperature and the interaction effect between the temperature and viscosity. The thermal efficiency (Th), shows no significant effect of any of the factors studied

Table 5.3: R-squared of the polynomial models and P-values of both linear and interaction effects of responses.

	Dch (µm)	Cyl (µm)	Wd (No)	Th (%)
R^2	0.927	0.983	0.931	0.753
Constant	**0.0244968**	**0.00135861**	**0.00724614**	**0.00334566**
T	0.469034	**0.00963096**	**0.0478375**	0.163836
Vis	**0.00932733**	**0.00399236**	0.67494	0.779783
Fl	0.598449	**0.0249767**	0.0691368	0.171827
T*T	0.643463	0.0980198	0.18169	0.899009
Vis*Vis	0.671059	0.0568478	0.820538	0.281473
Fl*Fl	0.357181	0.57073	0.820539	0.428324
T*Vis	0.484315	**0.0118029**	**0.0466619**	0.681941
T*Fl	0.504349	0.26445	0.0790955	0.897009
Vis*V	0.697936	0.0889562	1	0.862531

Eliminating the non significant coefficients (P-value<0.05), the reduced model response can be expressed as follows (Figure 5.2-5.5):

Model 1: **Drying chamber particle size = 21.42 + 10.7738 (Viscosity of feed).**

Model 2: **Cyclone particle size = 16.72 + 3.00375 (Temperature) + 4.08875 (Viscosity of feed) + 2.12 (Airflow rate) + 3.95 (Temperature x Viscosity of feed).**

Model 3: **Wall deposition = 5 - 0.875 (Temperature) + 0.75 (Airflow rate) + 0.125 (Viscosity of feed) + 1.25 (Temperature x Viscosity of feed)**

The first model (1) shows that, when the atomisation energy is constant, the drying mean chamber particle size depends only the viscosity of the feed. The atomisation is produced by kinetic energy (via the external two-fluid nozzle) in the form of a wave which is

indirectly proportional to mean particle size [**1-8**]. The model clearly shows a constant value which acts as the initial energy required to break-up the feed into droplets. The mean particle size increases directly with an increase in the viscosity of HA slurry (Figure 5.2). This behaviour can be attributed to the fact that, according to the basic atomization theory, an increase in viscosity leads to as increase in droplet size [**1,8**]. These results are also in agreement with those reported by Luo and Nieh [**122**] who demonstrated that the increase of the HA slurry solid concentration increases the viscosity from 1 to 45.9 cst and then the mean particle size of the sprayed HA from 1.7 to 7.84 μm.

The second model (2) describing the cyclone particle size shows that temperature, viscosity and flow rate of hot inlet air, have a positive effect on the HA particle size (Figure 5.3). This can be explained by the fact that the increase of temperature with the higher airflow rate led to faster evaporation especially at 461 K; where the HA slurry dries into a solid sphere with porous pores, becomes a lighter particle and is therefore carried away to the cyclone. Moreover, the high HA slurry viscosity produces over all a higher particle size distribution at constant atomization energy. The second model also demonstrates also that the interaction between viscosity and temperature has a positive influence on the particle size. This is due to the evidence that an increase of temperature decreases the slurry viscosity, therefore requires less particle break down energy to produce finer particle size distributions, which have more surface area to dry, hence improves their drying rate.

Model (3) demonstrates on the contrary, that high viscosity will cause wall deposition, however high temperature avoids this phenomenon. This behaviour can be due to the drying process itself. During spray drying, the particle jet stream encounters the hot air, where particle drying takes place according the drying models. In fact; the first drying step consists of a primary drying which causes the outer surface to dry or free surface drying, followed by a secondary drying where the core is dried due to continuous higher temperature. If the particles reach the chamber walls before the end of the primary drying stage, the chances of particles sticking to the wall, is high and the rate depends upon the particles material properties.

As illustrated in the surface response shown in Figure 5.4, the lowest wall deposition is obtained only when a low viscosity slurry (Vis<35 mPa.s) is sprayed at high temperatures (T>445 K). The model shows also a positive effect for hot air flowrate. Figure 5.4 shows that higher flow rate turbulence increases wall deposition effects. Numerous authors [**89-95**] have described this turbulence effect on wall deposition. Master [**91**] provided a solution, that if a spray dryer is scaled-up by 20%, it greatly reduces the wall deposition because it allows more space for the particles to dry before hitting the wall during first flight. The quantity of particle deposition it can be assessed also by taking photographs of the walls of the spray dryer and observing simulation of the velocity vectors as shown in Figure 5.6.

The thermal efficiency of the dryer does not have a strong significant effect, however the inlet temperature is significant, and the thermal efficiency is a function of the inlet and outlet temperatures of the spray dryer. The higher the temperature difference between inlet and outlet temperatures of the spray dryer, the higher the thermal efficiency, thus more energy is utilised in the evaporation of the water from the HA slurry. In this statistical analysis (Figure 5.5), the temperature of the hot air entering was high (from 398 to 461K) compared the outlet leaving the chamber (65 to 90K) temperature.

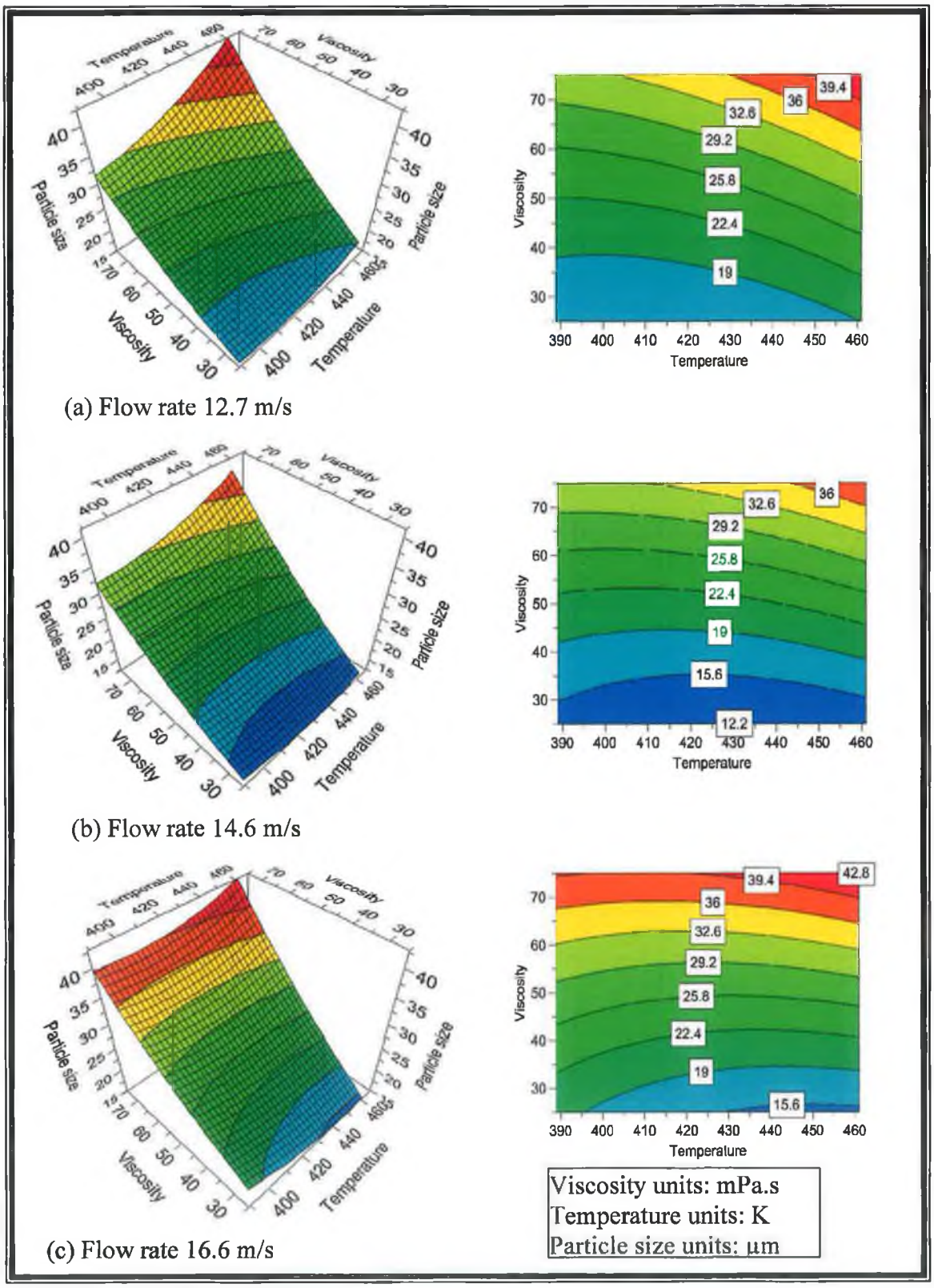

(a) Flow rate 12.7 m/s

(b) Flow rate 14.6 m/s

(c) Flow rate 16.6 m/s

Figure 5.2: 3D surface and contour response of particle size collected in the main drying chamber of the spray dryer for various flow rates.

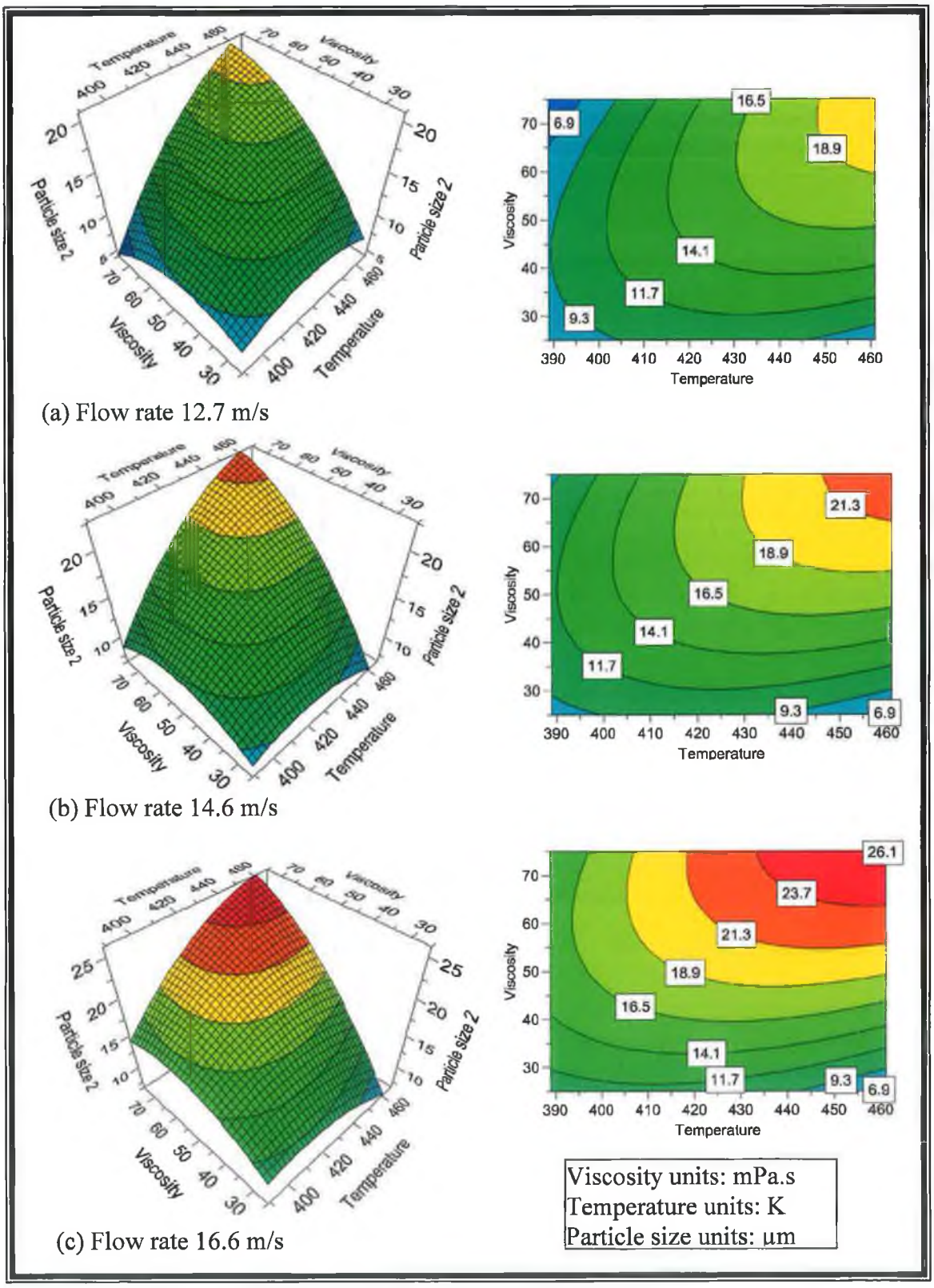

Figure 5.3: 3D surface and contour of response of Particle size collected in Cyclone of the spray dryer.

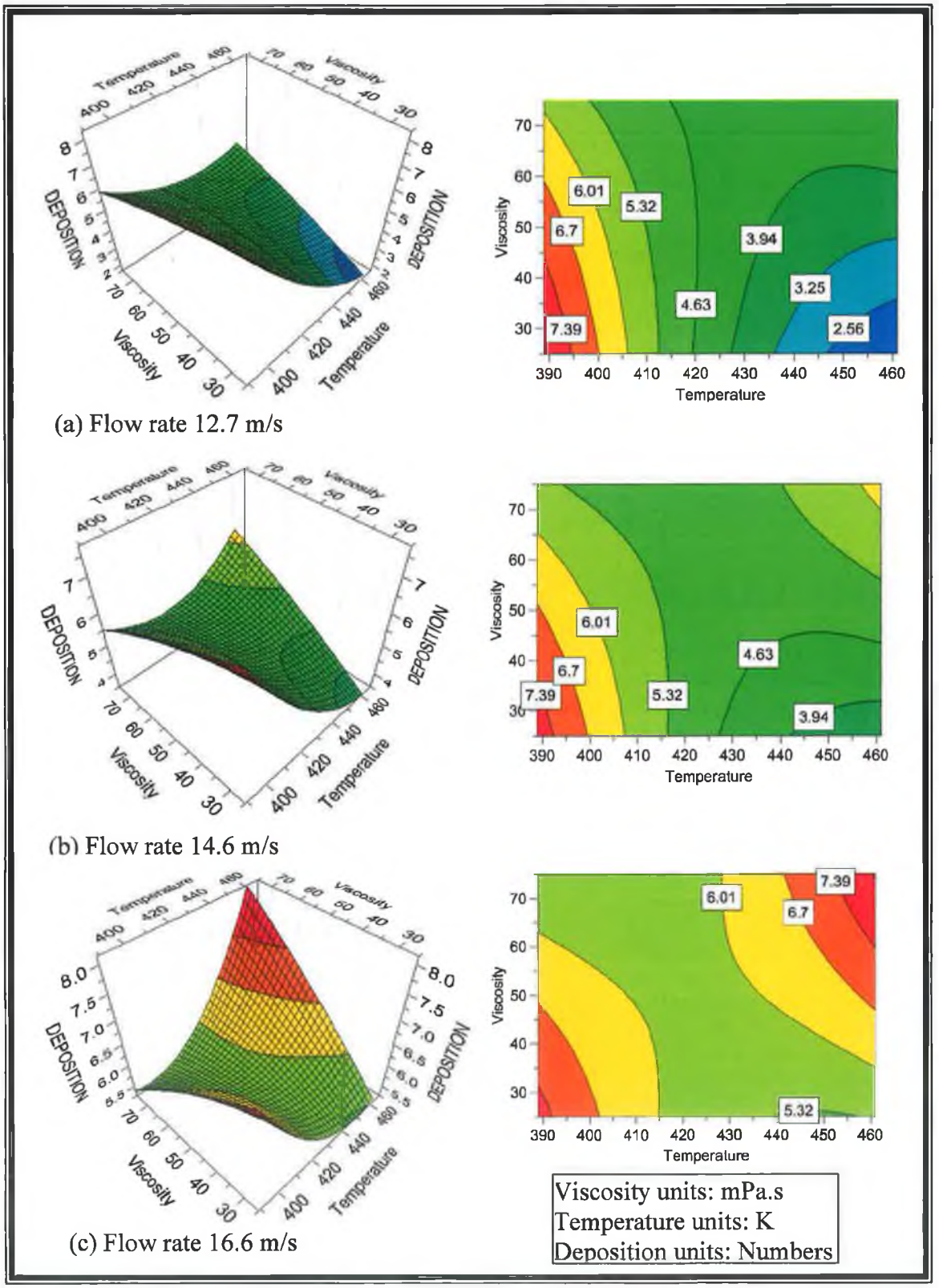

Figure 5.4: 3D surface and contour of response of wall deposition inside the spray dryer.

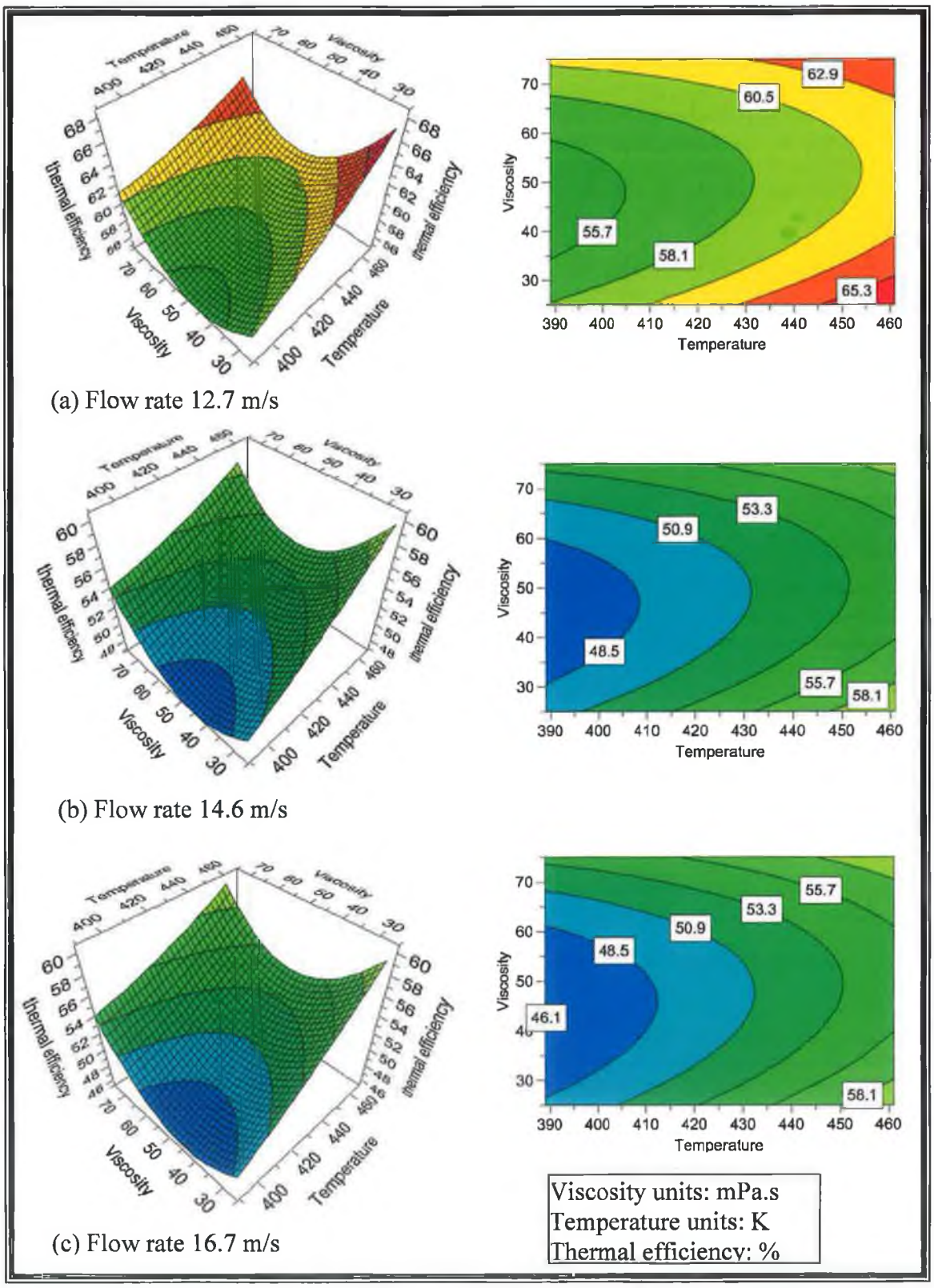

Figure 5.5: 3D surface and contour of response of over-all thermal efficiency of the spray dryer.

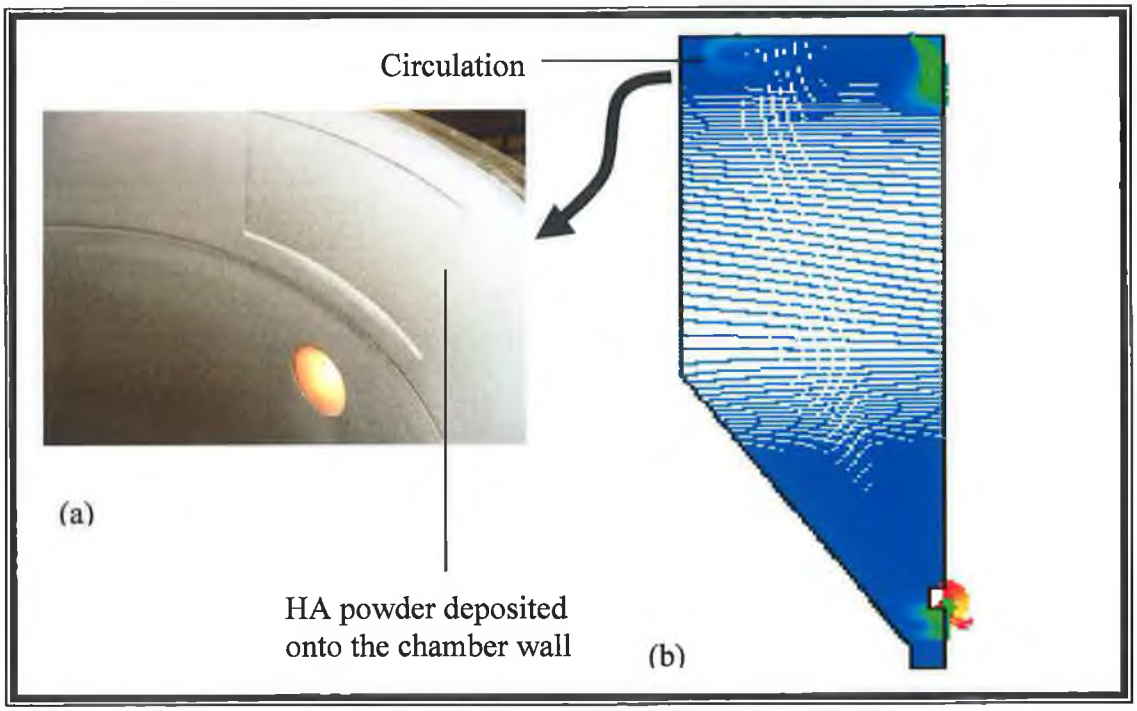

Figure 5.6: Side wall deposition and the circulation of the velocity vector inside the spray dryer.

5.3.3 PARTICLE SIZE DISTRIBUTION

In the present research, a large range of mean particle size of HA were obtained, which is predominately dependent upon the feed viscosity at constant atomization energy and the significant effects like temperature and flow rate of the hot inlet air (Figure 5.7-5.9). Figure 5.7 shows at low viscosity 25 mPa.s and low temperature 398 K to high temperature 461 K, mean particle size ranges from 8.5 μm to 18.8μm, Figure 5.8 shows at medium viscosity 50 mPa.s and low temperature 398 K to high temperature 461 K, mean particle size ranges from 9.92 μm to 36.85 μm and Figure 5.7 shows at high viscosity 75 mPa.s and low temperature 398 K to high temperature 461 K, mean particle size ranges from 24.45 μm to 41.60 μm. For all of the sample particle sizes analysed a quite narrow distribution was found (Figure 5.7-8). At low viscosity 25 mPa.s the distribution is normal distribution spread over the entire area as compare to high viscosity 75 mPa.s and the distribution is narrower at higher temperature level. Figure 5.7 shows that at low viscosity a unimodal distribution for all three temperatures 398, 421 and 461 K results. However at all viscosities an increase in temperature, caused some of the particle size distribution attained to start to develop a little bump in normal distribution, where the effect is more pronounce at the temperature of 461K for the chamber powders (Figure 5.9). This can be explained by agglomeration of the powder due to its low particle size [**219**]. The agglomeration during spray drying process can be defined as the association of smaller particles into clusters due to bringing independent particles into contact with one another, enhancing or controlling interparticle adhesion, and stabilizing the created agglomerates in some cases under the action of external forces (for an example temperature difference), where as in a particular their moisture content which affect the adhesiveness of the particles [**18,17,33**]. At the higher temperature drying profile, the concentration of primary spray particles at a vicinity of the nozzle has much temperature difference as atomisation of feed temperature is very low with compare to the inlet drying temperature and few particles which may give a chance to collide with small particles to primary particles that formed just after atomisation. The agglomeration observed at the higher temperature (461K) may be due to fast evaporation, exploding of droplet into doughnut shape and release instant moisture to surrounding (Figure 5.9) [**219, 216**].

The mean particle size is an important factor which determines the feed stock powder characteristics for thermal spray deposition. Thermal spray powders are formed when the spray dried powder is calcinated and milled. From a particle size point of view, these two processes further increase the size and alter their shape [**220**]. The spray drying HA powder can be highly porous or in an amorphous state. The sintering of HA powder is required to improve the crystallinity of the powder of up to 99% for medical implant substitute applications [**221**]. It has been reported that the microstructure of HA powder increases in grain size exponentially by increasing sintering temperature [**222**]. The HA phase is stable when sintered below 1400 °C for 2 hours [**133**]. However, sintering at temperatures greater than 1400 °C resulted in the decomposition of HA from (Tricalcium Phosphate) TCP, (Tetracalcium Phosphate Monoxide) TTCP and (Calcium oxide) CaO products [**126,133, 137**].

The typical HA powder sizes for plasma spray has been reported **[125,133]** to be in the range of 20 to 75 μm to retained its original crystallinity, however, particle sizes lower than 20 μm, become partial melted and decomposed into calcium phosphate (TCP), tetra-calcium phosphate (TTCP) or amorphous calcium (ACP) and the crystallinity is generally less than 30 percent, where as if the particle size is larger than 75 μm the heating of the HA powders is insufficient during plasma thermal spraying, which resulted in extremely poor bonding of the deposited powders with the medical implant to form a coating and most of the particles that impacted on the substrate rebound off. In this research, the spray drying of HA slurry at 50 mPa.s viscosity and hot inlet temperature 461 K produced a the mean average particle size of 36 μm in the drying chamber which further increases the powder size after sintering as a result of some agglomeration that would be ideal for the plasma spray. For an example, a typical plasma spray powder range is 20 μm to 58 μm to get a desire coating characteristic [**104**]. In this research, HA powder produce at 50 mPa.s viscosity and temperature 461 K produced mean particle size 34 μm in the drying chamber and 20 μm particle size in the cyclone of the spay dryer. To achieve the desired powder range (20 to 58 μm) for the plasma spray of HA powder, these powders must be sieved out to this specific range and the rest of the HA powder would be further treated so as to be

used in other processes such as electro chemical processes also used to deposit HA coatings onto hip implants where the HA powder needs low particle size [**227**].

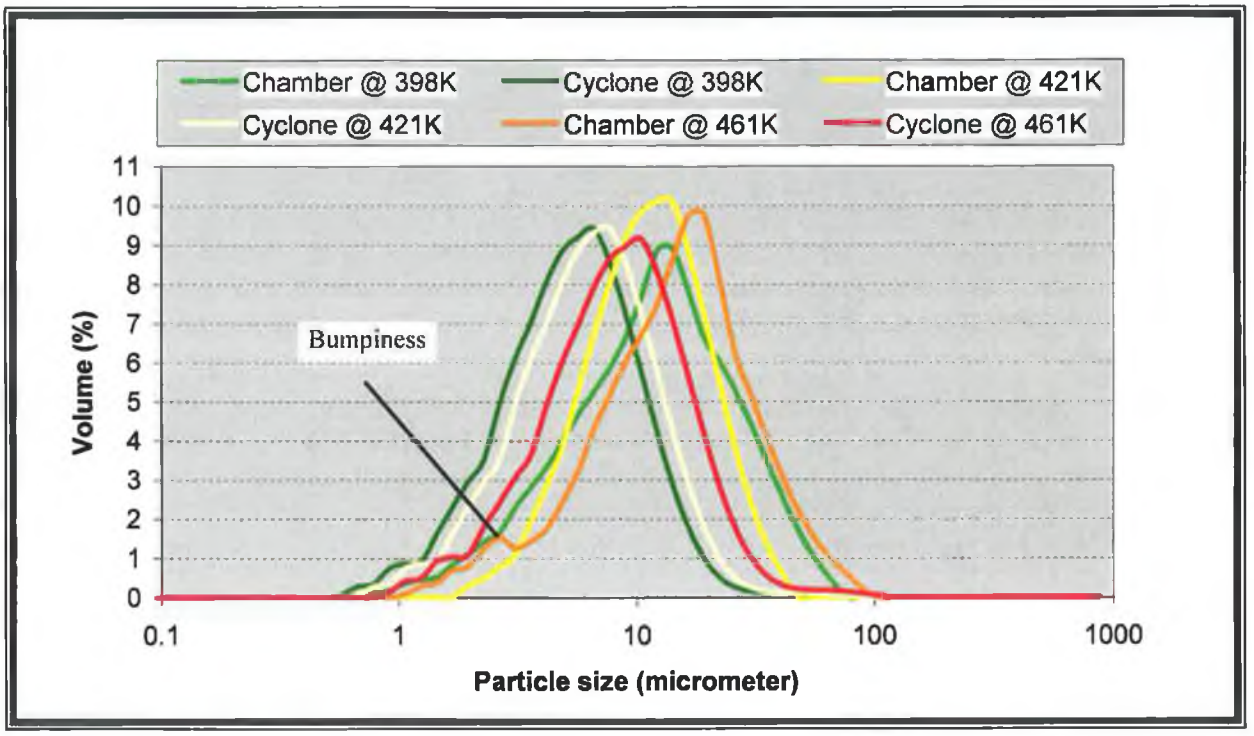

Figure 5.7: Particle size distribution at feed viscosity of HA slurry 25 mPa.s.

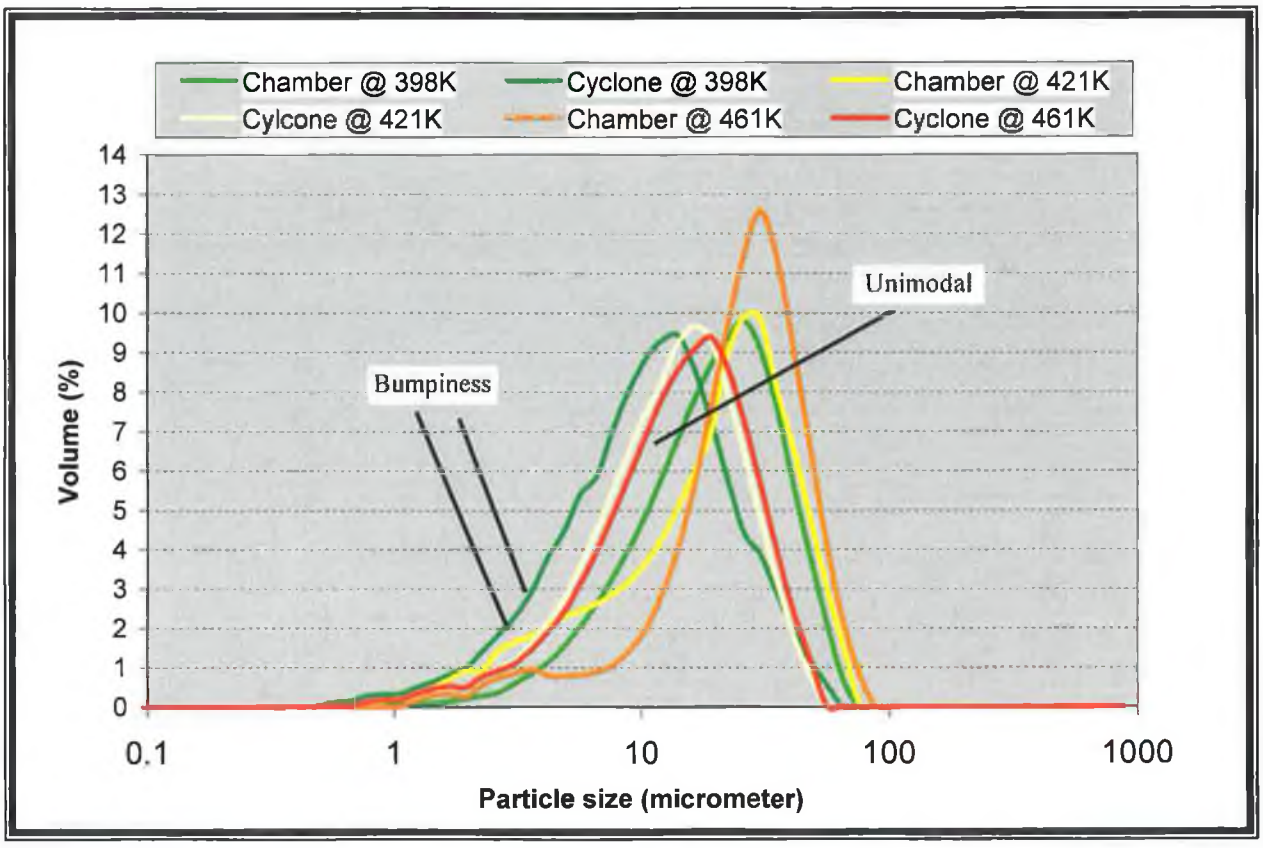

Figure 5.8: Particle size distribution at feed viscosity of HA slurry 50 mPa.s

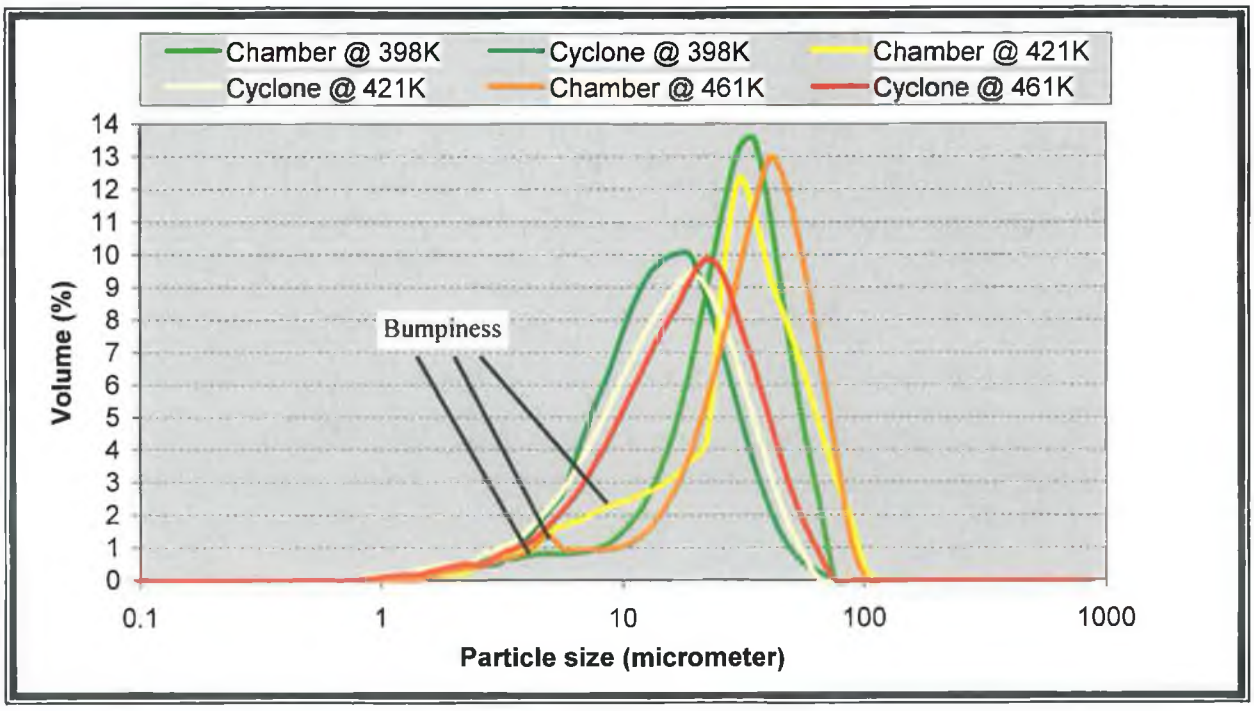

Figure 5.9: Particle size distribution at feed viscosity of HA slurry 75 mPa.s.

5.3.4 MORPHOLOGY OF HA SPRAY DRIED POWDER

Figures 5.10 to 5.14 show HA particles morphology produce (at different magnifications) for different levels of viscosity (25, 50 and 75 mPa.s) and inlet temperatures (398, 421 and 461K) respectively. The micrographs produced by the SEM clearly show the shape of entire samples of powder collected from the drying chamber and the cyclone, which were spherical and quite regular with large distribution sizes. In general, spherical powders have better rheological properties than irregular powders and thus produce better coatings for hip implants [**131**]. The plasma spray equipment uses tiny nozzles to input its powder into its melting flame, thus requires spherical powders to increase the efficiency of the system. The spray drying HA powder has free flowing characteristic however has low percentage of crystallinity as compared to FDA requirements (99.9%) [**137**], therefore these powders do require sintering before been used to produce thermal spray coatings. However, sintering or calcination has shown to reduce the flowability of the powder due to surface roughness effects [**122**], where HA spray dried powder particles in the range of 20-45 μm, had a flowrate of 0.21g/s for uncalcinated powder compared to 0.15 g/s after calcination for 24 hrs.

The two main shapes found in this research were a solid and a doughnut sphere shaped morphology (Figure 5.13-5.14). After initial break down of the slurry into fine droplets by the high speed air, the droplet surface temperature of the droplet quickly reaches the drying temperature and the surface moisture begins to evaporate when the moisture content on the droplet surface falls below its critical value. The shape of dried powder depends upon the viscosity of the HA slurry (solid concentration). It was also observed that the particles shape had blow holes, spikes, catering and shrivelling which would be explained by looking at each particle's history.

A solid sphere of HA spray dried powder with pores was observed when of a viscosity 75 mPa.s was applied to all three levels of drying temperature (398, 421 and 461K) (Figure 5.10-5.12 (c)). However at 398K the powder had a more fracture porous particle, while on the other hand, at the 461 K the particles were more solid (Figure 5.12 (c)). This can be explained by the fact that at higher viscosity, the HA slurry contains more insoluble

precipitates; thus the surface temperature of the droplets would exceed the boiling temperature of the water during drying and moisture would rapidly flow to the droplet surface by capillary action. In the dense slurry, a thick shell of insoluble precipitates would quickly form. As a result, heat transfer into the centre of the droplet becomes difficult and the temperature at the centre may never reach boiling point. The drying process is thereby controlled by the outward diffusion process of water. This leads to the formation of solid spheres (Figure 5.13) and the denser the starting slurry, the denser the solid sphere. The same was also reported by Luo et al. [**122**], where at a HA slurry concentrations of 0.25 volume fraction, the spray dried powder shapes were solid spheres with pores.

If the moisture evaporation rate exceeds the rate of solute diffusion back into the droplet interior, the solute precipitated at the droplet surface forms a shell. At the same time, pressure builds up due to moisture. If the shell is porous, this pressure would be released and a hollow sphere would be formed. If the shell is non-porous, a hollow sphere would erupt under high internal pressures.

Doughnut shaped particles were observed in the spray drying of HA slurry when a slurry viscosity of 50 mPa.s was utilized. This doughnut phenomenon was more pronounced with an increase in the spray drying air temperature (461K) (Figure 5.10-5.12 (b)) in the chamber powders. A doughnut shape HA powder may be formed due to the dilute HA slurry. This may be explained due to the mobility of the insoluble precipitates in the droplet been high, under external forces (such as gravitational forces), these insoluble particles can tend to move to the bottom of the drying chamber and elongate the droplet into an elliptical shape (Figure 5.13 (b)). This phenomenon may be increases the surface area of the droplet and thus, the associated surface tension. At the moment the droplet detaches from the HA slurry spray stream, a strong effect of surface spring-back occurs, following the tendency to minimise its surface to volume ratio. This spring-back action can lead to an inward collapse of the opposite faces of an elongated droplet and the formation of a doughnut-shaped granule (Figure 5.14). This mechanism of doughnut formation has previously been described by several authors [**41,50,117,119**], where the drying process can also be

diffusion controlled, similar to that for the solid-sphere formation, but higher temperatures can accelerate this.

While a viscosity of 50 mPa.s and temperature of 461 K yield the ideal particle size and range, in terms of HA morphology, a mix of solid and doughnut shape powder was produced. For thermal spray applications, solid spherical powders are desired to retain its bulk properties and dense coating on the substrate. However, HA thermal spray coating requires porous coatings to help the growth of the cells inside the coating to provide a strong bioactive bond between the implant and bone [**128**]. However it is felt that the mixture of solid and doughnut powder shaped particles may provide a strong deposit with pores for cellular growth.

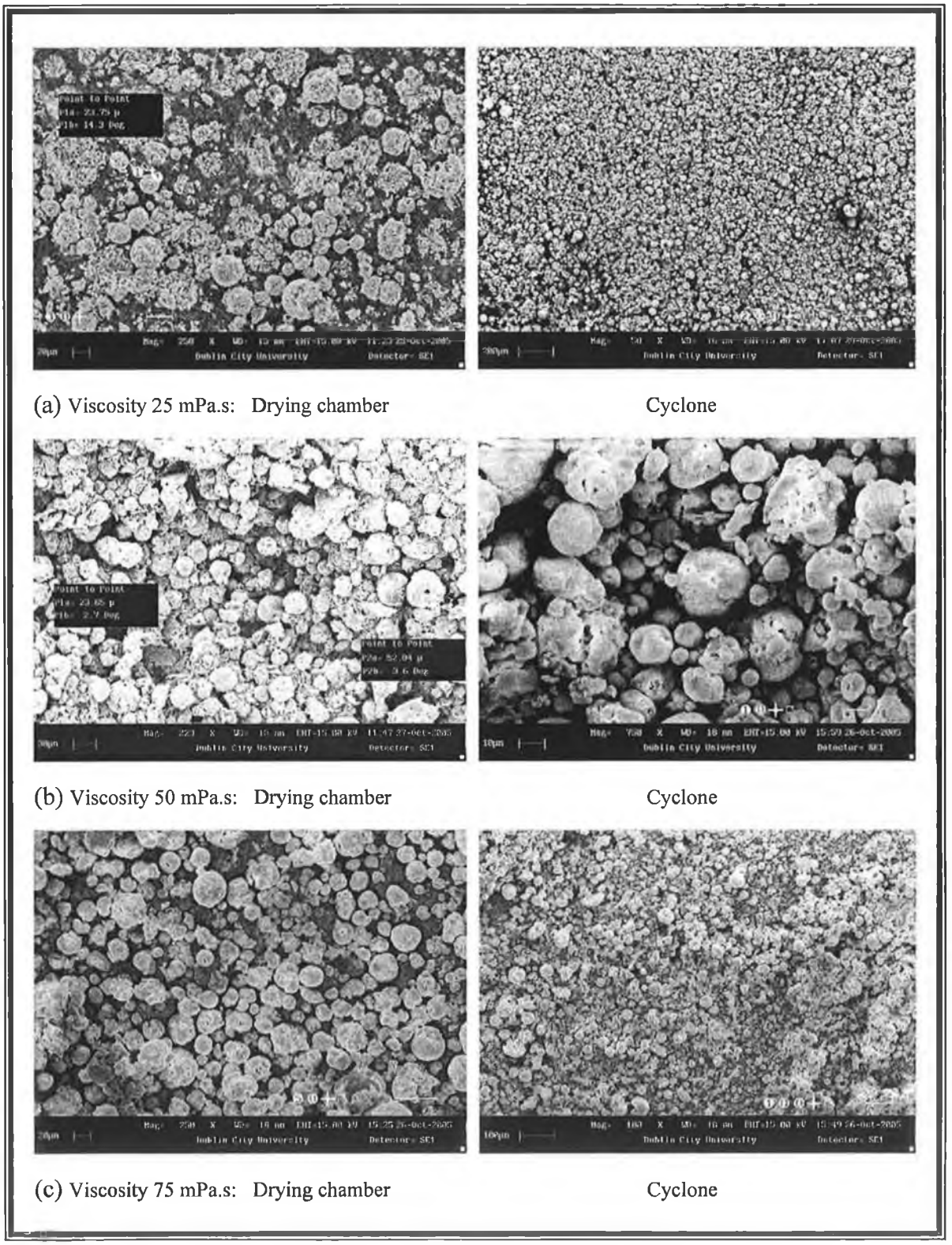

(a) Viscosity 25 mPa.s: Drying chamber Cyclone

(b) Viscosity 50 mPa.s: Drying chamber Cyclone

(c) Viscosity 75 mPa.s: Drying chamber Cyclone

Figure 5.10: SEM micrographs of spray drying (for an inlet temperature of 398K) HA powder.

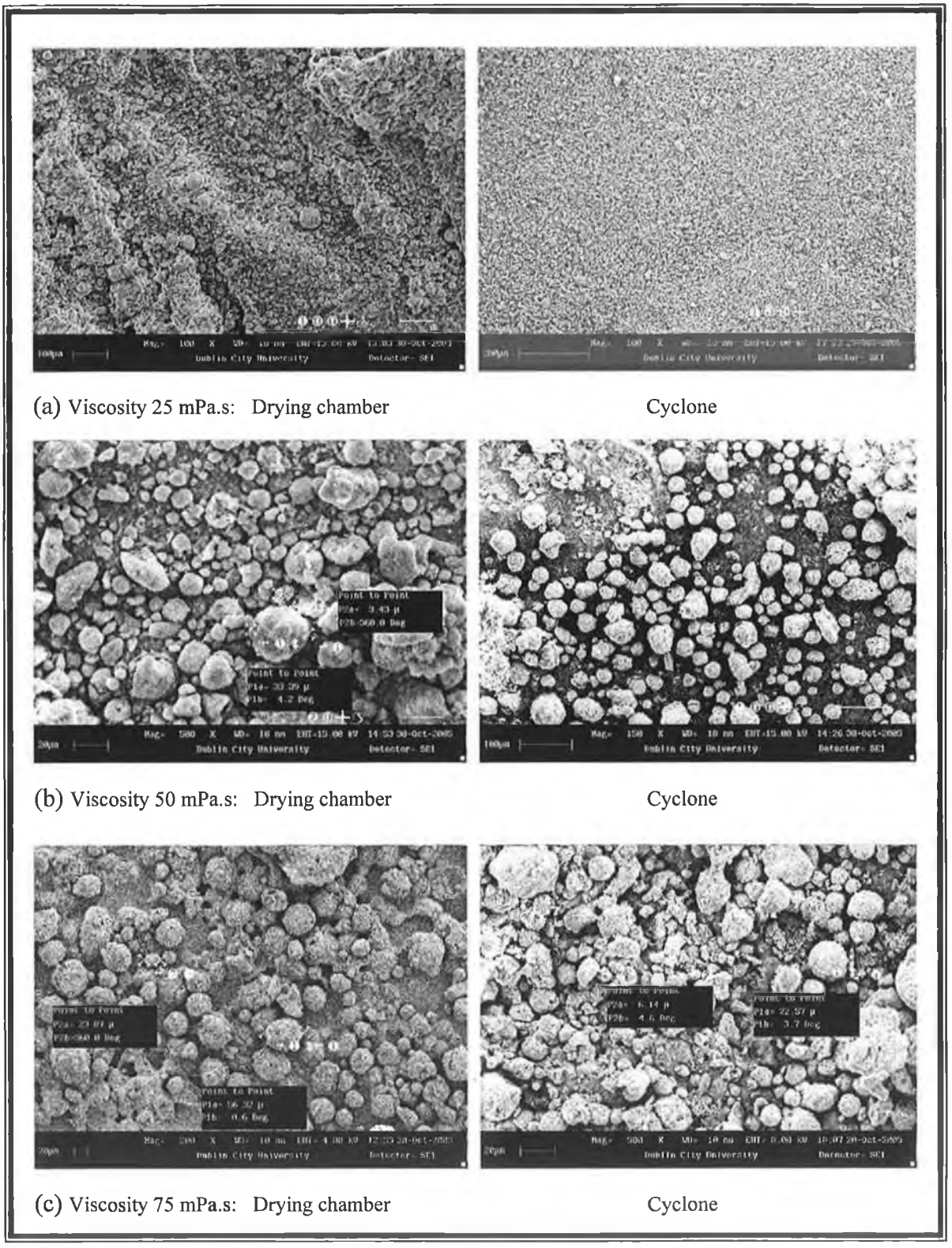

Figure 5.11: SEM micrographs of spray drying (for an inlet temperature of 421K) HA powder.

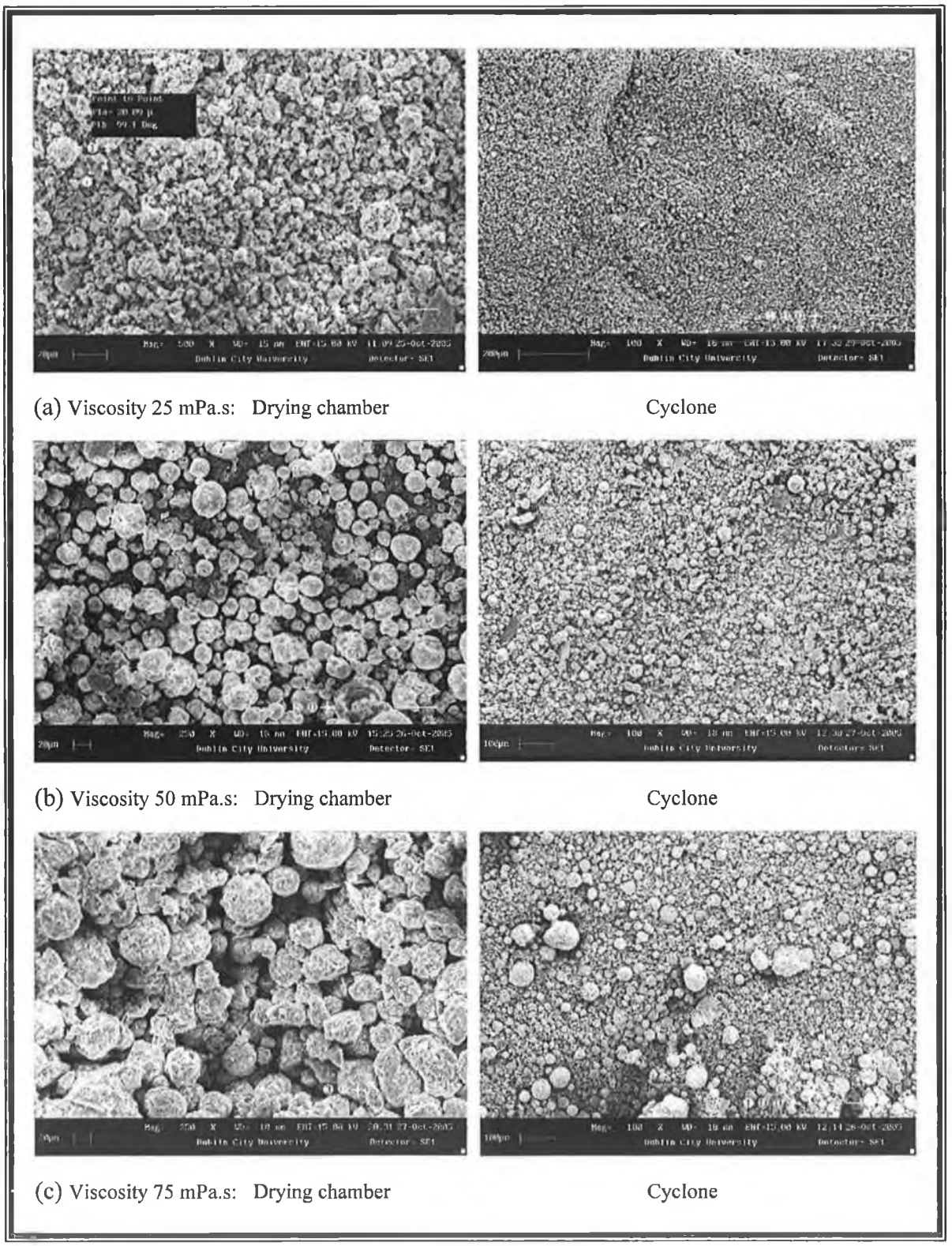

(a) Viscosity 25 mPa.s: Drying chamber Cyclone

(b) Viscosity 50 mPa.s: Drying chamber Cyclone

(c) Viscosity 75 mPa.s: Drying chamber Cyclone

Figure 5.12: SEM micrographs of spray drying (for an inlet temperature of 461K) HA powder.

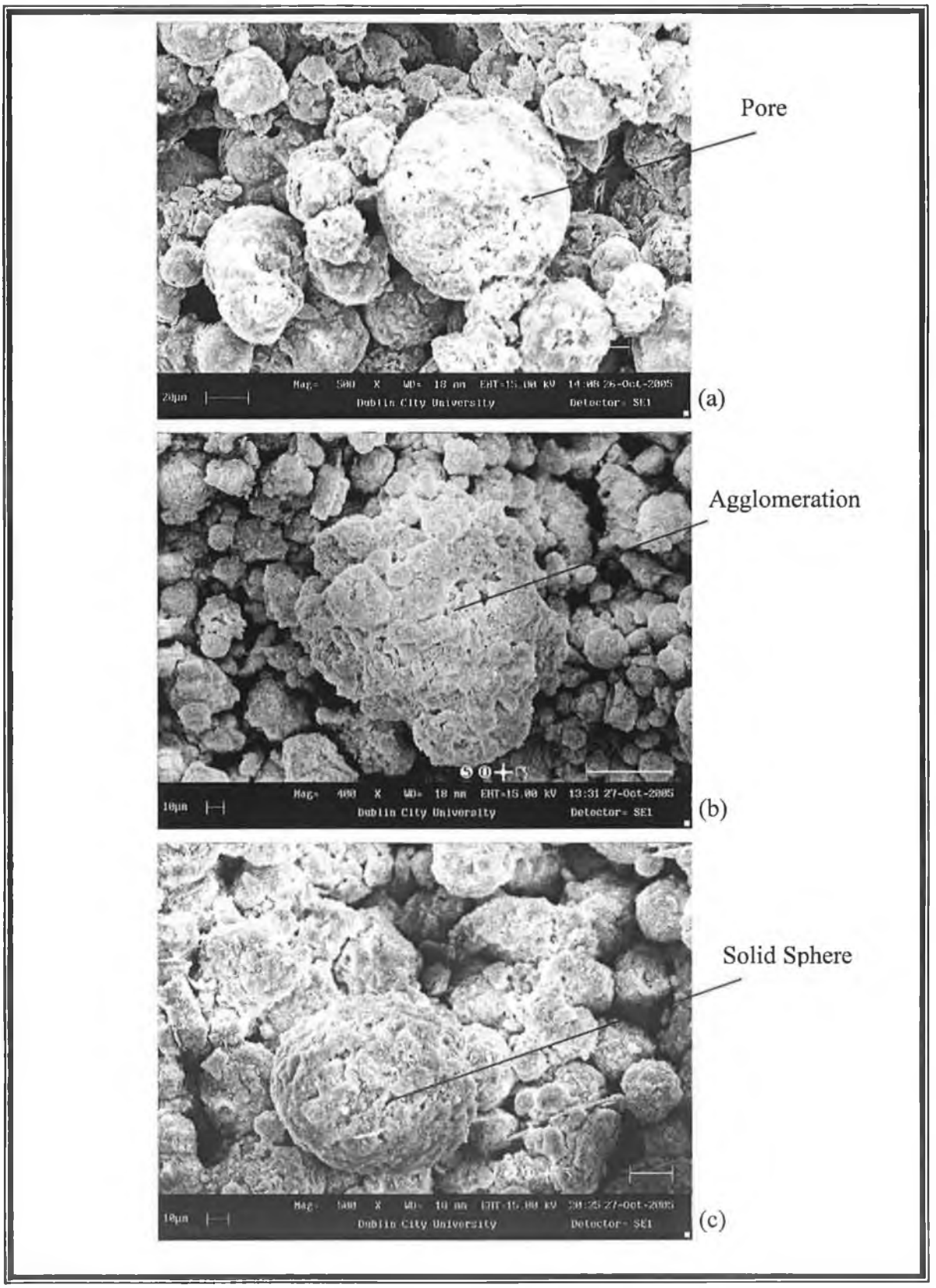

Figure 5.13: Different solid sphere shapes of HA powder.

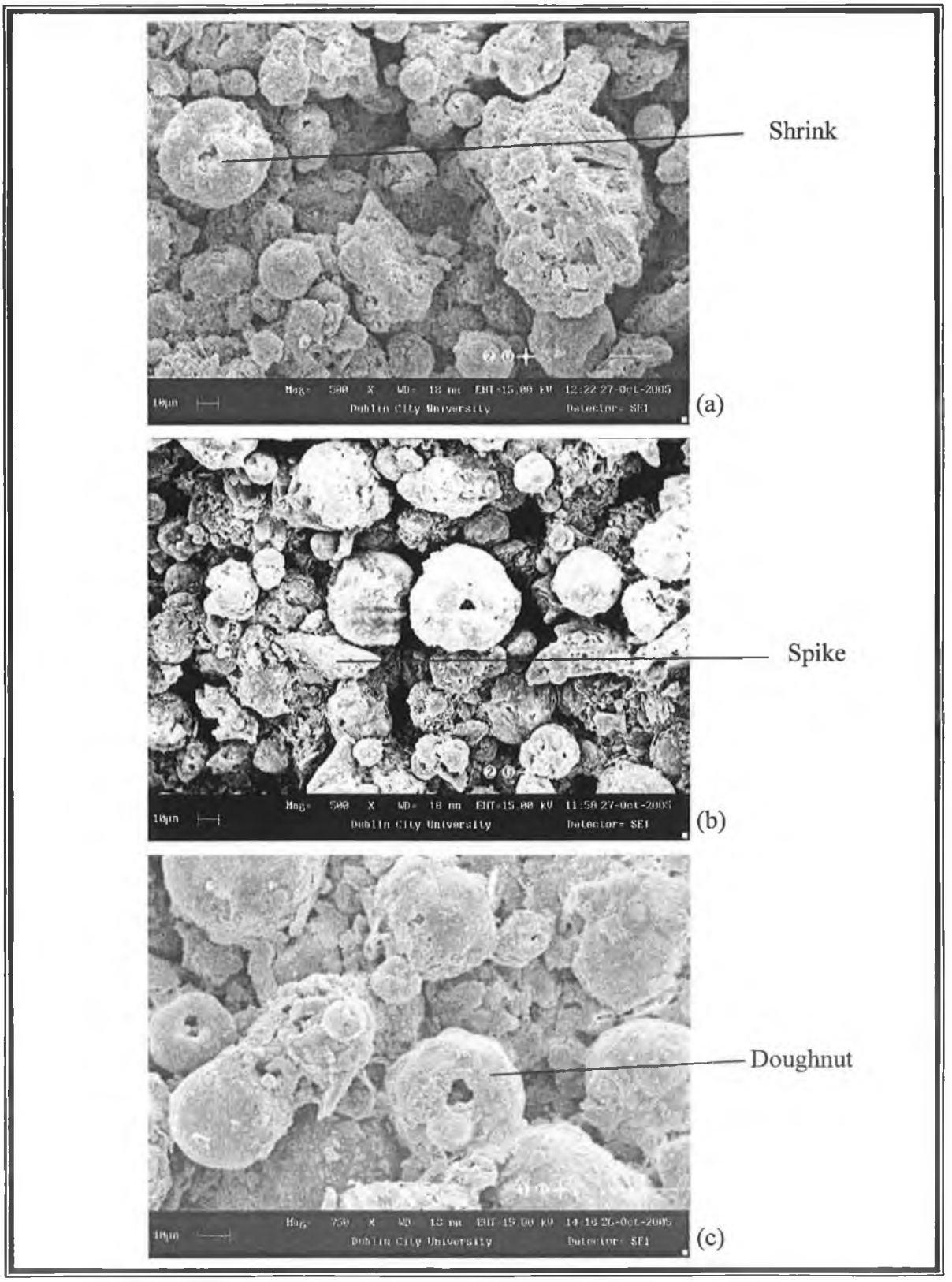

Figure 5.14: Different doughnut shapes of HA powder.

5.3.5 COMPARISION OF STATISTICAL MODEL

The MODDE 7.0® software was used to analyse the factors and to compare to the experimental data target (Table 5.4). The optimised value of input factors; temperature, viscosity and flowrate, were 460.99 K, 25.86 mPa.s and 12.76m/s respectively and the same factors levels (461 K, 26 mPa.s and 12.7m/s) were examined by an additional independent experiment performed. The experiment indicates good agreement between the statistical simulation the data for mean particle size of chamber (14.84% difference), mean particle size of cyclone (27.11% difference), wall deposition (1.5% difference), and thermal efficiency (17.24% difference), (Figure 5.15) implying that empirical model can be used to describe the relationship between the factors (Figure 5.1). These differences may be due to iterations errors, interaction effect, energy losses and statistical model errors.

Table 5.4: Optimisation factors and responses for comparison of the statistical model.

Factors			Responses			
	Low	High		Min.	Target	Max.
Temperature (K)	398	461	Chamber particle size (µm)	5	22	50
Viscosity (mPa.s)	25	75	Cyclone Particle Size (µm)	1	10	15
Flow rate (m/s)	12.7	16.6	Wall Deposition (points)	0	1	3
			Over-all Thermal Efficiency (%)	50	60	80

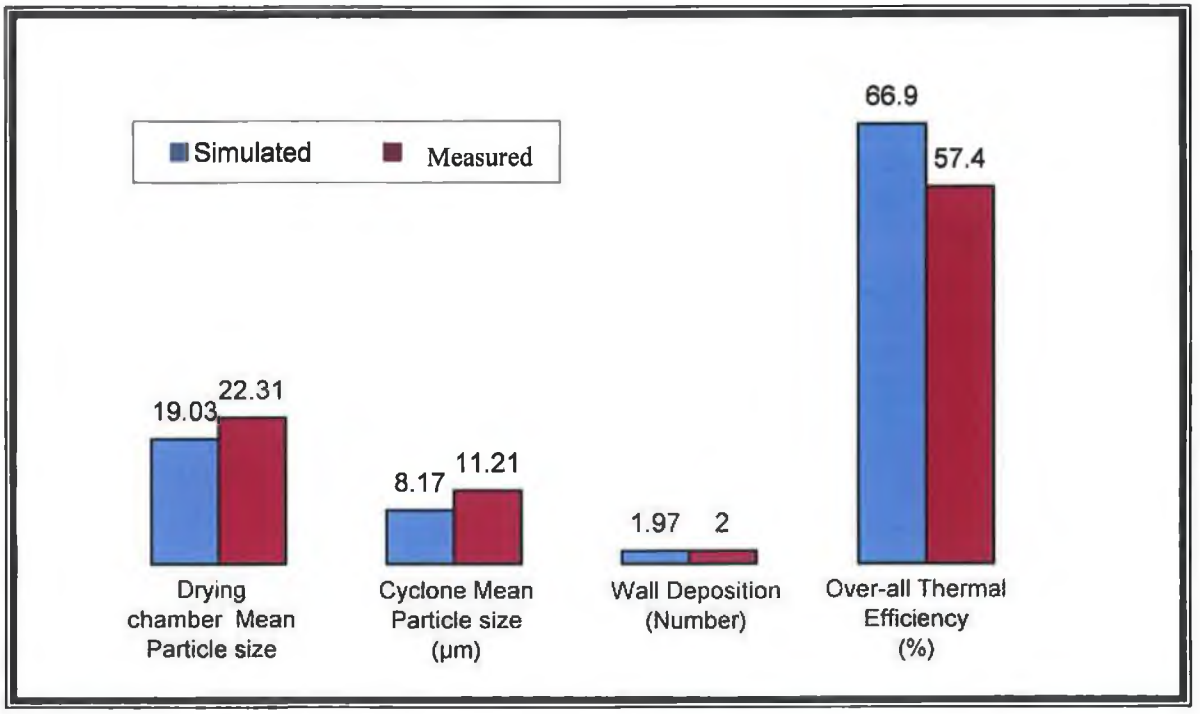

Figure 5.15: Comparison of responses of experiment and statistical model for optimization of the spray dryer factors (Temperature, Viscosity and Flowrate).

5.4 THE EXTERNAL TWO-FLUID NOZZLE SIMULATION

The external two-fluid nozzle has two pipe systems; air and feed pipe. Each pipe was analysed separately to predict each internal and exit velocities and their relative velocities.

5.4.1 AIR PIPE SIMULATION

Initially the velocity achieved for interval 10 percentage of calibrated atomising scale (5kg/mm) was measured, by reading the input velocity value for each equivalent scale setting Reynolds no at the inlet of air pipe were calculated Table 5.5.

Table 5.5: Inlet and exit velocity of air nozzle pipe for various atomising scales.

% of Calibrated Atomising Scale (100% = 5.0 Nm^3/hr)	Inlet Velocity of Air Nozzle (Measured) (m/s)	Reynolds No. (at the inlet of air pipe)	Exit Velocity (Simulated) (m/s)	Reynolds No. at the exit of air pipe
100	7.31	5421	118.5	53325
80	5.85	4338	91.5	41175
75	5.48	3990	85.5	38475
60	4.38	3249	72.3	32535
50	3.65	2707	58.4	26280
40	2.95	2165	47.6	21420
30	2.19	1624	36.5	16200

Table 5.4 shows the nozzle simulated velocities for 30 to 100% calibration of atomising scale (100% = 5.0 Nm^3/hr). For each increase in calibrated scale 50 to 60% a proportional change in input (and final output) velocity was found (with minimum error of 1.5 %). Generally, it has been established that for internal fluid flow such as in pipes, laminar flow exits when Re $\leq$ 2300 and turbulence exits at Re>4000. In this air pipe analysis, the Reynolds number is calculated at the entry point by the following equation [**135**]:

$$\mathrm{Re} = \frac{\rho V D_h}{\mu} \quad \text{----------Equation 5.1}$$

Where ρ is the density, μ is the dynamic viscosity and D_h is the hydraulic diameter, v is the velocity and Re is the local value of Reynolds Number. In this research, the hydraulic

diameter is 0.011 m at the inlet diameter of the air pipe. Equation 5.1 was used to check if turbulence flow of air occurred at the inlet point of the air pipe. Table 5.4 shows that the exit velocity of the air feed starts out as laminar flow and reaches turbulent flow as the scale is changed from 30 to 100% (100% = 5.0 Nm^3/hr) respectively. The calibration of atomizing scale was performed at 30 to 100 % with the interval of 10, because it was observed that below 30% atomisation a minimum energy or threshold kinetic energy was needed to start atomisation which only occurred at 30%. All the levels (30%-100%) of atomising calibrated scale were analysed, but the 75% or 5.48 m/s inlet velocity experimental run is described because preliminary spray drying tests showed that at 75% calibrating atomising scale gives full atomisation of HA slurry with minimum wall deposition and desired particle size distribution were found (all of there results are shown in Appendix D2-6).

Figure 5.16 shows the velocity, turbulence intensity and temperature of the air inside the air pipe for 5.48 m/s inlet velocity. Figure 5.16 (a) shows that the velocity profile is well developed and its vectors in Figure 5.17 indicates that at the sharp edges of the air nozzle circulations are present. Figure 5.16 (b) shows the turbulent intensity in the air nozzle and it is 293% at the throat of initially assigned value at the inlet (5%) which is very clearly indicated that is the critical point of nozzle as the air nozzle is only a convergent type nozzle. Air is a compressible gas therefore it is effected by temperature which changes the fluid density, viscosity, and thermal conductivity, therefore one must evaluate its importance. Figure 5.16 (c) shows only a slight change in temperature which means that the air almost acts as an incompressible fluid.

Figure 5.18 shows the velocity at the outlet of the air nozzle for 5.48 m/s inlet velocity. The results compare the three turbulence models (Standard K-ϵ, Realizable K-ϵ, and RSM) and the variation between the turbulence models was found to be within the range of 5 to 10%. This suggests that the standard K-ϵ produces good results when compared to other two methods. The same was reported by Fletcher [**173**] that the standard K-ϵ, model

produced reasonable results in the simulation of spray dryer performance using CFX5 codes.

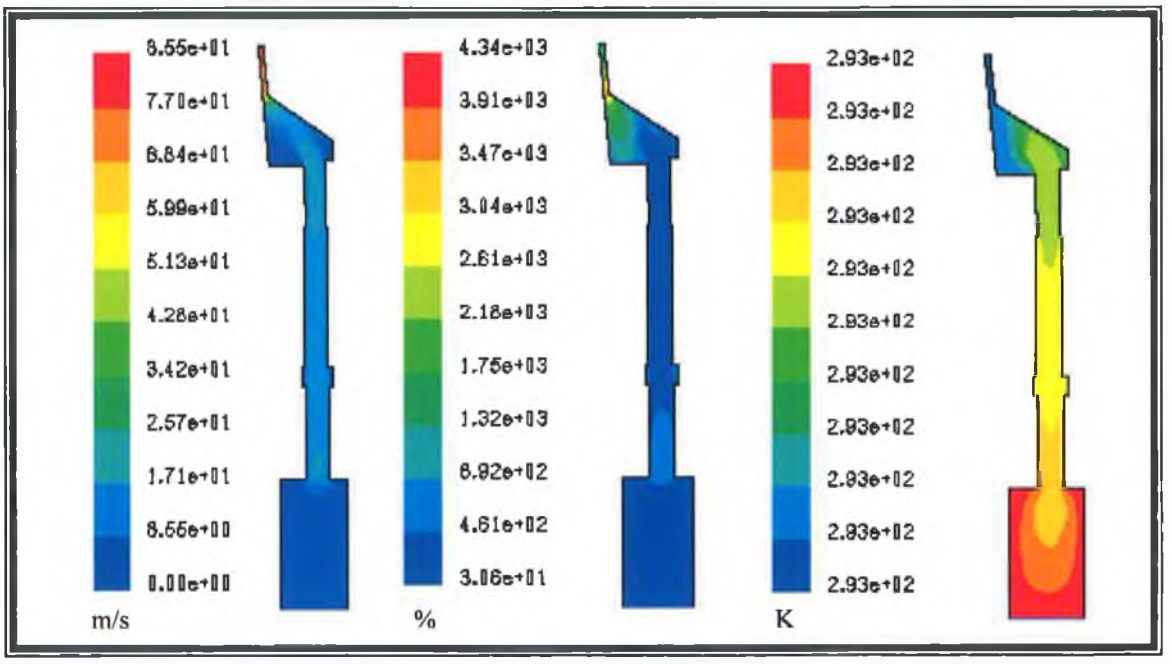

Figure 5.16: (a) Velocity profile (b) turbulence intensity and (c) temperature distribution at 5.48 m/s inlet.

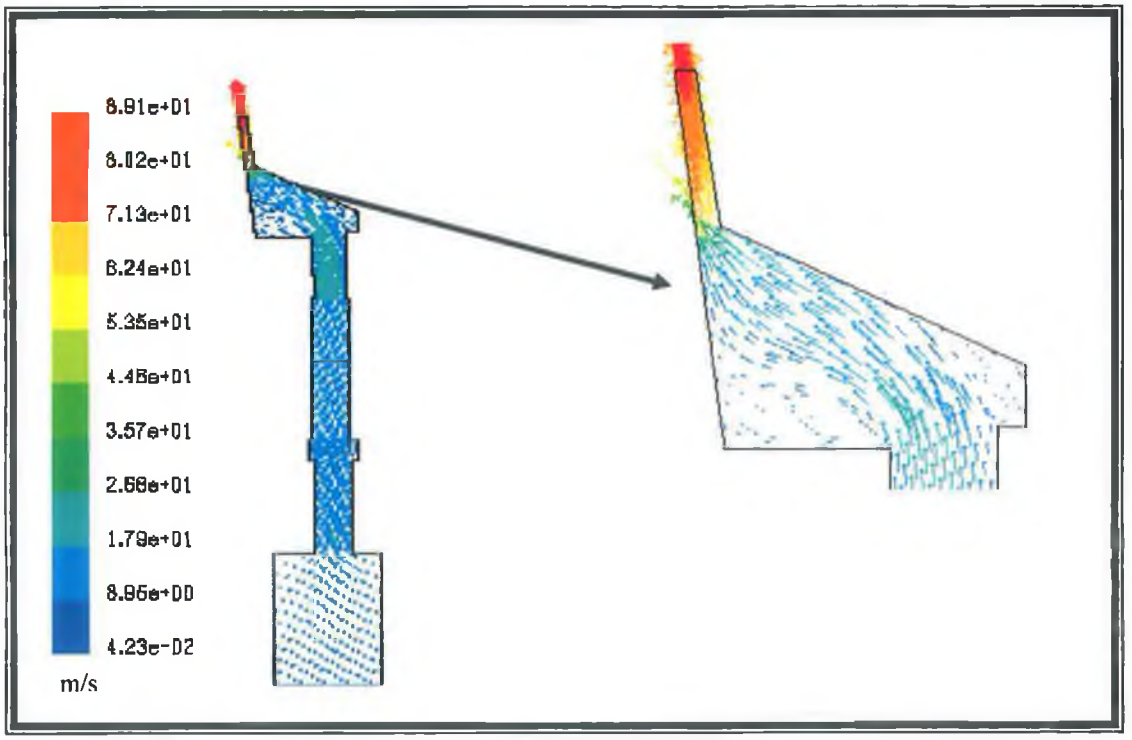

Figure 5.17: Velocity vector at 5.48 m/s inlet velocity of the air pipe.

accuracy is hardly reduced. Further more the standard K-ϵ has two equations to describe the complete turbulence model, where as the realizable K-ϵ contains new transport equations for dissipation rate ϵ derived from the Navier-Stokes equations, therefore it has five complex equations for two dimensional flow [**142-152**].

Table 5.6:- Iterations to converge the solution with standard criteria at 5.48 m/s inlet velocity of air pipe nozzle.

Number of Iterations			
	S K-ϵ	R K-ϵ	RSM
Air Nozzle	1789	2595	8121

Further analysis of the Standard K-ϵ method used to predict the exit velocity at the entire range of atomizing scales in can be observed in Figures D1-5 (Appendix D). As a swirl wheel does not exist in the nozzle, the Standard K-ϵ method is quite fast at predicting the results, however if a swirl wheel was considered, the Realizable K-ϵ would be a more efficient turbulent method to predict the exit velocity [**155**].

The Mach number was estimated, to determine whether the compressible behaviour in the air pipe existed or not. In the simulation, if Mach numbers were above approximately 0.3, the compressible solution algorithm would be activated and at a Mach number above approximately 0.7, significant differences between incompressible and compressible results would be expected [**144**]. The air pipe simulation with full range of atomizing scale showed clearly that the maximum velocity achieved was less than the critical velocity (Mach number 1 or the speed of sound). The maximum Mach number calculated for the air pipe was less than 0.3, so there is no chance of a shock wave and stagnation conditions occurring inside the nozzle. Figures D1-5 (Appendix D) shows the velocity, turbulence intensity and temperature profile at different inlet velocities, which produces exit velocity and turbulence that were directly proportional to the break-up of the feed flow from the external two-fluid nozzle inside the spray dryer. The higher velocity of the air pipe, results

The exit velocity profile shows (Figure 5.6) a slight attacking angle toward the feed pipe flow which helps to break-up the feed due to the design of nozzle shape. The RSM predicted the highest velocity at the outlet of the air pipe and this maybe due to the fact that the air pipe exit orifice is circular and symmetric in shape which is beneficial when modelling with the RSM method as the convergent part of the nozzle causes the flow to stabilise by redistributing normal stresses near the walls. The RSM tends to damp the normal stresses perpendicular to the wall, while enhancing the stresses parallel to the wall thus giving a higher value at the centre point of the nozzle [**150**]. The outer regions of all three models predicted similar results due to using a standard wall function and low residual effects at the wall boundaries of the nozzle.

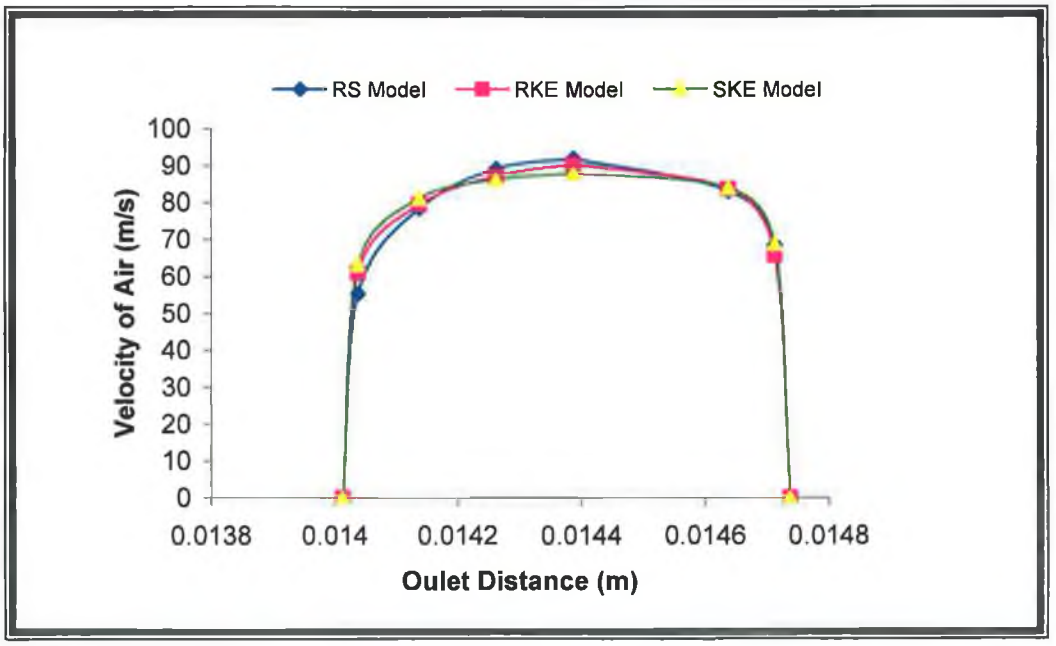

Figure 5.18: Outlet velocity at air pipe of the two-fluid nozzle at 5.48 m/s inlet velocity.

The air nozzle was simulated under the same conditions and standard convergence criteria with different turbulence models (Table 5.6). It has been shown that the Standard K-ϵ, model gives fast and reliable results without much expense of time and memory as it contained the lowest number of equations to compute compared to the Realizable K-ϵ, and RSM model [**179-183**]. The Standard K-ϵ also assumes that turbulence is an isotropic flow region, this assumption sharply reduces the intensity of the calculation, while the

in the more energy required to break-up the feed, and at constant flow rates of feed this produces narrow particle size distributions [**1, 8,10**].

5.4.2 FEED PIPE SIMULATION

For the feed pipe, a peristaltic pump was used to pump the HA slurry through the external two-fluid pipe into the spray dryer. The peristaltic pump was set at different rpm and measured amount of flow was collected using a graduated cylinder. The resulting velocities (Figure 5.19) were used as the initial values for the feed pipe simulation.

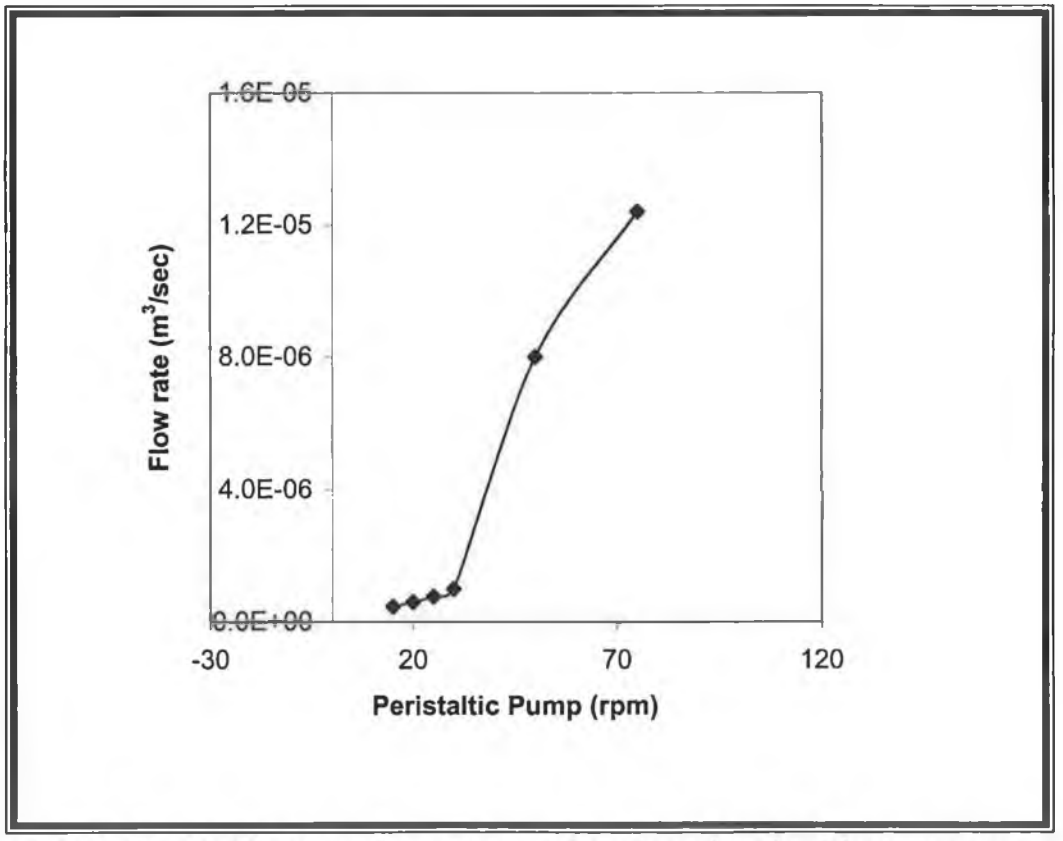

Figure 5.19: Peristaltic pump flow rate as a function of peristaltic pump rpm.

Figure 5.19 shows an almost linear relationship between the pump rpm and the flow rate, as the property of peristaltic pump works on the positive fixed displacement principle. The peristaltic pump use rotating rollers pressed against feed pipe (special flexible tube) to create a pressurized flow and this feed pipe is compressed at a number of points in contact with the rollers to flow the HA slurry through the feed pipe with each rotating motion

However, there is a drastic change of flow rate after 30 rpm, because at the lower rpm, these the rollers slip over the feed pipe.

The exit velocity ranged for the condition 10 to 100 rpm of peristaltic pump provided the inlet feed velocity of 0.163 to 0.694 m/s or a feed rate 10 to 1000ml/min to the spray dryer for drying. Figures D- 6-8 (Appendix-D) show the simulated profiles of velocity of the feed pipe. Again one pump setting (7.6e-7 m^3/s) and its respective flow rate will be described in this section. It has been shown that as the feed flow develops inside the feed pipe, circulation occurs at the sharp edges of the feed pipe (Figure 5.20).

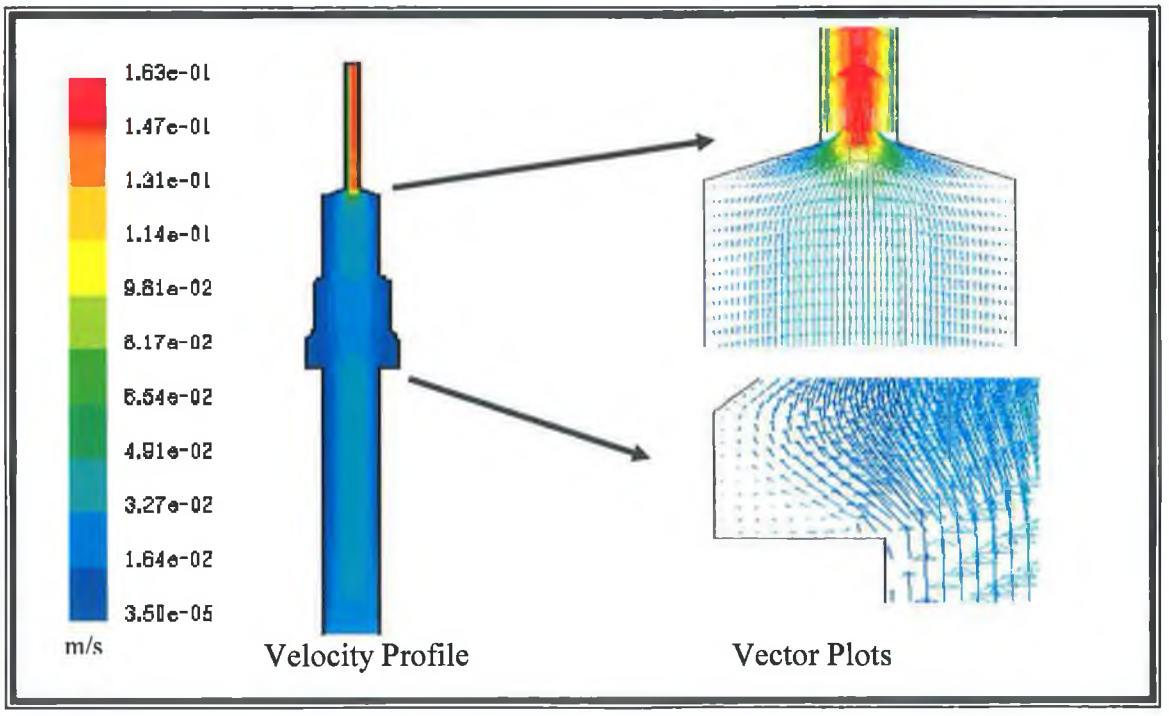

Figure 5.20: The feed pipe velocity profile and vector at 7.6e-7 m^3/s flowrate of peristaltic pump.

The simulation of feed nozzle was simulated under the same conditions and standard convergence criteria using the three different turbulence models (Table 5.7). The RSM predicted the highest velocity (Figure 5.21) at the outlet of the feed pipe and this maybe due to the fact that the feed nozzle is circular and symmetric in shape which is beneficial when modelling with the RSM method, as the convergent part of the nozzle causes the

flow to stabilise [**150**]. The standard *K*-Є predicted reasonable feed velocities with at less expense of computation (Table 5.6) within an acceptable limit.

Table 5.7:- Iterations to Converge the Solution with Standard Criteria for the feed nozzle.

	Number of Iterations		
	S *K*-Є	R *K*-Є	RSM
Feed Nozzle	1082	1545	5026

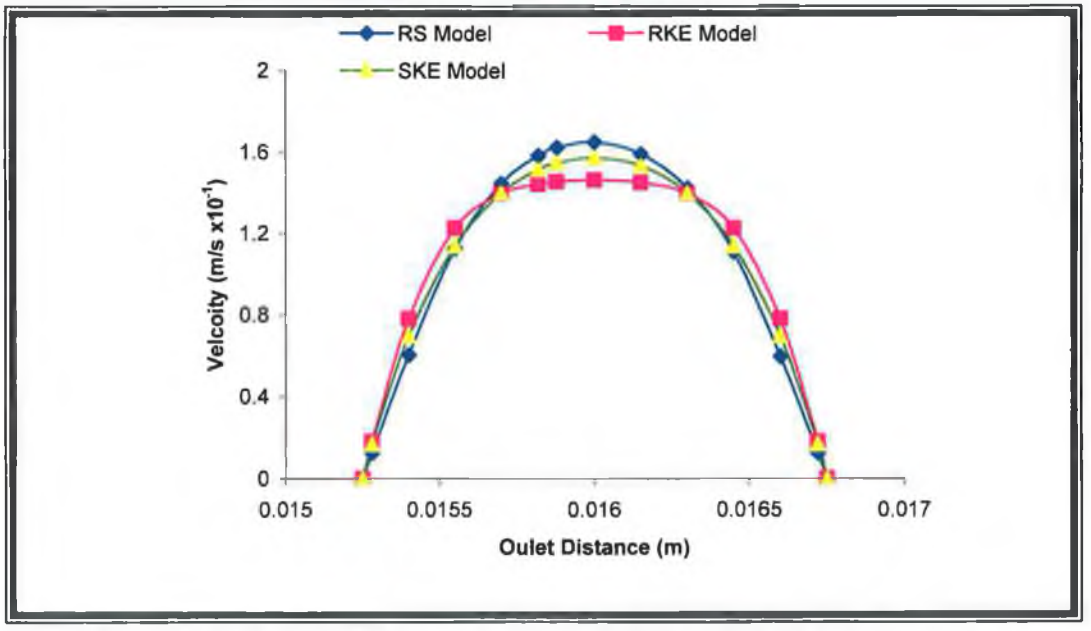

Figure 5.21: Velocity profile at outlet of Feed pipe of two-fluid nozzle.

5.5 TEMPERATURE PROFILE SIMULATION IN THE SPRAY DRYER

In this section, the temperature and velocity distribution of the hot air inside the drying chamber for different conditions (temperature and air velocity) were studied. The three different levels of temperature (398, 421, and 461K) and velocity (12.7, 14.6 and 16.6 m/s) were used to analyse the temperature profile and velocity vector inside the spray dryer. The temperature levels were selected on the basis of temperature range available on the spray dryer and maintained to gives sufficient evaporation. The highest level chosen was 461K, as Luo [**123**] reported that in the spray dryer process the 373 to 473K for HA slurry drying, neither changed the structure of HA nor caused any grain coarsening. The velocity levels were chosen to cover the whole range of hot air velocity available by the spray dryer to find out its effect on flow rate in the spray drying of HA slurry. These models were simulated according to the condition of hot air coming in from the top of the drying chamber. Initially the heat transfer coefficient was found to be 0.25 $W/m^2.K$ for each model, which was in good agreement with the real conditions of the spray dryer [**217**]. Experimentally the spray dryer would be left to heat until the outlet and inlet temperatures reach the set temperatures (for example inlet temperature 398K and outlet temperature 373K) and then spray drying would start, so the simulations were carried out in the same way. The amount of hot air defines how much heat enters in the main drying chamber and its profile gives an idea of where evaporation occurs inside the dryer. The velocity vector shows the circulation and movement of the hot air, which would both directly affect the quality of the dried product and be responsible for the evaporation of the liquid. For all of these inlet conditions, the drying chamber was simulated using the three turbulent models, Standard K-ϵ, Realizable K-ϵ and RSM and later these were compared experimentally to predict the best results.

Figure D 9-16 (a) in Appendix-D shows all of the results simulated for the temperature and velocity levels. Figure 5.22 shows an example of one of these results inlet temperature for 398K at a hot air velocity of 12.7 m/s. Table 5.8 shows the temperature the found at different zones (see Figure 5.22 (a)) in the chamber where different velocities were used.

The temperature profile results for each inlet temperature (398K) and increasing velocity (12.7, 14.6 and 16.6m/s), showed that the hot region increased with an increased in velocity. The temperature profile for the Standard *K*-Є method at a velocity 12.7m/s, showed the hot region developed from the inlet point to Zone A axially downwards while this region increased to Zone B when the velocity was increased to 14.6m/s; and to 0.7m (Zone B) with the increase of hot air to 16.6m/s. The Realizable *K*-Є method for the same conditions was slower to develop, with the hot region ending at 0.2m and remaining in Zone A upto 16.1m/s. Whereas the RSM method hot region started in Zone B and increased with higher velocity but not to the same extent as that for the standard *K*-Є method results. A similar observation was found when the temperature input was increase from 398 to 421 and 461K for all three models. This shows that the temperature profile is dependent on the velocity vector, as the velocity vector carries heat from the source. However, along the axis of the spray dryer, the temperature gradient line is almost same by these turbulent models (Figure 23). The temperature of central axis area is an important as major drying process of HA droplet was done there. Figure 5.23 shows R*K*-Є predict the temperature gradient along the axis is highest as compared with RSM which has the lowest due to narrow temperature distribution.

Figures D 9-16 (b) in Appendix-D show that the velocity vector increased from its inlet velocity 12.7, 14.6 and 16.6m/s at the constant temperature in each S*K*-Є, R*K*-Є and RSM models respectively. It has been shown that the inlet hot air is responsible for the distribution the heat inside the spray dryer, which affects the movement of the spray dried particles. In the Standard *K*-Є method, (Figure 5.24) a maximum vector of 23.8 m/s was attained at the outlet of the spray dryer and had three circulations regions; one at the corner of the roof and two on side the walls of the spray dryer. The Realizable *K*-Є had a maximum vector 22.2m/s (Figure 5.25) and again three circulations with one more dominated at the corner of the spray dryer. Whereas the RSM, had a maximum vector of 24.5 m/s (Figure 5.26) at the outlet, but due to its narrow distribution velocity down the

centre of the chamber, the three areas of circulations were located in different regions to that found in the Standard *K*-Є and Realizable *K*-Є methods.

The temperature profile produced was quite different in each of the three turbulent models; Standard *K*-Є, Realizable *K*-Є and RSM methods. Inspite of the different turbulent models, the temperature profile depended on the flow rate of the hot air. At an inlet hot velocity of 16.6 m/s (Figure D-10, 13 and16 (a) Appendix-D) a maximum wide distribution of temperature resulted regardless of inlet temperature, however, at 12.7 m/s a minimum distribution was found. For fast and uniform drying, it is recommended [**86,90,123,148**], to have a uniform temperature profile and more turbulent hot air flow, so on this basis the hot air at 16.6 m/s velocity and inlet temperature 461K would give the best drying rate of HA slurry. The temperature profile using the Realizable *K*-Є method was selected for the atomisation of the HA slurry as its temperature profile was more uniform, less computational expensive and incorporated swirl motion [**82,84**] as will be shown in section 5.6.

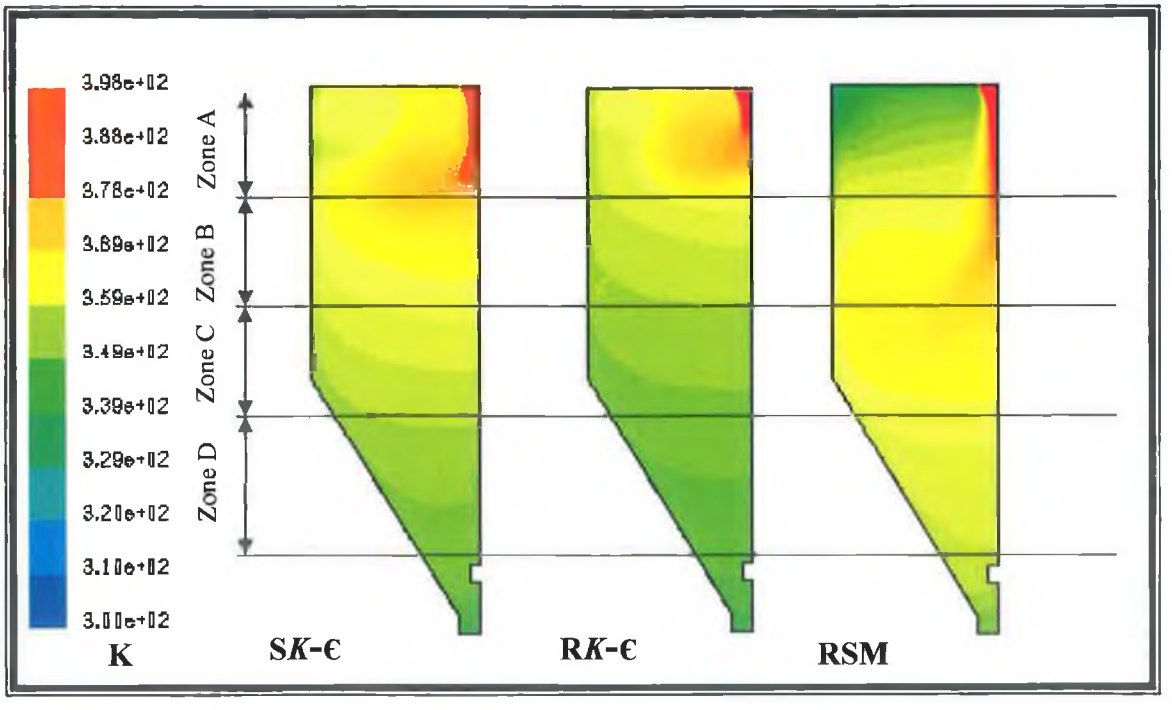

Figure 5.22: Temperature profile by S*K*-Є, R*K*-Є and RSM methods (inlet condition Temp-398 K, velocity-12.7m/s).

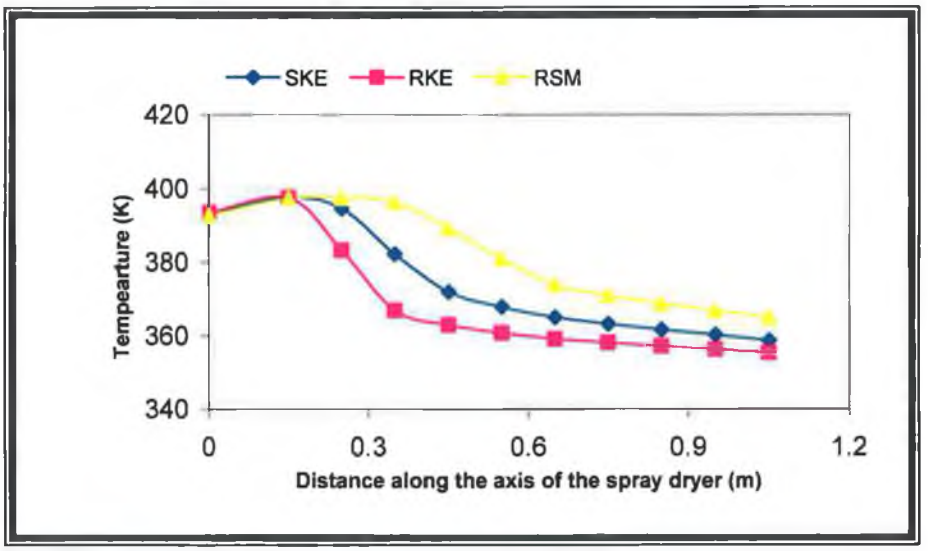

Figure 5.23: Temperature gradient along the axis of the spray dryer (inlet condition; temperature 398K and Velocity 12.7m/s).

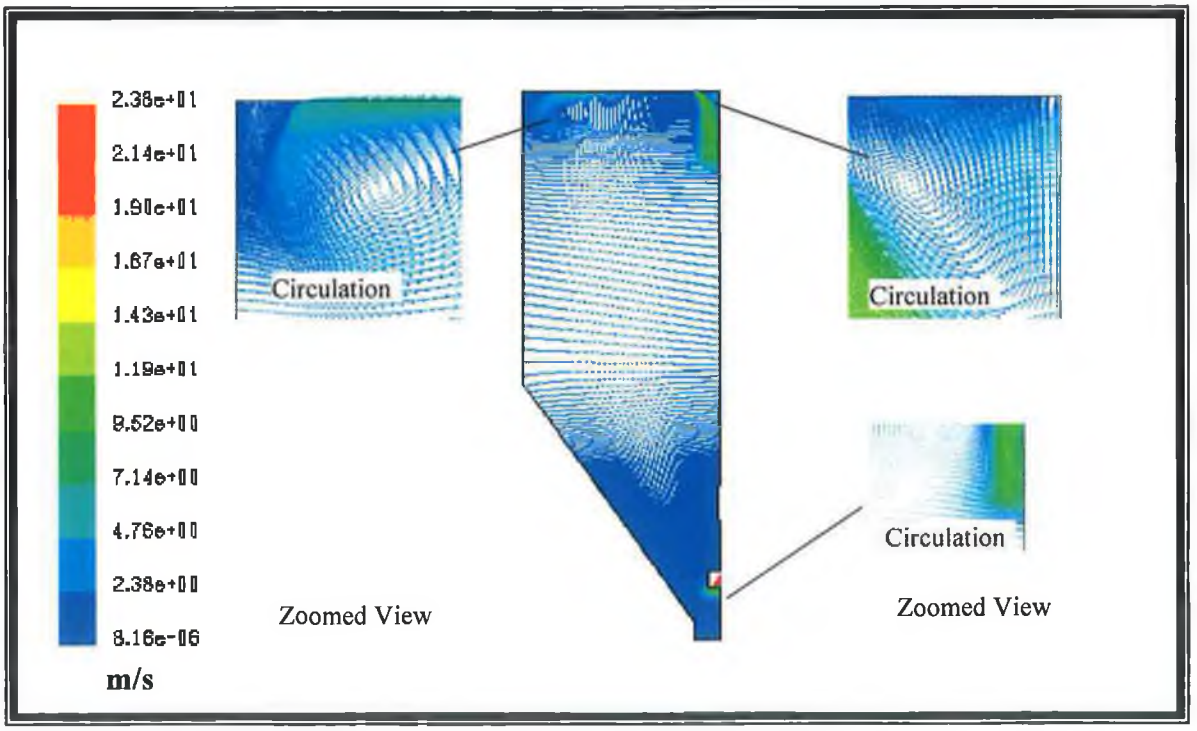

Figure 5.24: Velocity vector using the SK-ϵ methods (inlet condition Temp-398 K, velocity-12.7m/s)

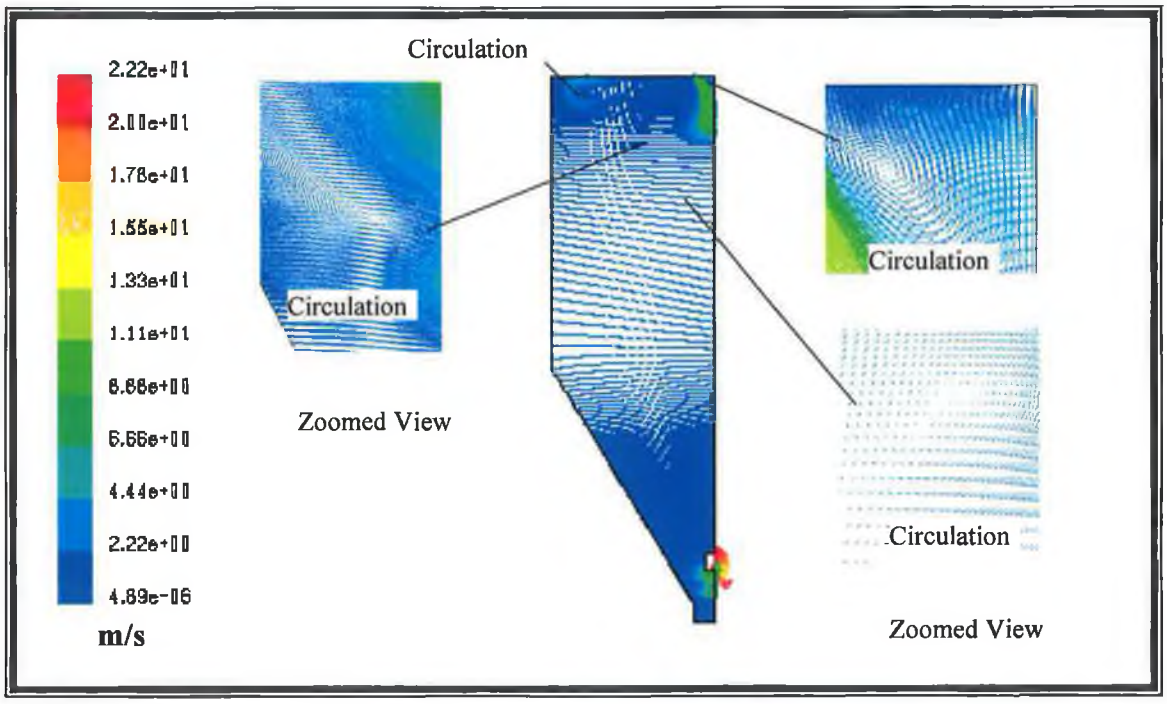

Figure 5.25: Velocity vector using the R*K*-Є method (inlet condition Temp-398 K, velocity-12.7m/s)

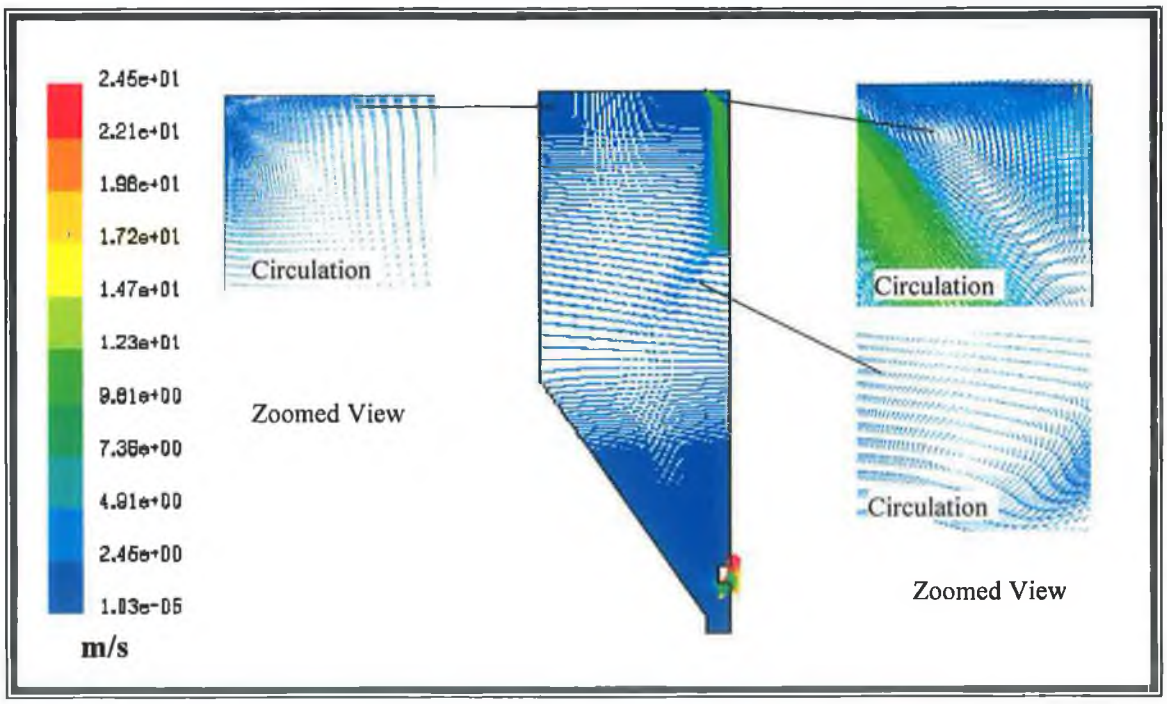

Figure 5.26: Velocity vector by RSM method (inlet condition Temp-398 K, velocity-12.7m/s)

Table 5.8: Mean zone temperatures found for varying hot air velocities.

Hot air Velocity	Zones	Input Temperatures (K)								
		Setting 398K			Setting 421K			Setting 461K		
		S*K*-ϵ	R*K*-ϵ	RSM	S*K*-ϵ	R*K*-ϵ	RSM	S*K*-ϵ	R*K*-ϵ	RSM
12.7 (m/s)	A	378	369	388	380	393	403	421	429	439
	B	355	350	365	371	370	383	403	395	417
	C	350	344	362	366	361	376	386	386	403
	D	345	341	352	359	356	364	379	376	401
14.6 (m/s)	A	384	376	384	387	396	406	424	433	440
	B	368	364	369	379	382	394	408	403	421
	C	362	354	364	376	371	387	394	388	406
	D	357	351	356	371	368	376	380	379	388
16.6 (m/s)	A	386	374	392	399	399	409	434	433	446
	B	374	369	372	389	392	394	415	418	423
	C	367	359	370	377	384	391	396	403	410
	D	362	355	363	374	379	376	388	396	395

*** Range of standard deviation ± 2.75 to 4.50.**

5.6 ATOMISATION SIMULATION

In the preliminary test runs of the spray dryer, it was found by visualization, that at the 30 rpm speed peristaltic pump and 75% atomising yields a complete spray in this specific case of spray dryer. These parameters where fixed to look at the other parameters of spray dryer, to determine how the particle size and spray dryer performance affects; like viscosity, temperature and hot air flow rate. It was decided to look at this because little because much literature is available about the spray formation and the affect of feed and atomising energy [**1, 3-6**]. The boundary conditions chosen for the atomisation simulation of the 25 mPa.s viscosity of HA slurry is given in Table 5.9 and HA slurry properties with injection properties are given in Appendix-D.

Table 5.9: Boundary conditions used for atomisation simulation (HA slurry of 25 mPa.s).

Hot Air Mass flowrate (Kg/hr)	**Air Temperature (K)**	**Total Spray Rate (kg/s)**	**Feed Temperature (K)**	**Feed Density (Kg/m^3)**	**Pressure Outlet (Pa)**
80	461K	4.730×10^{-4}	300K	1134.85	101325
Air Radial Velocity (m/s)	**Air Axial Velocity (m/s)**	**Air Nozzle Axial (m/s)**	**Air Radial Velocity (m/s**		
13.85 m/sec.	8.0 m/sec	54.6	16.6		
Chamber Wall thickness (m)	**Wall Material**	**Wall Heat Transfer Coeff. (W/m^2K)**	**Air temperature outside wall (K)**	**Injection type**	**Evaporating species**
0.01	AISI-316 Steel	0.25	300K	Air blast atomizer	H_2O
Spray Model	**Spray Angle (degrees)**	**Relative Velocity of Atomisation**	**Sheet constant**	**Turbulent Dispersion**	**Interaction B.C(wall and droplets)**
Droplet collision, Break-up and Wave Models	-22.5	85	12	Stoichastic and Random Eddy models	Escape*

*Indicates that the particles are lost form the calculation domain the point of impact with the wall.

In the atomisation model, the simulation was carried out at 461 K and the hot air velocity inlet 16.6 m/s at three levels of viscosities (25, 50 and 75 mPa.s) at constant atomising energy (5.48 m/s inlet velocity pressure and the feed flow rate 4.730×10^{-4}) to compute the particles drying histories (Figures 5.27-5.29). The graphs represent droplets diameter,

evaporation and temperature of droplets at different atomisation time such as, 0.1, 0.2 and 2 seconds. It is clearly shown that at viscosity has a great impact on the atomisation, initial particle distribution, and evaporation rate. The atomisation time at 2 seconds and 25, 50 and 75 mPa.s, HA slurry viscosities, produce minimum droplets diameter of 2.13, 2.24 and 12.7 μm. it is quite understandable, the higher viscosity needs more energy to break down the slurry sheet into fine droplets [**210**]. The model also show the particles hitting the conical wall, due to turbulent the hot air flow rate and also due to stoichastic effects during the particle trajectories [**123,124**].

The atomisation model predicted (Figures 5.27- 5.29) the evaporation rate of HA slurry at viscosity of each 25, 50 and 75 mPa.s for a time of 2 seconds to be 1.34×10^{-8}, 2.79×10^{-9} and 1.7×10^{-9} kg/sec respectively. The rate of evaporation decreased with an increase in viscosity because the HA slurry viscosity was produced at the varying contents of water; such as at 75 mPa.s, the HA slurry density was 1180.35 kg/m^3 compare to 1134.85 kg/m^3 at 25 mPa.s, thus the at 75 mPa.s slurry had a higher solid content. In this research, only the simulation results were presented, a validation was not possible due to lack of funds to purchase high powdered equipment. Each atomisation model of the three levels of viscosities (25, 50 and 50 mPa.s) (Figures 5.27-5.29), showed that the evaporation rate was higher initially and then reduced because the drying of the droplets was carried out in two stages. First, at the saturated condition; as long as this lasts evaporation can be maintained at a constant rate and is known as the first period of drying [**1**]. When the moisture content reaches a critical point, the evaporation rate becomes dependent on the moisture diffusion through the dried surface shell and lowered by the evaporation rate and this is called the falling rate of or the second period of drying [**1,26**].

The particles temperature in the atomisation model, at all three levels of viscosities (25, 50 and 75 mPa.s) increased with time as evaporation rate slowed down and the particles dried out (Figures 5.27-29 (c)). For an example in Figure 5.27, temperature of few particles above the boiling point of water before collection. It showed these particles were completely dried out and still in contact with the hot air as the temperature can be exceed the boiling point depends upon the heat balance between the convective heart transfer rate

form air and heat absorption due to evaporation [**177**]. However, for HA dried particles, temperature upto 473K could be quite saved as no decomposition of HA phase was reported [**129,138**].

In this simulation the drying model used was already built-in into the FLUENT software. When compare with other models (polynomial secondary drying rate) in the atomisation, it was reported that the built-in model in FLUENT possibly over-estimates the drying rate in the falling rate period because the droplet is only dried fully if the surrounding temperature is higher than its the boiling temperature [**217**].

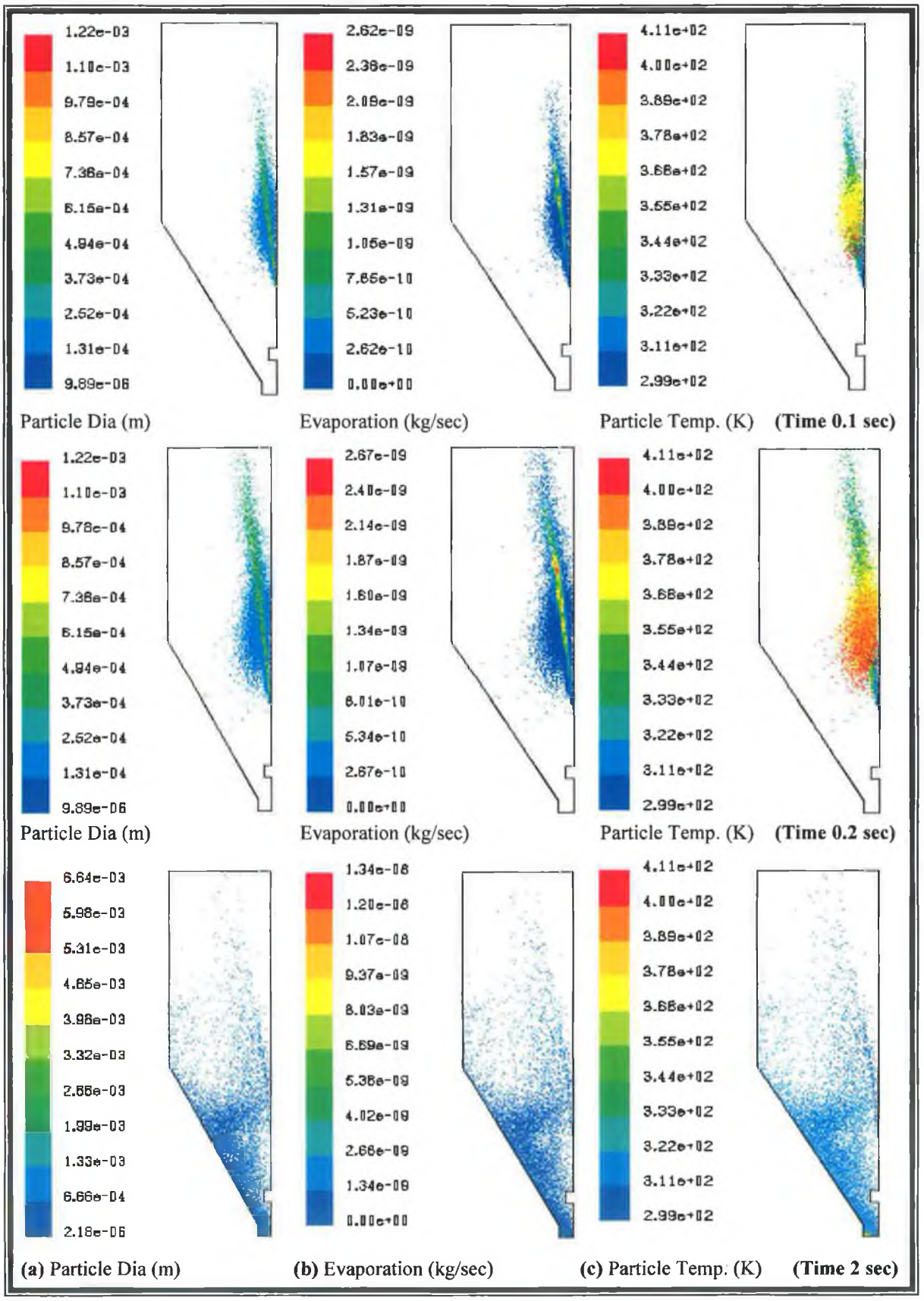

Figure 5.27: Particles diameter, evaporation and temperature of HA slurry (Viscosity 25 mPa.s) atomisation at the hot inlet temperature 461K and flowrate 16.6 m/s.

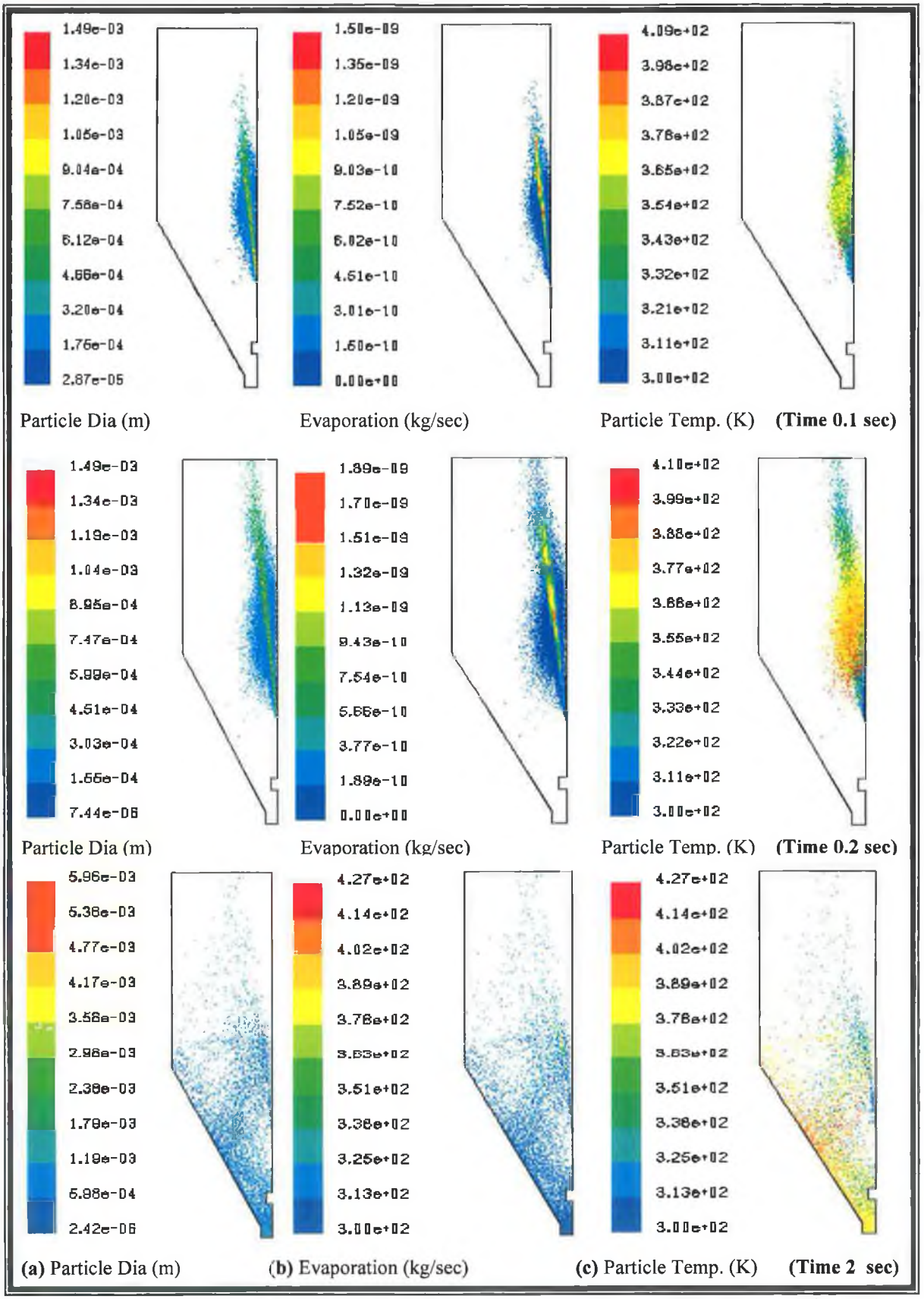

Figure 5.28: Particles diameter, evaporation and temperature of HA slurry (Viscosity 50 mPa.s) atomisation at the hot inlet temperature 461K and flowrate 16.6 m/s.

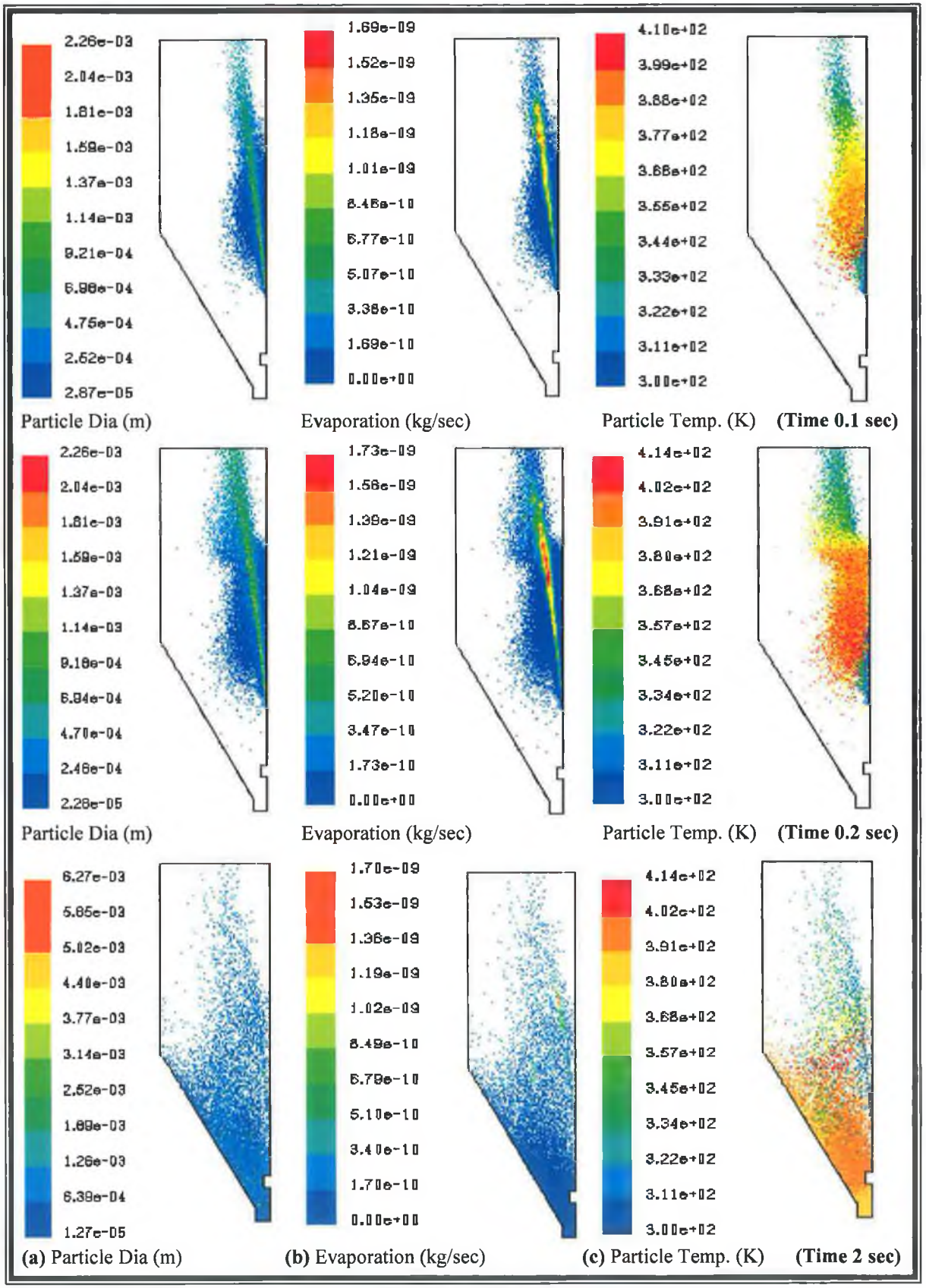

Figure 5.29: Particles diameter, evaporation and temperature of HA slurry (Viscosity 75 mPa.s) atomisation at the hot inlet temperature 461K and flowrate 16.6 m/s.

5.7 THE EXTERNAL TWO-FLUID NOZZLE COMPARISION

This approach to compare of air pipe of the external two-fluid nozzle was used because experimental results could not be measured in the nozzle, so the simulated output results of the air nozzle were applied as input results onto the drying chamber model. In the comparison model, initially a half axis symmetrical model was analysed but the results did not converged due to sharp quadrilateral cell shapes near the inlet velocity point which caused residuals during the start of the simulation and caused errors during the calculations in each turbulence model. Many attempts were made to converge the simulations however none succeeded. Then a full model was constructed and the same conditions were applied, this gave predicted results and a convergent solution, achieved in both steady and unsteady states.

The air pipe comparison procedure was applied at the different atomising pressures, where the air velocity (outputted from the nozzle model) was measured for a series of distances from the exit point and compared to similar simulated results in a model that contained the drying chamber. The velocity experimental results found for the top of spray dryer were compared simultaneously to the results found at the same position in the model. Figure 5.30 shows the simulation of the velocity vector at different inlet velocities (2.19, 2.95, 3.65, and 4.38 m/s) of the external two-fluid nozzle by according to the standard K-ϵ method. The results show that the maximum velocity for the 2.19, 2.95, 3.65, and 4.38 m/s inlet velocities were 33.3, 415 and 48.6 m/s respectively found at nozzle tip. These velocities decreased as the air flowed from the bottom to the top of the chamber. At 2.19 m/s inlet velocity, the air only travelled approximately one third of the way up the chamber, where as the remaining atomising pressures forced the air up into the final third of the chamber, the region where heating occurs. This means these atomising pressures give sufficient kinetic energy to the feed particles to travel into the hot region of the spray dryer.

Figure 5.31 shows the velocity vectors at 5.48 m/s inlet velocity of the nozzle using the three turbulence models; Standard K-ϵ, Realizable K-ϵ, and RSM methods. The aim here was to identify which model provided the best results without compromising on

computational time. All of these simulations were carried out in unsteady states for a constant time of 2 minutes (Table.10).

It was observed that the Standard K-ϵ method, provided a velocity profile much closer to natural phenomena as compare to the Realizable K-ϵ and RSM methods. The Realizable K-ϵ, and RSM methods a velocity vectors diverted away from the axis up to 2 minutes, but for longer time durations (20 minutes) the velocity vector showed much similar results that of the Standard K-ϵ, velocity profile (Figure 5.32). Therefore it was obvious that these turbulence methods; the Realizable K-ϵ, and RSM have more parameters to calculate hence the results were much more sensitive. Again, one can say that the Standard K-ϵ method gave fast and more accepted results in the terms of velocity vector, even if the model misses other important fluid parameters like shear, skin stress and wall function which can be predicted by more rigorous turbulence models (R K-ϵ and RSM).

Table 5.10:- Iterations to Converge the Solution with Standard Criteria for the air nozzle.

Number of Iterations			
	S K-ϵ	R K-ϵ	RSM
Feed Nozzle	3412	4954	15456

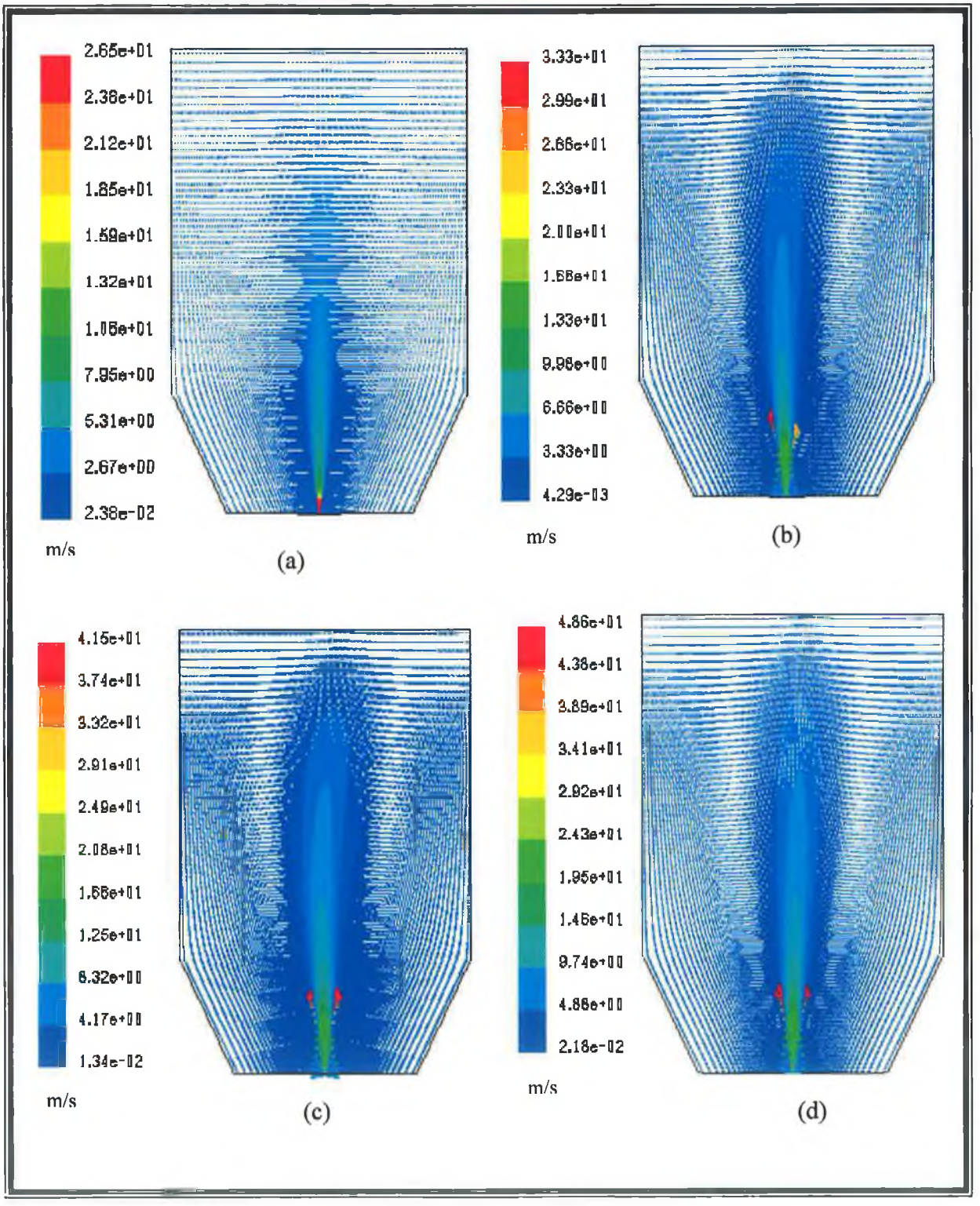

Figure 5.30: Velocity vector (at 2 mins unsteady simulation) at (a) 2.19 (b) 2.95 (c) 3.65 and (d) 4.38 m/s inlet velocity (by S *K*-Є method) in the spray dryer to compare the nozzle exit velocity.

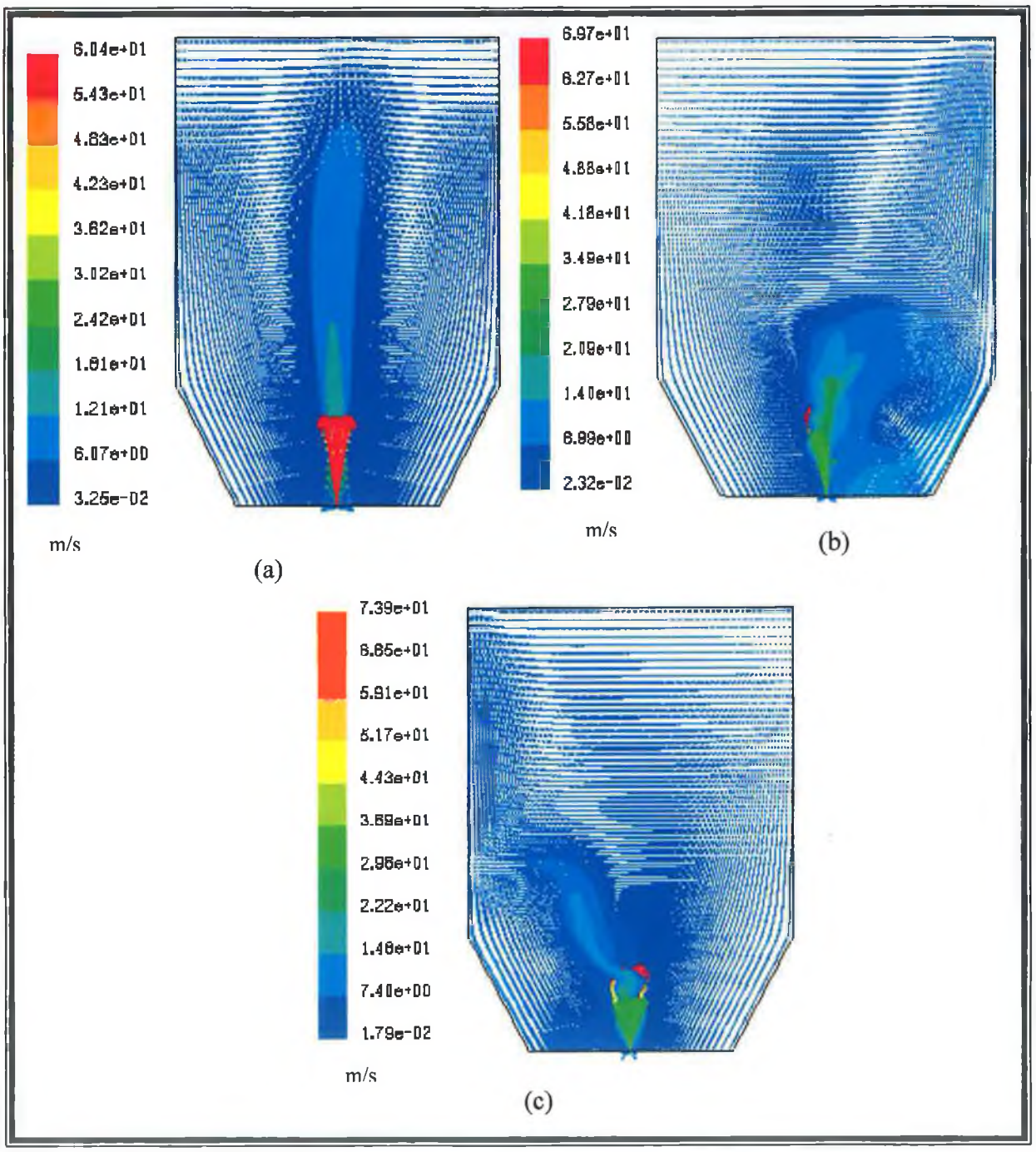

Figure 5.31: Velocity vector and profile at 5.48 m/s inlet velocity the nozzle (for 2 minutes (a) S *K*-Є (b) RSM, and (c) R *K*-Є method) in the spray dryer to compare the nozzle exit velocity.

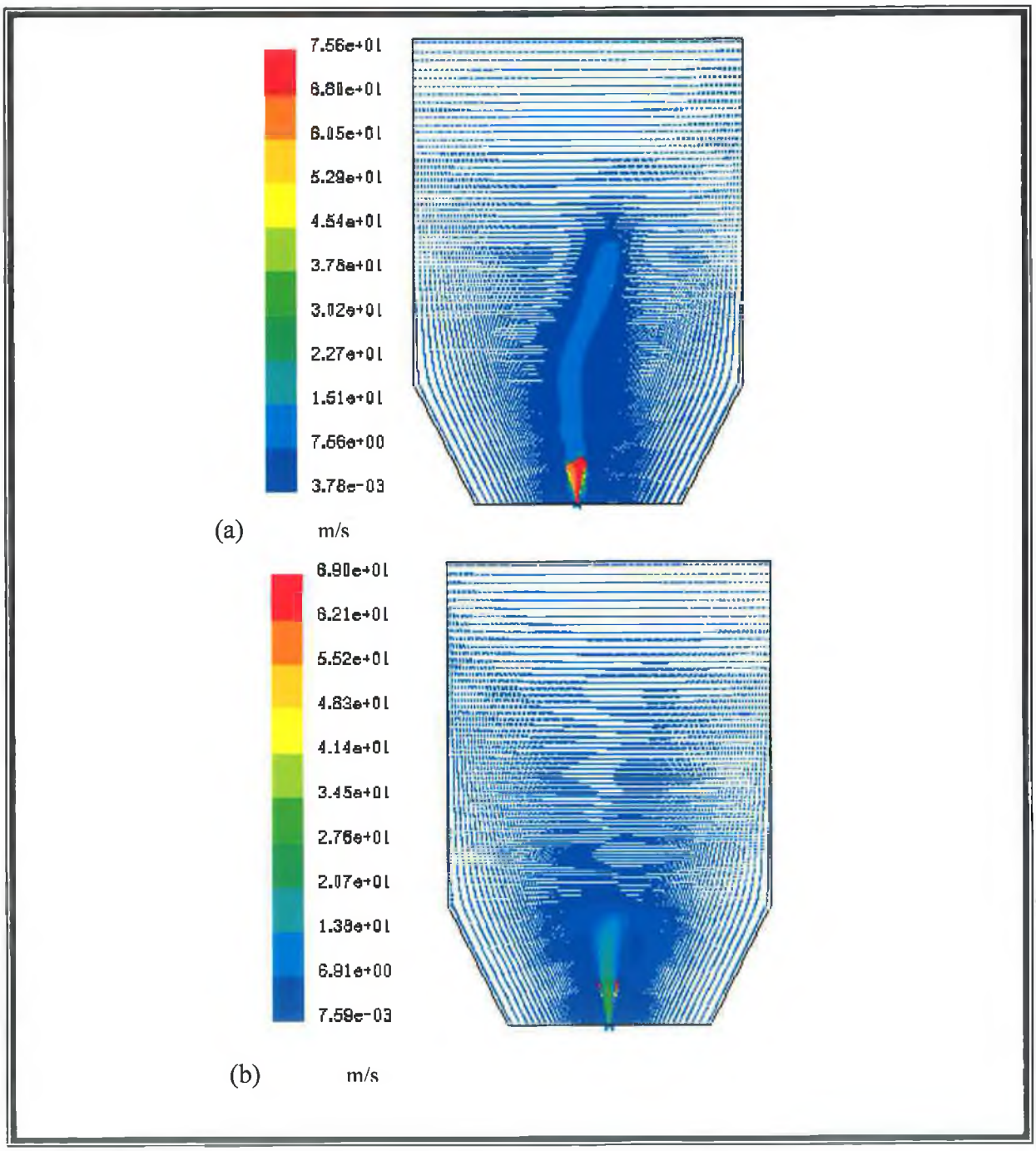

Figure 5.32: Velocity vector and profile at 5.48 m/s inlet velocity the air pipe nozzle (for 20 minutes (a) R *K*-€ and (b) RSM method) in the spray dryer to compare the nozzle exit velocity.

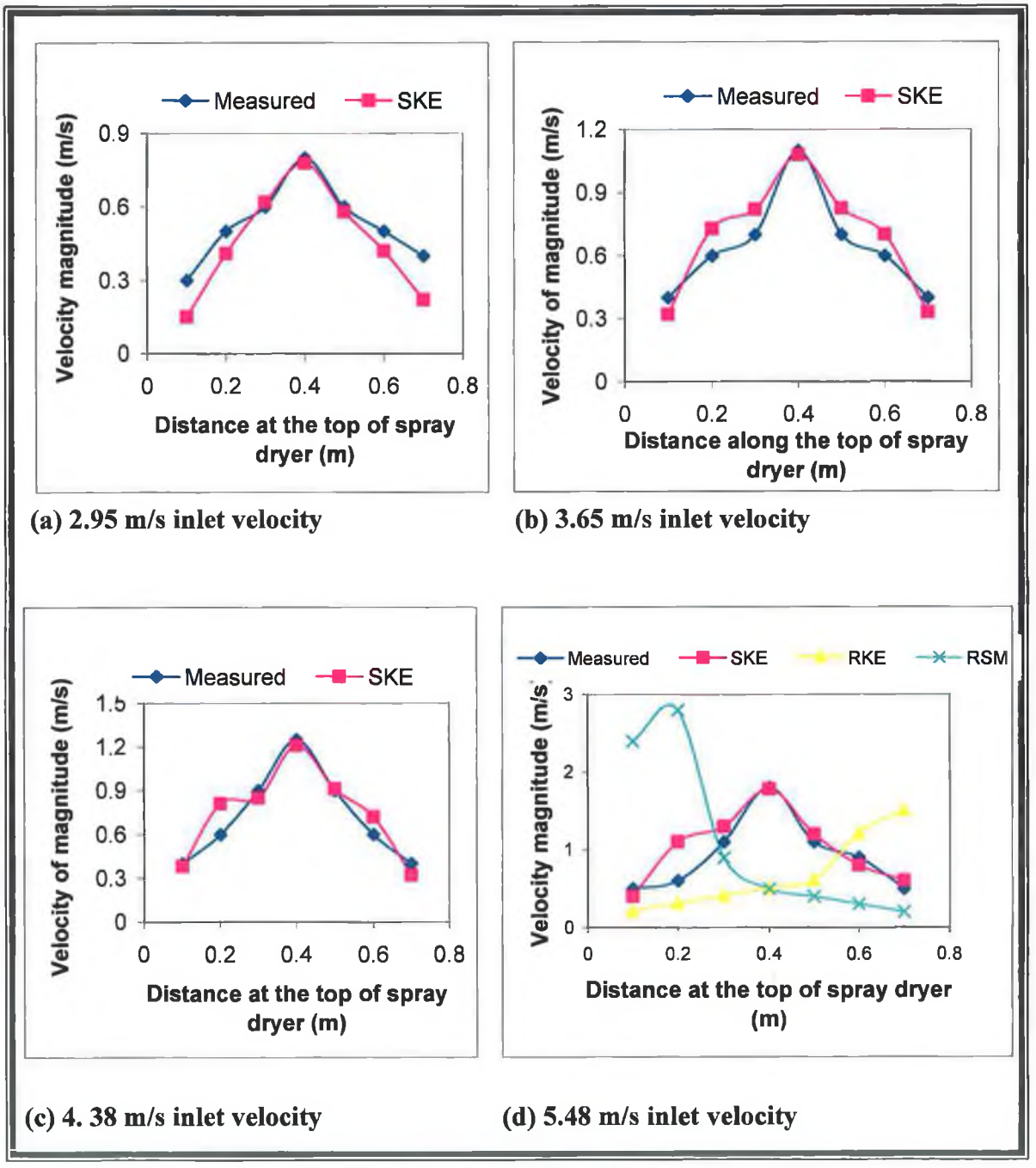

(a) 2.95 m/s inlet velocity **(b) 3.65 m/s inlet velocity**

(c) 4. 38 m/s inlet velocity **(d) 5.48 m/s inlet velocity**

Figure 5.33: Velocity Profile at the Top of Spray Dryer.

Figure 5.33 shows the measured (experimental data) and simulated velocity profile at the top of spray dryer chamber. The measured profile gave a smooth profile as compared to the simulated. It can be clearly seen that the velocity profile were not the same as those

measured, however, the maximum velocity at the centre was the same for all the conditions of atomising pressure. The profile changed due to the local turbulence factors, as the models predicted the high Re to low Re number from the inlet point of velocity (exit point of nozzle) to the top of the spray dryer. Figure 5.33 (d) shows the three turbulence model and measured velocity profile at 5.48 m/s inlet velocity. The Standard K-ϵ is quite similar to that of the measured pattern of velocity but Realizable K-ϵ and RSM produce quite different profiles at the top of the spray dryer as the nozzle air velocity jet drifts towards one side of spray dryer wall (Figure 5.31).

Figure 3.34 shows the comparison between simulated and measured velocity from exit of air nozzle pipe to open atmosphere along the axis of it. It shows both simulated and measured air velocity is the same falling trend. Distance from the exit point of the nozzle to 0.3 m, the falling trend is very close to each other, however after 0.3m from the exit tip of the nozzle, the gap is wider that due to local disturbance [**183**]. In Figure 3.34 (d) shows the Standard K-ϵ is quite similar to that of the measured pattern of velocity but Realizable K-ϵ and RSM produce quite different profiles after 0.3m from the exit of air pipe nozzle the nozzle air velocity jet drifts towards one side of spray dryer wall.

The errors found in the results may be due to some leakages in the system when the experimental equipment was used and to limitations in the Relizaible K-ϵ model. The model shows that the feed and air combination velocity becomes steady with time. Differences between the profile of the model results and the experimental results may be associated with external disturbances not simulated in the model. It must be noted that the simulated results compared here to the experimental results are a combination of three models (air, feed and chamber model). Hence inaccuracies would build up in each model; therefore the final results are credible. The model however can demonstrate the spray profile leading upward (due to kinetic energy) towards the roof of the dryer and circulates towards the side walls at the top of spray dryer.

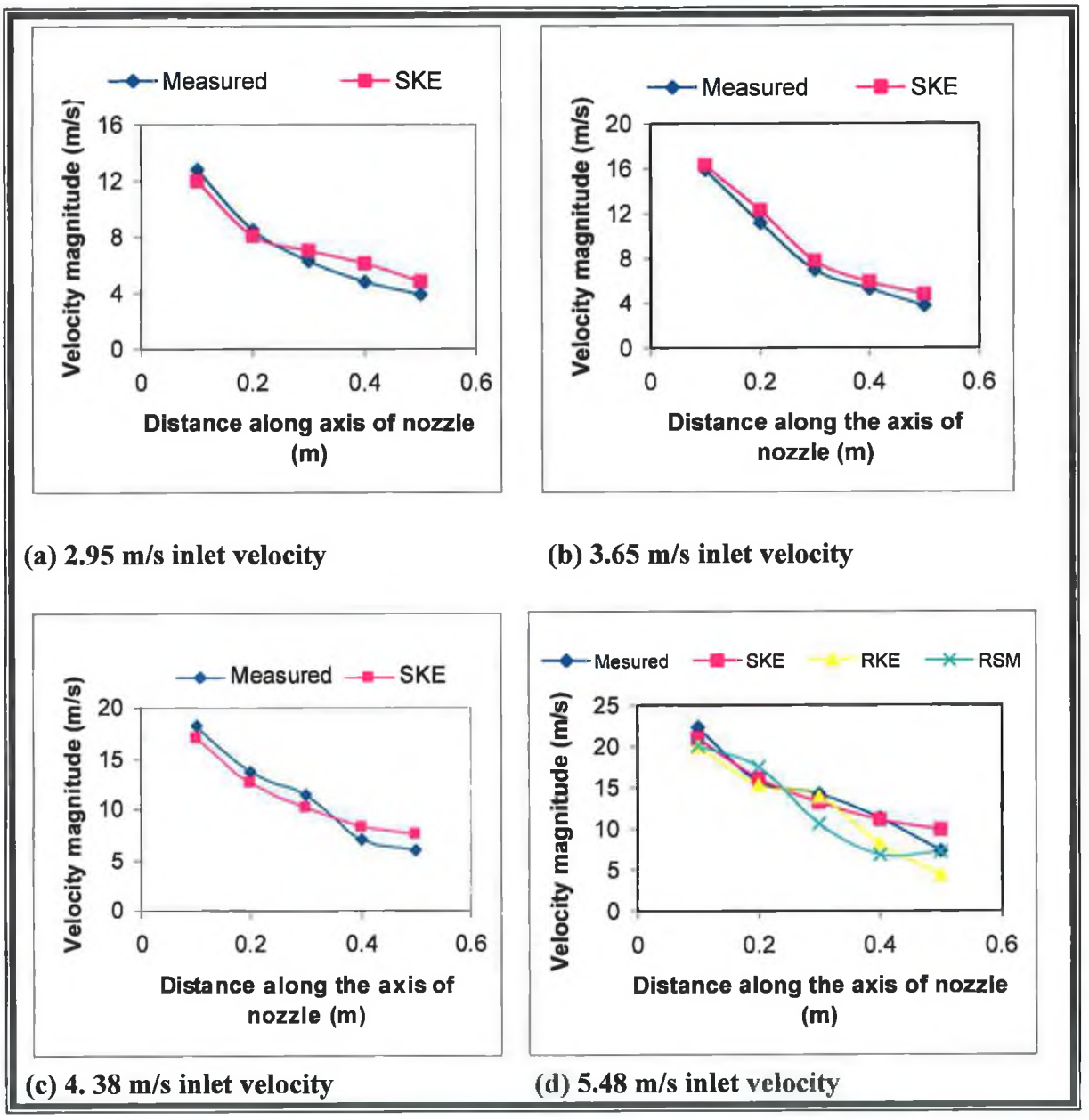

(a) 2.95 m/s inlet velocity

(b) 3.65 m/s inlet velocity

(c) 4. 38 m/s inlet velocity

(d) 5.48 m/s inlet velocity

Figure 5.34: Velocity profile along the axis of air nozzle pipe.

5.8 TEMPERATURE PROFILE COMPARISION

Figures D9-16 in Appendix-D shows the temperature results measured experimentally at different points in the chamber (Figure 3.12). Figure 5.35 shows the results found for an input temperature and velocity of 398K and 12.7 m/s respectively. Results (a) to (e) show the temperatures found going from the top of the chamber towards the two nozzle assembly, at for different positions in the chamber as described in Figure 3.12. The results (experimentally and simulated) all decreased from the top of the chamber towards the nozzle.

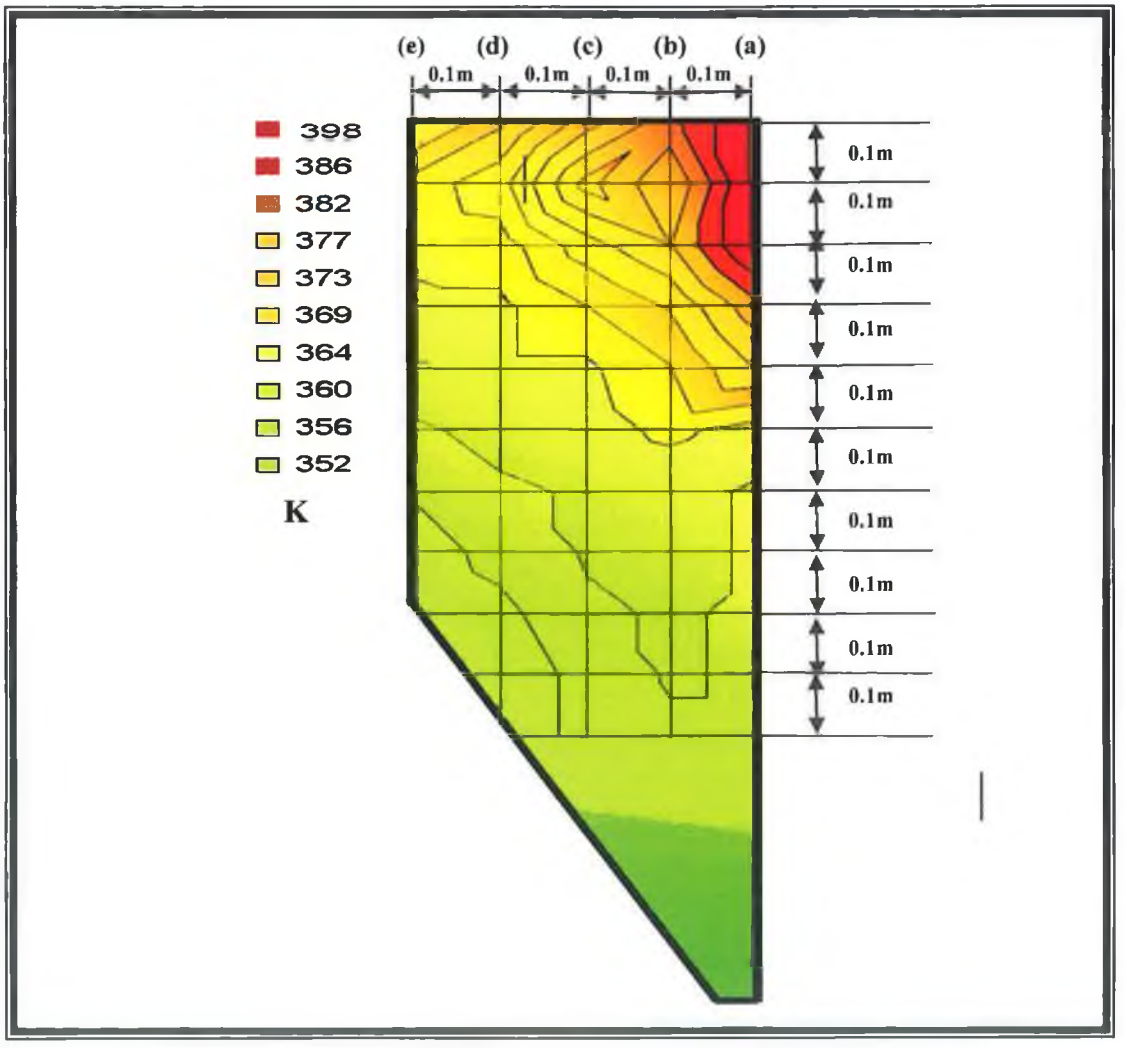

Figure 5.35: Temperature profile measured experimentally (inlet condition tem-398 K, velocity-12.7m/s).

The Measurement results and the simulation results did not differ by a major amount (maximum difference was approximately 20%). The major difference in temperature profiles was found particularly at the inlet point of the hot air. However, at the middle part

of drying chamber each model produced results close in range to that found experimentally (Figure 5.37). The measured values at the top of spray dryer were much higher in all cases as hot air comes down from the top. But at the middle section of the drying chamber, the measured values were very close to the simulations values. Many researcher have [**157-161**] shown the temperature profile to be in good agreement with the Standard K-ϵ method, but this method does not simulate swirl movement which is common in the spray drying processes to disperse the feed spray more uniformly in contact with the hot air [**144, 150,153**]. To incorporate the swirl inside the spray dryer, one has only two options; the Realizable K-ϵ and RSM method, however the Realizable K-ϵ method provides more promising results [**177**]. Though the Reynolds stress model (RSM) is the most descriptive turbulence model, the reliability of RSM predictions is still limited by closure assumptions (modelling of the pressure-strain and dissipation-rate) employed by the model [**185,190**]. Thus why the RSM may not always yield results that are clearly superior to the Standard K-ϵ and Realizable K-ϵ models in all classes of flows, to warrant the additional computational expense.

Figure 5.22 shows that the Standard K-ϵ and Realizable K-ϵ produced results are close to that found from the experimental data. The Realizable K-ϵ method simply combines the Boussinesq relationship and an eddy viscosity definition to obtain the normal Reynolds stress in an incompressible strained mean flow, and its eliminates the few deficiency that exist in the Standard K-ϵ method like the prediction of the spreading rate for axisymmetric model [**181**].

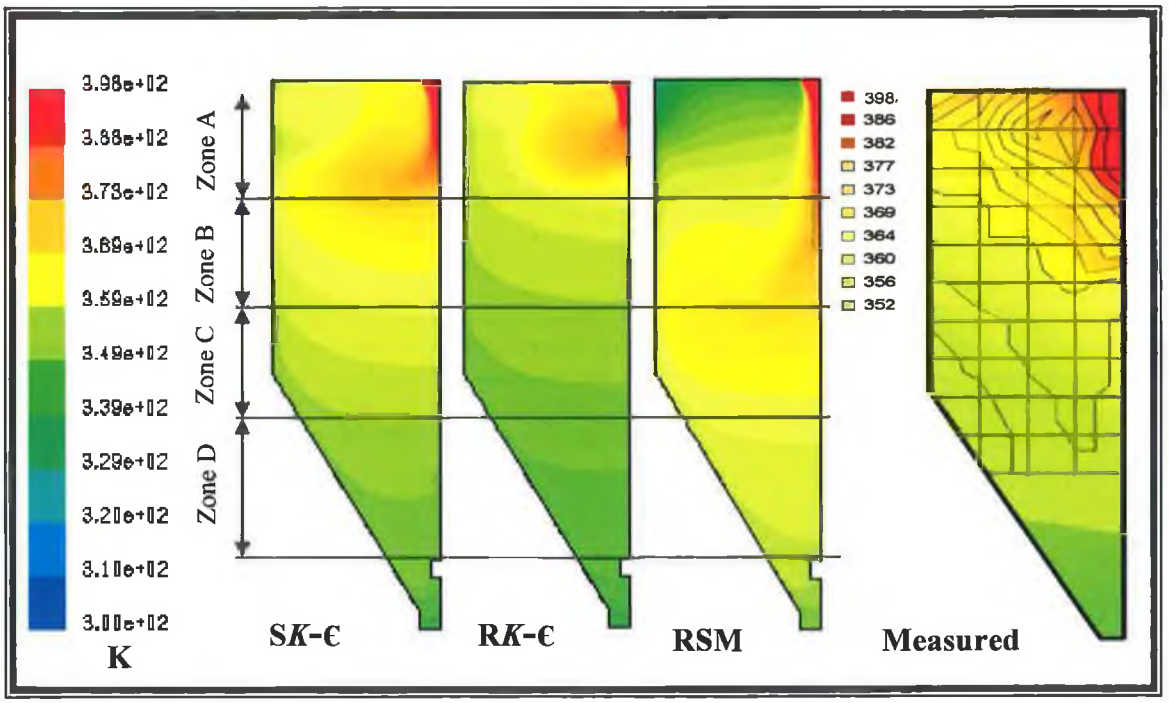

Figure 5.36: Temperature profile by S*K*-ϵ, R*K*-ϵ and measured (inlet condition tem-398 K, velocity-12.7m/s).

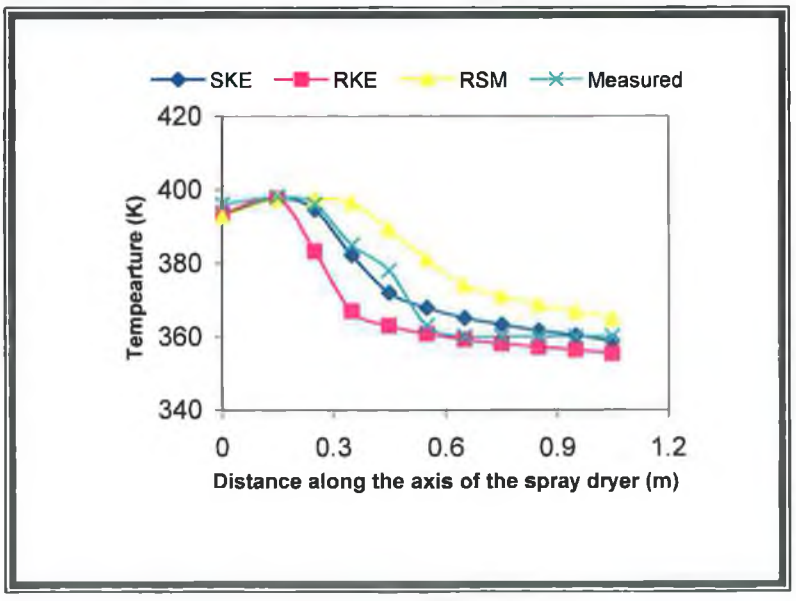

Figure 5.37: Comparison of temperature gradient along the axis inside the spray dryer (inlet condition; temperature 398K and Velocity 12.7m/s).

5.9 ATOMISATION COMPARISION

Figure 5.38 shows the comparison of mean particle size of spray dried HA powder with the simulation of atomisation at three different viscosities (25, 50 and 75 mPa) and same spray dryer drying conditions (hot inlet air temperature 461K and flow rate 16.6 m/s).Both the results show mean particle size increase with the increase of HA slurry however simulated atomisation mean particle size is higher than experiment value at all three levels of HA slurry. It shows the simulated mean particle size is over estimated with the experimental data. Difference in these two results may be modelling assumption of droplet drying, spray drying time of simulation (a short duration due to computer limitation) and measurement of spray dried of HA powder in master-size analyser. The atomisation model assumed all particles were spherical which was not the case in the experiments as monographs showed the HA powder was the mixture of solid and doughnut shape. The doughnut shape powder may collapse in the preparation of the sample for particle size analyser. In the droplet drying model, the secondary drying or falling drying rate estimated the heat and mass transfer due to connective boiling of the discrete phase droplet when the temperature of droplet was reached the boiling point as long as the mass of the droplet exceeded the non-volatile fraction of water in the HA powder. This model assumption gave fast evaporation and drying of all moisture form the HA droplet that may cause earlier drying and gave the higher mean particle size [**217**]. However, with these limitations, the atomisation can give an estimation of mean particle size of spray drying process.

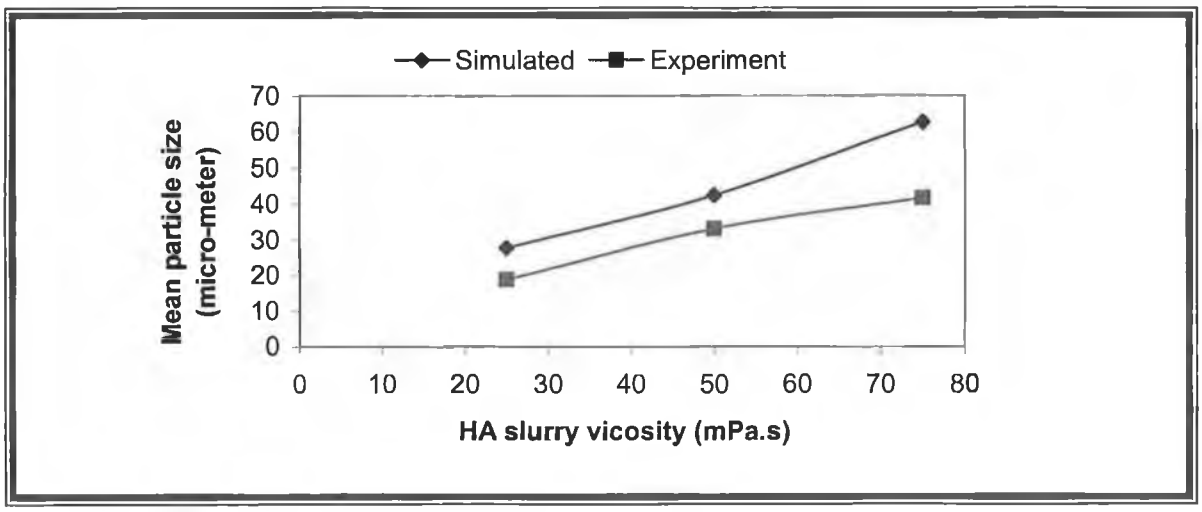

Figure 5.38: Comparison of mean particle size of simulated and experimental data of spray dried HA powder.

In Figure 5.28 (b), the particles reach the top of the roof of the spray dryer at the time 2 seconds. If these particles were not dried out completely, then there would be a chance that deposition would occur to deposit on the roof. When this simulation was compared with the experiment under the same conditions (Figure 5.39) particles were found to have deposited onto the roof of the spray dryer near the hot inlet air entrance because the particles had not dried out completely before hitting the roof.

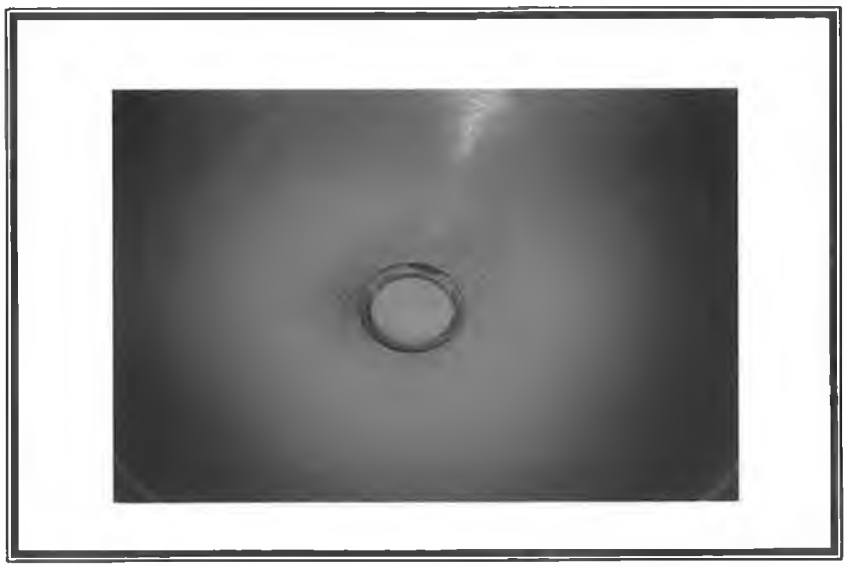

Figure 5.39: The roof of the spray dryer with deposition of HA slurry after spray drying of HA slurry (inlet temp 461K, flow rate 16.6 m/s).

6

Conclusions and Recommendations

6.1 CONCLUSIONS

In this study, a critical investigation into the spray-drying of Hydroxyapatite powder for thermal spray applications was carried out. The investigation was divided into two parts, statistical analysis for the analysis of the spray drying process and the CFD modelling of the spray dryer of HA powder. An optimisation of spray drying process was done using a statistical design of experiments. In the modelling procedure, the spray dryer was divided into three parts; nozzle, drying chamber and atomisation, and these results were compared using experimental data. Good agreement was found between the model and the experimental results. The conclusions resulting from the investigation are summarised as follows:

- In the preliminary test runs of the spray dryer, it was found by visualization that when the peristaltic pump and the air atomisation were set at 30 rpm (4.73×10^{-4} kg/s) and 75% air atomisation pressure (5.48 m/s inlet velocity of the air pipe), this provided a fully developed spray with minimum deposition on the wall of spray dryer.

- In the statistical experiment analysis, at the constant atomisation energy the drying mean chamber particle size depends only upon its feed viscosity. The mean particle size increases directly with an increase in the viscosity of HA slurry.

- The cyclone particle size showed that both the temperature and viscosity have a positive significant effect on the HA particle size and also the interaction between viscosity and temperature has a positive influence on the particle size.

- The high viscosity reduces the effect of particle wall deposition within the spray dryer.

- The statistical model did not provide any strong significant effects on thermal efficiency, however, the significant inlet temperature would effect thermal efficiency as it is a function of the inlet and outlet temperatures of the spray dryer.

- In the spray drying of HA slurry experiments, a large range of mean particle size (6.8 μm to 38.7 μm) of HA powder was obtained which predominately depends upon the feed viscosity at the constant atomization energy and all of the other factors had little significant effect, like temperature and flow rate of the hot inlet air.

- The spray dried HA powder showed a quite narrow particle size distribution. At low viscosity (25 and 50 mPa.s) an unimodal distribution at all three temperatures of drying was observed, which is an ideal condition for the flowablity of the thermal spray powder. However when the viscosity was increased from 50 to 75 mPa.s, the particle size distribution attained was a more bimodal distribution with an increase in temperature (461K).

- The spray drying HA powder was highly porous, however sintering of the HA powder is still compulsory to improve the crystallinity up to 99% for medical applications.

- The spray dried HA powder (viscosity of HA slurry; 25, 50 and 75 mPa.s and inlet temperatures 398, 421 and 461K) SEM micrographs showed that the shape of the entire set samples of powder were spherical. In general, spherical powders have better rheological properties than irregular powder and thus produce better coatings for hip implants.

- The resulting spray dried HA powder, showed two main morphological shapes, a solid and a doughnut sphere. The shape of dried powder depended upon the viscosity of HA slurry (solid concentration). It was also observed on a number of particles the occurrence of blow holes, spikes, cratering and shrivelling that would be explain by their drying history.

- The Air pipe of the external-two fluid nozzle was modelled using the Standard K-ϵ, Realizable K-ϵ and RSM using FLUENT software. It was found that all three models predicted almost the same results. However, computational time varied considerably (100, 140.74 and 464.50 % iterations) for the SK-ϵ, R K-ϵ and RSM methods respectively. In the validation, it was observed that the Standard K-ϵ method, provided a velocity profile much closer to the natural phenomena when compared to the Realizable K-ϵ and RSM methods. For the Air pipe modelling (without swirl), the Standard K-ϵ produced fast and reasonably accurate exit velocity prediction, within ±15% mean velocity of those found from the experimental results.

- The feed pipe of the external-two fluid nozzle was modelled under the same conditions using the turbulence models (Standard K-ϵ, Realizable K-ϵ and RSM); the best result was again predicted by the Standard K-ϵ method which was in good agreement (17%) with experimental data. However, the RSM predicted the highest velocity at the outlet of the feed pipe. The simulated flow rate using all three turbulence models was lower than that measured, because in the model, the peristaltic pump flow rate pulsates which was not accounted in the models.

- In the context of the spray dryer, this external two-fluid nozzle analysis enhanced this research in two ways; it gives an insight of the complexity of the air nozzle, such as mimicking the inside in the term of fluid mechanics. The air nozzle pipe has shown clearly that the atomising air is well-under the critical limits of throat conditions for the nozzle (less than 0.3 Mach) therefore can be used for higher atomising pressures to produce higher air velocities at the exit of nozzle. This system could also provide higher feed rates to produce the desired particle sizes. From a

scale up principle, this CFD analysis can be applied to any size of spray dryer, or in the analysis of new designs. This procedure of analysis would save time and money in the analysis of industrial spray dryer units.

- During the spray dryer temperature profile modelling, the simulation and measurement results did not differ by a major amount (maximum difference was approximately 9.0%). The Standard K-ϵ and Realizable K-ϵ produced results closer to that of the experimental data. To incorporate the swirl inside the spray dryer, the Realizable K-ϵ method, provided more promising results than the RSM method.

- The atomisation model allows the user to gain an understanding into the complex nature of the spray drying techniques. The evaporation rate of the HA slurry at different viscosities, showed with time that the evaporation rate was higher at the initial stage (1.34×10^{-9} kg/s) and then reduced (1.44×10^{-10} kg/s at 25mPa.s and a drying temperature of 398K) because the drying of the droplets occurs out in two stages; saturated drying and so called falling rate.

- The atomisation model showed that the particles temperature raised to and remains at their boiling point because the temperature exceeded the boiling point due to the heat balance of the convective heat transfer rate from the air and heat absorption due to evaporation.

- In the atomisation model, the built-in model in FLUENT possibly over-estimates the drying rate in the falling rate period because the droplet was dried fully only if the surrounding temperature was higher than its boiling point.

- Knowledge of the aforementioned mechanisms, will aid researchers and industrialists to select ideal input parameters to produce HA particles with the desired size and morphologies. This will not only benefit thermal spray powders but also provide more efficiency during the process, without the associated loss of produced material currently been experienced in industry.

6.2 RECOMMENDATIONS FOR FUTURE WORK

- The spray dryer modelling could be carried out on the three dimensional scale with the help of higher speed or parallel computing to compare these results, and could be applied to the drying of other thermal spray powders for example tungsten carbide cobalt (WC-Co) which uses "wax" fluid as a binder.

- The model could be used with other spray dry techniques such as ultrasonic atomisation to enhance the design of the spray dryer to provide smaller nano sized particles, an area of extreme interest in the materials engineering world today.

- The atomisation model could be validated using proper arrangement of equipment in the spray dryer such as; Interferometric Laser Imaging Technique (ILIDS) which provides instantaneous spatial distribution of the droplets and the Global Rainbow Thermometry Technique (GRT) for measuring directly averaged temperature and average droplet size of spray. These new techniques ILIDS and GRT would give a detail analysis and insight of the atomisation in spray dryers, by identifying the exact phenomena of breakdown of the liquid sheet into droplets coming out from the nozzle in spray dryers together with thermal behaviour of droplets when using modelling techniques, and are quite useful to validate the simulation of droplets size, temperature and velocity inside the spray dryer.

- In this research, FLUENT was used to build the drying model, however, different ceramic drying models could be used to predict the particle thermal histories and then be compared with experimental results.

- The rejected HA powder from thermal spray powder size range (< 20 μm or > 58 μm) can be investigated to determine the HA powder can be recycled and use for other methods of coating hip implants (such as electro-chemical coating) or bio-applications to reduce the amount of waste achieved from the process.

Publications Arising From This Research

- Q. Murtaza, J. Stokes, M. S. J. Hashmi, "A critical Investigation into the Spray Dryer of Powders for Thermal Spray Applications" Poster, 7th Annual Sir Bernard Crossland Symposium and Postgraduate Research Workshop", 2004, Dublin, Ireland, pp. 118

- Q. Murtaza, M. Ardhaoui, J. Stokes, M. S. J. Hashmi, "Spray Dryer Simulation and Validation used in the Production of Thermal Spray HA Powder", Euro Powder Metallurgy 2005 conference, 2005, Prague. Czech.Rep.

- Q. Murtaza, M. Ardhaoui, J. Stokes, "Spray Dryer Temperature Simulation used in the Production of Hydroxyapatite Thermal Spray Powder", Proceeding of the 12th Annual Conference of Section of Bioengineering of the Royal Academy of Medicine in Ireland, 2006, Galway, Ireland, pp. 41

- Q. Murtaza, M. Ardhaoui, J. Stokes, M. S. J. Hashmi, "Computation Fluid Dynamic Analysis of the Production of Bio-Thermal Spray Powders", International Conference on Materials-Energy-Design, March 15th to 16th, 2006, Dublin. (leading to publication in Journal) from Institute of Materials, Minerals and Mining)

Following papers are been considered to be sent to the Journal of Biomaterials

- Q. Murtaza, M. Ardhaoui, J. Stokes, M. S. J. Hashmi, "Experimental Analysis of Spray Dryer used in Hydroxyapatite Thermal Spray Powder".

- Q. Murtaza, M. Ardhaoui, J. Stokes, M. S. J. Hashmi, "Modelling of Atomisation of HA Powder for Thermal Spray Applications".

References

1 Masters, K., "Spray Drying Handbook", 4th ed., George Gowdin, London, ISBN 0-7114-5805-7 (1985)

2 ASM, Metal Handbook, "Powder Metal Technologies and Application" 1st ed., 7, (1998)

3 Bertrand, G., et al., "Spray-Dried Ceramic Powders: A Quantitative Correlation Between Slurry Characteristics and Shapes of the Granules" Chemical Engineering Science Vol. (1) 60, (2005), pp. 95-102

4 Stokes, J., "Production of Coated and Free Standing Engineering Components using the HVOF (High Velocity Oxy-Fuel) Process", Ph D. Thesis, Dublin City University, Ireland, (2003)

5 Cheang, P. and K. A. Khor, "Thermal Spraying of Hydroxyapatite (HA) Coatings: Effect of Powder Feedstock", Journal of Materials Processing Technology, 48 (1995), pp. 429-436

6 Pawlowski, L., "The Science and Engineering of Thermal Spray Coatings", John Wiley & Sons; 1st ed. ISBN: 0471952532, (1995)

7 Wei-Cheng Lih, et al., "Effects of Process Parameters on Molten Particle Speed and Surface Temperature and the Properties of HVOF CrC/NiCr Coatings", Surface and Coatings Technology, 133-134, (2000), pp. 54-60

8 Wigren, J. et al., "Effect of Powder Morphology, Microstructure, and Residual Stresses on Thermal Barrier Coating Thermal Shock Performance", National Thermal Spray Conference, USA, (1996), pp. 855–861

9 Cao, X.Q, et al., "Ceramic Materials for Thermal Barrier Coatings", Journal of the European Ceramic Society, 24 (2004), pp.1-10

10 Chistopher, C. B., "Materials Production for Thermal Spray Processes- A Lesson From Thermal Spray Technology" ASM, The Materials Information Society, USA, (1998)

11 Britton, C. R., "Manufacturing Methods and Quality Control Procedures for Thermal Spray Powders", Metco Ltd., Metal Powder Report, 47 (3), (1992), pp. 62-63.

12 Houck, D.L., "Thermal Spray: Advances in Coatings Technology", Published ASM Intl. USA, (1989)

13 McPherson, R., et al., "Structural Characterisation of Plasma-sprayed Hydroxyapatite Coatings", Journal of Mater, Sci. Mater. Med., Vol. 6, (1995), pp.327-334

14 Derama, V., et al., "Microstructural Characterizations of Plasma Sprayed Hydroxyapatite Coatings", Surface and Coatings Technology, Vol. 166, (2003), pp. 153-159

15 Haung, L. and Mujumdar, A.S., "classification and Selection of Spray Dryer, Chemical Industry Digest (India), vol. 7-8, (2003), pp.75-84

16 Online Publication, "Powder Manufacturing Methods". http://www.surfaceweb.com, Published on SurfaceWeb on 24/06/98. (access date 20 Nov 2004)

17 Fayed, E. M., and Lamber, O., "Handbook of Powder Science and Technology", Chapman and Hall, (1997), pp. 273-276

18 ASM, Metals Handbook, "Powder Metallurgy", 9th ed., Vol. 7, (1995)

19 Lawley, A., "Preparation of Metal Powders", Annual Review of Materials Science, Vol. 8, (1978) pp. 49

20 Upadhyaya, G.S., "Cemented Tungsten Carbides: Production, Properties, and Testing.", Noyes Publications, USA, ISBN: 0-8155-14175-4 (1998)

21 Roy, R., "Ceramic Fabrication Processes", New York, Publication, Academic Press, 1976

22 Pramanik, P. and Ghosh, N.N., "Aqueous Sol-gel Method for the Synthesis of Nano-sized Ceramic Powders" Ceramic Trans. Vol. 94, (1999), pp. 195-203

23 Pramanik, P. and Ghosh, N.N., "Aqueous Sol–gel Synthesis of Nanosized Ceramic Composite Powders with Metal-formate Precursors", Materials Science and Engineering: C , Vol. 16, 1-2 , (2001), pp. 113-117

24 Hsieha,M., et al., "Phase Purity of Sol–gel-derived Hydroxyapatite Ceramic ", Biomaterials, Vol. 22 (19), (2001), pp. 2601-2607

25 Kim, S., et al., "Effect of Calcinations of Starting Powder on Mechanical Properties of HA-Alumina Bioceramic Composite", Journal of Materials Science: Materials in Medicine, Vol.13, (2002), pp 307-310

26 Mujumdar, A.S., "Advance in Drying", Vol. 1, Hemisphere Publishing Corporation, USA, ISBN 0-89116-185-6, (1980)

27 Rayleigh Lord, "On the Instability of Jets", Proceeding London Math Soc., Vol. (4)10, (1878)

28 Weber, C., and Angew, Z., "Zum Zerfall eines Flussigkeitsstrables", Math. Mechanical, Vol. 11, (1931) pp. 136-139

29 Haenllin, A., "Disintegration of a Liquid sheet jet", National Advisory Committee: Aergonaut Technical Member. No 659, (1932)

30 Ohnseorge, W., Angew, Z., "Formation of Drops by Nozzles and the Break-Up of Liquid Jets. Z. Angew. Math. Mechanical, Vol. 16, (1936) pp. 355-358

31 Hagers, J.J., "Basic Technical Considerations for Application of Spray Nozzles to Chemical Processing", Experts in Spray Technology", 47th Chemical Processing Industry Exposition, New York, (1997)

32 Shaw, F.V., and Andrews, M.H., "Spray Drying: Carbide, Nitride and Boride materials Synthesis and Processing", Chapman and Hall, London, ISBN 0 412 54060 6, (1997)

33 Niro, Product Information, http://www.niroinc.com/html/pharma/phpsd.html (access date 15 March 2005)

34 Duffie, J. A and Marshall, W.R, "The Effect of Process Variables of Spray Dried on its Products", Chem. Eng Prog., Vol. 49 (1953), pp. 417-423

35 Gauvin, W. H. and Katta, S., "Basic Concepts of Spray Drying Design", American Institute of Chemical Engineers, Vol. (4) 22, (1976), pp.713-724

36 Crowe, C.T., "Modelling Spray –Air Contact in Spray-Drying Systems", Journal Advances in Drying1, Vol. 1, (1980), pp. 63-99

37 Farid, M., "A New Approach to Modelling of Single Droplet Drying", Chemical Engineering Science, Vol. 58, (2003), pp. 2985-2995

38 Sachdeva, R.C., "Fundamentals of Engineering Heat and Mass Transfer", Wiley Eastern Limited, ISBN 81-224-0076-0, (1993)

39 Cheong, H.W., Jeffreys G.V., and. Mumford, C.J., "A Receding Interface Model for the Drying of Slurry droplets", American Institute of Chemical Engineers (A.I.Ch.E) Journal, Vol. 32, (1986), pp. 1334–1346

40 Mermelstein, N.H., "Spray drying", Food Technology, Vol. (4) 55, (2001), pp 92-96

41 Kieviet, F. G., "Modelling Quality in Spray Drying", Ph.D. Thesis, Eindhoven University of Technology, Netherlands, (1997)

42 Takahashi, H., Shinohara, N. and Uematsu, K., "Influence of Spray-Dryer Slurry Flocculation on the Structure of Sintered Silicon Nitride", Journal of Ceramic Society of Vol. (1) 104, (1996), pp. 59–62

43 Walker, W.J, Reed, J.S and S.K. Verma, "Influence of Slurry Parameters on the Characteristics of spray-dried Granules", Journal of the American Ceramic Society, Vol. (7) 82, (1999), pp. 1711–1719

44 Tsubaki, J., Yamakawa, H., Mori, T. and Mori, H., "Optimization of Granules and Slurries for Press Forming", Journal of the Ceramic, Vol.(10) 110 , (2002), pp. 894–898

45 Sizgek E., Barlett, J.R. and M.P. Brungs, "Production of Titanate Microspheres by Sol–Gel and Spray-Drying", Journal of Sol-Gel Science and Technology, Vol. 13, (1998), pp. 1011–1016

46 Walton, D.E. and Mumford, C.J, "Spray Dried Products: Characterization of Particle Morphology", Trans International Chemical Engineering, Vol. 77, (1999), pp 21-33

47 Berndt, C.C, "Thermal Spray Coatings: Research Design and Applications", ASM International, ISBN: 0871704706, (1993)

48 US. Food and Drug Administration, "Calcium phosphate (CA-P) coating Draft Guidance for Preparation of FDA Submission for Orthopaedic and Dental Endosseous Implants", (1992)

49 ASTM F185, "Standard specification for composition of Hydroxyapatite for Surgical Implant", (2003)

50 BS ISO 13779-3, "Implants for Surgery- Hydroxyapatite-Part3: Chemical Analysis and Characterisation of Crystallinity and Phase Purity", (2000)

51 BS ISO 13779-1, "Implants for Surgery- Hydroxyapatite-Part3: Ceramic Hydroxyapatite", (2000)

52 ISO 10993-17, "Biological Evaluation of Medical Devices-Part 17: Establishment of allowable Limits of Leachable Substance using Health-Based Risk Assessment", (2002)

53 U.S. Food and Drug Administration, "510(K) Information Needed for Hydroxyapatite Coated Orthopaedic Implants", (1997)

54 Chu, J. C., Stout, L.E and Bushche, R. M., "Spray-Drying of Santomerse" Chemical Engineering Progress, Vol. (1) 47, (1951), pp. 29-38

55 Walton, D.E., "The Morphology of Spray Dried Particles", Ph.D. Thesis, Aston University, United Kingdom, (1994)

56 Ghadiri, M., "Attrition and Cominution", SERC Summer School in Particle Technology, University of Surrey, (1992)

57 Walton, D.E., "The Morphology of Spray-Dried Particles a Qualitative View", Drying Technology, Vol. 18, (2000), pp. 1943-1986

58 Buckham, J. A and Moultoun, R.W., "Factors Affecting Gas Recirculation and Particle Expansion in Spray Drying Chemical Engineering Process, Volume 51 (3), (1955), pp.126-133

59 Dlouhy, J. and Gauvin, W.H., "The Evaporation of Water Droplets: A Single Droplet Drying Experiment", American Institute of Chemical Engineers, Volume (1) 6, (1960), pp. 29-31

60 Alamilla-Beltran, et al., "Description of Morphological Changes of Particles along Spray Drying", Journal of Food Engineering, Vol.67, (2005), pp 179-184

61 Minoshima, H, Matsushima, K., Liang, H.and Shinohara, K., "Basic model of spray drying granulation", Journal of Chemical Engineering of Japan, Vol. 34 (4), (2001), pp. 472–478

62 Liang, H., Shinohara, K., Minoshima, H.and Matsushima, K., "Analysis of Constant Rate Period of Spray drying of slurry", Chemical Engineering Science, Vol. 56 (2001), pp. 2205–2213

63 Charlesworth, D.H. and Marshall, W.R., "Evaporation from Drops Containing Dissolved Solids", American Institute of Chemical Engineers Journal, Volume- 6, (1960) (1), pp. 9–23

64 Oakley, D.E and Bahu, R.E., "Computational Modelling of Spray Dryers", European Symposium on Computer Aided Process Engineering-2, Supplement-1, (1993), pp. 493-498

65 Zbicinski, I., "Development and Experimental Verification of Momentum, Heat, and Mass Transfer Model in Spray Drying", The Chemical Engineering Journal, Vol. 58, (1995), pp.123-133

66 Parti, M. and Palancz, B., "Mathematical Model for Spray Drying", Chemical Engineering Science, Vol. 29, (1974), pp. 355-362

67 Crowe, C.T, Sharma, M.P., and Stock, D.E., "The Particle-Source in –Cell (PSI-Cell) Model for Gas-Droplet Flows", Journal Fluid Engineering, (1997), pp. 99-101

68 Online Publication, http://www.computational-fluid-dynamics.com, accesses date: 24.10.2005.

69 Sommerfeld, M., "Review on Numerical Modelling of Dispersed Two phase Flows", Proc. 5th International Symposium On Refined Flow Modelling and Turbulence Measurement, Paris (1993)

70 Kadja, M. and Bergeles, G., "Modelling of Surry Droplet Drying", Applied Thermal Engineering, Vol. 23, (2003), pp. 829-844

71 Varonos, A. and Bergeles, G., "Development and Assessment of a Variable order Non Oscillatory Scheme for Convention Term Discretization" International Journal Numerical Method of Fluids, Vol.26, (1998), pp.1-16

72 Ruger, M., Hohmann, S., Sommerfeld, M., Kohhneen, G., "Eluer/Largrange Calculations of Turbulent Spray: The Effect of Droplet Collisions and Coalescence", Journal of Atomisation Sprays, Vol. 10 (2000), pp. 47-81

73 Mashayek, F., "Direct Numerical Simulations of Evaporating Droplet Dispersion in Forced Low Mach Number Turbulence", International Journal Heat Mass Transfer, Vol. 41 (17), (1998), pp. 2601–2617

74 Godsave, G.A.E., "Studies of the Combustion of Drops in a Fuel spray: the Burning of Single Drops of Fuel", Proceedings of the Fourth Symposium (International) on Combustion, Combustion Institute, Baltimore, MD, (1953), pp 818–830

75 Spalding, D.B., "The Combustion of Liquid Fuels", Proceedings of the Fourth Symposium (International) on Combustion. Combustion Institute, Baltimore, MD, (1953), pp. 847–864

76 Mashayek, F., "Droplet-Turbulence Interactions in Low Mach Number Homogeneous Shear Two-phase Flows", Journal Fluid Mech., Vol. 376, (1998), pp. 163–203

77 Crowe, C.T., Sharma, M.P. and Stock, D.E., "The Particle Source in Cell (PSI-cell) Model for Gas-Droplet Flows", Journal Fluids Eng., Vol. 6, (1977), pp. 325–332

78 Stevenson, M. J., Chen, X. D., and Fletcher, A. "Modelling the Drying of Milk", Australasian Chemical Engineering Conference (CHEMECA 98), Queensland, Australia, (1998)

79 Nesic S., "The Evaporation of Single Droplets—Experimental and Modelling", Drying Vol. 89 (1989), pp. 386-393

80 Chen, X. D., et al., "A New Model for the Drying of Milk Droplets for Fast Computation Purposes", Australasian Chemical Engineering Conference (CHEMECA 99), Newcastle, Australia, (1999)

81 Burns, A.D., et al., "FlOW3D: The Development and Application of Release", AERE-R 12693, HMSO, London (1987)

82 Harvine, D.J.E., Langrish, T. A. G., and Fletcher, D. f., "A Computational Fluid Dynamics study of a Tall-form Spray Dryer", Institution of Chemical Engineers. Vol. (c) 80, (2002), pp. 163-175

83 Langrish, T. A. G., and Kockel, T.K., "The Implementation of a Characteristic Drying Curve for Milk Powder using a Computational Fluid Dynamics Simulation", Chemical Engineering Journal, Vol. (1) 84 , (2000), pp. 69-74

84 Verdurmen. R.E.M., et al. "Modelling Spray Drying Processes for Diary Products" 1st International Symposium on Spray Drying of Milk Products, Rennes, France, (2001), pp.453-463

85 Southwell, D.B., Langrish, A. G., and Fletcher, D. F., "Use of Computational Fluid Dynamics Techniques to Assess Design Alternatives for the Plenum Chamber of a Small Spray Dryer", Drying Technology, Vol. 19 (2), (2001), pp. 257-268

86 Oakley, D. E., Bahu, R.E. and Reay, d., "The Aerodynamics of Co-current Spray Dryers", Sixth International Drying Symposium IDS, Versailles, France, (1998), pp. 373-378

87 Velic, d., Bilic, M., Tomas, S., and Planinic, M., "Simulation, Calculation and Possibilities of Energy Saving in Spray Drying Process", Applied Thermal Engineering Journal, Vol. 23, (2003), pp. 219-2131

88 Fontana, F., Grossi, A., and Molari, P. G., "Study Concerning Flow distribution Inside a Spray Drier", CERAMICA ACTA, Vol. (1) 11, (1999), pp. 15-21

89 Dukowicz, J.K., "A Particle-Fluid Numerical Model for Liquid Sprays". Journal Computational Physic, Vol. 35, (1980), pp. 229-305

90 O'Rourke, P.J., "Collective Drop Effects on Vaporizing Liquid Sprays", Ph.D. Thesis, Princeton University, USA, (1981)

91 Reitz, R.D., "Modelling Atomisation Processes in High-Pressure Vaporizing Sprays" Atomisation Spray Tech. Vol. 3, (1987), pp 307-311

92 Lefebvre, A.H., "Atomisation & Sprays", Hemisphere, New York (1989)

93 Tanner, F.X., "Liquid Jet Atomisation and Droplet Break-Up Modelling of Non-Evaporating Diesel Fuel Spray", SAE Transactions: J. Engines Vol.106, (1998), pp. 127–140

94 Apte, SV, Gorokhovski, M., Moin, P., "LES of Atomising Spray with Stochastic Modelling of Secondary Breakup", International Journal of Multiphase Flow, Vol.29, (2001), pp.1503-1522

95 Langrish, T.A.G, and Zbicinski, I., "The Effect of Air Inlet Geometry and Spray Cone Angle on the Wall Deposition Rate in Spray Dryers", Translational Institute of Chemical Engineering, Vol. 72 (A), (1994), pp. 420-430

96 Gimbum., J., "The influence of Temperature and Inlet Velocity on Cyclone Pressure Drop: a CFD study", Chemical Engineering and Processing, Vol. (1) 44, (2005), pp 7-12

97 Bhushan, B., and Gupta, B.K., "Handbook of Tribology: Material Coating and Surface Treatments", McGraw-Hill, New York, ISBN 0070052492, (1991)

98 Deutscher, O.,A, Document online " Wear Technology and Surfaces", http://www.bfi.de/en/fields_of_activity/surface_and_wear_technology/surface_and_wear_technology.htm (access date 20 June 2005)

99 Online ASM Document, "Thermal Spraying: Practice, Theory, and Application", http://www.asm-intl.org/tss/glossary/tssgloss.htm (access date 29 June 2005)

100 Online Document, "Coating and Technique", Advance Coating Co. Belgium, http://www.advanced coating.com/en/techniques/references.html (access date 20 June 2005)

101 Jordan, G. M., et al., "Development and Implementation of Plasma Sprayed Nanostructured Ceramic Coatings", Surface and Coatings Technology, Vol.146-147, (2001), pp. 48-54

102 Lih, W.C., et al., "Effects of Process Parameters on Molten Particle Speed and Surface Temperature and the Properties of HVOF CrC/NiCr Coatings", Surface and Coatings Technology Vol. 133-134 , (2000), pp. 54-60

103 Steinhäuser, S., et al., "Plasma-Sprayed Wear-Resistant Coatings with Respect to Ecological Aspects", Surface and Coatings Technology, Vol. 131 (1-3), (2000), pp. 365-371

104 SULZERMETCO, "Thermal Equipments Manual", (2005), www.sulzermetco.com

105 Fauchais, P. and Vardelle, A., "Heat, Mass and Momentum Transfer in Coating Formation by Plasma Spraying" International Journal of Thermal Science, Vol. 39, (2000), pp. 852-870

106 Nicoll, A.R., "Production Plasma Spraying in the Automotive Industry: A European Viewpoint ", Proceedings of the 7th National Thermal Spray Conference, Boston, (1994), pp. 7-17

107 ASM, "Thermal Spray Coatings: Properties, Process and applications", Conference Proceedings, ISBN 0-871-437-4, (1992)

108 METCO /Perkin Elmer, "Diamond Jet System and Gun Manual", (1989)

109 Kowalsky, K.A., et al., "HVOF: Particle, Flame, and Coatings Characteristics", Proceedings of the 3rd National Thermal Spray Conference, Ca, USA, (1990), pp. 587-596

110 Kreye, H., Schwetzke, R., Zimmerman, S., "High Velocity Oxy-Fuel Flame Spraying-Process and Coating Characteristics", C.C. Berndt (Ed.), Thermal Spray: Practical Solutions for Engineering Problems, ASM International, Materials Park, OH, (1996), pp. 451–456

111 Mingheng Li, Dan Shi and Panagiotis D. Christofides, "Model-Based Estimation and Control of Particle Velocity and Melting in HVOF Thermal Spray", Chemical Engineering Science, Vol. 59, (2004), pp. 5647-5656

112 Fedrizzi, L., Rossi, S., Cristel, R. and Bonora, P. L., "Corrosion and Wear Behaviour of HVOF Cermet Coatings Used to Replace Hard Chromium", Electrochimica Acta Vol. 49 (17-18) , (2004), pp. 2803-2814

113 Online Publication "Powder Manufacturing Methods". http://www.surfaceweb.com, Published on SurfaceWeb on 24/06/98. (access date 20 Nov 2004)

114 Lawley, A., "Preparation of Metal Powders", Annual Review of Materials Science, Vol. 8, (1978) pp. 49-51

115 Roy, R., "Ceramic Fabrication Processes", New York, Publication, Academic Press, 1976

116 Online Publication, "The Canadian Encyclopaedia 2005 Historica Foundation of Canada", Toguri, J.M, http://www.canadianencyclopedia.ca/PrinterFriendly.cfm?Params=A1ARTA0005250 (access date 15 March 2005)

117 Online Publication, "Ametek Metals, Product Information", http://www.ametekmetals.com/mp-thermal.asp (access date 15 Nov 2005)

118 Schulz, U., et al., "Some Recent Trends in Research and Technology of Advanced Thermal Barrier Coatings", Aerospace Science and Technology, Vol. 7, (2003), pp. 73–80

119 Allen, A.J., et al., "Microstructural Characterization Studies to Relate the Properties of Thermal Spray Coatings to Feedstock and Spray Conditions", Surface and Coatings Technology, Vol. 146–147, (2001), pp. 544–552

120 Chuankian, D., Zatorski, R.A., Herman, H. and Ott, D., "Oxide Powders for Plasma Spraying: The Relationship Between Powder Characteristics and Coating Properties", Thin Solid Films, Vol. 118, (1984), pp. 467–475

121 Lukasiewicz, S.J., "Spray-Drying Ceramic Powders", Journal of the American Ceramic Society, Vol. 72 (4), (1989), pp. 617–624

122 Kweh, S.W.K., et al., "The Production and Characterization of Hydroxyapatite (HA) Powder", Journal of Materials Processing Technologies, Vol. 89-90, (1999), pp. 373-377

123 Luo, P., and Nieh, T.G., "Synthesis of Ultrafme Hydroxyapatite Particles by a Spray Dry Method", Journal of Materials Science & Engineering, Vol. 3 (C), (1995), pp. 75-78

124 Suchanek, W. and Yoshimura, M., "Processing and Properties of Hydroxyapatite-Based Biomaterials for Use as Hard Tissue Replacement Implants", Journal of Materials Research, Vol. 13, (1998), pp. 94-114

125 Cheang, P. and Khor, K.A., "Thermal Spraying of Hydroxyapatite (HA) Coatings: Effect of Powder Feedstock", Journal of Materials Processing Technology, Vol. (48), (1995), pp. 429-436

126 Cheang, P. and Khor, K.A., "Addressing Processing Problems Associated with Plasma Coating of Hydroxyapatite Coatings", Journal of Biomaterials, Vol.17, (1996), pp. 537-544

127 Kim, S., et al., "Effect of Calcinations of Starting Powder on Mechanical Properties of HA-Alumina Bioceramic Composite", Journal of Materials Science: Materials in Medicine, Vol.13, (2002), pp. 307-310

128 Gabriel, P. R., et al., "Measurement of Thermal Diffusivity of Bone, Hydroxyapatite and Metals for Biomedical Application", The Japan Society for Analytical Chemistry, Vol.17, (2001), pp. S-357-360

129 Guipont, V., et al., "High Pressure Plasma Spraying of Hydoxyapatite Powders", Materials Science and Engineering A, Vol. 325, (2002), pp. 9-18

130 Knets, I., et al., "Glass and Hydroxyapatite Coating on Titanium Implants", Journal of Biomechanics, Vol. 31 (1), pp.166

131 Yip, C., S., et al., "Thermal Spraying of Ti-6Al-4V/ Hydroxyapatite Composites Coatings: Powder Processing and Post-Spray Treatment", Journal of Materials Processing Technology, Vol.65, (1997), pp. 73-79

132 Li, H., Khor, K.A, Kumar, R., and Cheang, P., "Characterization of Hydroxyapaptite/ Nano-Zircinia Composite Coatings Deposited by High Velocity Oxy-Fuel (HVOF) Spray Process", Surface and Coatings Technology, Vol. 182 (2004), pp. 227-236

133 Khor, K. A., Li, H. and Cheang, P., "Significance of Melt-Fraction in HVOF Sprayed Hydroxyapatite Particles, Splats and Coatings", Biomaterials, Vol. 25, (2004), pp.1177-1186

134 Shanmugavelayuthama, G., et al., "In-Flight Particle Behaviour and its Effect on Co-spraying of Alumina–titania", Current Applied Physics Vol. 6 (1), (2006), pp. 41-47

135 Rhee, S., "Synthesis of Hydroxyapatite via Mechanochemical Treatment", Journal of Biomaterials, Vol. 23, (2002), pp 1147-1152

136 Gomez-Morales, J., "Precipitation of Stoichiometric Hydroxyapatite by a Continuous Method", Journal of Crystal Research Technology, Vol. 36 (1) , (2001), pp15-26

137 Raynaud. et al., "Calcium Phosphate Apatites with Variable Ca/P Atomic Ratio, Synthesis, Characterisation and Thermal Stability of Powders", Journal of Biomaterials, Vol. 23, (2002), pp. 1065-1072

138 Luo, P., Nieh, T. G., "Preparing Hydroxyapatite Powders with Controlled Morphology", Journal of Materials Processing Technology, Vol. 89-90, (1999), pp. 550-555

139 Manual, NIRO ATOMIZER Co. (1997)

140 Senecal, P.K, et al., "Modelling High Speed Viscous Liquid Sheet Atomisation", International Journal of Multiphase Flow, Vol. 25, (1999), pp.1073-1097

141 Levich, V.G., "Physicochemical Hydrochemical Hydrodynamics, Prentice-Hall, New Jersey, (1962)

142 Reitz, R. D., Bracco, F.V., "Mechanism of Breakup of Round Liquid Jets: Encyclopaedia of Fluid Mechanics", Gulf Publication, Houston, (1986), pp. 233-249

143 Barnes, H.A., Hutton, J.F., Walters, K., "An Introduction to Rheology", Elsevier Science Publications, (1989)

144 Holland, F.A, Bragg, R., "Fluid flow for Chemical Engineers" 2nd ed., Edward Arnold, (1995)

145 Tanner, R.I., Rheology International series 2 Viscometer, Manual, "Engineering Rheology", Oxford University Press, New York (1985)

146 Testing Procedure of Spray Dryer, NIRO ATOMIZER CO. (2005)

147 Fieg, G., Wonzny, G., and Jeromin, L., "Estimation of the Drying Rate and Moisture Profiles in an Industrial Spray Dryer by Means of Experimental Investigations and a Simulation Study", Chemical Engineering and Technology, Vol. 17, (1994), pp. 235-241

148 Papadakis, S. E., "Air Temperatures and Humidities in Spray Drying", Ph.D. Thesis, University of California, Berkeley, USA, (1987)

149 Goldberg, J., "Modelling of Spray Dryer Performance" PhD Thesis, University of Oxford, United Kingdom, (1987)

150 Nijhawan, S., et al., "Measurement of Vapour Superheat in Post-Critical-Heat –Flux boiling", Journal of Heat Transfer, Vol. 102, (1980), pp 465-469

151 Kievit, F.G., et al., "A Device for Measuring Temperature and Humidity in a Spray Drying Chamber" Trans International Chemical Engineering, Vol. 75 (A), (1997), pp. 29-38

152 Gemci, T., Hom, J., and Chigier, H., "Simulations of Evaporating Spray and Comparison with Droplet Temperature Measurement obtained by Rainbow Refractometer", Proceedings of ASME-Fluid Engineering Division, Vol. 253, (2000), pp. 59-66

153 Glover, A.R., Skippon, S. M., and Boyle, R.D., "Intreferometric Laser Imaging for Droplet Sizing: A Method for Droplet Size Measurement in Sparse spray System", Application Optimisation, Vol. 34, (1995), pp. 8409-842

154 Maeda, M., Kawaguchi, T. and Hishida, K., "Novel Interferometric Measurement of Size and Velocity Distribution of Spherical Particles in Fluid Flow", Measurement Science Technology, Vol. 11, (2000), pp. 13-18

155 Maeda, M., Kawaguchi, T. and Hishida, K., "Improvements of the Interferometric Technique for Simultaneous Measurement of Droplet Size and Velocity Vector Field and its Application to a Transient Spray", Experimental Fluid, Vol. 33, (2002), pp.125-134

156 Kawaguchi, T., Akasaka, Y. and Maeda M., "Size Measurements of Droplets and Bubbles by Advanced Interferometric Laser Imaging Technique", Measurement Science Technology, Vol. 13, (2002), pp. 308-316

157 Sommerfeld, M. and Qiu, H., "Detailed Measurements in a Swirling Particulate Two-Phase Flow by a Phase Doppler Anemometer" International Journal Heat and Fluid Flow, Vol. 12, (1991), pp. 20-28

158 Takeuchi, G., et al., "Spatial Distributions of droplet Size and Velocity in Air Heated Spray Measured by Interferometric Laser Imaging Technique", 12th International Symposium on an Application of Laser Techniques to Fluid Mechanics, Lisbon, (2004)

159 Kobayashi, T., Kawaguchi, T. and Meada, M., "Measurement of Spray Flow by an Improved Interferometric Laser Imaging Droplet Sizing System" 10th International Symposium on an Application of Laser Techniques to Fluid Mechanics, Lisbon, (2002)

160 Beeck, J. P., et al., "Global Rainbow Thermometry for Average Temperature Measurement of Spray Droplets", 10th International Symposium on Application of Laser Techniques to fluid Mechanics, Lisbon, (2002)

161 Vetrano, M.R., et al., "Experimental validation of Global Rainbow Thermometry simulations", Optical technology and image processing for fluids and solids diagnostics SPIE-Beijing, (2002)

162 Online Pbulication, " Manual of Mastersizer", http://www.malvern.co.uk/LabEng/products/Mastersizer/MS2000/mastersizer2000.htm (access date 02 Nov, 2005)

163 Brundle, C.R., et al., "Encyclopaedia of Materials Characterization", Manning Publications Company, Greenwich, ISBN No 0750691689, (1992)

164 ASM Handbook, "Materials Characterization", Vol. 10, The Materials Information Society, ISBN No 0871700077, (1986)

165 Shames, I. H., "Mechanics of Fluid", McGraw Hill, Singapore, 3rd ed. ,ISBN 0-07-05638-X, (1992)

166 Fluent Inc, Introductory FLLUENT Notes, FLUENT v6.1, (2003)

167 Hirsch, C., "Numerical Computational of Internal and External Flows", Vol.,1, 2, John Wiley & Sons, U.K, ISBN 0471 923516, (1992)

168 Hoffmann, K. A. and Chiang, S. T., "Computational Fluid Dynamics for Engineers", Vol. III, 4th ed., Engineering Education Systems, (2000)

169 Anderson, J. D., "Computational Fluid Dynamics: The Basics with Applications", McGraw Hill, ISBN 0-07-001685-2, (1995)

170 Mostafa A. A. and Elghobashi S. E., "A Two-equation Turbulence Model for Jet Flows Laden with Vaporizing Droplets" ,International Journal of Multiphase Flow, Vol. 11, (4), (1985), pp. 515-533

171 Online document, http://www.cfd-online.com, (accesses date: 24.6.2005)

172 Mohammad, B., "Analysis of the K-Epsilon Turbulence Model", Wiley, Paris, ISBN 0471944602, (1994)

173 Fletcher, C. A. J., "Computational Techniques for Fluid Dynamics", Springer-Verlag, 2nd ed., New York, ISBN 3540530584, (1991)

174 Schick, R.J., and Brown, K., "Spray Dryer Scale-up from Laboratory to Production", Spray Analysis and Research Services, Spraying Systems Co., Wheaton, IL, USA, (2001)

175 Masters, K., "Scale-up of Spray Dryers", Drying technology, Vol. (1-2) 12, (1994), pp. 235-257

176 Online article, Pordal, HS, and Matice, C.J., and Fry, T.J., "Analysis of Chemical Processing Equipment", http://www.cheresources.com/cfdanalysis.shtml (access date 8th January 2005)

177 Fluent Inc. FLUENT 6.2 User Guide, Vol. 1-6, Published by FLUENT Inc., Lebanon, New Hampshire, USA, (2004)

178 Launder B.E, "Second-Moment Closure and Its Use in Modelling Turbulent Industrial Flows", International Journal for numerical Methods in Fluids, Vol., (1989), pp. 963-985

179 Reynolds. W.C., (Fundamentals of Turbulence for Turbulence Modelling and Simulations", Lecture Notes for Von Karman Institute Agard Report no. 755, (1987)

180 Launder, B.E. and Spalding, D.B., "The Numerical Computation of Turbulent Flows", Computer Methods in Applied Mechanics and Engineering, Vol. 3, (1974), pp 269-289

181 Yakhot and Orszag, S. A., "Renormalization Group Analysis of Turbulence: I. Basic Theory", Journal of Scientific Computing, Vol. 1, (1986), pp. 1-51

182 Shih, T.H., et al., "A New - Eddy-Viscosity Model for High Reynolds Number Turbulent Flows - Model Development and Validation", Computers Fluids, Vol. (3) 24, (1995), pp. 227-238

183 Wilcox, D.C., "Turbulence Modelling for CFD", 2nd Editions, DCW Industries, ISBN-192872910X, (1994)

184 George, P.L., " Automatic Mesh Generation and Finite Element Computation", Handbook of Numerical Analysis, Vol. 5, Elsevier, (1996), pp. 69-190

185 Lanunder, B.E., Reece, G.J. and Rodi, W., "Progress in the Development of a Reynolds Stress Turbulence Closure", Journal of Fluid Mechanics, Vol. 3, (1975), pp. 537-566

186 Gambit 2.1., "User Guide", Published by Fluent Inc., Lebanon, New Hampshire, USA, (2004)

187 Jones, B.W., et al., "Parallel Unstructured Mesh CFD Codes: A Role for Recursive Clustering Techniques in Mesh Decomposition", Parallel Computational fluid Dynamics, (1993), pp. 207-216

188 Thakker, A. and Hourigan, F., "Technical Note; A Comparison of Two Schemes for CFD Analysis of the Impulse Turbine for Wave Energy", Renewable Energy, Vol. (9) 30, (2005), pp. 1401-1410

189 Bastarrica, M.C. and Kaher, H.N., "Designing a Product Family of Meshing Tools", Advances in Engineering Software, (2005), pp. 1-10

190 Ferziger, J.H, Peric, M., "Computational Methods for Fluid Dynamics", 3rd ed., Springer, New York, ISBN-3-540-42074-6, (2002)

191 Wesis, J.M, Maruszewski, J.P. and Smith. W.A., "Implicit Solution of the Navier-Stokes Equations on Unstructured Meshes", Technical ReportAIAA-97-2103, 13th AIAA CFD Conference, Snowmass Co., (1997)

192 Wilcox, D.C., "Multi-scale Model for Turbulent Flows", American Institute of Aeronautics and Astronautics Journal, Vol. 26, (1998), pp.1311-1320

193 Gouesbet, G., and Berlemont, A., "Eulerian and Lagrangian Approaches for Predicting the Behaviour of Discrete Particles in Turbulent flows" Programming Energy Combustion science, Vol. 25 (1999), pp. 133-159

194 Guo, B., Fletcher., D.F., and Langrish, T.A.G., "Simulations of Agglomeration in a Spray Using largrangain Particle Tracking", Applied Mathematical Modelling, Vol. 28, (2004), pp. 273-290

195 Morsi, S. A. and Alexander, A.J., "An Investigation of Particle Trajectories in Two-Phase Flow Systems", Journal of Fluid Mechanics, Vol. (2) 55, (1972), pp. 193-208

196 Clift, Grace, and Weber, "Bubbles, Drops, and Particles", Technical report, Academic Press, (1978)

197 Talbot, L., et al., " Thermophoresis of Particles in a Heated Boundary Layer" Journal of Fluid Mechanics, Vol. (4) 101, (1980), pp. 737-758

198 Csanady, G.T., "Turbulent Diffusion of Heavy Particles in the Atmosphere", Journal Atmosphere Science, Vol. 20, (1963), pp. 201-208

199 Li, A.and Ahmadi, G., "Dispersion and Deposition of Spherical Particles from Point Sources in a Turbulent Channel Flow", Aerosol Science and Technology, Vol. 16, (1992), pp. 209-226

200 Saffman, P.G., "The Lift on a Small Sphere in a Slow Shear Flow", Journal Fluid Mechanics, Vol. 22, (1965), pp. 385-400

201 Haider, A and Levenspiel, O., "Drag Coefficient and Terminal Velocity of Spherical and Nonspherical Particles", Powder Technology, Vol. 58, (1989), pp 63-70

202 Ranz, W.E and Marshall, Jr. W.R., "Evaporation from Drops, Part I", Chemical Engineering Programme, Vol. (3) 48, (1952), pp. 141-146

203 Ranz, W.E and Marshall, Jr. W.R., "Evaporation from Drops, Part II", Chemical Engineering Programme, Vol. (4) 48, (1952), pp. 173-180

204 Gouesbet, G., and Berlemont, A., "Eulerian and Lagrangian Approaches for Predicting the Behaviour of Discrete Particles in Turbulent flows" Programming Energy Combustion science, Vol. 25 (1999), pp. 133-159

205 Beck, J.C., "Computational Modelling of Poly-disperse Spray Without Segregation into Droplet Size Classes", Ph.D. Thesis, UMIST Manchester, (2000)

206 Beck, J.C. and Watkins, A.P., "The Droplet Number Moments approach to Spray Modelling: The Development of Heat and Mass Transfer Sub-models" International Journal of Heat and Fluid Flow, Vol. 24, (2003), pp. 242-259

207 Schmidt, D.P., et al., "Pressure-Swirl Atomisation in the Near Field", SAE Paper 01-0496, SAE, (1997)

208 Han, Z., Perrish, S., Farrell, P.V., and Reitz, R.D., "Modelling Atomisation Processes of Pressure-Swirl Hollow-Cone Fuel Sprays", Atomisation and Sprays, Vol. (6) 7, (1997), pp. 663-688

209 Lichtarowicz, A.K., Duggins, R.K., and Markland, E., "Discharge Coefficients for Incompressible Non-Cavitating Flow Through Long Orifices", Journal of Mechanical Engineering Science, Vol. 7, (1965), pp. 2-3

210 Dombrowski, N. and Johns, W.R., "The aerodynamic Instability and Disintegration of Viscous Liquid Sheets", Chemical Engineering Science, Vol. 18, (1963), pp 203-206

211 Schmidt, D.P., Corradini, M.L. and Rutland, C.J., "A Two-Dimensional, Non-Equilibrium Model of Flashing Nozzle Flow", In 3rd ASME/JSME Joint Fluids Engineering Conference, (1999)

212 Ruger, M., et al., "Eluer/Largrange Calculations of Turbulent Spray: The Effect of Droplet Collisions and Coalescence", Journal of Atomisation Sprays, Vol. 10, (2000), pp. 47-81

213 Taylor, G.I., "The Shape and Acceleration of a Drop in a High Speed Air Stream", Technical report, In the Scientific Papers of G. I. Taylor, ed., G. K. Batchelor, (1963)

214 Reitz, R.D., "Modelling Atomisation Processes in High-pressure Vaporizing Sprays" Atomisation Spray Technology, Vol. 3, (1987), pp. 307-311

215 Athena, T., et al., "Optimization of the Reologicval Properties of Alumina Slurries for Ceramic Processing Applications", Journal of the European Ceramic Society, Vol.21, (2001), pp. 493-506)

216 Iskander, F., et al., "Control of the Morphology of Nanostructured Particles Prepared by the Spray Drying of a Nanoparticle Sol", Journal of Colloid and Interface Science, Vol. 265, (2003), pp. 296-303

217 Huang. L., et al., "Computational Fluid Dynamic Simulation of Droplet Drying in a Spray Dryer", Drying 2004, Brazil, (2004), pp.326-332

218 Ardhaouia, M., et al., "Effect of Acyl Donor Chain Length and Substitutions Pattern on the Enzymatic Acylation of Flavonoids", Journal of Biotechnology, Vol 110, (3), (2004), pp. 265-272

219 Kothapalli, C. et al., "Influence of Temperature and Concentration on the Sintering Behaviour and Mechanical Properties of Hydroxyapatite". Acta Materialia, Vol. 52 (2004), pp.5655-5663

220 Juang, H.Y et al., "Effect of Calcination on Sintering of Hydroxyapatite", Biomaterials, Vol. 17, pp. 2059-2064

221 Sung, Y.M. et al., "Crystallization and Sintering Characteristics of Chemically Precipitated Hydroxyapatite Nanopowder", Journal of Materials Science: Materials in Medicine, Vol. 13, (2004), pp 307-2064

222 Ramesh, S. et al., "Grain Size-Properties Correlation in Polycrystalline Hydroxyapatite Bioceramic", Malaysian Journal of Chemistry, Vol. 3, No1., 92001), pp. 35-40

223 Ducheyene., P et al., "The Effect of Calcium Phosphate Ceramic Composition and Structure on in Vitro Behaviour; Dissolution" Journal Biomed Mater Research, Vol. 17, (1993), pp 25-34

224 Liu, C et al., "Kinetics of hydroxyapatite precipitation at pH 10 to 11". Biomaterials, Vol. 22 (2001), pp. 301-306

225 Pang, Y.X., et al., " Influence of Temperature, Ripening Time and Calcination on the Morphology and Crystallinity of Hydroxyapatite Nanoparticles", Journal of the European Ceramic Society, Vol.23 (2003), pp. 167-1704

226 Tampieri, A., et al., (2002) " Characteristics of Synthetic Hydroxyaptites and Attempts to Improve their Thermal Stability", Materials Chemistry and Physics, Vol 64, (200), pp. 4-61

227 Chung, R., "Hydroxyapatite Layers Deposited from Aqueous Solutions on Hydrophilic Silicon Substrate", Surface and Coatings Technology, Vol. 165, (2003), pp. 194-200

Appendix-A

A 1 CHEMICAL AND CRYSTALLOGRAPHIC OF CA-P POWDER

US Food and Drug Administration (FDA) requires the following test data to be reported when using or proposing HA products:

A1.1 Elemental analysis

An elemental analysis for the powder noting any impurities including, but not limited to, 50 ppm heavy metals, as identified in ASTM F1185-03 [**44**] and ISO 13779-3 [**45**] is required. The limits for specific trace elements are outlined in the following table.

Table A-1: Limit of allowable trace elements in HA product [49].

Elements	Maximum limit (mg/kg)
Arsenic	3
Cadmium	5
Mercury	5
Lead	30

Limit of allowable Trace Elements [**49**] based on the assessment of the risk posed by other chemical impurities is carried out in accordance with BS ISO 10993-17 [**50**]

A1.2 Calcium to Phosphorous (Ca/P) Ratio

The Ca/P ratios in atomic percent for the powder should be reported. In order to account for the deviation that may occur form the ideal sotichiometric ratio; a sufficient number of samples are required for analysis in order to produce a statistically meaningful mean and variance (95%) confidence interval) [**46**]. The ideal stoichiometric ratio for HA is 1.667 according to its chemical formula $Ca_{10}(PO_4)_6(OH)_2$ [**43,48**]. However, the acceptable range of calcium and phosphorous ratio, Ca/P shall have a value of $1.65 \leq Ca/P \geq 1.82$ for the atomic ratio in accordance to ISO 13779-1:2000 [**49**]. This must be determined using the specifications described in ISO 13779-3:2000 [**48**].

A 1.3 X-ray Diffraction (XRD)

Individually superimposed spectra of the formed HA powder over the standard given for the relevant calcium phosphate compound (such as, Hydroxypapatite, JCPDS 9-3348) in the powder diffraction files of the JCPDS (joint committee on powder diffraction standards) must be determined. A minimum of 95 % crystallinit6y and purity is required for the HA powder as in accordance with ISO 13779-1 [**49**] and ASTM F185-03 [**47**]. The quantitative and qualitative determination of the content of the HA phase and of other crystalline phases may be determined in accordance with ISO 13779-3 [**48**]

A 1.4 Infrared spectrometry (IR)

The IR spectra of the HA powder must also be indicated. Spectra must be plotted as percent transmittance versus wave number [**46**]. The characteristic absorption bands for HA are as follows [**46**] $PO4^{3-}$: 570cm^{-1}, 962 cm^{-1}, 1050 cm^{-1} and OH-: 630 cm^{-1}, 3540 cm^{-1}

A 1.5 Solubility of Ca/P compound

A complete report regarding the solubility testing is required and should be conducted in a physiologically similar solution to tris-HCL buffered solution at 37°C, tested at a pH of 3.0 and 7.3 [**46**]. Room temperature and 100°C measurements are optional. Alteration in pH must also be recorder with the solubility product of HA being based upon the normal stoichiometric formula $Ca_{10}(PO_4)_6(OH)_2$ [**49**]

Table A.2: Properties of HA and Plasma spray parameter for coating [48,49,133]

Physical properties	**Metric units**	**Mechanical properties**	**Metric units**
Density	3.00-3.219 g/cc	Ultimate Tensile Strengths	38-48 MPa
Porosity	0.1-3%	Modulus of Elasticity	7-13 GPa
Lattice parameters a lattice constant b lattice constant	 9.432-0.9841 A° 6.881-06884 A°	Flexural Strength	100-120 MPa
Crystallinity index	33-37	Compressive Strength	350-450 MPa
Crystallite Size	0.025 x 0.03 (nm)	Fracture Toughness	<1.0 MPa.$m^{1/2}$
Ignition Products	HA + CaO	Poisson's Ratio	0.27

Plasma spray parameters used for depositing HA onto orthopaedic implant

Coating	Power (KW)	Currrent (A)	Distance (mm)	Work gas Rate (L/min)	Carrier gas Rate (L/min)	Powder feed rate (g/min)
HA	30	500	80-90	Ar: 50 $H_{2:3}$	Ar: 3	20

Properties of Ha applied onto Ti-Alloy substrates

Surface	Average Roughness (μm)	Initial Powder size (μm)
HA coating on Ti substrate	4.96 ± .043	30 - 160

Appendix-B

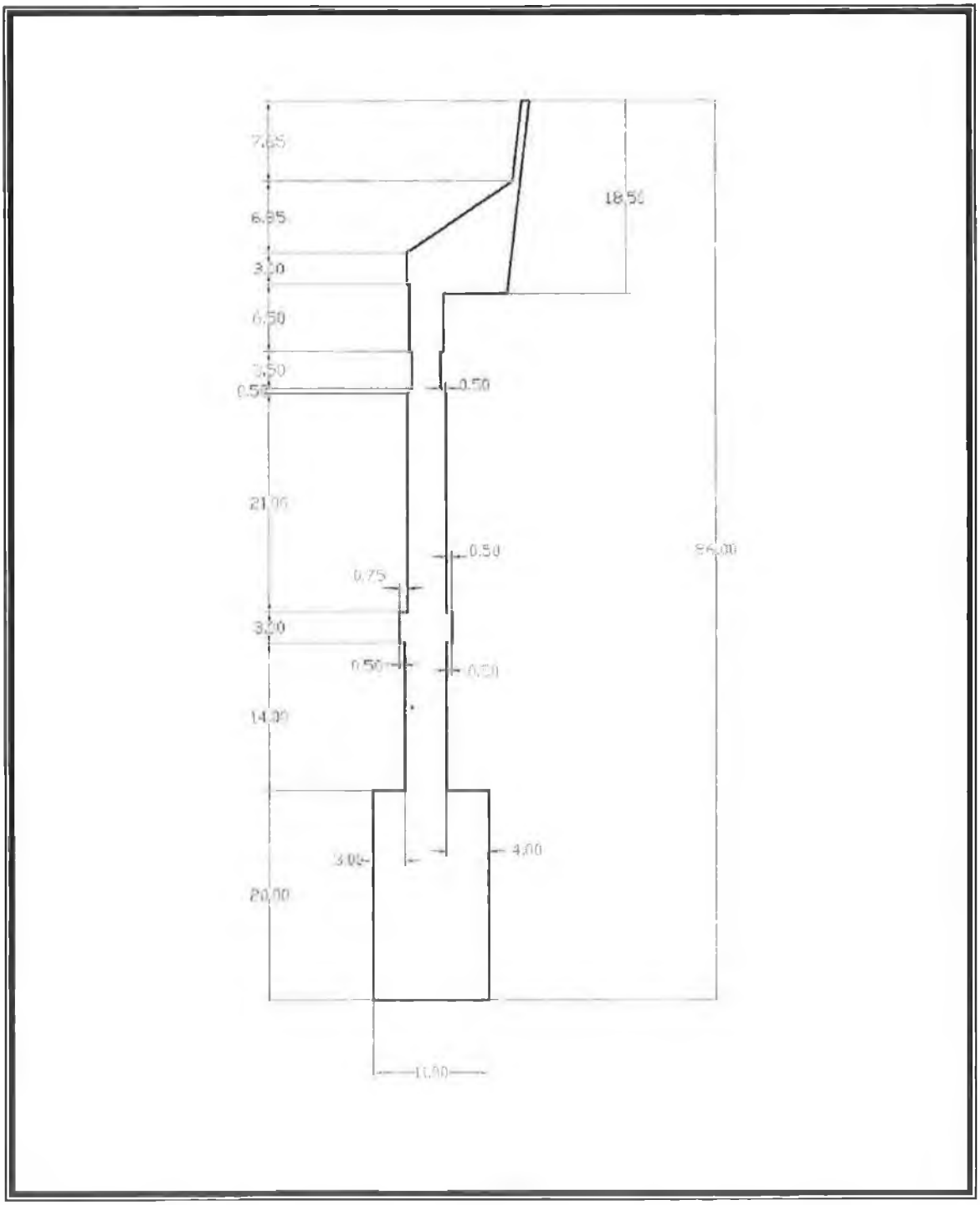

Figure B.1: Air nozzle pipe (Niro Production Minor).

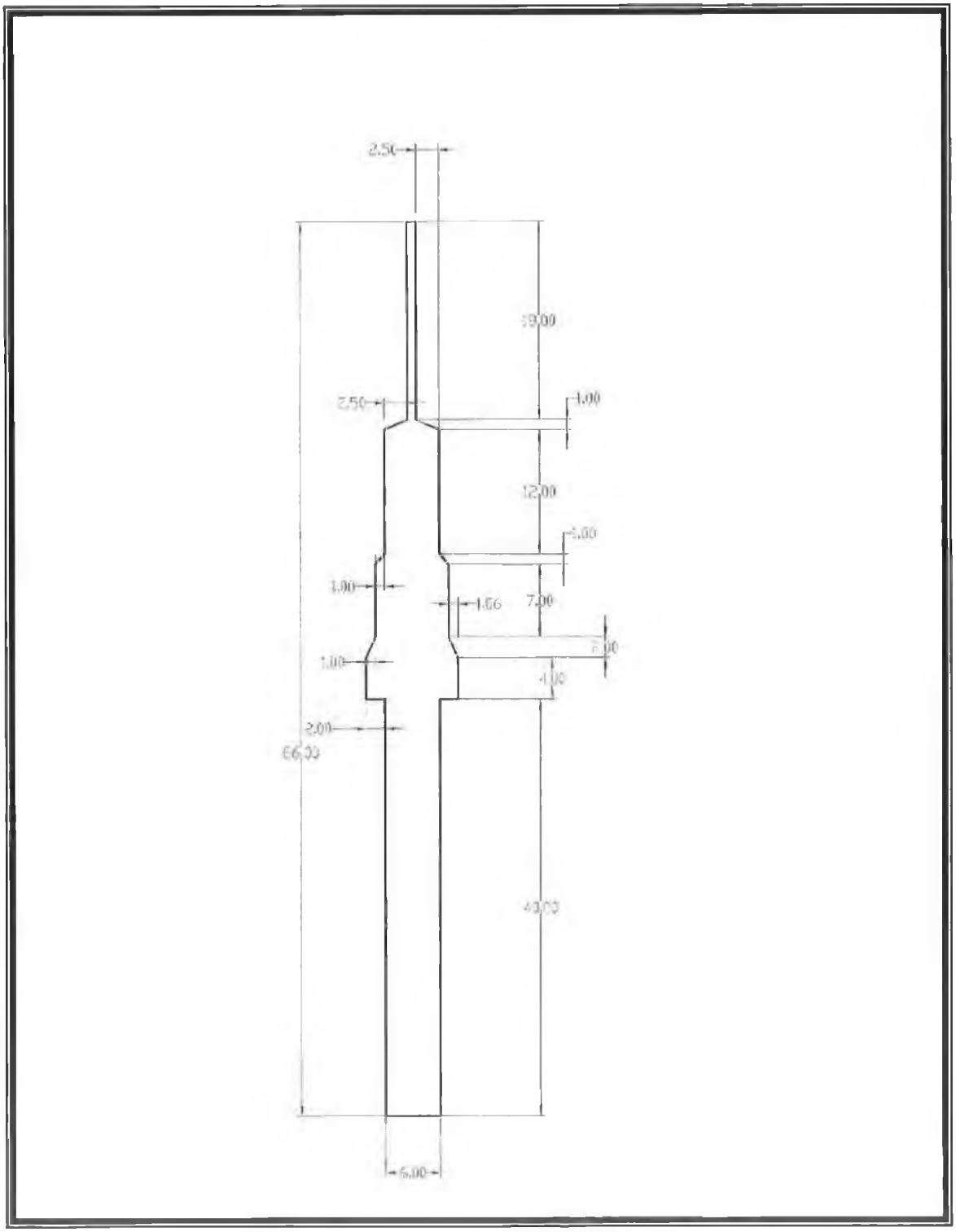

Figure B.2: Feed nozzle pipe (Niro Production Minor).

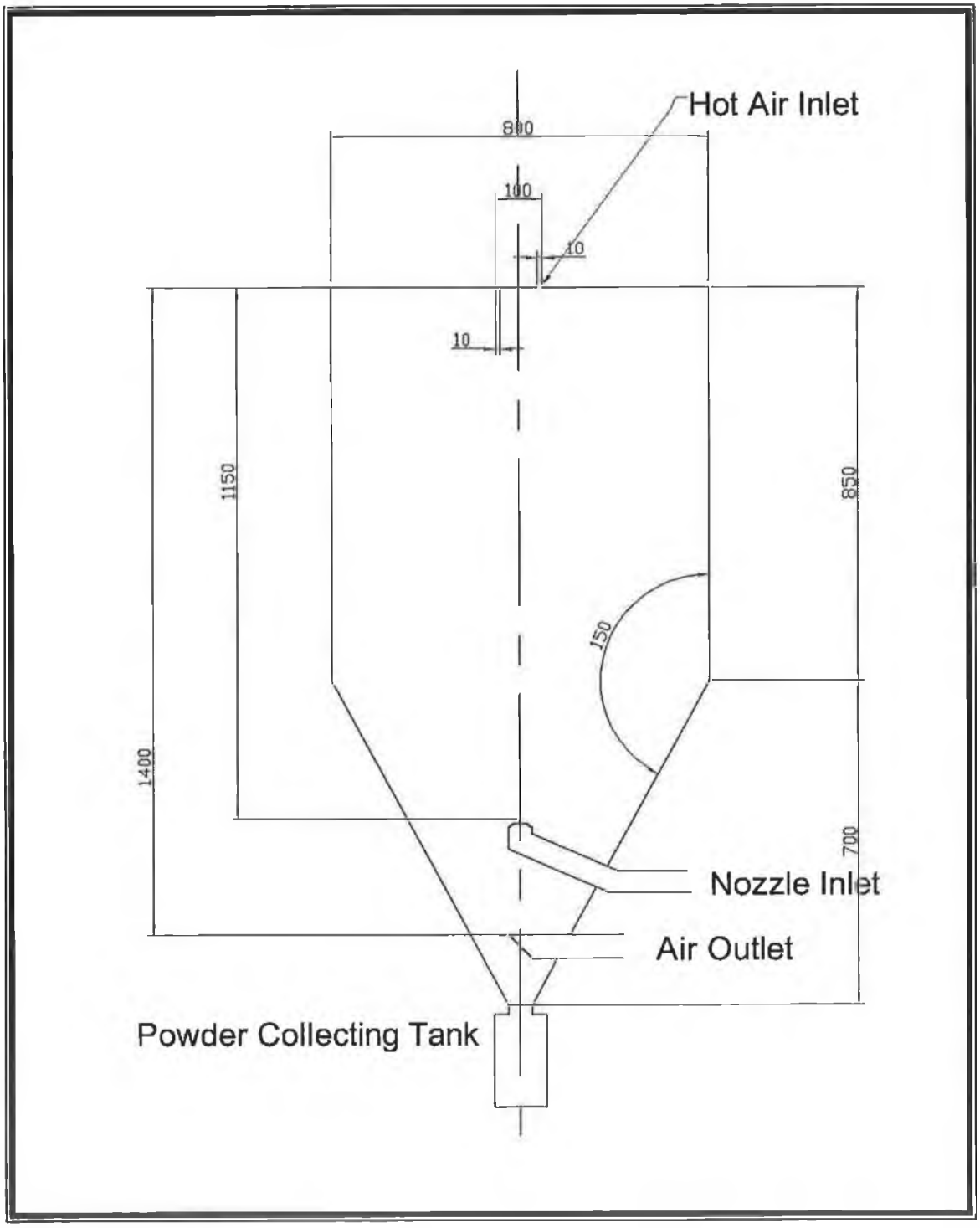

Figure B.3 Spray dryer (Niro Production Minor).

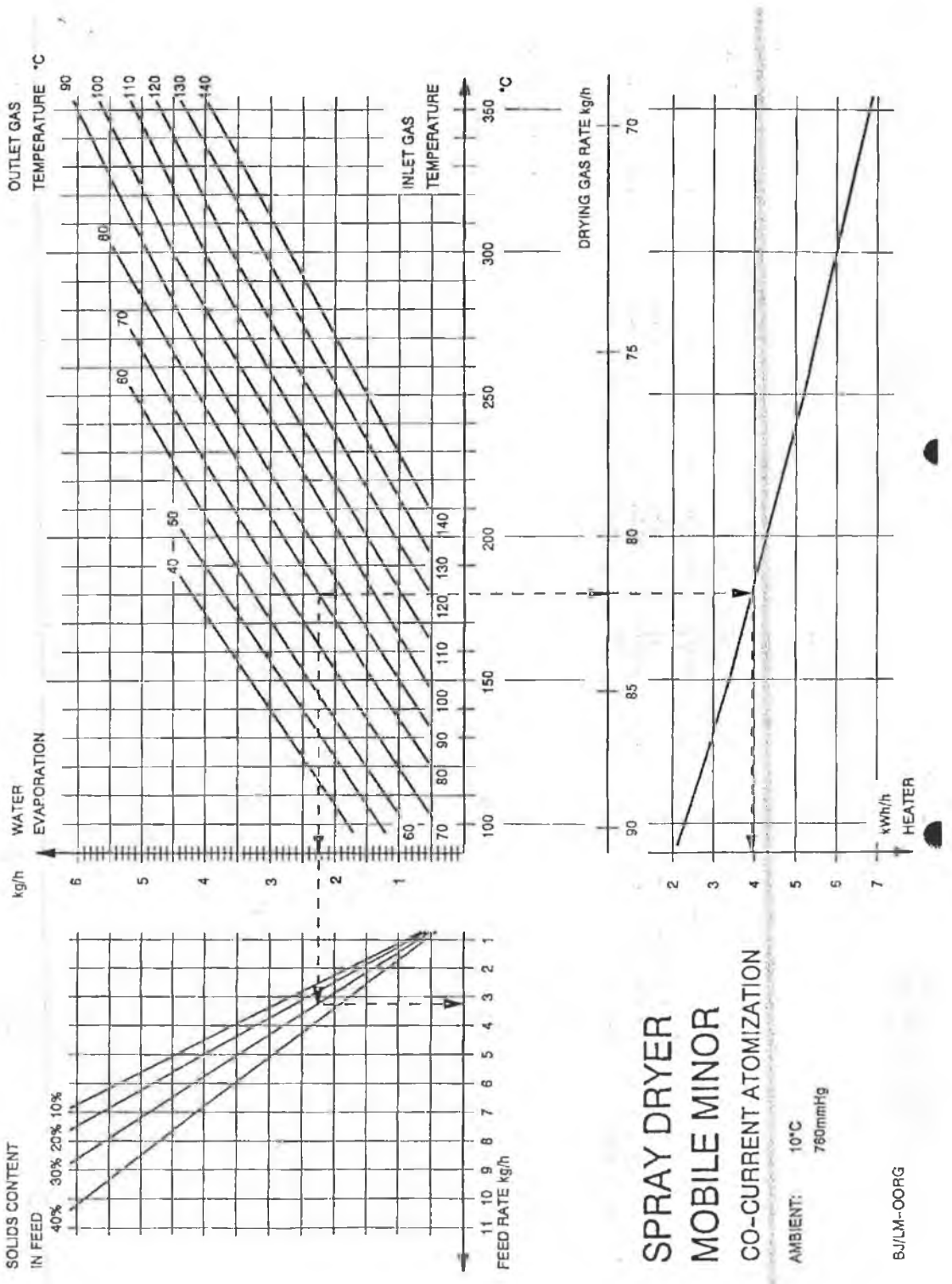

Figure B.4: Atomisation condition of the spray dryer.

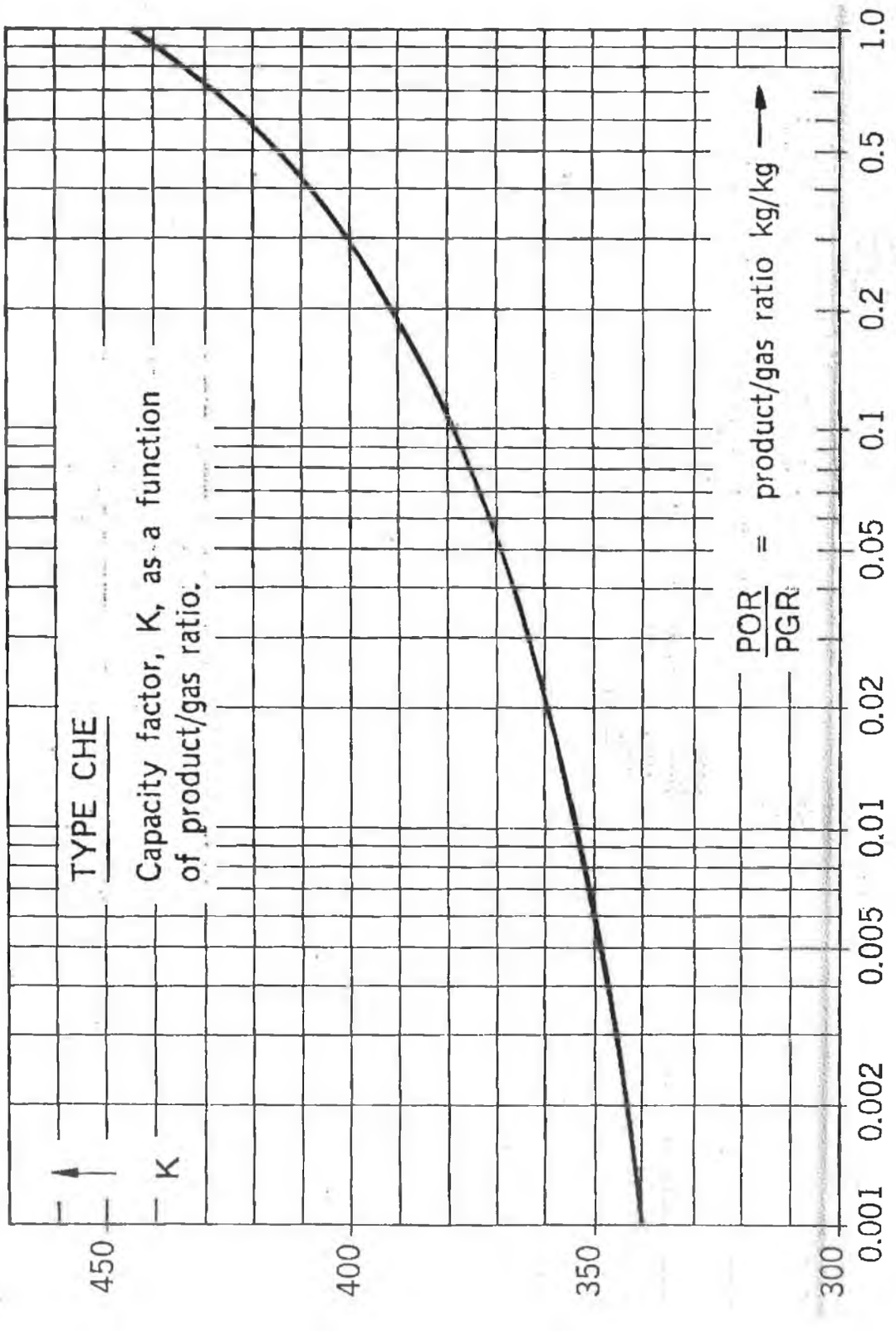

Figure B.5: K factor as a function of product and gas ratio.

B.1 INLET HOT AIR FLOW RATE OF SPRAY DRYER

B.1.1 A sample calculation for open condition:

Gauge reading 100 mm of H_2O;

The air flow rate PGR is given by equation 3.5

$$PGR = k * D^2 * \sqrt{\rho * \Delta p} \text{ (Kg/hr)}$$ ----------Equation B.1

The Cyclone diameter D= 0.14m

Gas density at 100 °C = $\rho = \frac{P}{RT} = \frac{101325}{287 * 373}$ Kg/m³ ----------Equation B.2

And, K read out K= 406 (at 25 % product/ gas ratio)

So, PGR = (0.19068) (406)

PGR = 80 Kg/hr

Therefore, this flow rate is the same in the spray dryer as the inlet air flow rate with the correction of air density of inlet temperature.

Inlet Outer diameter = 0.01m and inner diameter = 0.08m

Inlet air velocity (m/sec) as axis symmetric V =1/2 ρ ($\pi(0.05^2 - 0.04^2)$)/ m (m/sec)

Where V is inlet velocity, m air mass flow rate Kg/sec and ρ is the density (kg/m³ at a given temperature

V = 16.6 m/sec.

This inlet air enter at 61.18° with the vertical axis of spray dryer

So the component of inlet hot air is as follows

Horizontal component 16.6 Cos 61.18° = 8.0 m/sec

Vertical component 16.6 Sin 61.18° = 13.85 m/sec.

Table B1: Inlet air flow rate of the spray dryer.

S.No.	Different point of control knob of air flow rate	Manometer Reading across the Cyclone (mm of H_2O)	Air flow rate of spray dryer (kg/hr)	Inlet Velocity of the spray dryer (m/s)	Horizontal component (m/s)	Vertical component (m/s)
1	Open condition	100	80	16.6	8.0	13.86
2	At 4 points knob	90	75	14.7	7.35	12.73
3	At 6 points knob	75	65	12.7	10.99	6.35

B.2 AIR PIPE NOZZLE

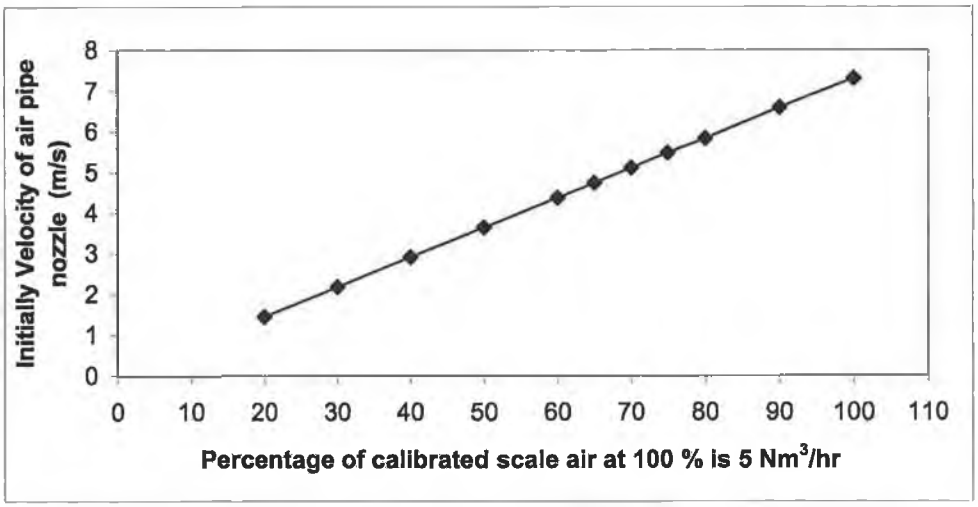

Figure B.6: Initial air velocity of air pipe nozzle at calibrated scale.

A sample calculation

At 100 % of calibrated scale is 5 (Normal condition m^3/hr) at 1 bar.

This atomising air initially flows thorough 4 air pipes:

$$Q=AV;\ 4x\,\pi r^2 = 5/\ 3600\ m^3/sec \quad \text{----------Equation B.3}$$

The radius of the air pipe, r = .0055 m

Therefore; V = 7.307 m/sec

B.3 FEED PIPE NOZZLE

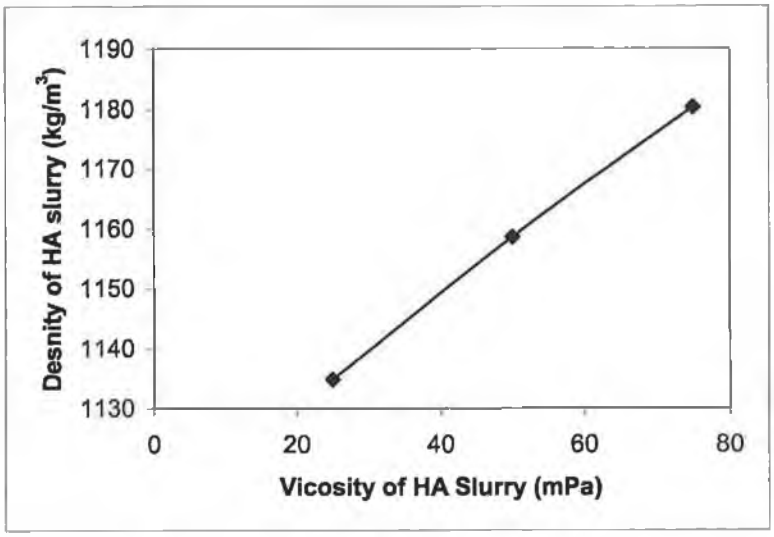

Figure B.7: Calibration graph between HA feed slurry viscosity and density.

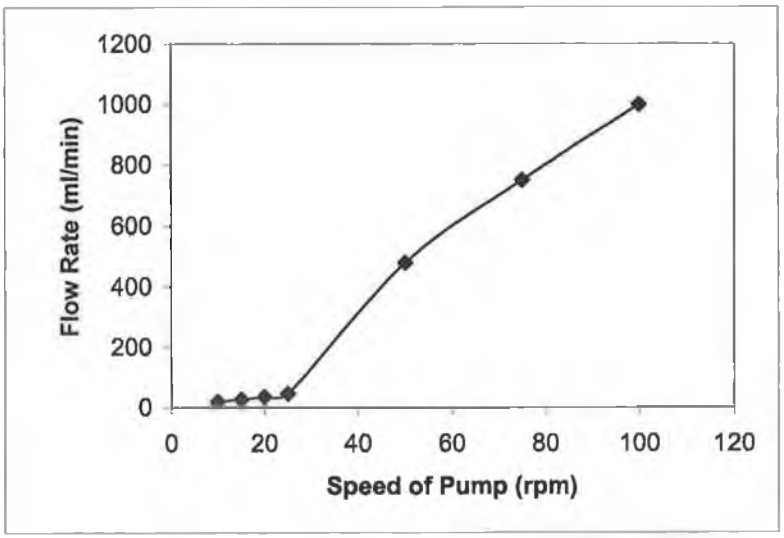

Figure B.8: Calibration graph between HA feed slurry flowrate and rpm of peristaltic pump.

A Sample Calculation:

Flow rate at 25 mPa.s HA slurry feed at 30 rpm of pump:

As the spray drying simulation is axis – symmetric

At 25 mPa the flow rate at 30 rpm of peristaltic pump:

Flow rate of HA slurry (kg/sec) = 1/2ρQ---------Equation B.4

ρ is the density of HA slurry at a 25 mPa Viscosity from the graph 2 = 1134.85 kg/m^3:

Q is the volume flow rate of HA slurry at the given rpm of the pump, for 30 rpm is 50ml/min = 8.33×10^{-6} form the graph 3

Therefore; Flow rate of HA slurry feed = $1/2 \times 8.33 \times 10^{-6} \times 1134.85 = 4.73 \times 10^{-4}$ Kg/sec

Table B.2: Properties of HA slurry; viscosity, density and flowrate.

S.No	Viscosity of HA slurry (mPa.s)	Density (Kg/m^3)	Flowrate (kg/sec) x 10^{-4}
1	25	1134.85	4.730
2	50	1158.66	4.833
3	75	1180.35	4.918

B.4 PREPARATION OF HA SLURRY INHOUSE

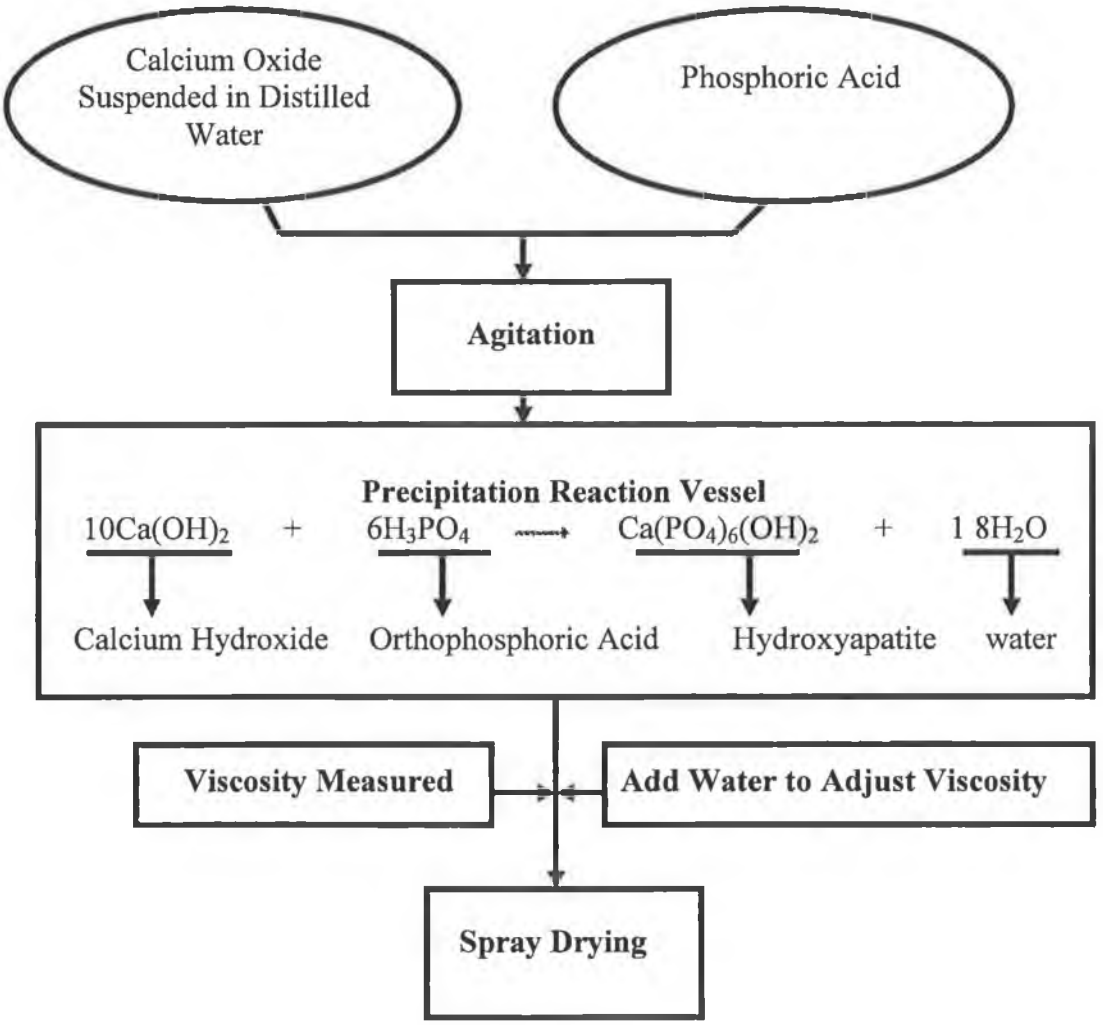

Figure B.9: Preparation of HA slurry in-house for the spray drying.

The route taken in this research to produce stoichiometric HA slurry for spray drying:

1 An analytical weighing scale was used to accurately weigh CaO powder. Reagent grade 1.42 mol (79.55g) CaO (JT Baker, Analysed , 100% pure) powder were added to 500ml of distilled water in a 100 ml – enclosed beaker and vigorously stirred Heidolph stirrer at 1000 rpm at the reaction temperature for 24 hrs to react and from a suspension of Ca in an access of deionised water. The beakers were covered in order to avoid possible contamination via contact with atmospheric conditions. The temperature of the reaction (20 °C) was maintained by thermostat- controlled water bath.

2 An analytical weighing scale was also used to accurately weigh the required quantity of orthophosphoric acid 97.32 g of 85% H_3PO_4 (JT baker, Analysed) used added to the $Ca(OH)_2$ solution at an addition rate of 1.5 ml/min using a peristaltic pump. During the course of the acid addition, the pH of solution was monitored via handheld pH meter (HI9183, Hanna Instrument, Inc.) with an accuracy of 0.2. The reactants were stirred for a further 24 hrs to aid in the maturation stage, under continuous stirring conditions at 1000rpm, held at the respective reaction temperature of 20 C, 0.28 mol (9.94g) NH_4OH, was added to slurry after 24 hrs ripening period to stabilise the pH of the super-saturated solution to above9 and then ready to spray drying.

B 4.1 Physical Analysis of HA

Table B.3: Physical properties of HA Powder.

Phase Present in HA	Crystallinity (%)	Purity (%)	Density (kg/m³)	
HA, TTCP, αTCP, βTCP	95.4876	90.444	Chamber dried	Cyclone dried
			2.9128	3.2331

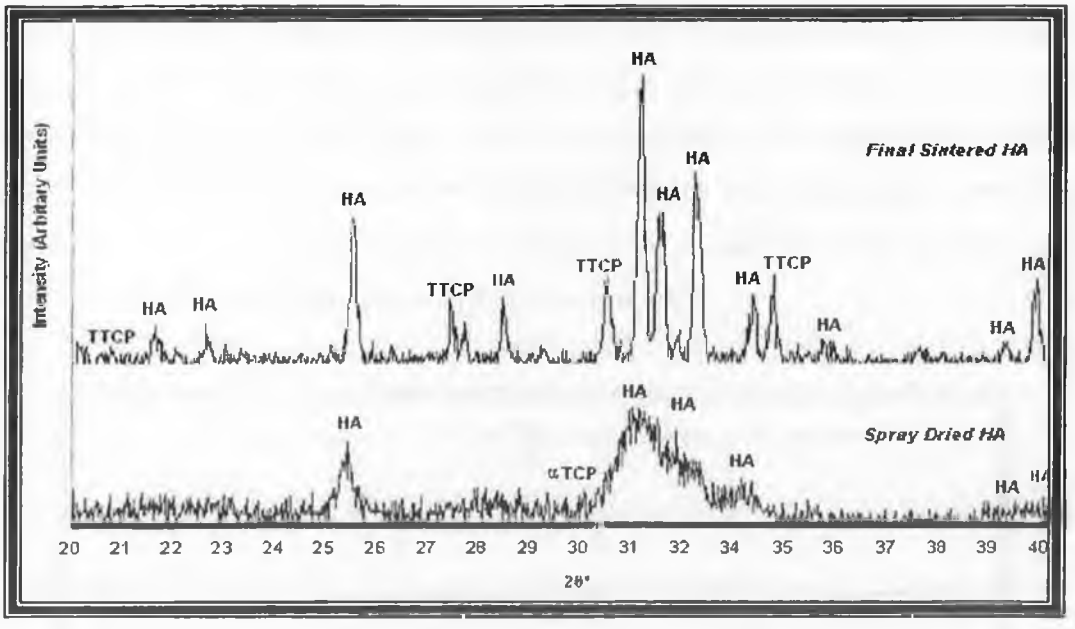

Figure B.10: HA XRD spectra and final sintered HA XRD spectra.

Appendix C

C.1 GENERAL TRANSPORT EUATION FOR MASS, MOMENTUM AND ENERGY

The equations used in the modelling of spray dryer in the FLUENT software are given below [**177-180,183,190,192,200-203,207-214**].

$$\frac{\partial}{\partial t}\int_V \rho\phi dV + \oint_A \rho\phi V.dA = \oint_A \Gamma\nabla\phi.dA + \int_V S_\phi dV \quad \text{---------Equation C.1}$$

Unsteady convection diffusion generation

Where, ϕ is a property per unit mass, ρ density, V control volume, A surface area, and ∇ gradient of ϕ , Γ diffusion coefficient ϕ, and S_ϕ surface of ϕ per unit volume.

These partial differential equations are discretized into a system of algebraic equations by finite volume method (FVM). These algebraic equations are then solved numerically to give a solution to the problem.

C.1.1 MASS CONSERVATION EQUATION

The general equation for conservation of mass, or continuity equation is as follows:

$$\frac{\partial\rho}{\partial t} + \nabla.(\rho\vec{v}) = S_m \quad \text{----------Equation C.2}$$

This general form of the mass conservation equation is valid for incompressible as well as compressible flows. The source S_m is the mass added to the continuous phase from the dispersed second phase (for an example in this research due to vaporisation of liquid droplets) and any other defined sources.

C.1.2 MOMENTUM CONSERVATION EQUATION

The general Conservation of momentum is given by:

$$\frac{\partial}{\partial t}(\rho\vec{v}) + \nabla.(\rho\vec{v}\vec{v}) = -\nabla p + \nabla.(\bar{\bar{\tau}}) + \rho\vec{g} + \vec{F} \text{ ----------Equation C.3}$$

where p is the static pressure, $\bar{\bar{\tau}}$ is the stress tensor , and $\rho\vec{g}$ and $\vec{F}$ are the gravitational body force and external body forces (that arise from the interaction with the dispersed phase), respectively.

The stress tensor $\bar{\bar{\tau}}$ can be described by:

$$\bar{\bar{\tau}} = \mu[(\nabla\vec{v} + \nabla\vec{v}^T) - \frac{2}{3}\nabla.\vec{v}I \text{ ----------Equation C.4}$$

where μ is the molecular viscosity, I is the unit tensor, and the second term ($\frac{2}{3}\nabla.\vec{v}I$) on the right hand side is the effect of volume dilation.

C.1.3 ENERGY EQUATION

General energy equation is as follows;

$$\frac{\partial}{\partial t}(\rho E) + \Delta.(\vec{v}(\rho E + p)) = \nabla.(k_{eff}\nabla T - \sum_j h_j\vec{J}_j + (\bar{\bar{\tau}}_{eff}.\vec{v})) + S_h \text{ ---Equation C.5}$$

where k_{eff} is the effective conductivity defined according to the turbulence model and $\vec{J}_j$ is the diffusion flux of species j. The first three terms on the right-hand side of Equation C.5 resent energy transfer due to conduction, species diffusion, and viscous dissipation, respectively. S_h includes the heat of chemical reaction, and any other volumetric heat sources is defined.

Where,

$$E = h - \frac{p}{\rho} + \frac{V^2}{2}, \quad h_j = \int_{Tref}^{T} C_{p,j}dt \text{ ----------Equation C.6}$$

Where, p is the given pressure, ρ is the density of gas, V is the velocity, C_p is heat at the constant pressure, and sensible enthalpy h is defined for ideal gases. Sensible enthalpy h is defined for ideal gases as $h = \sum_j Y_j h_j$, and Y_j is the mass fraction of species j and T_{rej} is 298.15 K.

C.2 DISCRETISATION (FVM)

Discretisation of the fluid flow governing equations can be illustrated simply by considering the steady-state conservation equation for transport of a scalar quantity ϕ. This can be written in integral form for an arbitrary control volume V as follows:

$$\oint \rho\phi\vec{v}.d\vec{A} = \oint \Gamma_\phi \nabla\phi.d\vec{A} + \int_V S_\phi dV \quad \text{----------Equation C.7}$$

Where,

ρ	Density
$\vec{v}$	Velocity Vector
$d\vec{A}$	Surface area vector
Γ_ϕ	Diffusion coefficient ϕ
$\nabla\phi$	Gradient of ϕ
S_ϕ	Surface of ϕ per unit volume

C.3 THE STANDARD $k-\varepsilon$ MODEL

The turbulence kinetic energy k and its rate of dissipation ε are obtained from the following transport equations:

The general transport equations for the Standard $k-\varepsilon$ model are as follow:

$$\frac{\partial}{\partial t}(\rho k) + \frac{\partial}{\partial x_i}(\rho k u_i) = \frac{\partial}{\partial x_i}\left[\left(\mu + \frac{\mu_t}{\sigma_k}\right)\frac{\partial k}{\partial x_j}\right] + G_K + G_b - \rho\varepsilon - Y_M + S_K \quad \text{----------Equation C.8}$$

and

$$\frac{\partial}{\partial t}(\rho\varepsilon)+\frac{\partial}{\partial x_i}(\rho\varepsilon u_i)=\frac{\partial}{\partial x_i}\left[\left(\mu+\frac{\mu_t}{\sigma_\varepsilon}\right)\frac{\partial\varepsilon}{\partial x_j}\right]+C_{1\varepsilon}\frac{\varepsilon}{k}+(G_K-C_{3\varepsilon}G_b)-C_{2\varepsilon}\rho\frac{\varepsilon^2}{k}+S_\varepsilon \text{-------}$$

Equation C.9

where,

G_K represents the generation of turbulence kinetic energy due to the mean velocity gradients, G_b is the generation of turbulence kinetic energy due to buoyancy. Y_M represents the contribution of the fluctuating dilatation in compressible turbulence to the overall dissipation rate. $C_{1\varepsilon}$, $C_{2\varepsilon}$ and $C_{3\varepsilon}$. σ_K and σ_ε are the turbulent Prandtl numbers for k and ε, respectively. S_K and S_ε are defined source terms.

Modelling the Turbulent Viscosity:

The turbulent (or eddy) viscosity, μ_t is computed by combining k and ε as follows:

$$\mu_t=\rho C_\mu\frac{K^2}{\varepsilon}$$ ----------Equation C.10

Where, C_μ is a constant. Model Constants are $C_{1\varepsilon}$, $C_{2\varepsilon}$, C_μ. σ_K and σ_ε have the following default values:

$$C_{1\varepsilon}=1.44,\ C_{2\varepsilon}=1.92,\ C_\mu=0.09,\ \sigma_K=1.0,\ \text{and}\ \sigma_\varepsilon=1.3$$

C.4 The Realizable $k-\varepsilon$ Model

The modelled transport equations for k and ε in the realizable $k-\varepsilon$ model are as follow:

$$\frac{\partial}{\partial t}(\rho K)+\frac{\partial}{\partial x_j}(\rho K u_j)=\frac{\partial}{\partial x_j}\left[\left(\mu+\frac{\mu_t}{\sigma_k}\right)\frac{\partial K}{\partial x_j}\right]+G_K+G_b-\rho\varepsilon-Y_M+S_K$$ -------Equation C.11

and

$$\frac{\partial}{\partial t}(\rho\varepsilon)+\frac{\partial}{\partial x_j}(\rho\varepsilon u_j)=\frac{\partial}{\partial x_j}\left[\left(\mu+\frac{\mu_t}{\sigma_\varepsilon}\right)\frac{\partial\varepsilon}{\partial x_j}\right]+\rho C_1 S_\varepsilon-\rho C_2\frac{\varepsilon^2}{K+\sqrt{\nu\varepsilon}}+C_{1\varepsilon}\frac{\varepsilon}{K}C_{3\varepsilon}G_b)+S_\varepsilon \quad \text{----}$$

-Equation C.12

Where,

$$C_1=\max\left[0.43,\frac{\eta}{\eta+5}\right],\ \eta=S\frac{K}{\varepsilon},\ S=\sqrt{2S_{ij}S_{ij}}$$

In these equations, G_K represents the generation of turbulence kinetic energy due to the mean velocity gradients. G_b is the generation of turbulence kinetic energy due to buoyancy. Y_M represents the contribution of the fluctuating dilatation in compressible turbulence to the overall dissipation rate. C_2 and $C_{1\varepsilon}$ are constants. σ_K and σ_ε are the turbulent Prandtl numbers for k and ε, respectively. S_K and S_ε are defined source terms. Note that the k equation is the same as that in the Standard $k-\varepsilon$ model, except for the model constants. However, the form of the ε equation is quite different from those in the Standard $k-\varepsilon$ models.

Modelling the Turbulent Viscosity

As in The Standard $k-\varepsilon$ models, the eddy viscosity is computed from:

$$\mu_t=\rho C_\mu\frac{K^2}{\varepsilon}$$ ----------Equation C.13

$$C_\mu=\frac{1}{A_0+A_s\dfrac{KU^*}{\varepsilon}}$$ ----------Equation C.14

Where,

$$U^*=\sqrt{S_{ij}S_{ij}+\widetilde{\Omega_{ij}\Omega_{ij}}}$$ ----------Equation C.15

and

$$\overline{\Omega_{ij}}=\Omega_{ij}-2\varepsilon_{ijk}w_K,\ \Omega_{ij}=\overline{\Omega_{ij}}-\varepsilon_{ijk}w_K$$ ---------- Equation C.16

where $\overline{\Omega_{ij}}$ is the mean rate-of-rotation tensor viewed in a rotating reference frame with the angular velocity w_K. The model constants $A_0 = 4.04$, $A_s = \sqrt{6}\cos\phi$.

Where,

$$\phi = \frac{1}{3}\cos^{-1}(\sqrt{6W}),\ W = \frac{S_{ij}S_{jk}S_{ki}}{\overline{S}^3},\ \overline{S} = \sqrt{S_{ij}S_{ij}},\ S_{ij} = \frac{1}{2}(\frac{\partial u_j}{\partial x_i} + \frac{\partial u_i}{\partial x_j})$$ -----Equation C.17

C_μ is a function of the mean strain and rotation rates, the angular velocity of the system rotation, and the turbulence fields (k and ε).

The model constants are;

$$C_{1\varepsilon} = 1.44,\ C_2 = 1.9,\ \sigma_k = 1.0,\ \sigma_\varepsilon = 1.2$$

C.5 THE REYNOLDS STRESS TRANSPORT MODEL

The exact transport equations for the transport of the Reynolds stresses, $\overline{\rho u_i' u_j'}$, may be written as follows:

Local Time Derivative + Convection = - Turbulent Diffusion + Molecular Diffusion - Stress Production - Buoyancy Production + Pressure Strain - Dissipation - Production by Rotation + Source Terms

$$\frac{\partial}{\partial t}(\overline{\rho u_i' u_j'}) + \frac{\partial}{\partial x_k}(\rho u k \overline{u_i' u_j'}) = -\frac{\partial}{\partial x_k}(\overline{\rho u_i' u_j' u_k'}) + \overline{p(\delta_{kj}u_i' + \delta_{ik}u_j')} + \frac{\partial}{\partial x_k}[\mu \frac{\partial}{\partial x_k}(\overline{u_i' u_j'}] -$$

$$\rho(\overline{u_i' u_k'}\frac{\partial u_j}{\partial x_k} + \overline{u_i' u_j'}\frac{\partial u_i}{\partial x_k}) - \rho\beta(g_i\overline{u_j'\theta} + g_j\overline{u_i'\theta}) + p(\frac{\partial u_i'}{\partial x_j} + \frac{\partial u_j'}{\partial x_i}) - 2\mu\frac{\overline{\partial u_i'}}{\partial x_k}\frac{\overline{\partial u_i'}}{\partial x_k} -$$

$$2\rho\Omega_k(\overline{u_j' u_m'}\varepsilon_{ikm} + \overline{u_i' u_m'}\varepsilon_{jkm}) + S_{source}$$ ----------Equation C.18

Where,

ρ is density of fluid, u_i', u_j', u_k' are velocity fluctuation in direction x_i', x_j', x_k' respectively, k is kinetic energy, ε is a dissipation tensor, β is thermal expansion, μ is viscosity, g is gravity, Ω is the rotation and θ is an angle of strain.

C.6 DISCRETE PHASE MODEL

The general equations for setting up and solving an unsteady discrete-phase problem are as follows:

C.6.1 EQUATIONS OF MOTION FOR PARTICLES

The trajectory of a discrete phase particle (or droplet or bubble) by integrating the force balance on the particle, which can be written in a Lagrangian reference frame. This force balance equates the particle inertia with the forces acting on the particle, and can be written (for the x direction in Cartesian coordinates) as:

$$\frac{du_p}{dt} = F_D(u - u_p) + \frac{g_x(\rho_p - \rho)}{\rho_p} + F_x \quad \text{----------Equation C.19}$$

Where, the drag force per unit particle mass is $F_D(u - u_p)$ and

$$F_D = \frac{18\mu}{\rho_p d_p^2} * \frac{C_D \,\mathrm{Re}}{24} \quad \text{----------Equation C.20}$$

Where, u is the fluid phase velocity, u_p is the particle velocity, μ is the molecular viscosity of the fluid, ρ is the fluid density, ρ_p is the density of the particle, and d_p is the particle diameter. C_D is discharge coefficient and Re is the relative Reynolds number, which is defined as

$$\mathrm{Re} = \frac{\rho d_p |u_p - u|}{\mu} \quad \text{----------Equation C.21}$$

$$C_D = \frac{24}{\mathrm{Re}}(1 + b_1 \mathrm{Re}^{b_2}) + \frac{b_3 \,\mathrm{Re}}{b_4 + \mathrm{Re}} \quad \text{----------Equation C.22}$$

Where,

b_1	$\exp(2.3288 - 6.4581\phi + 2.4486\phi^2)$
b_2	$0.0964 + 0.5565\phi$
b_3	$\exp(4.905 - 13.8944\phi^2 - 10.2599\phi^3)$
b_4	$\exp(1.4681 + 12.2584\phi - 20.7322\phi^2 + 15.8855\phi^3)$

The shape factor, ϕ, is defined as

$$\phi = \frac{s}{S} \text{----------EquaitonC.23}$$

Where s is the surface area of a sphere having the same volume as tat of the particle, and S is the actual surface area of the particle.

For sub-micron particles, a form of Stokes' Drag law is available. In this case, F_D is defined as:

$$F_D = \frac{18\mu}{d_p^2 \rho_p C_c} \text{----------Equation C.24}$$

The factor C_c is the Cunningham correction to Stokes' Drag law, which it can be compute from:

$$C_c = 1 + \frac{2\lambda}{d_p}(1.257 + 0.4e^{-(1.1d_p/2\lambda)}) \text{----------Equation C.25}$$

Where λ is the molecular mean free path.

C.6.2 THERMOPHORETIC FORCE

Small particles suspended in a gas that has a temperature gradient experience a force in the direction opposite to that of the gradient. This phenomenon is known as thermophoresis. FLUENT includes a thermophoretic force on particles in the additional force term, F_x, in Equation C.26:

$$F_x = -D_{T,p} \frac{1}{m_p T} \frac{\partial T}{\partial x} \text{----------Equation C.26}$$

where $D_{T,p}$ is the thermophoretic coefficient. It can define the coefficient to be constant, polynomial.

$$F_x = -\frac{6\pi d_p \mu^2 C_s (K + C_t Kn)}{\rho(1 + 3C_m Kn)(1 + 2K + 2C_t Kn)} \frac{1}{m_p T} \frac{\partial T}{\partial x} \text{----------Equation C.27}$$

Where,

Kn	Kundsen number = $2\lambda/d_p$
λ	Mean free path of the fluid
K	k/k_p
k	Fluid thermal conductivity based on translational energy
k_p	Particle thermal conductivity
C_s	1.17
C_t	2.18
C_m	1.14
m_p	Particle mass
T	Local fluid temperature
μ	Fluid viscosity

Where the expression in the model assumes that the particle is a sphere and that the fluid is an ideal gas.

C.6.3 BROWNIAN FORCE

For sub-micron particles, the effects of Brownian motion can optionally be included in the additional force term. The components of the Brownian force are modelled as a Gaussian white noise process with spectral intensity $S_{n,ij}$ given by;

$$S_{n,ij} = S_0 \delta_{ij} \text{ ----------Equation C.28}$$

Where δ_{ij} is the Kronecker delta function, and

$$S_0 = \frac{216\nu\sigma T}{\pi^2 \rho d_p^5 (\frac{\rho_p}{\rho})^2 C_c} \text{ ----------Equation C.29}$$

T is the absolute temperature of the fluid, ν is the kinematic viscosity, and σ is the Stefan-Boltzmann constant. Amplitudes of the Brownian force components are of the form

$$F_{bi} = \varsigma_i \sqrt{\frac{\pi S_0}{\Delta t}}$$ ----------Equation C.30

where ς_i are zero-mean, unit-variance-independent Gaussian random numbers. The amplitudes of the Brownian force components are evaluated at each time step. The energy equation must be enabled in order for the Brownian force to take effect. Brownian force is incorporated only when the model is non-turbulent.

C.6.4 SAFFMAN'S LIFT FORCE

The Saffman's lift force, or lift due to shear, can also be included in the additional force term as an option in FLUENT to model spray drying. The lift force can be expressed by:

$$\vec{F} = \frac{2k\nu^{1/2}\rho d_{ij}}{\rho_p d_p (d_{ik} d_{kl})^{1/4}} (\vec{v} - \vec{v}_p)$$ ----------Equation C.31

Where $k = 2.594$ and d_{ij} is the deformation tensor. This form of the lift force is intended for small particle Reynolds numbers. Also, the particle Reynolds number based on the particle-fluid velocity difference must be smaller than the square root of the particle Reynolds number based on the shear field. Since this restriction is valid for submicron particles, it is used in the model because the spray dryer produces small particles (submicron particles).

C.6.5 DROPLET SIZE DISTRIBUTIONS

For liquid sprays, a convenient representation of the droplet size distribution is the Rosin-Rammler expression. The complete range of sizes is divided into an adequate number of discrete intervals; each represented by a mean diameter for which trajectory calculations can be performed. If the size distribution is of the Rosin-Rammler type, the mass fraction of droplets of diameter greater than d is given by:

$$Y_d = e^{-(d/\bar{d})^n}$$ ----------Equation C.32

Where $\bar{d}$ is the size constant and n is the size distribution parameter.

C.7 Heat and Mass Transfer Calculations

For the heat and mass transfer calculations in the discrete models there are a number of laws are activated in the FLUENT such as:

Particle type	Laws activated
Droplet	Heating/ evaporation / boiling

C.7.1 LAW-INERT HEATING OR COOLING

The inert heating or cooling laws can be applied to the spray dryer models while the particle temperature is less than the vaporization temperature that the user defines as T_{vap} and after the volatile fraction, $f_{v,0}$ of a particle has been consumed. These conditions are written as;

Law of heating:

$$T_p < T_{vap}$$ ----------Equation C.33

Law cooling:

$$m_p \leq (1 - f_{v,0}) m_{p,0}$$ ----------Equation C.34

Where T_p is the particle temperature, $m_{p,0}$ is the initial mass of the particle, and m_p is its current mass.

The Law of heating can be applied until the temperature of the particle/droplet reaches its vaporization temperature. At this point a non-inert particle/droplet may proceed to obey one of the mass-transfer laws of vaporization and boiling.

The Heat in terms of balance to relate the particle temperature $T_p(t)$, can be related to the convective heat transfer and the absorption/emission of radiation at the particle surface is given:

$$m_p c_p \frac{dT_p}{dt} = hA_p(T_\infty - T_p) + \varepsilon_p A_p \sigma(\theta_R^4 - T_p^4)$$ ----------Equation C.35

Where,

m_p	Mass of the particle (kg)
c_p	Heat capacity of the particle (J/kg-K)
A_p	Surface area of the particle (m²)
T_∞	Local temperature of the continuous phase (K)
h	Convective heat transfer coefficient (W/m²-K)
ε_p	Particle emmissivity (dimensionless)
σ	Stefan-Boltzmann constant ($5.67*10^8$ W/m²-K^4)
θ_R	Radiation temperature = $(\frac{G}{4\sigma})^{1/4}$ (K)

Equation C.35 assumes that there is negligible internal resistance to heat transfer(that the particle is at uniform temperature throughout) G is the incident radiation in W/m² and define as :

$$G = \int_{\Omega=4\pi} I d\Omega$$ ----------Equation C.36

Where I is the radiation intensity and Ω is the solid angle.

Equation C.35 is integrated with respect to time using an approximate, linearised form that assumes that the particle temperature changes slowly from one time value to the next:

$$m_p c_p \frac{dT_p}{dt} = A_p\{-(h + \varepsilon_p \sigma T_p^3)T_p + (hT_\infty + \varepsilon_p \sigma \theta_R^4)\}$$ ----------Equation C.37

As the particle trajectory is computed, FLUENT integrates Equation C.37 to obtain the particle temperature at the next time value, yielding:

$$T_p(t + \Delta t) = \alpha_p + (T_p(t) - \alpha_p)e^{-\beta_p \Delta t}$$ ----------Equation C.38

Where Δt is the integration time step and

$$\alpha_p = \frac{hT_\infty + \varepsilon_p \sigma \theta_R^4}{h + \varepsilon_p \sigma T_p^3(t)} \text{ ----------Equation C.39}$$

and

$$\beta = \frac{A_p(h + \varepsilon_p \sigma T_p^3(t)}{m_p c_p} \text{ ----------Equation C.40}$$

FLUENT can also solve Equation C.37 using the equivalent mass transfer equation using a stiff coupled solver.

The heat transfer coefficient h is evaluated using the correlation:

$$Nu = \frac{hd_p}{k_\infty} = 2.0 + 0.6\,\mathrm{Re}_d^{1/2}\,\mathrm{Pr}^{1/3} \text{ ----------Equation C.41}$$

Where,

d_p	Particle diameter (m)
k_∞	Thermal conductivity of the continuous phase (W/m-k)
Re_d	Reynolds number based on the particle diameter and the relative velocity
Pr	Prandtl number for continuous phase ($c_p \mu / k_\infty$)

Finally, the heat lost or gained by a particle as it traverses each computational cell appears as a heat source or sink in subsequent calculations of the continuous phase energy equation. During Laws heating and cooling particles/droplets do not exchange mass with the continuous phase.

C.7.2 LAW OF DROPLET VAPORIZATION

The Law of droplet vaporization can be activated in models to predict vaporization from a discrete phase droplet. The law initiates when the temperature of a droplet reaches its vaporization temperature, T_{vap} and continues until the droplet reaches its boiling point, T_{bp}, or until the droplet's volatile fraction is completely consumed:

$$T_p < T_{bp}$$ ----------Equation C.42

$$m_p > (1 - f_{v,0}) m_{p,0}$$ ----------Equation C.43

The start of the vaporization law is determined by the user setting T_{vap}. Vaporization stops only when the droplet temperature falls below its dew point. During vaporization no evaporation is predicted. When the boiling point is reached, the droplet vaporization is the predicted using the boiling rate.

(a) Mass Transfer during the Law of Vaporization

The rate of vaporization is governed by gradient diffusion, where the flux of vapour in a gas phase is related to the gradient of the vapour concentration between the droplet surface and the bulk gas, as given by:

$$N_i = k_c (C_{i,s} - C_{i,\infty})$$ ----------Equation C.44

Where,

N_i	Molar flux of vapour (kgmol/m²-s)
k_c	Mass transfer coefficient (m/s)
$C_{i,s}$	Vapour concentration at the droplet surface (kgmol/m³)
$C_{i,\infty}$	Vapour concentration in the bulk gas (kgmol/m³)

When N_i is positive evaporation occurs. If N_i is negative the droplet temperature falls below the dew point and condensation conditions exist), the FLUENT treats the droplet as inert.

The concentration of vapour at the droplet surface has evaluated by assuming that the partial pressure of vapour at the interface is equal to the saturated vapour pressure, P_{sat}, at the particle droplet temperature, T_p:

$$C_{i,s} = \frac{p_{sat}(T_p)}{RT_p}$$ ----------Equation C.45

Where R is the universal gas constant, the concentration of vapour in the bulk gas can be calcualted is known from solution of the transport equation for species i:

$$C_{i,\infty} = X_i \frac{p_{op}}{RT_\infty}$$ ----------Equation C.46

Where X_i is the local bulk mole fraction of species i, p_{op} is the operating pressure, and T_∞ is the local bulk temperature in the gas. The mass transfer coefficient in Equation C.44 is used to calculate Nusselt correlation:

$$Nu_{AB} = \frac{k_c d_p}{D_{i,m}} = 2.0 + 0.6\,\mathrm{Re}_d^{1/2} Sc^{1/3}$$ ----------Equation C.47

Where,

$D_{i,m}$	Diffusion coefficient of vapour in the bulk (m²/s)
Sc	The Schmidt number = $\frac{\mu}{\rho D_{i,m}}$
d_p	Particle droplet diameter (m)

And the mass of the droplet is reduced;

$$m_p(t + \Delta t) = m_p(t) - N_i A_p M_{w,i} \Delta t$$ ----------Equation C.48

Where,

$M_{w,i}$	Molecular weight of species i (kg/kgmol)
m_p	Mass of the droplet (kg)
A_p	Surface area of the droplet (m²)

(b) Heat Transfer to the Droplet

The droplet is updated temperature according to a heat balance that relates the sensible heat change in the droplet to the convective and latent heat transfer between the droplet and the continuous phase:

$$m_p c_p \frac{dT_p}{dt} = hA_p(T_\infty - T_p) + \frac{dm_p}{dt} h_{fg} + A_p \varepsilon_p \sigma(\theta_R^4 - T_p^4) \text{--------Equation C.49}$$

where,

c_p	Droplet heat capacity (J/kg-k)
T_p	Droplet temperature (k)
h	Convective heat transfer coefficient (W/m²-K)
T_∞	Temperature of continuous phase (K)
h_{fg}	Rate of evaporation (kg/s)
ε_p	Latent heat (J/kg)
σ	Particle emissivity (dimensionless)
θ_R	Stefan- Boltzmann
$\frac{dm_p}{dt}$	Radiation temperature = $(\frac{I}{4\sigma})^{1/4}$, where I is radiation intensity

C.7.3 LAW OF DROPLET BOILING

The droplet boiling Law can be applied to predict convective boiling of a discrete phase droplet when the temperature of a droplet has reached its boiling temperature, T_{bp} and while the mass of the droplet exceeds its non-volatile fraction, $(1 - f_{v,0})$.

$$T_p \geq T_{bp} \text{----------Equation C.50}$$

and,

$$m_p > (1 - f_{v,0}) m_{p,0} \text{----------Equation C.51}$$

When the droplet temperature reaches the boiling point, a boiling rate equation is then applied:

$$\frac{d(d_p)}{dt} = \frac{4k_\infty}{\rho_p c_{p,\infty} d_p}(1 + 0.23\sqrt{\mathrm{Re}_d})\ln[1 + \frac{c_{p,\infty}(T_\infty - T_p)}{h_{fg}}]$$ -------Equation C.52

Where

$c_{p,\infty}$	Heat capacity of the gas (J/kg-k)
ρ_p	Droplet density (kg/m³)
k_∞	Thermal conductivity of the gas (W/m-K)

Equation C.52 was derived assuming steady flow at constant pressure. The model requires $T_\infty \geq T_{bp}$ in order for boiling occurring and that the droplet remains at fixed temperature T_{bp} throughout the boiling law.

C.8 SPRAY MODEL

C.8.1 THE AIR-BLAST/AIR-ASSIST ATOMIZER MODEL

The FLUENT air blasted model is used the Linearized Instability Sheet Atomization (LISA) model. The LISA model is divided into two stages:

1. Film formation
2. Sheet break-up and atomization

(1) Film Formation

The thickness of film, t, is related to the mass flow rate of feed by:

$$\dot{m} = \pi\rho u t(d_{inj} - t)$$ ----------Equation C.53

Where d_{inj} is theinjector exit diameter, and $\dot{m}$ is the mass flow rate, which must be measured experimentally. The unknown in Equation C.53 is u, the axial component of velocity at the injector exit. This quantity depends on internal details of the injector or the nozzle. The total velocity is assumed to be related to the injector pressure by:

$$U = k_v \sqrt{\frac{2\Delta p}{\rho l}} \quad \text{----------Equation C.54}$$

k_v is a function of the injector design and injection pressure. If the swirl ports are treated as nozzles or it is nozzle, Equation C.54 is then an expression for the coefficient of discharge for the swirl ports, assuming that the majority of the pressure drop through the injector or nozzle occurs at the ports or nozzle exit. The coefficient of discharge (C_d) for single-phase nozzles with sharp inlet corners and L/d of 4 is typically 0.78 or less. Hence, 0.78 should be a practical upper bound for k_v. Reducing k_v by 10% to allow for other momentum losses in the injector gives an estimate of 0.7 can be used.

Physical limits on k_v are such that it must be less than unity by conservation of energy, and it must be large enough to permit sufficient mass flow. To guarantee that the size of the air core is non-negative, the following expression k_v is given by:

$$k_v = \max(0.7, \frac{4\dot{m}}{\pi d_0^2 \rho_l \cos\theta} \sqrt{\frac{\rho l}{2\Delta p}}) \quad \text{----------Equation C.55}$$

It assuming that Δp is known, Equation C.54 can be used to find U. Once U is determined, u is found from:

$$u = U \cos\theta \quad \text{----------Equation C.56}$$

Where θ is the spray angle, which is assumed to be known and generally it is 45 degree. In the present the study the nozzle angle has set for 45 degree to get maximum disintegration of liquid feed.

(2) Sheet Break-up

The model assumes:

- Two-dimensional
- Viscous
- Incompressible liquid sheet of thickness $2h$ moves with velocity U through a quiescent
- Inviscid, incompressible gas medium.

The model defines the liquid and gas have densities of ρ_l and ρ_g, respectively, and the viscosity of the liquid is μ_l. A coordinate system moves the sheet, and a spectrum of infinitesimal disturbances of the form is given by:

$$\eta = \eta_0 e^{ikx+\omega t} \text{ ----------Equation C.57}$$

Where η_0 is the initial wave amplitude, $k = 2\pi / \lambda$ is the wave number, and $\omega = \omega_r + i\omega_i$ is the complex growth rate. It is described that the most unstable disturbance has the largest value of ω_r, denoted by Ω, and is assumed to be responsible for sheet break-up. Thus, it is desired to obtain a dispersion relation $\omega = \omega(k)$ from which the most unstable disturbance can be deduced the dispersion relation for the sinuous mode is given by:

$$\omega^2(\tanh(kh)+Q) + (4\nu_l k^2 QkU) + 4\nu_l k^4 \tanh(kh) - 4\nu_l^2 k^3 l \tanh(lh) - QU^2K^2 + \frac{\sigma k^3}{\rho_l} = 0 \text{ ----}$$

-----Equation C.58

Where,

$$Q = \rho_g / \rho_l \text{ and } l^2 = k^2 + \omega / \nu_l \text{ ----------Equation C.59}$$

A critical Weber number of We_g = 27/16 (based on the relative velocity, the gas density, and the sheet half-thickness), the fastest-growing waves are short. Below 27/16, the wavelengths are long compared to the sheet thickness.

The resulting expression for the growth rate has given in the model by:

$$\omega_r = \frac{1}{\tanh(kh)+Q}[-2\nu_l k^2 \tanh(kh) + \sqrt{4\nu_l^2 k^4 \tanh^2(kh) - Q^2U^2K^2 - (\tanh(kh)+Q)(-QU^2k^2 + \frac{\sigma k^3}{\rho_l})}]$$

----------Equation C.60

The Equation C.59 to Equation C.60 reduce with assumptions, an order-of-magnitude analysis using typical values from the inviscid solutions shows that the terms of second order in viscosity can be neglected in comparison to the other terms in Equation C.60. In

addition, the density ratio Q is on the order of 10^3 in typical applications and hence it is assumed that $Q << 1$.

The physical mechanism of sheet disintegration in the FLUENT only for long waves. For long waves, ligaments are assumed to form from the sheet break-up process once the unstable waves reach a critical amplitude. If the surface disturbance has reached a value of η_b at break-up, a break-up time, τ, can be evaluated is given by:

$$\eta_b = \eta_0 e^{\Omega\tau} \Rightarrow \frac{1}{\Omega}\ln(\frac{\eta_b}{\eta_0})$$ ----------Equation C.61

Where Ω, the maximum growth rate is represented by numerically maximizing Equation C.60 as a function of k.

Therefore;

The sheet breaks up and ligaments will be formed at a length given by:

$$L_b = U\tau = \frac{U}{\Omega}\ln(\frac{\eta_b}{\eta_0})$$ ----------Equation C.62

Where the quantity $\ln(\frac{\eta_b}{\eta_0})$ is an empirical *sheet* constant from 3 to 12, it is specified externally in the model.

It is assumed that the ligaments are formed from tears in the sheet once per wavelength, the resulting diameter is given by:

$$d_L = \sqrt{\frac{8h}{K_s}}$$ ----------Equation C.62

Where K_S is the wave number corresponding to the maximum growth rate Ω.

The ligament diameter depends on the sheet thickness, which is a function of the break-up length. The film thickness is calculated from the break-up length and the radial distance from the centre line to the mid-line of the sheet at the atomizer exit r_0:

$$h_{end} = \frac{r_0 h_0}{r_0 + L_b \sin(\frac{\theta}{2})} \text{----------Equation C.63}$$

The value of d_L is assumed to be linearly proportional to the wavelength that breaks-up the sheet is given by:

$$d_L = 2\pi C_L / K_s \text{----------Equation C.64}$$

where C_L, or the *ligament* constant, is equal to 0.5 by default in the model. The wavelength is calculated from the wave number K_s.

The variable Oh is the Ohnesorge number; it is a combination of Reynolds number and Weber number that is given by:

$$d_0 = 1.88 d_L (1 + 3Oh)^{1/6} \text{----------Equation C.65}$$

This procedure determines the most probable droplet size. The spread parameter has assumed to be 3.5, based on past modelling experience. The spray cone angle has defined externally input which has based on the setting of two fluid nozzle atomizer. The dispersion angle of the spray has assumed to be a fixed value of 6°.

C.8.2 DROPLET COLLISION MODEL

The FLUENT estimates the number of droplet collisions, tracking of droplets and their outcomes for N droplets, each droplet has $N-1$ possible collision partners. Thus, the number of possible collision pairs is approximately $\frac{1}{2}N^2$. (The factor of $\frac{1}{2}$ appears because droplet A colliding with droplet B is identical to droplet B colliding with droplet A. This symmetry reduces the number of possible collision events by half.) An important consideration is that the collision algorithm must calculate possible collision events at

every time step. A spray can consist of several million droplets; the computational cost of a collision calculation from first principles is prohibitive in the simulation models. The fluent uses the concept of parcels. Parcels are statistical representations of a number of individual droplets. For example, if the FLUENT tracks a set of parcels, each of which representing 1000 droplets, the cost of the collision calculation is reduced by a factor of 10^6. Because the cost of the collision calculation still scales with the square of N, the reduction of cost is significant; however, the effort to calculate the possible intersection of so many parcel trajectories would still be prohibitively expensive.

C.8.3 CALCULATION PROCEDURE OF DISCRETE AND CONTINUOUS PHASES OF SPRAY DRYER IN THE FLUENT SOFTWARE

(a) Momentum Exchange

The momentum transfer from the continuous phase to the discrete phase is computed by:

$$F = \sum \left(\frac{18\mu C_D \,\mathrm{Re}}{\rho_p d_p^2 24}(u_p - u) + F_{other}\right)\dot{m}_p \Delta t \quad \text{----------Equation C.66}$$

Where,

μ	Viscosity of the fluid
ρ_p	Density of the particle
d_p	Diameter of the particle
Re	Relative Reynolds number
u_p	Velocity of the particle
u	Velocity of fluid
C_D	Drag coefficient
$\dot{m}_p$	Mass flow rate of the particles
Δt	Time step
F_{other}	Other interaction forces

(b) Heat Exchange

The heat transfer from the continuous phase to the discrete phase is given by:

$$Q = [\frac{\overline{m}_p}{m_{p,0}} c_p \Delta T_p + \frac{\Delta m_p}{m_{p,0}} (-h_{fg} + h_{pyrol} + \int_{Tref}^{T_p} c_{p,i} dt)] \dot{m}_{p,o}$$ ----------Equation C.67

Where,

$\overline{m}_p$	Average mass of the particle in the control volume (kg)
$m_{p,0}$	Initial mass of the particle (kg)
c_p	Heat capacity of the particle (J/kg-K)
ΔT_p	Temperature change of the particle in the control volume (K)
Δm_p	Change in the mass of the particle in the control volume (kg)
h_{fg}	Latent heat of volatiles evolved (J/kg)
h_{pyrol}	Heat of pyrolysis as volatiles are evolved (J/kg)
$c_{p,i}$	Heat capacity of volatiles evolved (J/kg)
T_p	Temperature of the particle upon exit of the control volume (K)
T_{ref}	Reference temperature of enthalpy (K)
$\dot{m}_{p,o}$	Initial mass flow rate of the particle injection tracked (kg/s)

(c) Mass Exchange

The mass transfer from the discrete phase to the continuous phase can be computed by:

$$M = \frac{\Delta m_p}{m_{p,0}} \dot{m}_{p,0}$$ ----------Equation 2.60

Where,

$m_{p,0}$	Initial mass of the particle (kg)
Δm_p	Change in the mass of the particle in the control volume (kg)
$\dot{m}_{p,o}$	Initial mass flow rate of the particle injection tracked (kg/s)

The mass exchange appears as a source of mass in the continuous phase continuity equation and as a source of a chemical species defined in the model. The mass sources are included in any subsequent calculations of the continuous phase flow field.

Appendix D

D.1 ANOVA TABLE

Drying chamber Particle	DF	SS	MS (variance)	F	p	SD
Total	13	9687.38	745.183			
Constant	1	8587.91	8587.91			
Total Corrected	12	1099.47	91.6222			9.57195
Regression	9	1021.76	113.529	4.38301	**0.126**	10.655
Residual	3	77.7061	25.902			5.0894
Lack of Fit (Model Error)	--	--	--	--	--	--
Pure Error (Replicate Error)	--	--	--			--

N = 13	Q2 = .1631	Cond. no. = 7.1093
DF = 3	R2 = 0.929	Y-miss = 0
	R2 Adj. = 0.717	RSD = 5.0894

Cyclone Particle Size	DF	SS	MS (variance)	F	p	SD
Total	13	2889.03	222.233			
Constant	1	2526.21	2526.21			
Total Corrected	12	362.825	30.2354			5.49867
Regression	9	356.645	39.6273	19.2385	**0.017**	6.29502
Residual	3	6.17938	2.05979			1.4352
Lack of Fit (Model Error)	--	--	--	--	--	--
Pure Error (Replicate Error)	--	--	--			--

N = 13	Q2 = 0.727	Cond. no. = 7.1093
DF = 3	R2 = 0.983	Y-miss = 0
	R2 Adj. = 0.932	RSD = 1.4352

Wall DEPOSITION	DF	SS	MS (variance)	F	p	SD
Total	13	424	32.6154			
Constant	1	398.769	398.769			
Total Corrected	12	25.2307	2.10256			1.45002
Regression	9	23.4807	2.60897	4.47253	0.122	1.61523
Residual	3	1.75	0.583333			0.763762
Lack of Fit (Model Error)	--	--	--	--	--	--
Pure Error (Replicate Error)	--	--	--			--

N = 13 Q2 = 0.130 Cond. no. = 7.1093
DF = 3 R2 = 0.931 Y-miss = 0
R2 Adj. = 0.723 RSD = 0.7638

Over all Thermal η	DF	SS	MS (variance)	F	p	SD
Total	13	40961.2	3150.86			
Constant	1	40543.2	40543.2			
Total Corrected	12	417.965	34.8304			5.90173
Regression	9	314.85	34.9834	1.0178	0.557	5.91468
Residual	3	103.114	34.3715			5.86272
Lack of Fit (Model Error)	--	--	--	--	--	--
Pure Error (Replicate Error)	--	--	--			--

N = 13 Q2 = -0.2 Cond. no. = 7.1093
DF = 3 R2 = 0.753 Y-miss = 0
R2 Adj. = 0.013 RSD = 5.8627

D.2 AIR PIPE

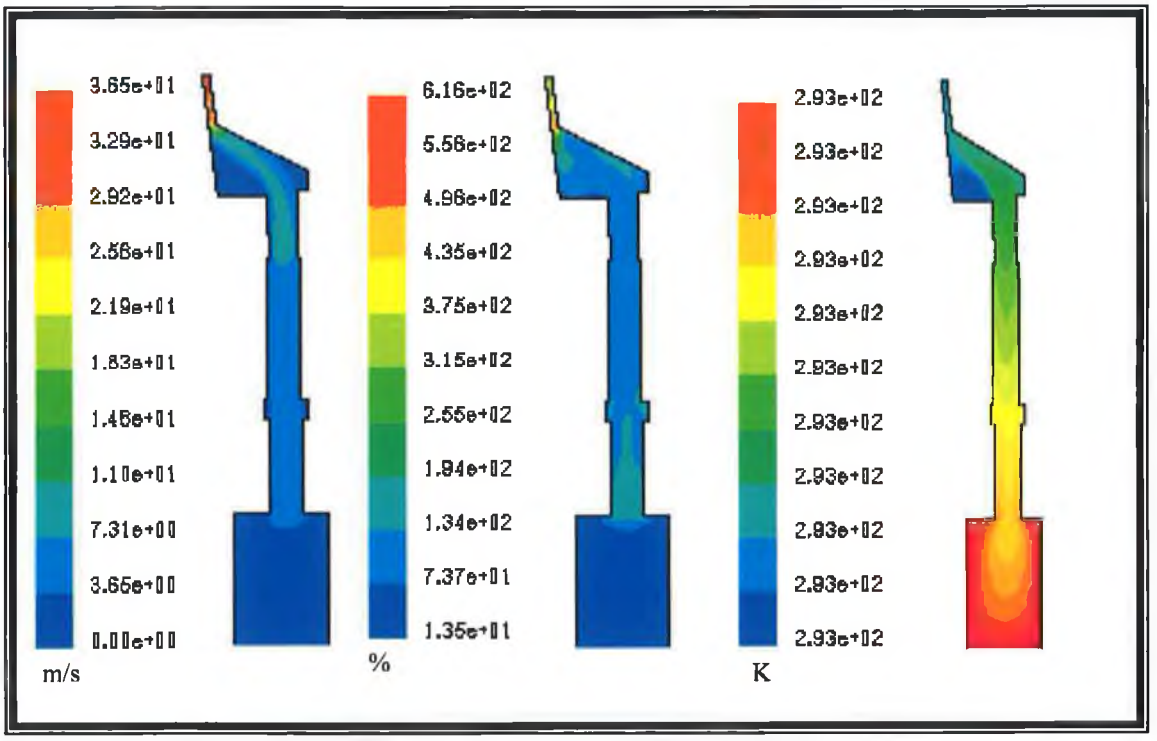

Figure D-1: Velocity profile at 2.19 m/s inlet velocity and turbulence intensity and temperature distribution.

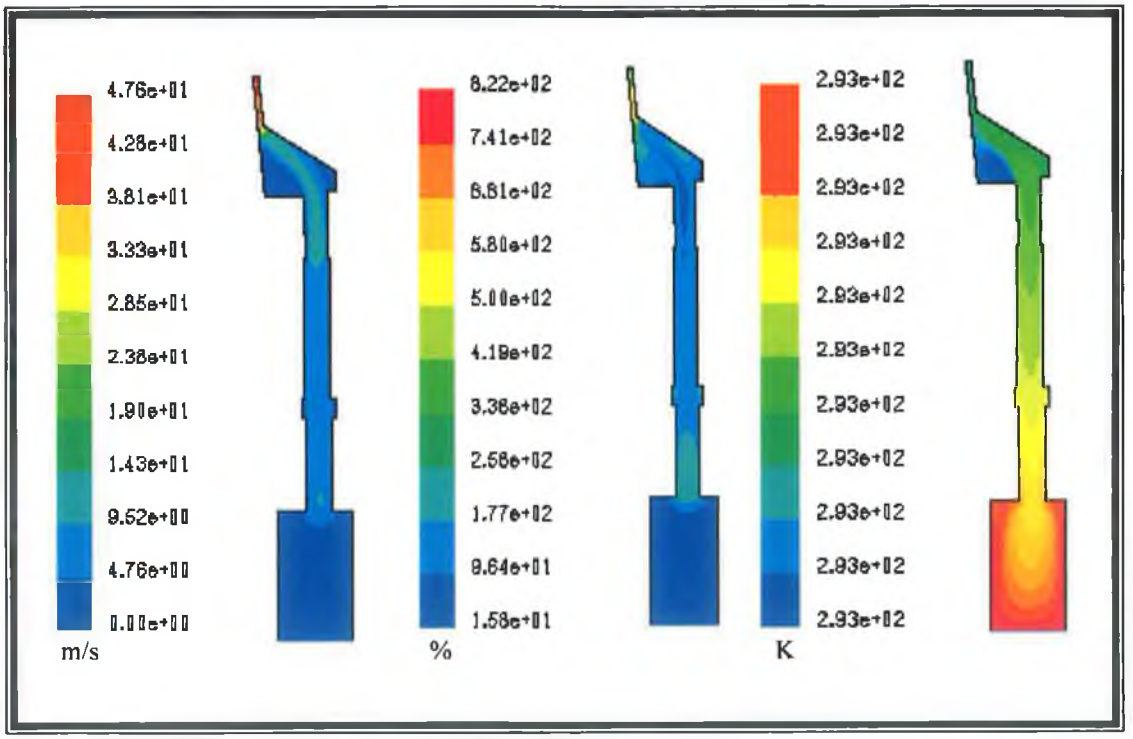

Figure D-2: Velocity profile at 2.95 m/s inlet velocity and turbulence intensity and temperature distribution.

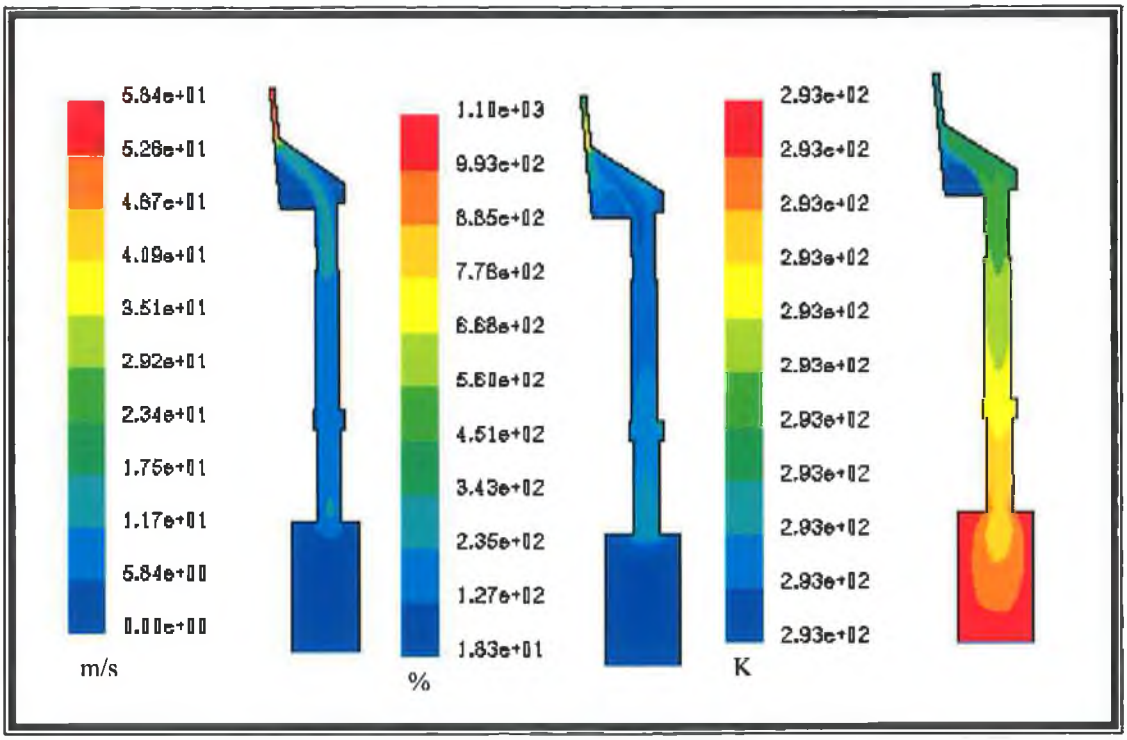

Figure D-3: Velocity profile at 3.65 m/s inlet velocity and turbulence intensity and temperature distribution.

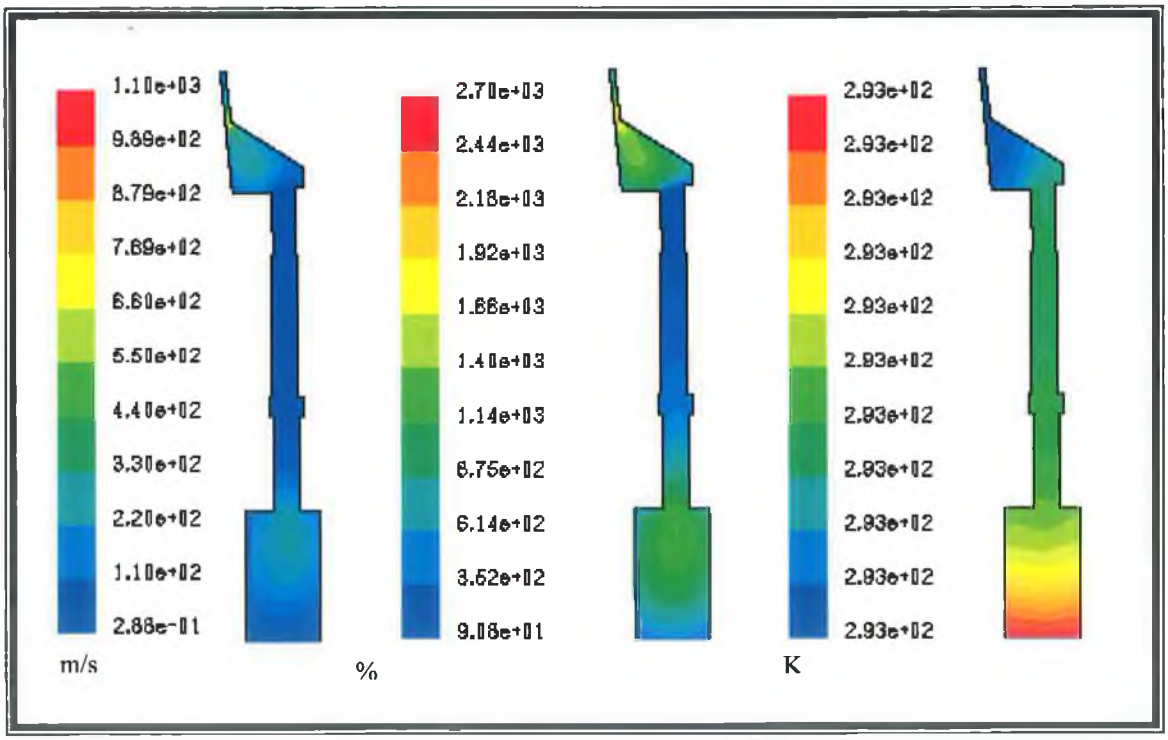

Figure D-4: Velocity profile at 4.38 m/s and turbulence intensity and temperature distribution.

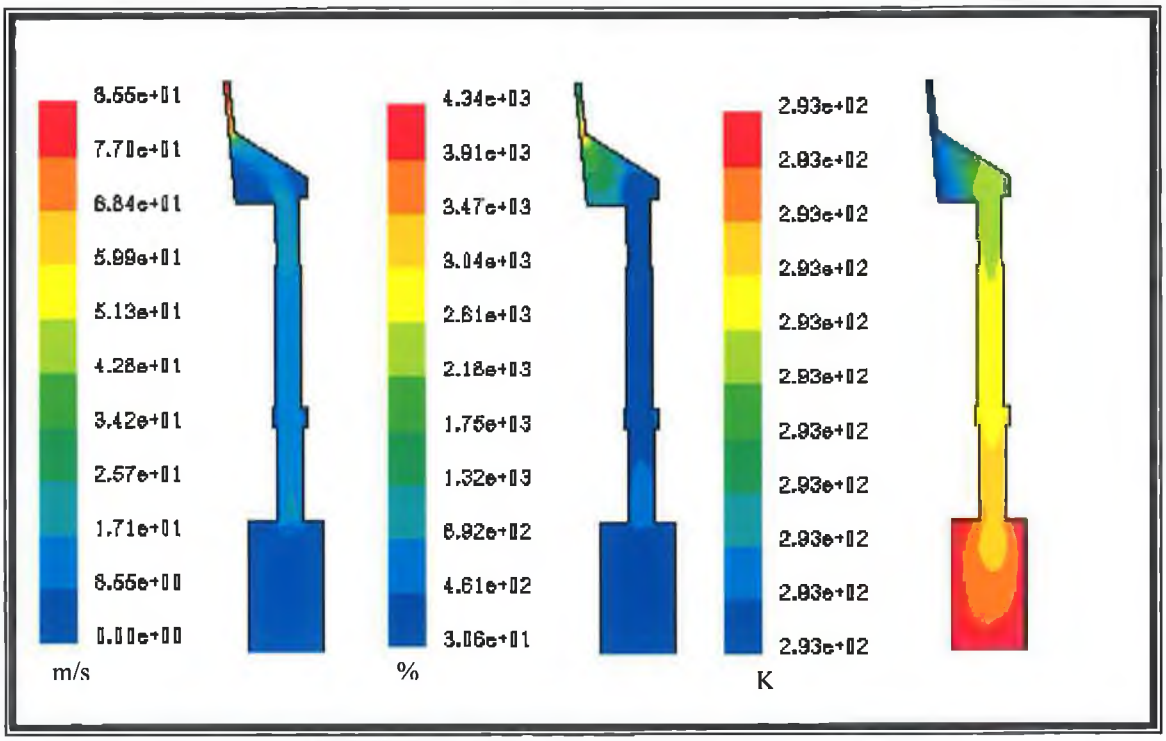

Figure D-5: Velocity profile at 7.31 m/s inlet velocity, turbulence intensity and temperature distribution.

D.3 Feed Nozzle

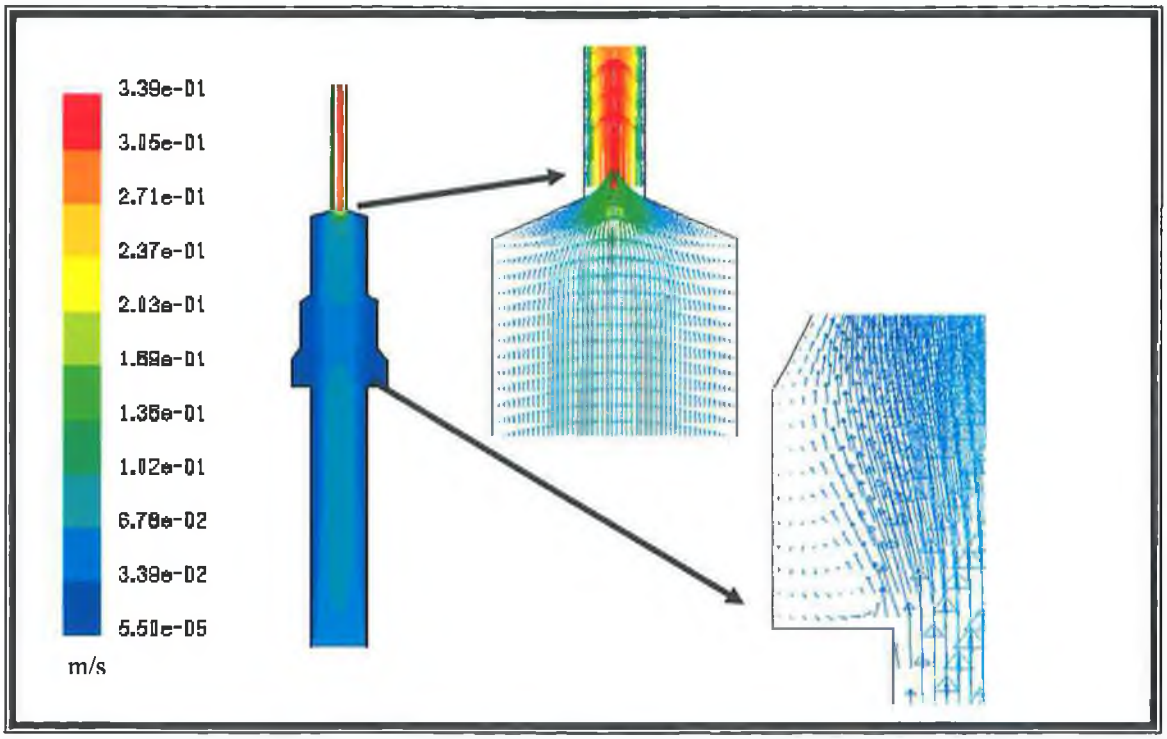

Figure D-6: The feed pipe velocity profile and vector at 50 rpm of peristaltic pump.

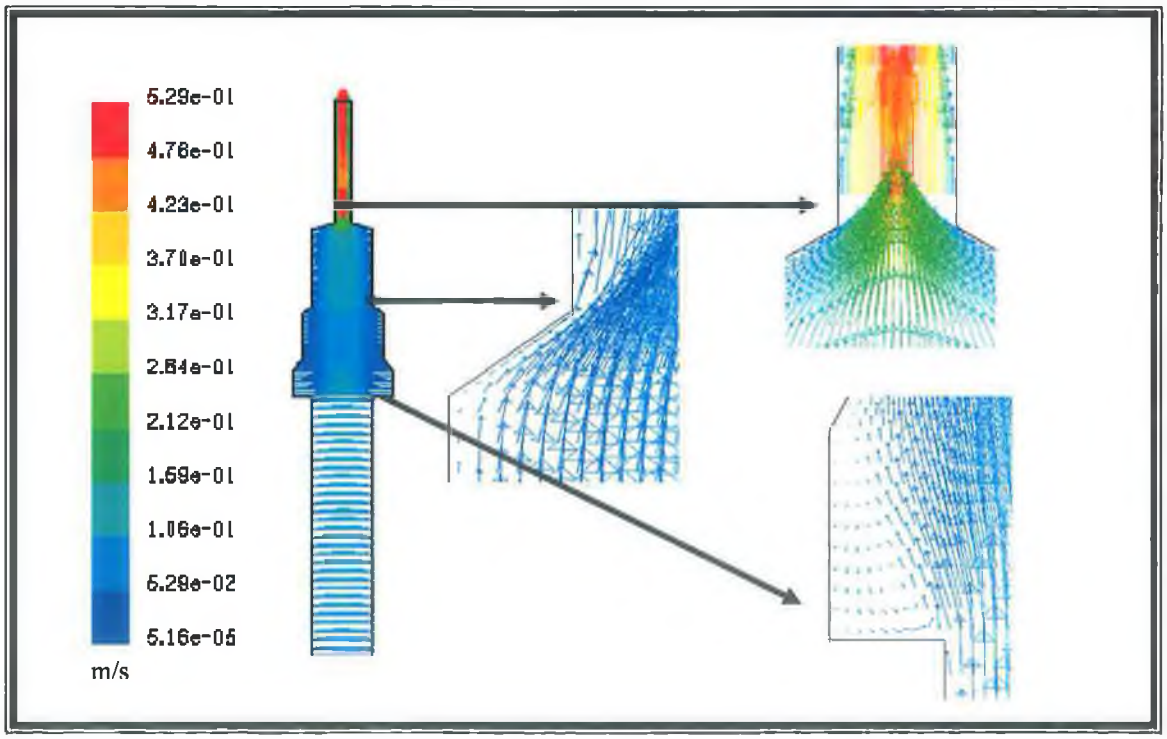

Figure D-7: The feed pipe velocity profile and vector at 75 rpm of peristaltic pump.

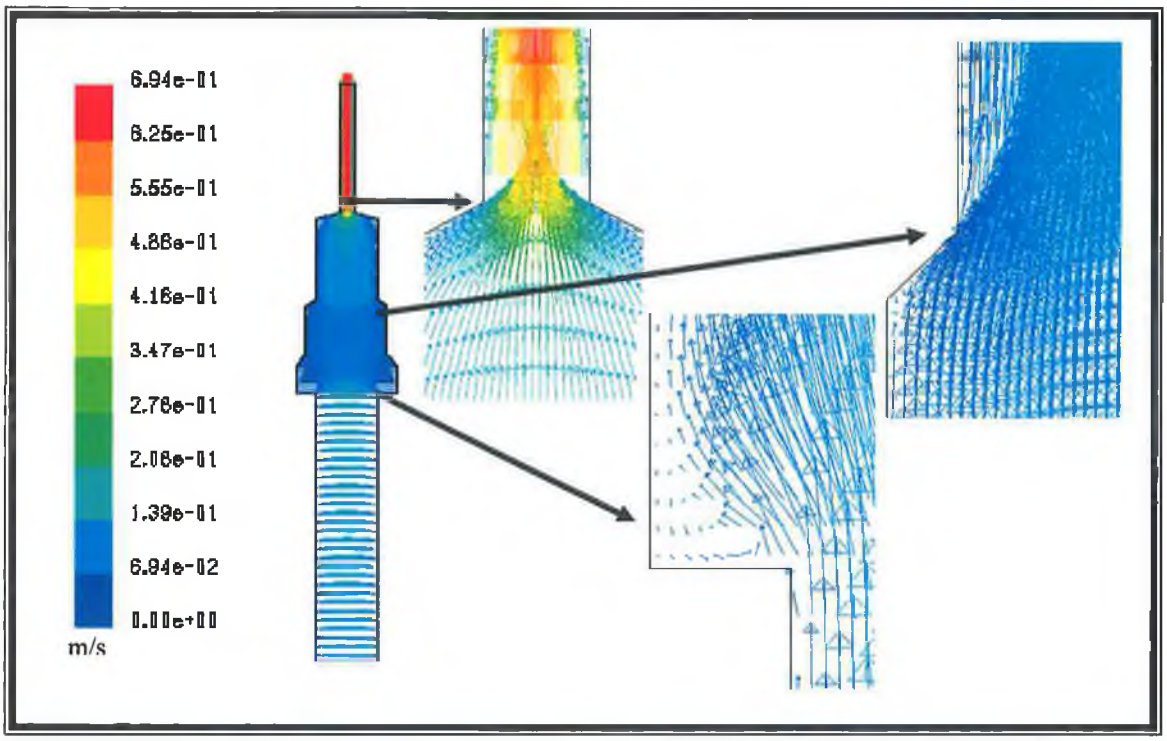

Figure D-8: The feed pipe velocity profile and vector at 100 rpm of peristaltic pump.

D.4 TEMPERATURE SIMULATED PROFILE

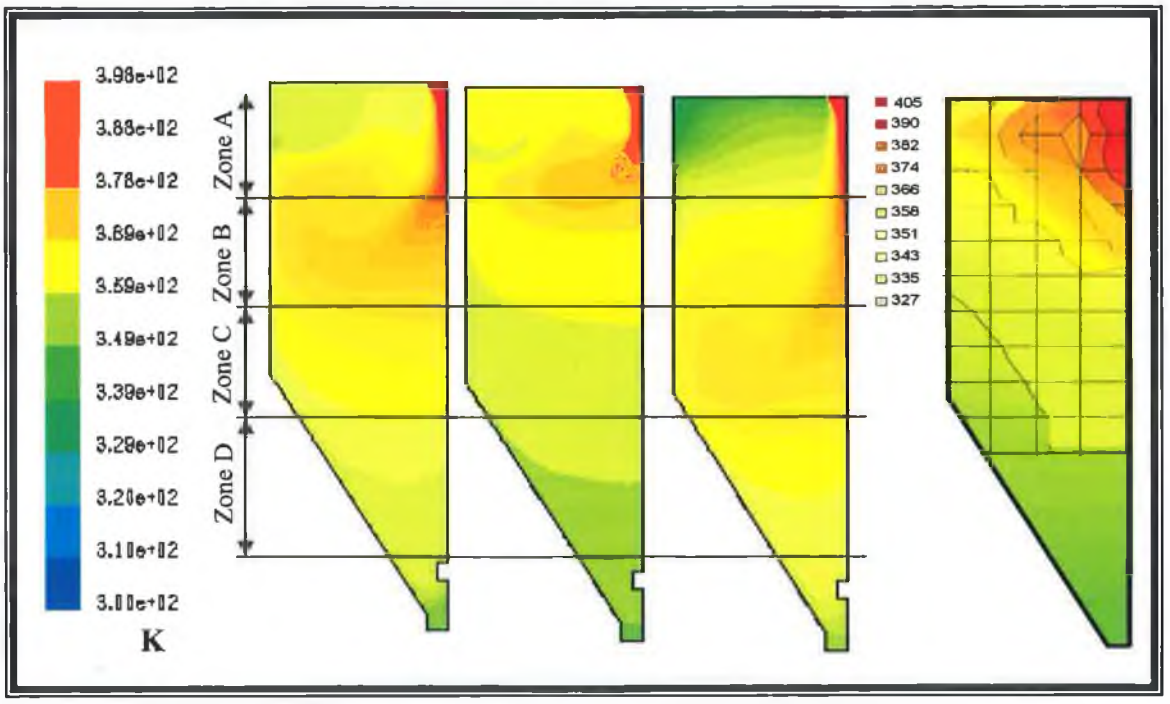

(a)

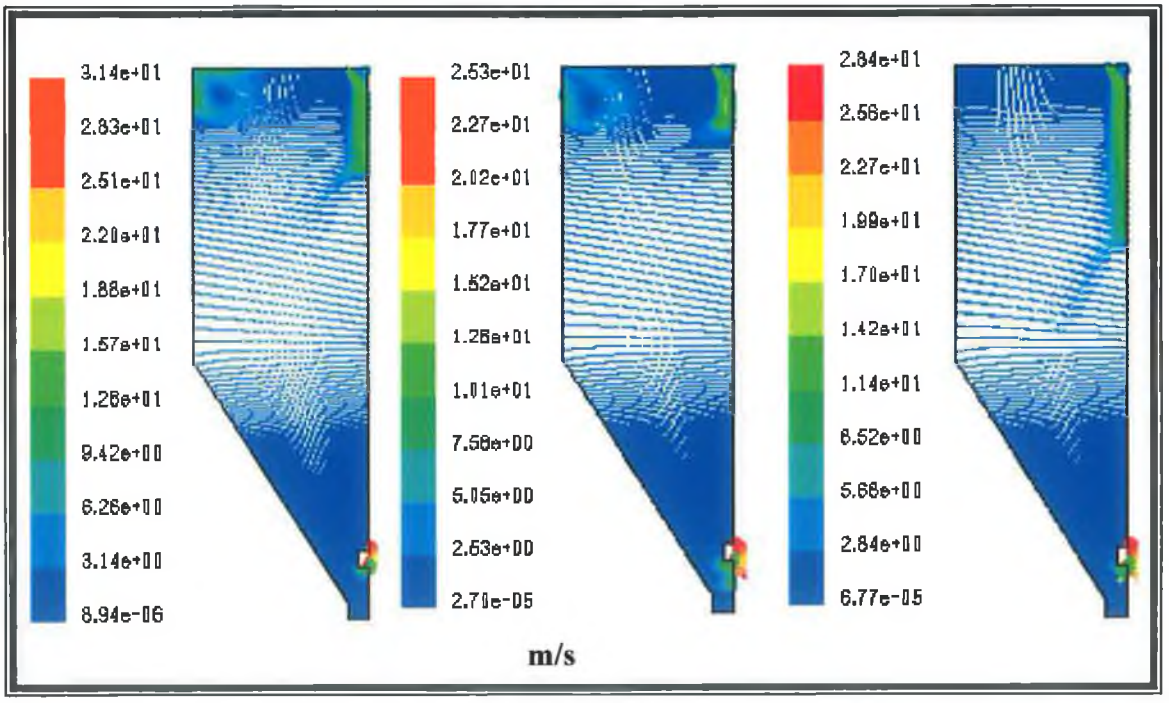

(b)

Figure D-9: Temperature profile and velocity vector by S*K*-Є, R*K*-Є, RSM methods, and measured (inlet condition tem-398 K, velocity-14.6m/s).

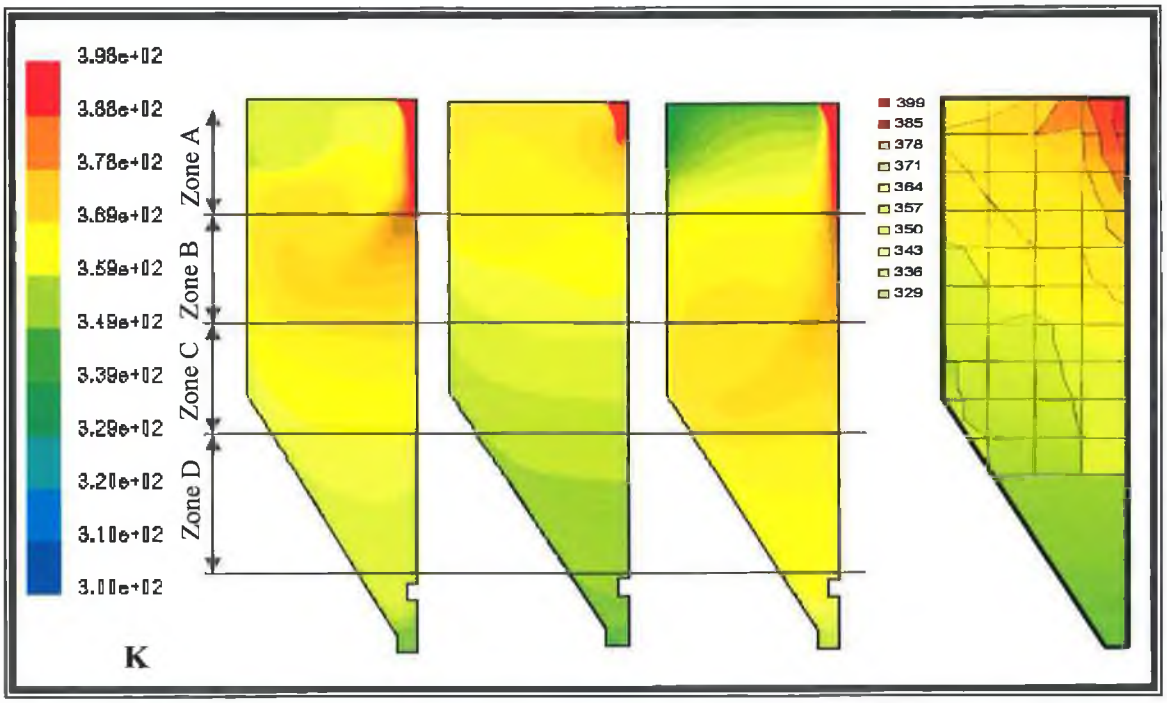

(a)

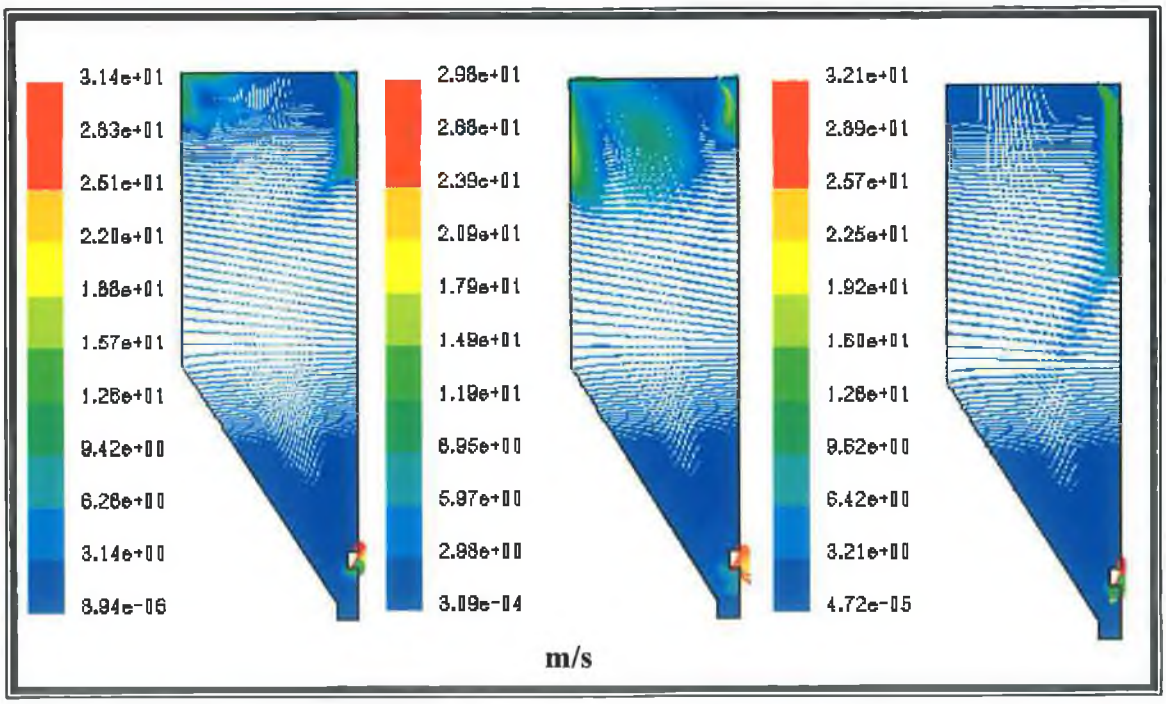

(b)

Figure D-10: Temperature profile and velocity vector by S*K*-ϵ, R*K*-ϵ, RSM method, and measured (inlet condition tem-398 K, velocity-16.6m/s).

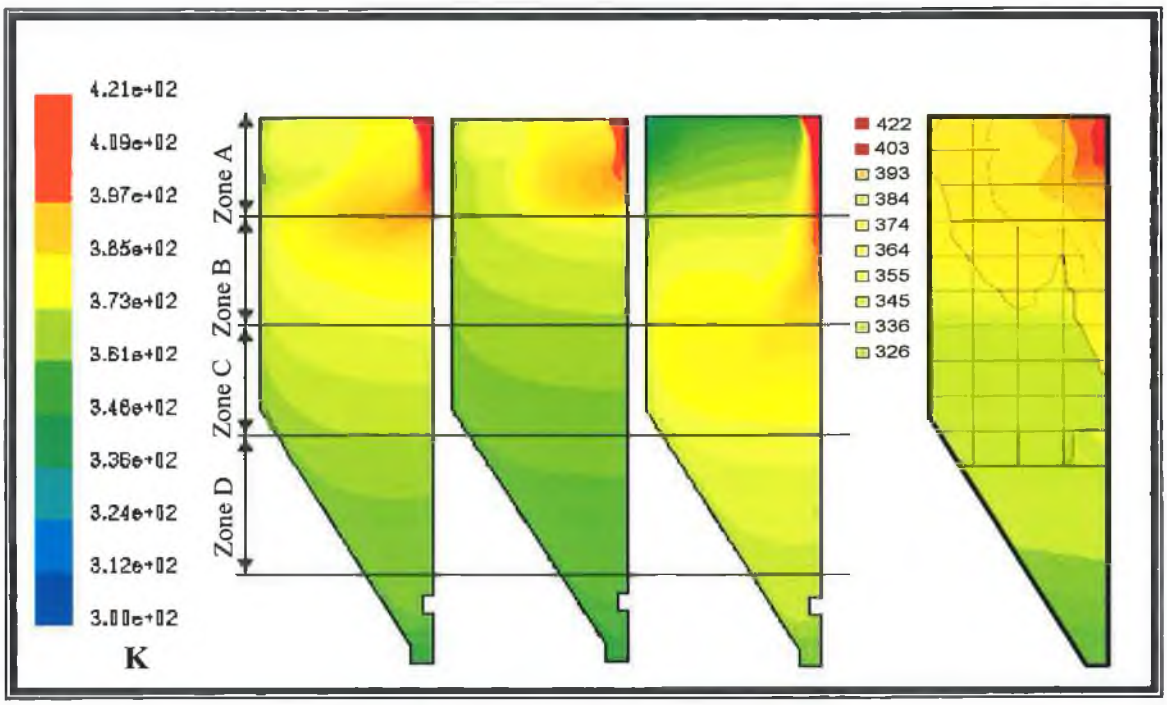

(a)

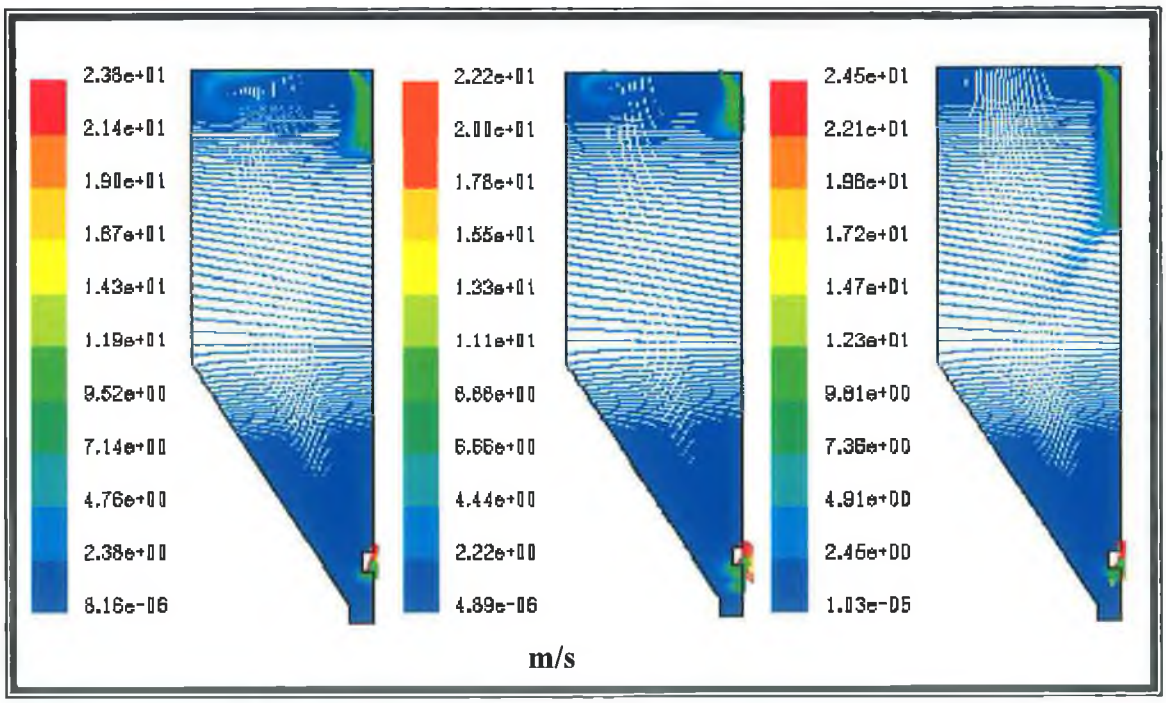

(b)

Figure D-11: Temperature profile (a) and velocity vector (b) by S*K*-Є, R*K*-Є, RSM methods, and measured (inlet condition tem-421 K, velocity-12.7m/s).

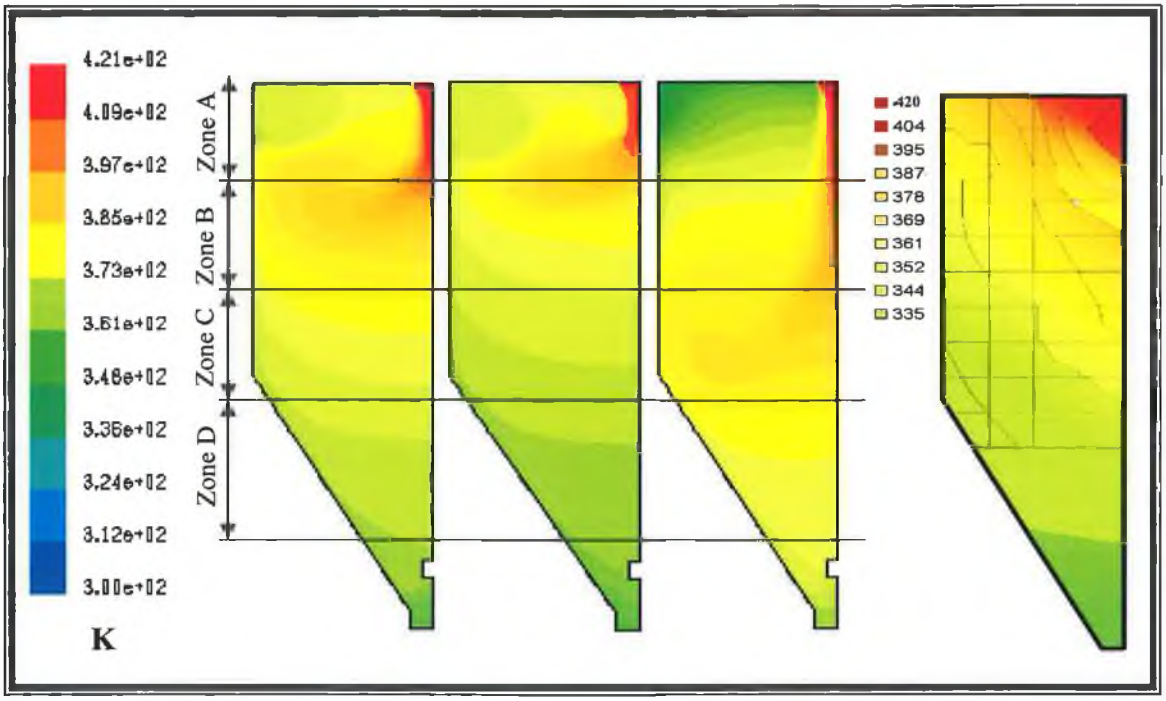

(a)

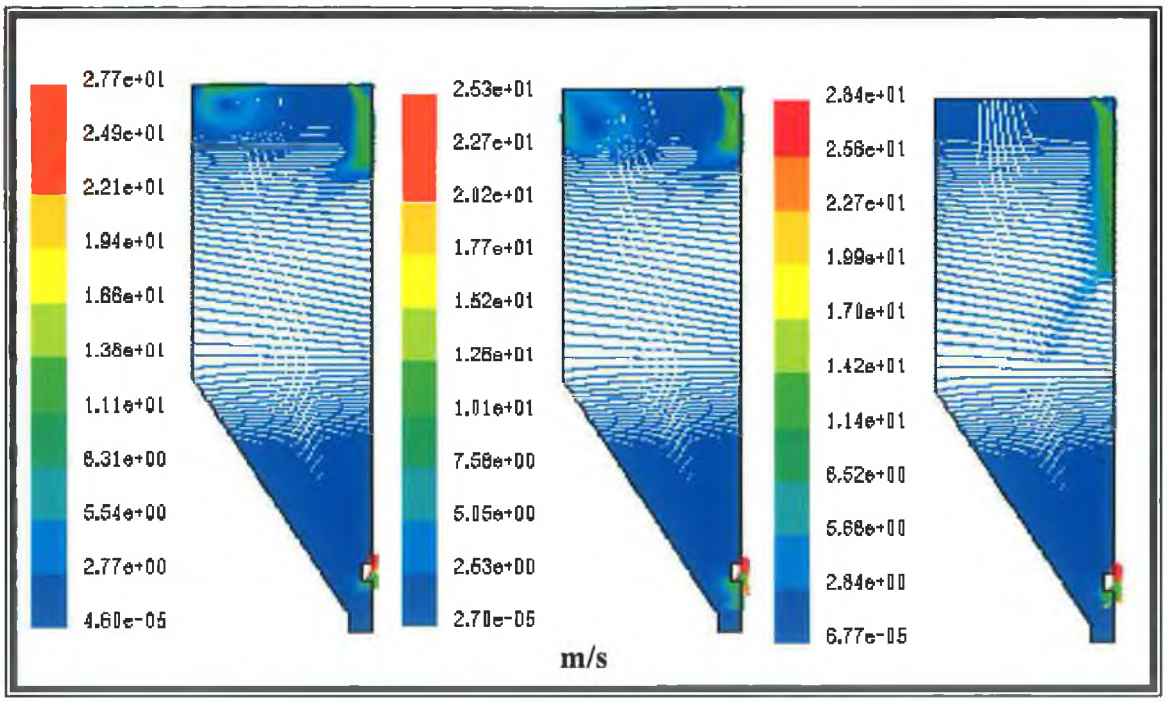

(b)

Figure D-12: Temperature profile (a) and velocity vector (b) by S*K*-ϵ, R*K*-ϵ, RSM method, and measured (inlet condition tem-421 K, velocity-14.6m/s).

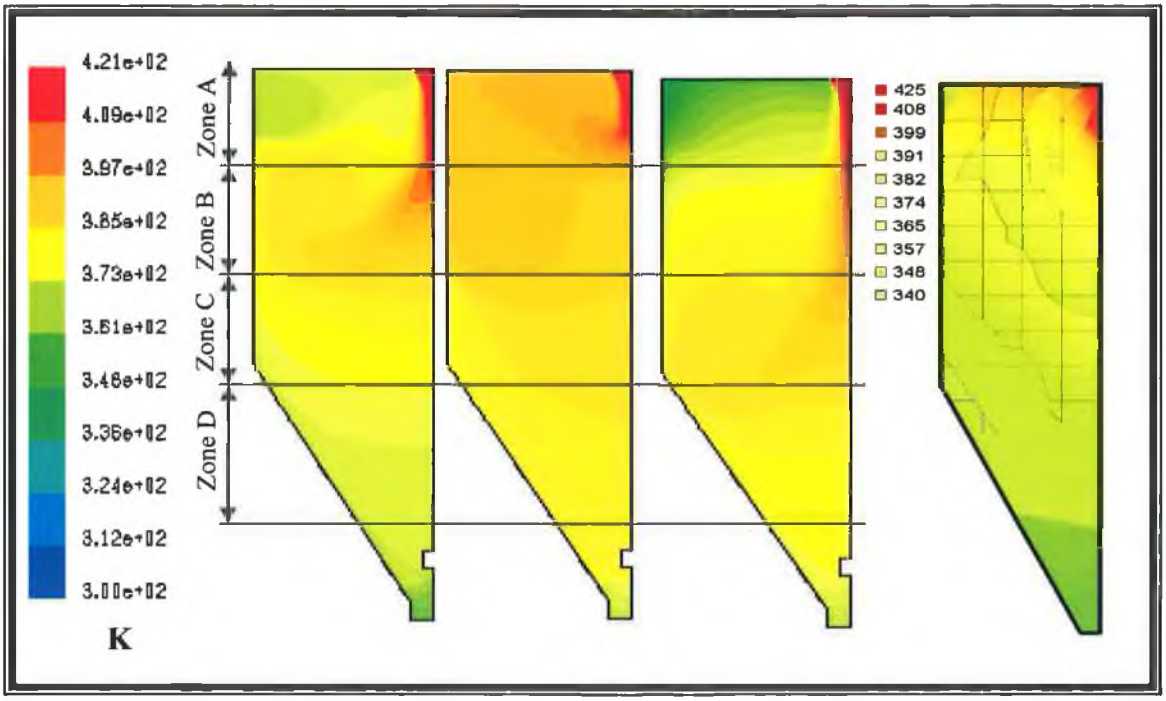

(a)

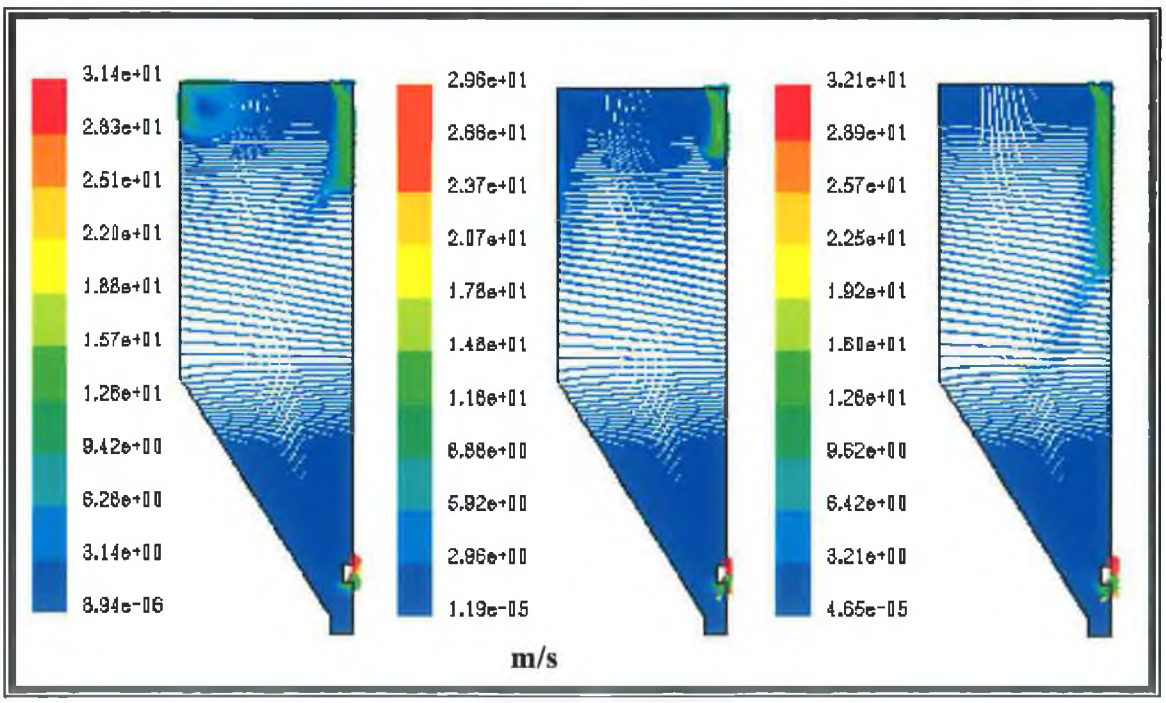

(b)

Figure D-13: Temperature profile (a) and velocity vector (b) by S*K*-ϵ, R*K*-ϵ, RSM method, and measured (inlet condition tem-421 K, velocity-16.6m/s).

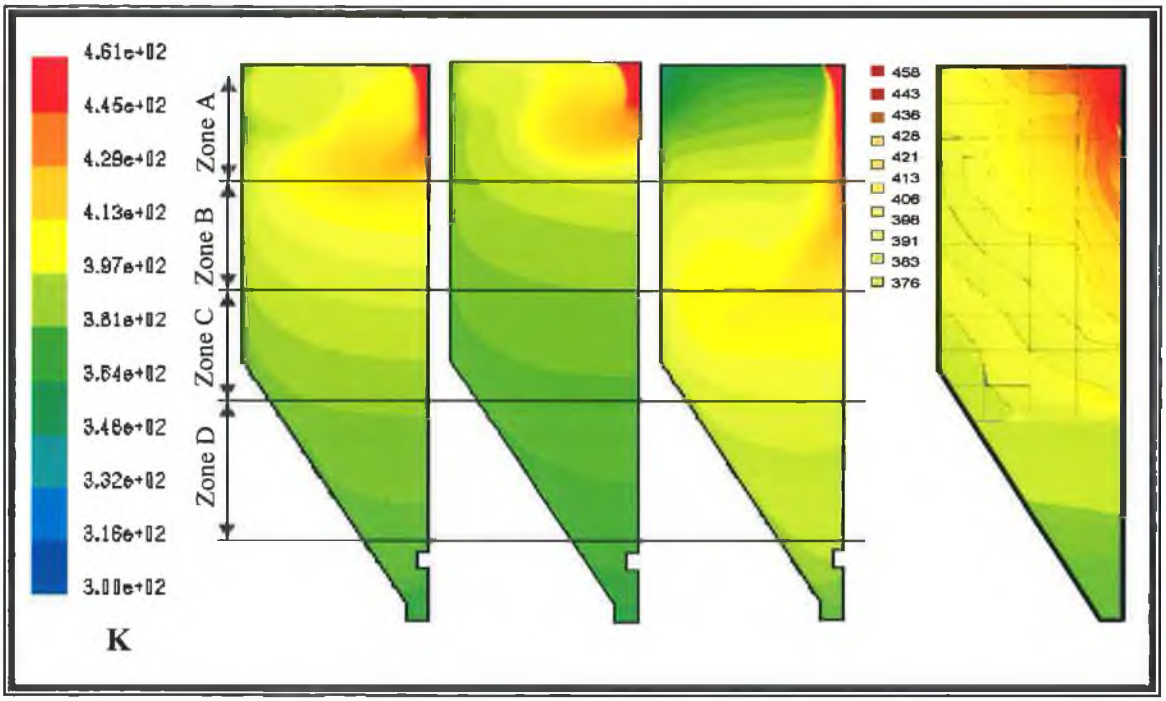

(a)

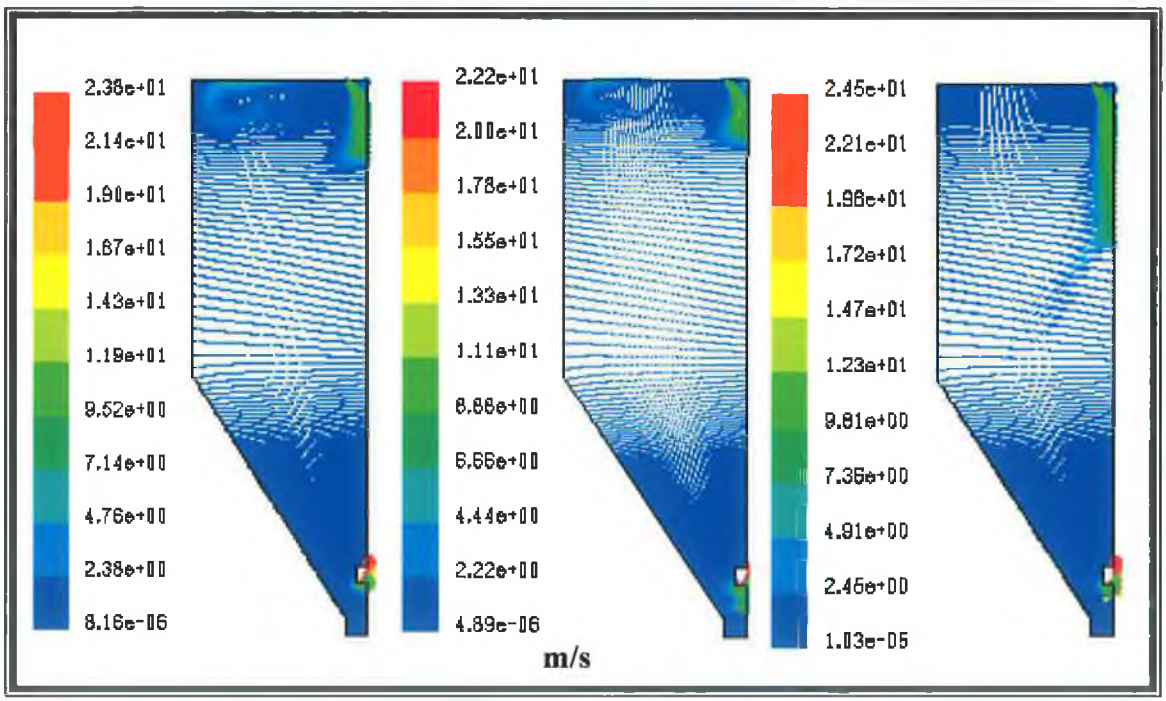

(b)

Figure D-14: Temperature profile (a) and velocity vector (b) by S*K*-ϵ, R*K*-ϵ, RSM method, and measured (inlet condition temperature-461 K, velocity-12.6m/s).

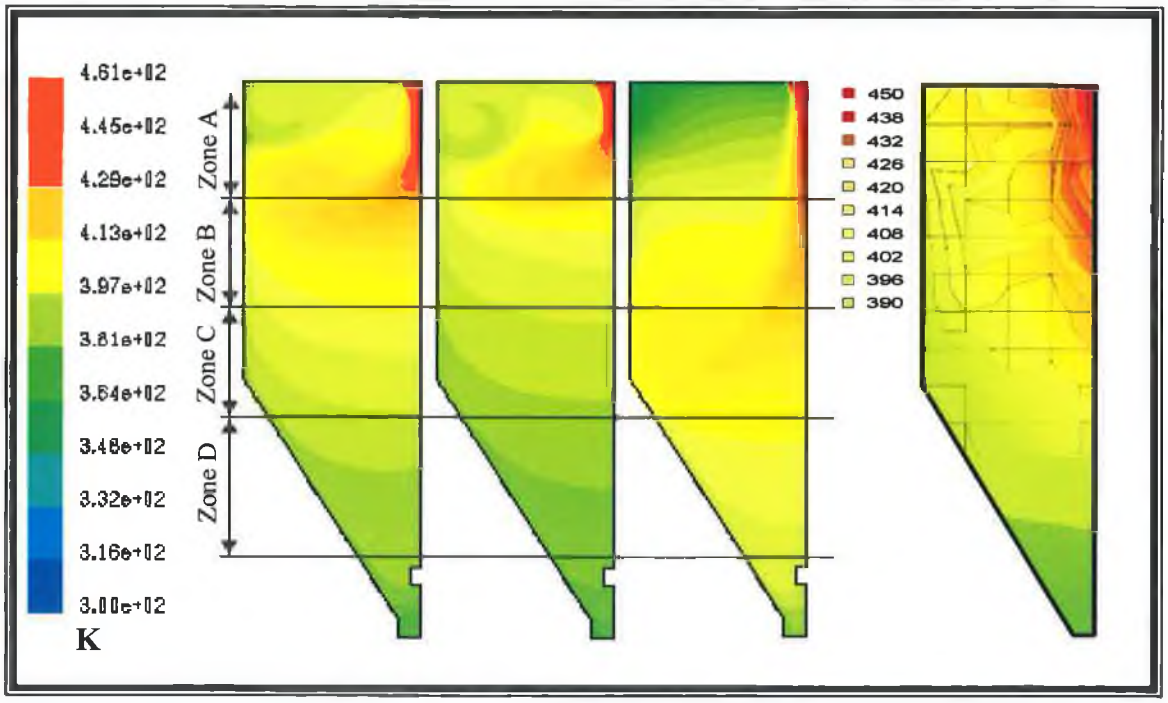

(a)

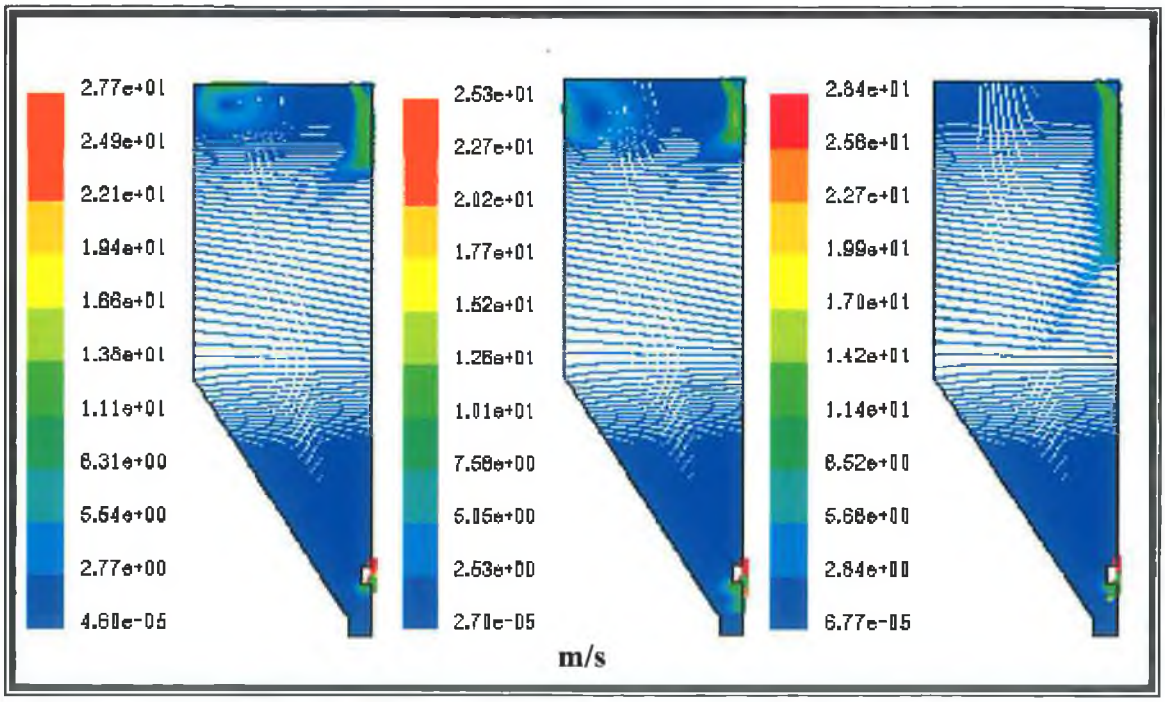

(b)

Figure D-15: Temperature profile and velocity vector by SK-ϵ, RK-ϵ, RSM method, and measured (inlet condition temperature-461 K, velocity-14.6m/s).

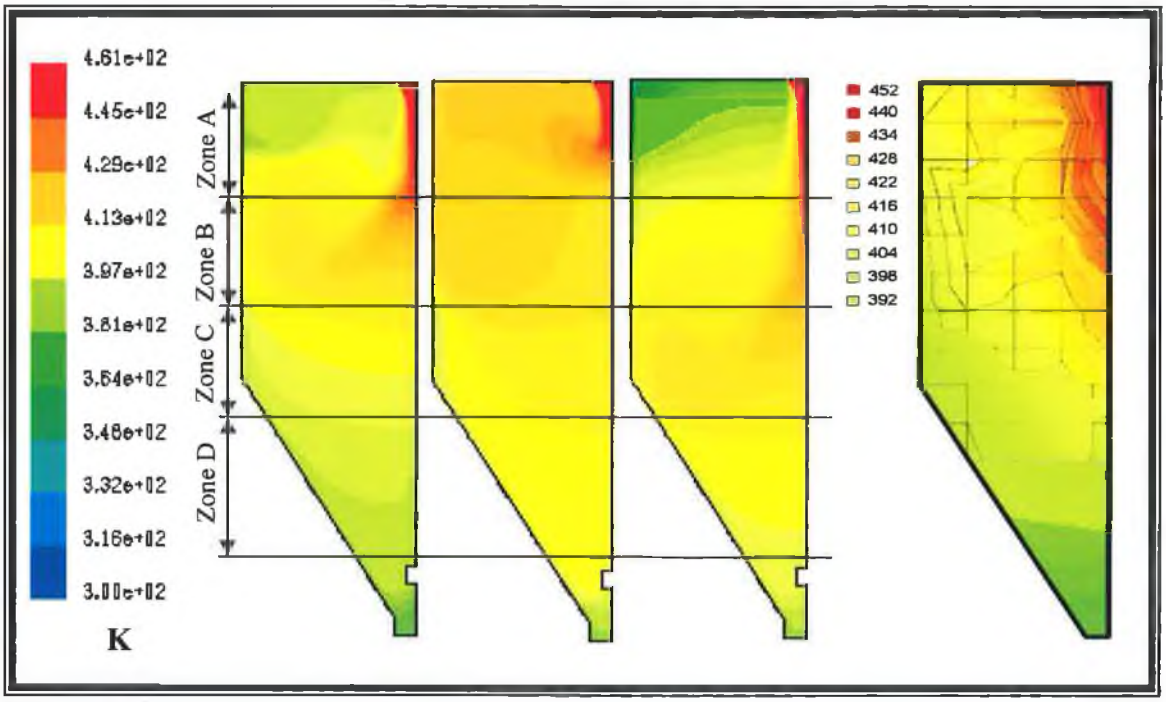

(a)

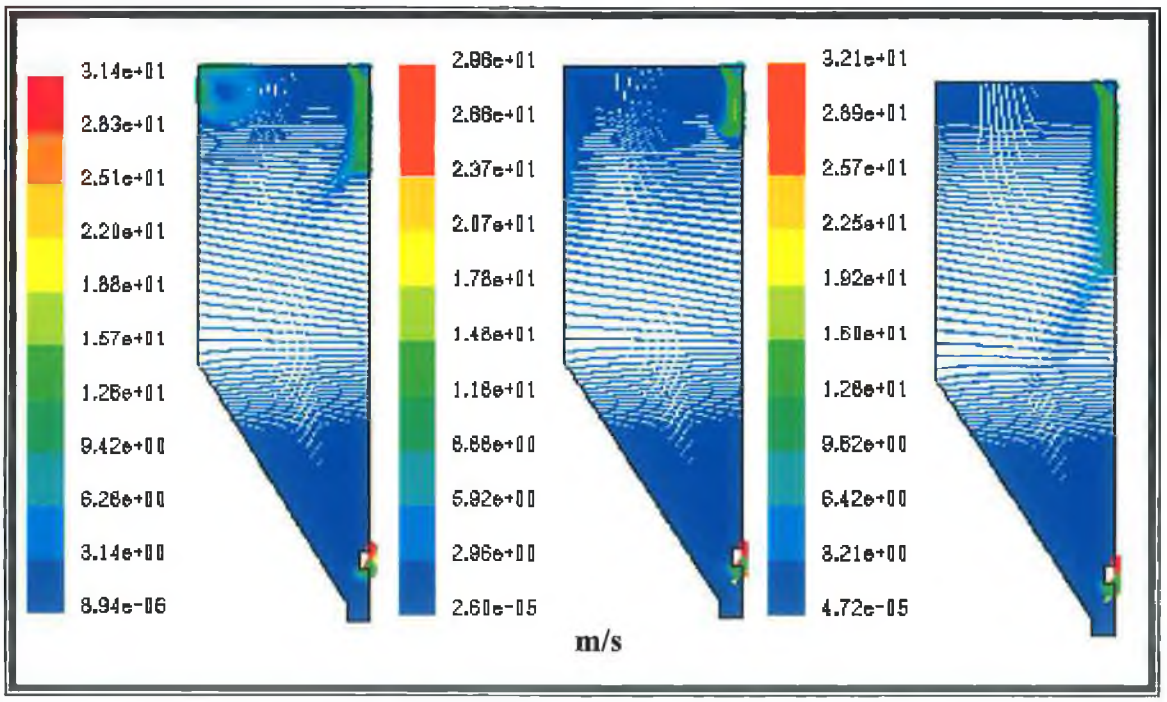

(b)

Figure D-16: Temperature profile and velocity vector by S*K*-Є, R*K*-Є, RSM method, and measured (inlet condition temperature-461 K, velocity-16.6m/s).

Table D2: HA SLURRY PROPERTIES USED IN ATOMISATION SIMULATION

Water –liquid / HA slurry

Density (kg/m^3)	1180.35
Cp (J/kg)	4182
Thermal Conductivity (W/mK)	0.6
Viscosity (mPa.s)	75
Latent heat (J/kg)	2263073
Vaporisation temperature (K)	284
Boiling point (K)	373
Volatile component fraction (%)	80
Binary Diffusion (m^2/s)	3.05×10^{-5}
Saturation Vapour pressure (P)	26501
Droplet surface tension (N/m)	0.07194

Table D3: INJECTION OF NOZZLE PROPERTIES

Injection type	Air blast Atomiser
Numbers of streams	60
Particle type	Droplets
Inlet slurry temperature(K)	300
Flowrate (kg/s)	4.730×10^{-4}
Start time (s)	0
Stop time (s)	2
Injector inner diameter (m)	0.0 m
Injector outer diameter (m)	0.0015
Spray half angle (degrees)	-22.5
Relative velocity (m/s)	86.0
Sheet constant	12
Ligament constant	0.5